Computational Fluid Dynamics Simulations of Personalised Ventilation

Natalie Ariana Gilkeson

Submitted in accordance with the requirements
for the degree of Doctor of Philosophy

The University of Leeds

School of Civil Engineering

August 2018

Intellectual Property and Publication Statements

The candidate confirms that the work submitted is her own, except where work which has formed part of jointly authored publications has been included. The contribution of the candidate and the other authors to this work has been explicitly indicated below. The candidate confirms that appropriate credit has been given within the thesis where reference has been made to the work of others.

Two peer-reviewed conference papers were produced from results presented in **Chapter 5: Temperature and placement of personalised ventilation with breathing zone measurements**:

1. Computational Fluid Dynamics simulations of Personalised Ventilation: The effect of distance and temperature on thermal comfort and air quality. Natalie A. Gilkeson, M. Amirul Khan, Catherine J. Noakes. RoomVent and Ventilation Conference, June 2018 [Gilkeson et al., 2018b].

2. Computational Fluid Dynamics simulations of Personalised Ventilation: Sampling air quality in the breathing zone. Natalie A Gilkeson, M Amirul I Khan, Catherine J Noakes. Indoor Air Conference, July 2018 [Gilkeson et al., 2018a].

The candidate defined the problems and conducted the research. The candidate was the lead author who wrote the draft papers. The candidate made any necessary revisions based on comments from co-authors and reviewers.

For my amazing family, without whom,
none of this would have been possible.

ACKNOWLEDGEMENTS

I would like to express my sincere gratitude to my primary supervisor, Professor Catherine Noakes, for the opportunity and guidance throughout this research. I would also like to thank Dr Amirul Khan and Dr Marco-Felipe King for their comments and inputs in this work. Finally, thank you to my husband, for his unwavering support.

This work was funded through a PhD studentship awarded through the EPSRC Doctoral Training Partnership and the EPSRC Refresh project EP/K021834/1.

This work was undertaken on ARC2, ARC3 and POLARIS, part of the High Performance Computing facilities at the University of Leeds, UK.

ABSTRACT

Personalised ventilation (PV) systems create a micro-climate around individuals in indoor environments, and they have the potential to improve personal comfort, indoor air quality and productivity of building occupants. The focus of the research undertaken in this Ph.D was to determine whether the use of PV strategies can enhance thermal comfort and air quality compared to a traditional displacement ventilation technique. The studies were simulation based and considered multiple configurations, with the methods validated against a benchmark test case. Computational Fluid Dynamics (CFD) simulations modelled the deployment of clean air to a seated computational thermal manikin (CTM) in a mechanically ventilated chamber. The effects of radiation were accounted for using the Discrete Ordinates (DO) model which enhanced the prediction of thermal properties in the domain. High-fidelity CFD simulations were computed on meshes of 5.4 million cells for single CTM cases and up to 9.4 million cells for two CTMs. Solutions were generated using the transition SST turbulence model which accounted for the range of Reynolds numbers from laminar to turbulent, in every single flow field.

Results showed that PV jet temperature and its proximity to a CTM face influences airflow patterns which in turn impacts the levels of thermal comfort and indoor air quality seen. It is important to use realistically shaped CTMs in conjunction with the heat flux thermal boundary condition if details of the flow and thermal comfort is important. In contrast, where details of the flow field in small spaces are unimportant, a simplified CTM in the form of an upright cylinder is suitable, simplifying the modelling process. A PV jet with no thermal mass in the domain can give an indication of where best to place the PV nozzle, for a given set of conditions.

For simulations using realistic CTM shapes, there exists a strong interaction between the PV jet, the convective boundary layer around the CTM and the thermal plume. If the PV jet is placed too far away from the CTM (outside of the zone of flow establishment), air quality can be impaired and may lead to worse air quality than room ventilation alone. Extending the work to two CTMs in a room highlighted the fact that both thermal plumes tended to move towards each other with the strength of attraction greater when the CTMs were in closer proximity. This mutual plume attraction phenomenon set up two large recirculation currents in the room which were somewhat different to the single CTM flow fields. Overall, a significant conclusion from this research is that PV systems can be very effective for improving air quality and thermal comfort if used appropriately, however they can also prove to be detrimental to the overall indoor environment when poorly placed.

Contents

List of Figures

List of Tables

ABBREVIATIONS

ACE	Air Change Effectiveness
AD	Absolute Deviation
AQI	Air Quality Index
BC	Boundary Condition
BZ	Breathing Zone
CAD	Computer Aided Design
CBL	Convective Boundary Layer
CFD	Computational Fluid Dynamics
CTM	Computational Thermal Manikin
DO	Discrete Ordinates
DV	Displacement Ventilation
GCI	Grid Convergence Index
IAQ	Indoor Air Quality
MAOA	Mean Age of Air
MV	Mixing Ventilation
NV	No Ventilation
PAQ	Perceived Air Quality
PDE	Partial Differential Equation
PMV	Predicted Mean Vote
PPD	Predicted Percentage Dissatisfied
PV	Personalised Ventilation
RANS	Reynolds Averaged Navier-Stokes
RMSE	Root Mean Square Error
RTE	Radiative Transport Equation
SBS	Sick Building Syndrome
SST	Shear Stress Transport
TC	Thermal Comfort
UDF	User Defined Function
UDS	User Defined Scalar
V & V	Verification and Validation
ZFE	Zone of Flow Establishment

NOMENCLATURE

Ar	Archimedes number
ach	Air changes per hour
α	Thermal diffusivity
β	Thermal expansion coefficient
C_p	Specific heat at constant pressure
c_{in}	Pollution concentration in supply air
c_{out}	Pollution concentration in extract air
c_{oz}	Pollution concentration in occupied zone
D	Dimension of a mesh
d	Diameter
E	Energy
E_{12}, E_{21}	Error estimates
ε	Turbulent dissipation rate
ϵ_a	Air change effectiveness
ϵ_t	Heat removal effectiveness
ϵ_v	Ventilation effectiveness
F_s	Safety factor
f_1, f_2	Solutions for grids 1 and 2
f_cl	Clothing surface area factor
f_d	Diffuse fraction
f_exact	Exact solution
Gr	Grashof number
$\vec{g}$	Acceleration due to gravity
Γ	Diffusion
h_1, h_2	Grid spacing for for grids 1 and 2
h_c	Convective heat transfer coefficient
h_r	Radiative heat transfer coefficient
I_t	Turbulent intensity
i_cl	Clothing insulation
k	Turbulent kinetic energy
κ	von Karmen constant
L	Characteristic length
M	Metabolic rate
μ	Dynamic viscosity
μ_t	Turbulent viscosity
NE	Number of elements in a mesh
N_θ, N_ϑ	Number of control angles
N_{θ_p}, N_{ϑ_p}	Number of pixels
n	refractive index
ν	Kinematic viscosity
$\tilde{\nu}$	Turbulent kinematic viscosity
ω	Specific dissipation rate
p	Pressure
p_s	Partial water vapour pressure
φ	Generic scalar term
Q	Air flow rate
R	Radius
Ra	Rayleigh Number
Re	Reynolds Number
R_ϵ	Ventilation effectiveness ratio
r	Grid refinement ratio
ρ	Density
ρ	Order of convergence of solution
S	Source term
St	Stokes number
T_a	Average air temperature
T_cl	Surface temperature of clothing
T	Temperature
T_{in}	Temperature of inlet air
T_op	Operative temperature
T_{out}	Temperature of exhaust air
T_{oz}	Temperature of air in occupied zone
T_r	Mean radiant temperature
t	Time
τ	Mean age of air
τ_n	Nominal time constant
τ_{out}	Age of extract air
θ	Polar angle
ϑ	Azimuthal angle
U	Typical flow speed
$\vec{u}$	Velocity
$\overline{u}$	Mean velocity
u^+	Dimensionless velocity
u_τ	Shear velocity
V	Volume
v	Air speed
v_ar	Relative air velocity
W	External work
x, y, z	Cartesian coordinates
y^+	Dimensionless wall distance

1. Introduction

Contents

1.1 Research overview

The focus of the research undertaken in this Ph.D was to determine whether the use of personal ventilation strategies can provide enhanced thermal comfort and air quality than traditional displacement ventilation techniques. The studies were simulation based and considered multiple configurations, with the methods validated against benchmark test cases. Computational Fluid Dynamics (CFD) simulations modelled the deployment of clean air to a seated computational thermal manikin (CTM) in a mechanically ventilated chamber, which involved understanding and accurately modelling the underlying physics of natural convection, radiation and jet flows, along with the effect of heat sources such as thermal manikins.

1.1.1 Research motivation, aims and objectives

Research motivation:

Almost half of worldwide energy consumption is dedicated to heating and ventilating non-industrial buildings, such as homes and offices [Ward, 2004]. Current thinking for sustainable buildings primarily focuses on energy efficiency, often neglecting the potential health implications on the humans who use the space. Increasing building air-tightness and reducing ventilation rate improves thermal efficiency but can be detrimental to the indoor air quality. A significant side effect of people staying indoors is the phenomenon of Sick Building Syndrome (SBS) which manifests itself through general lethargy and headaches in addition to non-specific effects to the eyes, nose, throat and skin [Jaakkola and Miettinen, 1995]. General SBS symptoms occur in all populations [Jaakkola et al., 1994], illustrating the widespread effect. Reducing SBS and related effects is important, not least for occupant health [Sundell, 2004].

Seppänen et al. [2002] suggested that pragmatic and functional solutions to lower energy demand indoors is to reduce the minimum ventilation required in such spaces. It has been shown that maintaining a thermally monotonous environment is energy intensive and that savings can potentially be made by incorporating personal control [Brager et al., 2015]. One way to do this is to allow occupants to create bespoke localised environments [Parkinson and De Dear, 2015]. The ability to assert individual control over, and interact with, an individual micro-climate's heating and ventilation is shown to have a significant impact on the level of thermal comfort experienced and the IAQ in the breathing zone [Boerstra et al., 2015; De Dear et al., 2013; Kaczmarczyk et al., 2010; Melikov and Knudsen, 2007; Roetzel et al., 2010; van Hoof, 2008].

Personalised ventilation (PV) is a targeted approach for delivering clean air to the breathing zone. This has the advantage of creating micro-climates around individuals with the potential for improving personal comfort, indoor air quality, productivity and potentially using less energy than standard ventilation. PV can be supplied through a variety of means, such as a nozzle facing the person as in Dalewski et al. [2014]; above the head as in Makhoul et al. [2013]; wearable devices as in Bolashikov et al. [2013]; or more novel approaches such as ventilated beds in Nielsen et al. [2007b] and chairs in Melikov et al. [2012]. These will be covered in more detail in Chapter 2.

This PhD is aligned with the multidisciplinary EPSRC funded ReFresh project [Refresh, 2015], working towards lower energy usage in offices (for a lower financial cost and carbon footprint) with long-term sustainability whilst simultaneously improving the conditions for occupants and positively impacting their productivity.

Research aim:

To develop an understanding of the relationships between airflows, thermal comfort and indoor air quality for personalised ventilation systems, and establish appropriate methods for modelling such systems using Computational Fluid Dynamics (CFD).

Research objectives:

1. Establish suitable computational methods for modelling personalised ventilation systems under steady state conditions including heat transfer and turbulence models.
2. Assess the influence of computational thermal manikin geometry on air distribution, air quality and heat transfer with and without the presence of a personalised ventilation system.
3. Quantify the influence of personalised ventilation system placement and temperature on air distribution, air quality and thermal comfort under steady state conditions.
4. Explore the impact that two occupants with personalised ventilation have on room and personal airflow patterns, thermal comfort and air quality.
5. Develop guidelines which will inform future modelling and simulation practice in the area of personalised ventilation systems.

1.1.2 Contribution to knowledge

The research undertaken in this PhD, and the findings presented in this thesis, extends and complement the current knowledge of computational modelling and use of PV systems in the following ways:

1. Extending the current knowledge of computational modelling of PV systems in indoor environments

with a computational thermal mass.

2. Guidelines for applicability of modelling simplifications.
3. Placement of PV systems.
4. Interaction of PV jet flow with the convective boundary layer and thermal plume.
5. Improvements to thermal comfort does not guarantee enhanced air quality - a poorly located PV jet can cause a significant deterioration in air quality compared to no PV, yet still improve the thermal comfort.
6. Effect of a PV system on another occupant.

1.2 Thesis Structure

In order to ascertain the current state of knowledge in the relevant areas, the thesis begins with a comprehensive literature review (Chapter 2). This chapter covers the wider topics, such as indoor air quality, ventilation (including personalised) and thermal comfort in addition to specifics such as guidelines and metrics. A background for the computational simulations is presented, covering the physical processes required. These include fluid flows with turbulence, natural convection and radiation modelling. Application of these methods in similar scenarios is also discussed. Finally, gaps in knowledge are identified and highlighted.

Building on this foundation, a robust modelling approach is established in Chapter 3 upon which the remainder of the research in this thesis will be based. The purpose of this chapter is demonstrate the reliability and accuracy of the computational predictions under known conditions in order to have confidence in the results in related scenarios. Elements of the simulations are systematically considered. Radiation modelling is validated against an analytical solution. An experimentally validated benchmark test case for personalised ventilation is used to gain understanding of the processes, challenges and physics involved in such simulations. Aspects of such simulations are considered in more detail, such as jet flow, meshing and boundary conditions. This chapter produces the computational domain and settings for the simulations used in the rest of the work undertaken.

Chapter 4 focuses on the factors involved in simulating indoor air quality and thermal comfort. A realistically shaped computational thermal manikin is compared with a simplified cylindrical thermal mass, with respect to their impact on the room air flow, air quality and thermal comfort. The impact of different thermal boundary choices is highlighted and methods for determining thermal comfort are compared. The findings from this chapter extend current knowledge on computational modelling of indoor air flows and personalised ventilation.

A parametric study directly follows in Chapter 5, implementing the recommendations from the previous work. Variations in the temperature of the personalised ventilation are examined, along with distance from the breathing zone and perturbations in the wider thermal boundary conditions. As in previous chapters, the ramifications of these modifications are explored in terms of the room air flow, air quality and thermal comfort. The primary contributions to knowledge from this chapter have been disseminated in two conference papers Gilkeson et al. [2018a,b].

Novel work on the effect of PV systems on adjacent occupants is shown in Chapter 6. The outputs from the results chapters are reviewed in Chapter 7, with the final conclusions and guidelines drawn in Chapter 8 .

2. Background

Contents

This chapter considers a range of background material relevant to the work which follows in Chapters $3-7$. Aspects such as indoor air quality (§2.1), ventilation (§2.2) and thermal comfort (§2.3) are described before an overview of relevant Computational Fluid Dynamics (§2.4) is covered. Finally, details of how indoor flows are modelled (§2.5), including key aspects of the current state-of-the art research in the field (§2.5.3) and knowledge gaps (§2.6). This paves the way for the detailed investigation into personalised ventilation which follows.

2.1 Indoor Air Quality (IAQ)

Indoor air quality (IAQ) is particularly important for health and well being given that people spend most of their time indoors [van Marken Lichtenbelt et al., 2017], on average 90 % in industrialised countries

[Höppe, 2002]. This section details some aspects of IAQ which have become increasingly topical as we approach the end of the second decade of the 21^{st} century.

2.1.1 Sick Building Syndrome (SBS)

It has been long established that the quality of indoor air can have a significant impact on human health [Sundell, 2004]. The Indoor Air Quality (IAQ) can vary from building to building, some buildings suffering more than others by unsatisfactory IAQ and the knock-on effects this causes - a phenomenon often termed Sick Building Syndrome (SBS) [McMullan, 2012; Mendell and Smith, 1990]. Occupants in open-plan offices, for example, are more likely to complain of poor air quality and SBS symptoms [Pejtersen et al., 2006]. General SBS symptoms occur in all populations [Jaakkola et al., 1994] and can include non-specific effects to the eyes, nose, throat and skin; in addition to general lethargy and headaches [Jaakkola and Miettinen, 1995], the symptoms of which decrease when the occupant leaves the building [Seppänen et al., 2002].

Typically, in developed countries 30-50% of energy used is by non-industrial buildings including homes and offices [Liddament and Orme, 1998] (for heating, cooling, lighting and ventilating) with an average consumption rate of 40% worldwide [Ward, 2004]. The largest single use is for air-conditioning in hot climates and heating in cold ones [Roetzel et al., 2010]. In some cities this alone accounts for almost all of the electricity required [Linden, 1999]. Changes in how buildings were constructed - typically with controlled lighting, ventilation and temperature - after the fuel crisis in the 1970s have coincided with the prevalence of SBS symptoms [Rostron, 1997].

Characteristics of a typical building whose occupants suffer SBS symptoms are that the building is air tight with air conditioning, with a large percentage of recycled air and has a large surface-to-volume ratio of surfaces covered in textiles such as carpets [Eastop and Watson, 1992]. The energy lost due to ventilation processes, dissipated externally into the surrounding air, is expected to increase as buildings become more thermally efficient [Liddament and Orme, 1998], yet increasing the air tightness of buildings for thermal efficiency is increases SBS symptoms and lower IAQ [Cao et al., 2014]. Pragmatic and functional solutions could reduce the minimum ventilation required and hence the energy consumption [Seppänen et al., 2002].

The increased SBS symptoms in air conditioned buildings when compared to those which are naturally or mechanically ventilated [Mendell and Smith, 1990; Wargocki et al., 2002] could in part be due to poorly maintained air conditioning units which may introduce pollutants internally and lower the IAQ [Seppänen and Fisk, 2002]. When suitably filtered and mixed with enough new external air, a large percentage of used air can be recirculated without ill effects [Jaakkola et al., 1994]. This, however, assumes that the external air is free from pollution such as that generated by vehicles and manufacturing

Studies have shown that men and women perceive psycho-social stresses differently [Runeson et al.,

2006], with women exhibiting a greater sensitivity to SBS symptoms than men [Rasche et al., 2001; Runeson et al., 2006; Skyberg et al., 2003]. Whilst it appears that the only additional work related risk factor for men is age, additional factors for women include the number of people per room and allergies [Rasche et al., 2001]. Therefore, when designing work environments, consideration should be given to all the needs and requirements of all the intended occupants [Rasche et al., 2001]. The workspaces should be uncrowded [Chao et al., 2003] with laser printers and similar machines (which can emit VOCs (volatile organic compounds) and ultrafine particles such as un-reacted toner) in separate, ventilated rooms [Skyberg et al., 2003].

2.1.2 Indoor pollutants, infection and contaminant transmission

Office cleanliness has also been shown to play a role in the prevalence of SBS symptoms reported, the number of which is reduced by frequent cleaning [Skyberg et al., 2003]. In part, this is due to a correlation between fungi and dust on office chairs in addition to the general floor dust with SBS symptoms [Chao et al., 2003]. Other pollutants include CO_2 and bio-effluents [Bivolarova et al., 2017; Zhang et al., 2017] emitted from occupants, as well as the potential for infection transmission from breathing, coughing and sneezing [Gao and Niu, 2006].

In terms of contaminant transmission, Licina et al. [2015a] found that the convective boundary layer (CBL) around a computational thermal manikin (CTM) has the potential to transport pollution around the human body. A non-linear dependence between air supply rate and personal exposure was found with a pollutant source at the feet of the CTM in a small room. This study underlines the necessity of understanding airflow patterns in these scenarios. Another related study [Licina et al., 2015d] found that the location of the pollutant source had a considerable effect on the breathing zone pollutant levels. For instance, a source release from the chest area leads to the greatest breathing zone pollutant levels whereas sources located behind the upper back or chair results in negligible exposure to the pollutant. Other factors affecting contaminant transmission include the angle of inclination of the simulated human [Licina et al., 2015d], the position of the chair [Licina et al., 2015c] and the air supply rate [Licina et al., 2015a].

Studies involving multiple occupants have also highlighted how pollutants can move from person-to-person. A review by Nielsen [2015] of CFD for room air distribution outlined how cross-infection is dependent on many factors including the ventilation regime, thermal load and room geometry. One CFD investigation showed, using a Lagrangian approach, how exhaled droplet-borne nuclei can spread from one occupant to another [Liu and Li, 2012]. Droplets of 100 microns were released from one occupant and evaporation was incorporated. A critical parameter was found to be the ambient relative humidity. For a low humidity of 35 % droplets evaporated by up to 60 % and they were shown to rise with the thermal boundary layers produced by both occupants. This meant that the droplets resided in the breathing zone, leading to a greater risk of cross-infection. In contrast, for a high relative

humidity of 95 %, the droplets showed significantly less evaporation (10 %) and they tended to sink to the floor level, thereby posing less of an infection risk [Liu and Li, 2012]. Experimental work by Nielsen [2009] had shown that tracer gas distributions can estimate airborne cross-infection risk in ventilated rooms. An important conclusion from this work was that personalised ventilation (PV) has great potential to reduce cross-infection for the intended recipient [Nielsen, 2009] as well as potential improvements to thermal comfort. In the context of multi-occupant spaces other authors have also shown that PV systems placed in chairs, desks and suspended from ceilings can offer potential improvements to both energy consumption and cross infection with targeted delivery of fresh air [Habchi et al., 2016a,b].

2.1.3 Productivity and economic benefits

Poor IAQ impacts negatively on productivity [Cao et al., 2014; Wargocki et al., 2000a; Wyon, 2004] which has economic side-effects [Brager et al., 2015]. The productivity of building occupants not only increases as the temperature tends towards a thermal comfort zone [Seppänen et al., 2006a; Shan et al., 2018] (decreasing outside of this zone [Seppänen and Fisk, 2003]), but also with increased ventilation rate [Seppänen et al., 2006b; Wargocki et al., 2002], which reduces indoor pollution and decreases SBS symptoms [Wargocki et al., 1999, 2000b].

Liddament [2000] notes that current ventilation approaches tend to favour displacement over other methods which frequently require independent systems to heat and cool a space. These strategies will have an economic consequence. Displacement ventilation, for example, cannot be used to heat a space. Notwithstanding the clear benefits of increasing ventilation rates, there may be a financial penalty incurred in the form of increased consumption of energy of the building [Seppänen et al., 2002]. However this may be negated by the higher productivity of the workers [Brager et al., 2015; Tanabe et al., 2015; Wargocki et al., 2000b] and other economic benefits [Wyon, 2004] such as reduced sick leave [Fisk et al., 2005; Wargocki et al., 2002], lower medical bills and lower building maintenance [Brager et al., 2015; Seppanen and Fisk, 2005]. Typically only the initial costs, energy and maintenance are considered in the economic calculations [Seppänen et al., 2005], however the costs associated with steps taken to improve the IAQ have been shown to be cost effective [Seppänen and Fisk, 2003]. Effective control of pollutants in the ventilation process could reduce the energy consumption of the building [Seppänen et al., 2002] yet still provide the benefits noted above whilst maintaining building sustainability with respect to the energy requirements. Eliminating pollutants at their source could reduce ventilation requirements (hence energy consumption and carbon footprint) further [Liddament and Orme, 1998]. Ensuring appropriate filters are used makes the filtration costs to remove pollutants insignificant in comparison to wages or health costs [Fisk et al., 2002].

2.2 Ventilation

The removal of used (stale) air and replacing it with new (clean) air is a process known as ventilation [McMullan, 2012]. Natural ventilation depends on external weather conditions [Etheridge, 2015], which are difficult to control [Linden, 1999]. The movement of the air can be driven by wind turbulence, a temperature difference or by pressure differences across building openings causing cross ventilation [Ward, 2004].

2.2.1 Mixing and displacement ventilation

In the case of mechanical ventilation, the new air can either mix with the used air or displace it. Mixing ventilation is the traditional method by supplying cool air from the walls or ceilings [Chen et al., 2015], diluting the pollutants in the air to a uniform level [Liddament, 2000]. This requires energy to heat and cool the air, in addition to moving it. Displacement ventilation separates the breathing zone from the pollutants [Liddament, 2000] by utilising the effects of buoyancy as the cool air supplied at a low level displaces the warm air above it [Chen et al., 2015]. Displacement supply methods cannot be used for heating spaces, however they are generally more efficient at ventilating than mixing methods [Chen et al., 2015] as the whole space does not require ventilating to achieve the same air quality in the breathing zone. Hybrid supply systems use elements from both types, however displacement methods are usually more efficient all round [Chen et al., 2015]. Cao et al. [2014] presents a summary of the literature for both mixing and displacement ventilation.

Ventilation is strongly associated with perceived air quality (PAQ) and SBS [Wargocki et al., 2002]. However current ventilation standards for IAQ are based on occupants' perception [Sundell et al., 2011]. Too high a ventilation rate, for example, may increase the risk of SBS symptoms [Skyberg et al., 2003]. Perceptions of air movement depend on a variety of personal and environmental factors which can change throughout the day [Toftum, 2004]. Given that perceptions are subjective [Rasche et al., 2001], it is necessary to combine the occupant perceptions with quantifiable and repeatable measurements of air quality [Engvall et al., 2005] for accurate and reliable data.

The likelihood of SBS symptoms in occupants of a building increase when the ventilation rate is low [Fisk et al., 2009; Jaakkola and Miettinen, 1995; Sundell et al., 2011] as the perception of the IAQ is lower [Engvall et al., 2005]. Inadequate levels of ventilation are also linked to the spread of some infectious diseases [Li et al., 2007]. Gender again plays a role as women have been shown to be more sensitive to low ventilation rates than men [Ishii et al., 1990].

One issue connected to a low ventilation rate is an increase in the relative humidity (RH) [Engvall et al., 2005]. This aspect of IAQ is often neglected in favour of temperature which is 'easier to sense, quantify and control' [Simonson et al., 2002]. Increasing both temperature and humidity reduces the PAQ [Fang et al.,

1998a,b]. Furthermore, the ability of materials within the building to attract and hold water molecules from the environment has an impact on the humidity, which can also affect PAQ [Simonson et al., 2002].

Increasing the ventilation rate improves IAQ, with the most improvement found when the lowest ventilation rates are increased [Wyon, 2004]. Consequently, there needs to be sufficient ventilation to maintain and promote occupant health. Insufficient ventilation rates will not prove effective at removing pollutants from the internal air. SBS symptoms are shown to increase in occupants of buildings with increased concentrations of indoor pollutants such as CO_2 [Apte et al., 2000]. Higher ventilation rates result in lower concentrations of CO_2 which significantly reduce SBS symptoms [Seppänen et al., 1999] and sick leave [Fisk et al., 2005]. Other studies indicate that certain chemical reactions emitting volatile organic compounds (VOCs) into the internal air supply are also linked to SBS [Wolkoff et al., 1997]. Effective ventilation will remove or reduce indoor pollutants to a tolerable level. Increasing or improving the effectiveness of the ventilation along with controlling indoor pollutants could have a drastic impact on SBS symptoms of up to 70-85% [Apte et al., 2000]. Outdoor air can be used to achieve this, however the external air quality will vary with location and may introduce further pollutants [Sundell et al., 2011; Wyon, 2004]. The aim of effective ventilation is to maintain good IAQ but prevent additional pollutants entering from external sources [Liddament, 2000]. Increasing ventilation rates with external air supplied from areas subject to less outdoor pollution (such as non-industrial areas) improves PAQ [Wargocki et al., 2002], with the benefits of higher ventilation shown to be greatest when the outdoor air quality is better [Sundell et al., 2011].

Studies have indicated that whilst displacement ventilation can offer better IAQ than mixing ventilation when considering the total volume of air, around half the occupants are dissatisfied [Melikov, 2004]. Displacement ventilation is known for causing uncomfortable temperature gradients between the cool air at the low supply level and the warmer air in the breathing zone [Chen et al., 2015]. Working towards a strategy to provide a homogeneous thermal environment would prove fruitless as this would not satisfy all the building occupants [Faulkner et al., 1999]. Displacement ventilation typically supplies air at a slightly lower temperature than the average internal temperature close to floor level, creating low level draughts and vertical temperature gradients leading to thermal discomfort [Bogdan and Chludzinska, 2010] (cold feet, warm head [Zhang et al., 2005]). It has been found that thermal comfort and sensations of draught can change over a period of time and as their environmental conditions change [Fang et al., 2015]. The ability to assert individual control over an individual micro-climate's heating and ventilation is shown to have a significant impact on the level of thermal comfort experienced and the IAQ in the breathing zone [Boerstra et al., 2015; Kaczmarczyk et al., 2010; Melikov and Knudsen, 2007; Roetzel et al., 2010; van Hoof, 2008], with women requiring greater flexibility than men [Karjalainen, 2012].

2.2.2 Personalised Ventilation (PV)

The aim of personalised ventilation (PV) [Melikov, 2004] is to create such a micro-climate around an individual with better IAQ in the breathing zone and improve thermal comfort whilst reducing the overall energy consumed by decreasing the background (mixing or displacement) ventilation rates and maintaining a higher (or lower) ambient temperature [Melikov, 2004]. In an office, a micro-climate around each work station utilises energy only where it is needed whilst simultaneously providing individual control over thermal comfort [Veselý and Zeiler, 2014]. On an aircraft, for example, the majority of passengers will adjust their personal air supply nozzles improving their PAQ [Fang et al., 2015]. Furthermore, PV need only deliver clean air when an individual work station is occupied [Chludzińska and Bogdan, 2015], raising the possibility of additional energy savings. PV can not only improve the PAQ and reduce SBS compared to traditional forms of ventilation [Kaczmarczyk et al., 2004], it can also improve the IAQ as the new air is delivered straight to the breathing zone [Faulkner et al., 1999] without travelling over a distance acquiring pollutants on the journey [Melikov, 2004]. A PV supply with a low turbulence level is associated with a higher PAQ [Sun et al., 2007]. These systems can provide part or all of the conditioned air to the office space [Faulkner et al., 1999].

PV systems not only have the potential to improve thermal comfort of building occupants, but also their productivity [Faulkner et al., 1999]. In addition, it has been shown that use of outdoor air in the PV system instead of recirculated air also improves PAQ and decreases SBS [Kaczmarczyk et al., 2004]. Reductions in energy required of up to 60 % can be obtained by allowing an ambient temperature several degrees higher or lower than those recommended by employing PV technology [Cruceanu et al., 2013; Veselý and Zeiler, 2014] whilst maintaining IAQ, PAQ and reducing SBS symptopms [Melikov et al., 2013]. van Marken Lichtenbelt et al. [2017] advocate use of personal comfort to expand range of temperatures but also create healthy conditions.

2.2.3 Guidelines

Workplace environments within the UK are governed by UK and EU laws, such as The Workplace (Health, Safety and Welfare) Regulations, SI 1992/3004. In addition there exist international standards including ISO 10551 [British Standards Institute, 2002], ISO 7730 [British Standards Institute, 2006], ISO 15251 [British Standards Institute, 2008] and ISO 13779 [British Standards Institute, 2014]. Further guidance can be sought from government bodies such as the HSE and professional bodies like the Chartered Institution of Building Services Engineers (CIBSE). Guidelines from other countries, for example the American Society of Heating, Refrigerating and Air-Conditioning Engineers (ASHRAE) reports, can offer persuasive but not binding guidance. Throughout this research, the default minimum legal requirement adhered to will be that outlined for medium indoor air quality [British Standards Institute, 2008, 2014] in a multi occupant office.

UK law states, in section 6(1) of The Workplace (Health, Safety and Welfare) Regulations, SI 1992/3004, that "effective and suitable provision shall be made to ensure that every enclosed workplace is ventilated by a sufficient quantity of fresh or purified air". There is no precise legal requirement to achieve this. Furthermore, the fresh air that is sourced should be uncontaminated by external pollution [British Standards Institute, 2014]. The ventilation rate can be given as either per person or per m^2 of floor area [British Standards Institute, 2008]. The suggested ventilation rates are shown in Table 2.1, typically the volume of fresh air per person each second. An alternative ventilation rate is presented in ISO 15251 [British Standards Institute, 2008] to cover both the occupants and also account for background ventilation to deal with general building pollution.

Property	**Value**	**Reference**
Default ventilation rate	$12.5\,\mathrm{l s^{-1} person^{-1}}$	British Standards Institute [2014]
Alternative ventilation rate	$7\,\mathrm{l s^{-1} person^{-1}} + 1\,\mathrm{l s^{-1}\,m^{-2}}$	British Standards Institute [2008]
Ventilation rate range	$10-15\,\mathrm{l s^{-1} person^{-1}}$	British Standards Institute [2014]

TABLE 2.1: Minimum ventilation requirements for offices with medium indoor air quality.

These values correspond with typical air change rates in offices of $2-6$ ach (air changes per hour) [McMullan, 2012]. The ach can be calculated by equation (2.1) below, where $V\,(\mathrm{m^3})$ is the room volume and $Q\,(\mathrm{m^3\,s^{-1}})$ is the supply air flow rate:

$$\mathrm{ach} = \frac{Q \times 60^2}{V} \tag{2.1}$$

For example, a room of size $4\mathrm{m} \times 4\mathrm{m} \times 2.5\mathrm{m}$ with three occupants a ventilation rate of $12.5\mathrm{l s^{-1} person^{-1}}$ corresponds to 3.75 ach, whilst a ventilation rate of $7\mathrm{l s^{-1} person^{-1}}$ plus $1\mathrm{l s^{-1}\,m^{-2}}$ corresponds to 3.33 ach. For four occupants, the air changes required are 4.5 ach and 3.96 ach respectively. The minimum airflow of $7\mathrm{l s^{-1} person^{-1}}$ accounts for dilution of bio-emissions only and would leave up to 20% of occupants dissatisfied with the environment. This figure is consistent with section 6 (paragraph 57) of the guidance [HSE, 2013] which recommends a minimum supply rate of fresh-air of $5-8\mathrm{l s^{-1}}$ per person. Paragraph 54 refers to CIBSE for more detailed guidance. CIBSE, Guide A [2015] recommend a minimum value of $10\mathrm{l s^{-1}}$ per person in an office environment [Clancy, 2011]. This figure is based on minimum respiratory requirements and odour-dilution, and does not guarantee a satisfactory ventilation rate. Linden [1999] states that an individual needs in the region of $7.5\mathrm{l s^{-1}}$ for respiration however at least ten times that amount is required for air changes needed to achieve thermal comfort (although this could be achieved through other means such as recirculated air). Seppänen et al. [2006b] found that studies show a continuous rate of improvement in productivity by increasing the ventilation up to around $45\mathrm{l s^{-1}}$ per person, with the most significant benefits shown up to $15\mathrm{l s^{-1}}$ per person. Sundell et al. [2011] found that the occurrence of SBS symptoms in an office environment was reduced with around $25\mathrm{l s^{-1}}$ per person. In the example room size above, $25\mathrm{l s^{-1} person^{-1}}$ for three occupants corresponds to 6.75 ach, for four it is 9 ach. For

$451\,s^{-1}person^{-1}$ this rises to 12.15 ach for three occupants and 16.2 ach for four, well above the current standard [McMullan, 2012].

Factors including the layout and design of office furniture [Zukowska et al., 2007b] and placement of ventilation ducts also need to be taken into consideration as these will dictate the pattern of airflow within a given room [Linden, 1999]. The air movement need not necessarily be due to ventilation, it may be caused by other factors such as natural convection [McMullan, 2012]. Whilst superfluous air movements can cause draughts, insufficient ventilation allows a build up of waste gases leading to feelings of a stale environment. There are no legal minimum or maximum values [British Standards Institute, 2006], however current recommendations state that during the summer months the air velocities should be in the region of $0.3\,m\,s^{-1}$ and $0.1\,m\,s^{-1}$ for winter months [Clancy, 2011]. Air movement over $0.1\,m\,s^{-1}$ requires an increase in temperature to compensate and maintain comfort levels [McMullan, 2012].

2.2.4 Measurements

Evaluating the performance of building ventilation generally falls into one of two camps: air change effectiveness (ACE) or pollutant removal effectiveness [Federspiel, 1999; Gao et al., 2006]. This can be achieved by measurement of either individual flows in air ducts or tracer gases [British Standards Institute, 2008; Etheridge, 2015]. The ACE can be defined by dividing the average age of the air in the building if it were fully mixed by the average age of air in the breathing zone [Federspiel, 1999; Fisk et al., 1997]. It is a measure of how quickly old air is replaced by new air [Cao et al., 2014]. Perfectly mixed air gives an ACE value of one [Fisk et al., 1997]. The ACE (ϵ_a) is given by equation 2.2 below [Chen et al., 2015]:

$$\epsilon_a = \frac{\tau_n}{2 < \tau >}, \tag{2.2}$$

where τ is the mean age of air, $< \tau >$ is the average age of air in the occupied (or breathing) zone and τ_n is a nominal time constant for a given room of volume $V\,(m^3)$ with an air flow rate of $Q\,(m^3\,s^{-1})$,

$$\tau_n = \frac{V}{Q}. \tag{2.3}$$

An alternative form of the ACE [Faulkner et al., 1999] is given in equation (2.4) where τ_{out} is the age of the extract air:

$$\epsilon_{a'} = \frac{\tau_{out}}{2 < \tau >}. \tag{2.4}$$

The local mean age of air (MAOA) is the statistically average time taken for fresh supply air to reach a spatial location [Chanteloup and Mirade, 2009; Meiss et al., 2013], therby providing a useful measure of ACE and a direct measure of air quality [Simons et al., 1999]. It can be measure experimentally with tracer gasses or numerically as a CFD post-process [Chanteloup and Mirade, 2009; Meiss et al., 2013; Simons et al., 1999]. The method assumes that the air from the supply is supplied and not recirculated or otherwise

mixed. Local MAOA is more sensitive than mean air velocity for evaluating the adequacy of ventilation [Chanteloup and Mirade, 2009].

For buildings where people are the main source of pollutants, the levels of carbon dioxide (CO_2) measured can be used as a tracer gas to approximate both the ventilation rate of a building occupant and also 'occupant-generated pollutants' [Apte et al., 2000]. However this approach should be used with caution as there is not a correlation between CO_2 and every other pollutant [Ramalho et al., 2015]. Moderate concentrations of pure CO_2 is not harmful [Zhang et al., 2017].

Strategies to determine the pollutant removal effectiveness (and hence pollutant exposure) can give a more accurate indication of the efficacy of the ventilation than the ACE as the two are not necessarily correlated [Fisk et al., 1997]. However, the value of the ventilation effectiveness, ϵ_v defined in equation (2.5), can vary between pollutants as it depends on the air distribution and type of pollutant [British Standards Institute, 2014]. When the air and pollutants are completely mixed, the ventilation effectiveness (ϵ_v) value is unity. Exposure effectiveness [Cao et al., 2014] considers the effectiveness of the personalised ventilation measures against pollutant contamination in the breathing zone.

$$\epsilon_v = \frac{c_{out} - c_{in}}{c_{oz} - c_{in}}, \tag{2.5}$$

where c_{in} is the pollution concentration in the supply air ($\mathrm{mg\,m^{-3}}$), c_{out} is the pollution concentration in the extract air ($\mathrm{mg\,m^{-3}}$) and c_{oz} is the pollution concentration in the indoor air or the breathing zone within the occupied zone ($\mathrm{mg\,m^{-3}}$). The heat removal effectiveness, ϵ_t given by equation (2.6), is another measure of ventilation effectiveness which describes how effective the air distribution method is at removing heat in occupied zone [Chen et al., 2015],

$$\epsilon_t = \frac{T_{out} - T_{in}}{T_{oz} - T_{in}}, \tag{2.6}$$

where T_{in} is the temperature of the inlet air, T_{out} is the temperature of the exhaust air and T_{oz} is the temperature of the air in the occupied zone. The ventilation effectiveness ratio, R_ϵ, [Awbi, 1998; Cao et al., 2014] is defined as

$$R_\epsilon = \frac{\epsilon_v}{\epsilon_t}. \tag{2.7}$$

2.3 Thermal comfort

Expectations of the indoor environment are highly subjective and dependent on individual people and what they are used to [Nicol and Roaf, 2017; Parkinson and De Dear, 2015]. The thermal expectations, perceptions, preferences and tolerances vary significantly between a person acclimatised to air-conditioning expecting homogeneity, and another used to natural ventilation with variations in the climate [de Dear and Brager, 2002]. People who are acclimatised to working in warmer climates

generally find it easier to adapt to working in higher indoor temperatures than those acclimatised to colder climates [British Standards Institute, 2006]. The Health and Safety Executive (HSE) is a UK government funded, independent watchdog for work-related health, safety and illness [GOV.UK, 2014]. The HSE defines thermal comfort as "a person's state of mind in terms of whether they feel too hot or too cold" [Health and Safety Executive, 2014], a statement based on the legal definition "that condition of mind which expresses satisfaction with the thermal environment" [British Standards Institute, 2006].

2.3.1 Factors involved in thermal comfort

Six factors are known to influence thermal comfort: four are environmental (air temperature, mean radiant temperature, humidity and air speed) whilst two are personal (activity/metabolic rate and clothing levels) [CIBSE, Guide A, 2015; de Dear and Brager, 2002; Fanger, 1972; Macpherson, 1962; Tham, 1993]. A person's thermal state (dependant on clothing levels and activity) is more important than the actual air temperature when considering how personal heat is lost and gained, although the air temperature is often considered the most important environmental variable [CIBSE, Guide A, 2015]. In addition to affecting thermal comfort the indoor temperature plays a role in PAQ, SBS and work performance [Seppänen et al., 2005].

Individual changes in temperature, humidity or air movement also change the perception of the other two parameters, indicating that they should not be treated as independent variables [Maier and Marggraf-Micheel, 2015]. Higher levels of humidity and lower temperatures can make the air feel cooler, whilst in higher temperatures greater humidity can suppress the ability to cool by perspiration [McMullan, 2012]. Clothing type, for example with a high vapour resistance as with clean room suits, can also impact thermal comfort [Havenith et al., 2002] as sweat evaporating is an important form of cooling. Another example which can influence clothing levels (and hence insulation levels) is local culture, such as fashion and expected business dress code [Fountain et al., 1996]. Studies show that significant differences exist between the sexes both in thermal comfort [Karjalainen, 2012] and indoor temperature tolerances [Ishii et al., 1990]. Women exhibit a heightened sensitivity to changes in temperature, especially at lower temperatures [Karjalainen, 2012]. It has been suggested that when studying thermal comfort, female subjects be used with a view to ensuring that both sexes are thermally satisfied [Karjalainen, 2012].

2.3.2 Thermal neutrality... or monotony?

Recent studies are challenging the traditional views of 'still air is best' [Brager et al., 2015; De Dear et al., 2013] and that a necessary (but not sufficient) condition for thermal comfort is thermal neutrality, where the need to adjust the ambient temperature (up or down) does not arise [Fanger et al., 1985]. Buildings designed to be closer to thermal neutrality have been found to not achieve the higher levels of occupant satisfaction that might be expected [Arens et al., 2010]. Insufficient air movement, even in cooler

environments, is a cause for complaint for occupants [Parkinson and de Dear, 2017]. Neutral conditions are at best 'comfortable', not reaching 'very comfortable' [Arens et al., 2006a]. Constantly neutral conditions may also be a significant factor in health deterioration [van Marken Lichtenbelt et al., 2017]. Slightly either side of thermal neutrality may also aid productivity in certain tasks, more relaxed in a slightly warm environment or more alert in a slightly cool one [CIBSE, Guide A, 2015]. Furthermore, air movement can compensate for higher temperature [Brager et al., 2015].

Thermal monotony is the concept that uniform, static thermal environments cause thermal boredom [Brager et al., 2015]. Higher thermal comfort can be found in non-steady state and non-uniform environments [Parkinson et al., 2016], where the levels of discomfort vary and are less definite [Zhang et al., 2010b]. Temporal alliesthesia is a short-term pleasant sensation that occurs when a person moves from a less comfortable thermal sensation to a more comfortable one [Brager et al., 2015]. This does not occur from a neutral starting point.

2.3.3 Personal control

Maintaining a thermally monotonous environment is energy intensive, energy savings can potentially be made incorporating personal control [Brager et al., 2015] and allowing occupants to create bespoke localised environments [Parkinson and De Dear, 2015]. The ability to assert personal control over, and interact with, individual micro climates has a significant impact on thermal comfort and occupant satisfaction [De Dear et al., 2013; van Hoof, 2008]. Personal control can achieve higher comfort in transient conditions [Zhang et al., 2010b]. However, to date there are no clear target areas or parameters guiding personalised environmental control [Parkinson and de Dear, 2017].

2.3.4 Thermal sensitivity

In a thermally neutral environment the core body temperature is found to be stable [Huizenga et al., 2004], however even in these uniform conditions the surface temperature of the skin is not constant [Arens et al., 2006a; Huizenga et al., 2004] and local skin temperatures can vary by up to 4 °C, more so with non-steady state environments or clothing distribution, for example [Parkinson and De Dear, 2015]. The core body temperature generally countered the skin temperature, rising when the skin was cooled and cooling when the skin was heated [Huizenga et al., 2004]. The exception to this was cooling the skin when the body started in a cool state.

Thermal comfort can be found with contrasting local and mean global skin temperatures [Parkinson and de Dear, 2017; Parkinson et al., 2016] as some areas of comfort can offset other discomfort [Zhang et al., 2010b]. Whilst both the global and local skin temperatures impact the thermal sensation, there is a higher correlation between local skin temperature and local sensation and a single, local, site can influence the

global thermal perception [Jin et al., 2012; Parkinson and de Dear, 2017]. Moreover, heating or cooling local body parts can impact the global thermal sensation and comfort more than changing the environment for the entire body [Arens et al., 2006b].

Participants in an experimental study showed a preference for warm feet, pelvis, back and chest; being most comfortable with cool head, neck and face [Zhang et al., 2010a]. The head has been found to be insensitive to colder environments but sensitive to warmer ones where it feels warmer than the rest of the body [Arens et al., 2006a]. The breathing zone has been found to be less sensitive that other areas of the head [Arens et al., 2006a], however breathing cooler air is preferential to breathing warmer air [Zhang et al., 2010a]. Overall, air movement in the facial area allows for higher general surrounding temperatures [Zhang et al., 2011].

.

2.3.5 Thermophysiology

A typical thermal exchange between a human and their environment is a 20 % loss by evaporation, 35% loss by convection from air movement over the body and 45 % either lost or gained by radiation from cold or hot surfaces respectively [Ward, 2004]. Less than 1 % is lost or gained through conduction. Any heat balance is satisfied when production equals losses; in the case of a biophysical model, metabolic heat production needs to equal heat losses. Figure 2.1 shows the energy processes involved in a biophysical model.

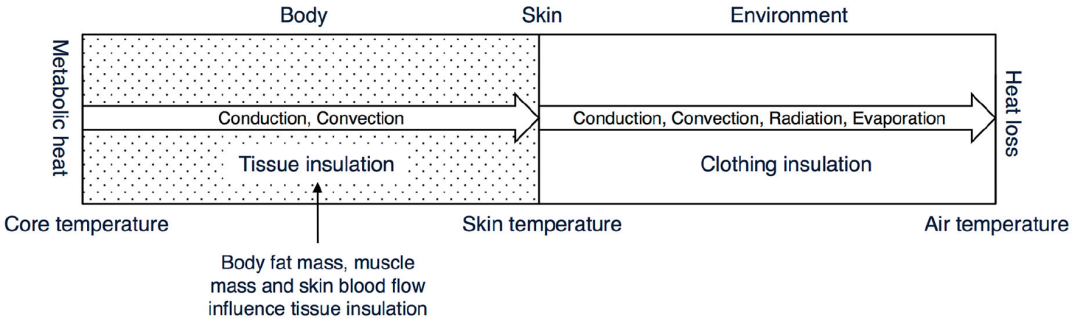

FIGURE 2.1: Image from Kingma et al. [2017] showing a schematic representation of a biophysical heat balance model.

The transportation of heat generated inside the body is conducted through tissues and convection through the cardiovascular system [Kingma et al., 2017]. The thermal regulatory system in a body works to keep the body working efficiently. Figure 2.2 illustrates how the constituent parts are interconnected. It can be seen that some factors require conscious input, for instance clothing, and others are involuntary, such as skin temperature.

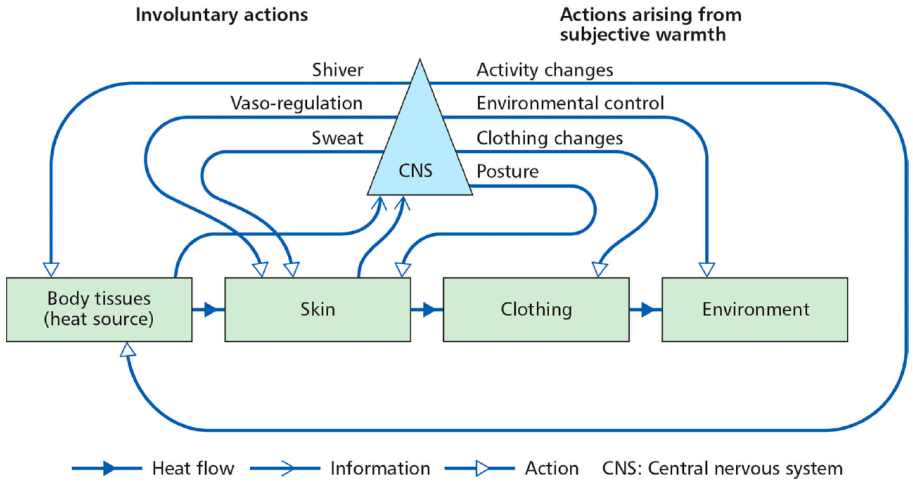

FIGURE 2.2: Image from Nicol and Roaf [2017] showing the thermal regulatory system.

The physiological thermoneutral zone is the minimal metabolic rate required to maintain the core body temperature [van Marken Lichtenbelt et al., 2017], support life functions and minimize water loss [Kingma et al., 2017], as shown in Figure 2.3. In a cold environment, the body increases the insulative properties of the tissue by restricting blood flow to skin and limbs through a process known as vasoconstriction [Kingma et al., 2017]. Metabolic rate is increased when the body falls below the lower critical temperature in order to raise the body temperature [Kingma et al., 2017]. In a warm environment, tissue insulation is reduced with increased blood flow (vasodilation), the body has to work harder to transport heat way from the core and water loss is increased through sweating [Kingma et al., 2017].

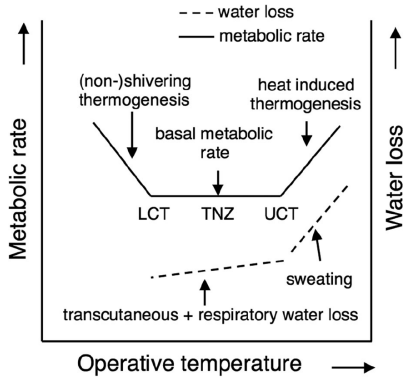

FIGURE 2.3: Image from Kingma et al. [2017] showing the thermoneutral zone (TMZ), lower critical temperature (LCT) and upper critical temperature (UCT).

2.3.6 Quantifying thermal comfort

A standard to quantify indoor thermal comfort is a thermal sensation scale [British Standards Institute, 2002, 2006] which assigns an index on a seven point scale to a thermal sensation, ranging from cold (-3) to neutral (0) to hot (3). The Predicted Mean Vote (PMV) [Fanger, 1972] equation estimates the average

thermal sensation of a population of people for a given set of factors. The model is based on European and American experiments in cold, temperate and warm environments [Fanger and Toftum, 2002]. It is not valid in warm and humid climates [d'Ambrosio Alfano et al., 2017], although modifications have been made to accommodate a wider range of climates and conditions [Enescu, 2017]. The PMV approach for determining thermal comfort is described in ISO 7730 [British Standards Institute, 2006], with the subject scales further defined in ISO 10551 [British Standards Institute, 2002], set out in Figure 2.4 below. This is also the scale adopted by ASHRAE. The Bedford scale (also Figure 2.4) is an alternative to PMV that accounts for a wider range of comfortable thermal environments [Nicol and Roaf, 2017].

ASHRAE descriptor	Numerical	Bedford descriptor	Numerical
Hot	3	Much too warm	7
Warm	2	Too warm	6
Slightly warm	1	Comfortably warm	5
Neutral	0	Comfortable neither warm nor cool	4
Slightly cool	−1	Comfortably cool	3
Cool	−2	Too cool	2
Cold	−3	Much too cool	1

FIGURE 2.4: Image from Nicol and Roaf [2017] showing the PMV / ASHRAE and Bedford thermal comfort scales.

Following ISO 7730 [British Standards Institute, 2006], the PMV values can also be calculated taking into account the six thermal parameters (namely clothing and activity levels; air and mean radiant temperatures; air velocity and humidity) as shown in equation (2.8) below [CIBSE, Guide A, 2015].

$$\mathrm{PMV} = \left(0.303\ \exp^{-0.036\,M} + 0.028\right)\left((M-W) - HL_1 - HL_2 - HL_3 - HL_4 - HL_5 - HL_6\right), \tag{2.8}$$

where M is the metabolic rate ($\mathrm{W\,m^{-2}}$) of body surface and W is the external work ($\mathrm{W\,m^{-2}}$) of body surface. The heat loss equations are defined in equations (2.9a - 2.9f), with heat losses through the skin (HL_1), sweating (HL_2), latent respiration (HL_3), dry respiration (HL_4), radiation (HL_5) and convection (HL_6).

$$HL_1 = 0.00305\ (5733 - 6.99(M-W) - p_\mathrm{s}), \tag{2.9a}$$

$$HL_2 = 0.42\ (M - W - 58.15), \tag{2.9b}$$

$$HL_3 = (1.7\times10^{-5})\ M\ (5867 - p_\mathrm{s}), \tag{2.9c}$$

$$HL_4 = 0.0014\ M\ (34 - T_\mathrm{a}), \tag{2.9d}$$

$$HL_5 = (3.96\times10^{-8})\ f_\mathrm{cl}\left((T_\mathrm{cl}+273)^4 - (T_\mathrm{r}+273)^4\right), \tag{2.9e}$$

$$HL_6 = f_\mathrm{cl}\ h_\mathrm{c}\ (T_\mathrm{cl} - T_\mathrm{a}), \tag{2.9f}$$

where p_s is the partial water vapour pressure in the air surrounding the body (Pa), T_r is the mean radiant temperature (°C), T_a is the average air temperature surrounding the body (°C), T_{cl} is the surface temperature of clothing (°C) as defined by equation (2.10), f_{cl} is the clothing surface area factor as defined by equation (2.11) and h_c is the convective heat transfer coefficient at the body surface ($\mathrm{W\,m^{-2}\,K^{-1}}$) as defined by equation (2.12):

$$T_{cl} = 35.7 - 0.028\,(M-W) - i_{cl}\,HL_5, \tag{2.10}$$

where i_{cl} is the clothing insulation ($\mathrm{m^2\,K\,W^{-1}}$),

$$f_{cl} = \begin{cases} 1.00 + 1.290\,i_{cl} & \text{for } i_{cl} \leq 0.078\ \mathrm{m^2\,K\,W^{-1}}, \\ 1.05 + 0.645\,i_{cl} & \text{for } i_{cl} > 0.078\ \mathrm{m^2\,K\,W^{-1}}. \end{cases} \tag{2.11}$$

$$h_c = \begin{cases} 2.38\,|T_{cl} - T_a|^{0.25} & \text{for } 2.38\,|T_{cl} - T_a|^{0.25} > 12.1\sqrt{v_{ar}}, \\ 12.1\sqrt{v_{ar}} & \text{for } 2.38\,|T_{cl} - T_a|^{0.25} < 12.1\sqrt{v_{ar}}, \end{cases} \tag{2.12}$$

where v_{ar} is the relative air velocity.

The Predicted Percentage Dissatisfied (PPD) estimates the percentage of the population who are dissatisfied with a given thermal sensation and is calculated using equation (2.13) [British Standards Institute, 2006; CIBSE, Guide A, 2015]. The PPD calculation accounts for not being able to satisfy everybody in a thermally neutral environment, even for a PMV index of 0, the PPD is 5 %. A draft is an undesirable local convective cooling [Liu et al., 2017]; the percentage dissatisfied in the presence of a draught (DR) can be calculated using equation (2.14).

$$\mathrm{PPD} = 100 - 95\,\exp^{-(0.03353\,\mathrm{PMV}^4 + 0.2179\,\mathrm{PMV}^2)}, \tag{2.13}$$

$$\mathrm{DR} = (34 - T_a)\,(v - 0.05)^{0.62}\,(0.37\,v\,I_t + 3.14), \tag{2.14}$$

for turbulent intensity I_t. In the case of mixing ventilation, the turbulent intensity is typically within the range of $30-60$ %, with an average of 40 %, whilst the values for displacement ventilation are generally lower [British Standards Institute, 2006].

The PMV/PPD model assumes a steady-state environment [Djamila, 2017; Fanger, 1972], where the occupants are passive and do not interact with their environment [Rupp et al., 2015]. However in a changing environment, people adapt their expectations of what constitutes thermal comfort and react accordingly leading to the proposal of adaptive models [CIBSE, Guide A, 2015; de Dear and Brager, 1998; Humphreys and Nicol, 1998; Rupp et al., 2015]. This could include altering their environment, activity or clothing for example, as illustrated in Figure 2.2 above.

Schweiker et al. [2017a] found that not only are the conceptual thermal comfort scales not perceived as

equidistant, the subjects had very different views on comfort levels. This can be seen in Figure 2.5, where subject 25, for example, is most comfortable in a neutral environment, whilst subject 19 prefers to be cold and subject 10 prefers to be warm. Many other subjects have a range of comfortable of sensations, albeit of different amounts. Subject 27, for example experiences comfort in a greater range of thermal environments than subjects 30 or 31 say.

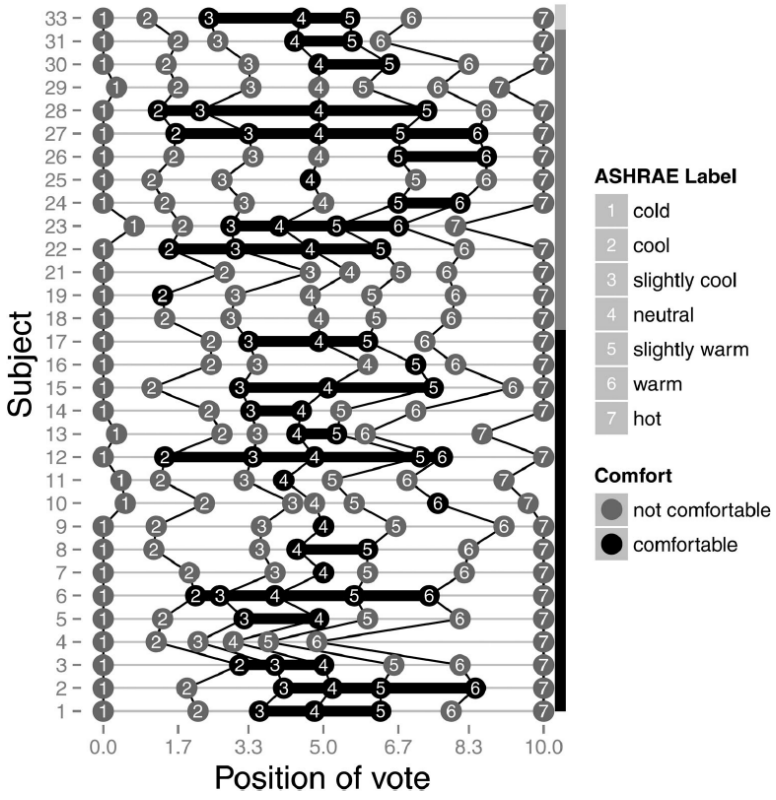

FIGURE 2.5: Image from Schweiker et al. [2017a] showing subjective thermal comfort and thermal comfort ranges of individual test subjects.

2.3.7 Biophysical modelling of thermal sensation

The individual factors of a thermoregulatory system each have a significant image on the thermoregulation of the body Davoodi et al. [2017]. A physiological model which accounts for such as system [Enescu, 2017] is a more sophisticated alternative for predicting thermal sensation than the more traditional PMV model. Figure 2.6 outlines the main processes involved in such a model. These biophysical models couple human thermoregulatory systems to the indoor environment and can also be coupled with numerical simulation [Babich et al., 2016; Fu et al., 2016; Schellen et al., 2013; Voelker and Alsaad, 2018; Yang et al., 2017]. Figure 2.7 illustrates how these processes can be coupled through an exchange of data [Fu et al., 2016].

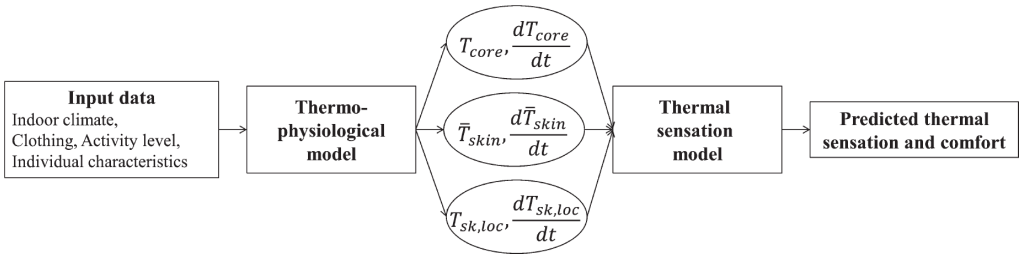

FIGURE 2.6: Image from Veselá et al. [2017] showing the concept of human thermal modelling.

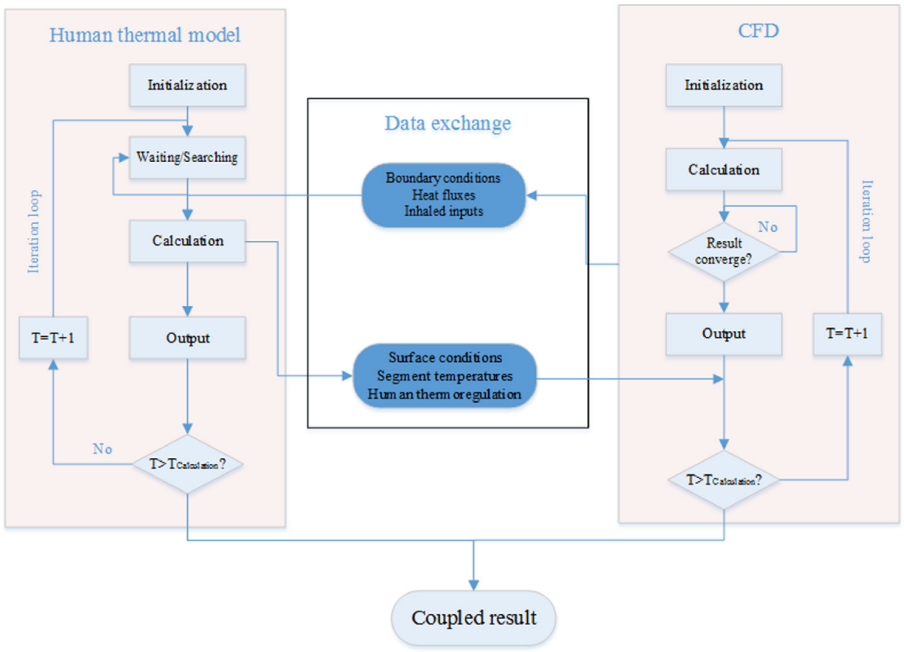

FIGURE 2.7: Image from Fu et al. [2016] showing an example of the coupling of CFD and a thermophysical model.

A major benefit of these models is that they are are capable of dealing with localised thermal sensations [Katić et al., 2016; Veselá et al., 2017] by subdividing the model into constituent body segments and thereby increase control over local properties like skin temperature [Veselá et al., 2017]. This presents an opportunity for enhanced thermal modelling and thermal sensation prediction because PMV requires estimates of the personal factors such as metabolic rate and clothing which are generally taken as single values and assumed applicable to the whole body [Veselá et al., 2017]. However these models may not yield superior results to the PMV model when considering the body as a whole [Schweiker et al., 2017b].

Any evaluation of thermal comfort is influenced by the choice of thermal sensation model [Koelblen et al., 2017], however none of the available models take into account psychological factors [Schweiker et al., 2017b]. Furthermore, no standard approach to these thermal sensation models has been developed yet [Koelblen et al., 2017], with many newer ones lacking in comprehensive validation [Koelblen et al., 2018]. Predictions of optimal temperatures differ substantially between models [Koelblen et al., 2017] and

there is no logical or dependable way to scale any predictions to improve the accuracy or comparability of the thermal sensation models [Koelblen et al., 2018]. Figure 2.8 highlights the disparity between several of the models, illustrating that no direct comparisons can be made [Koelblen et al., 2018].

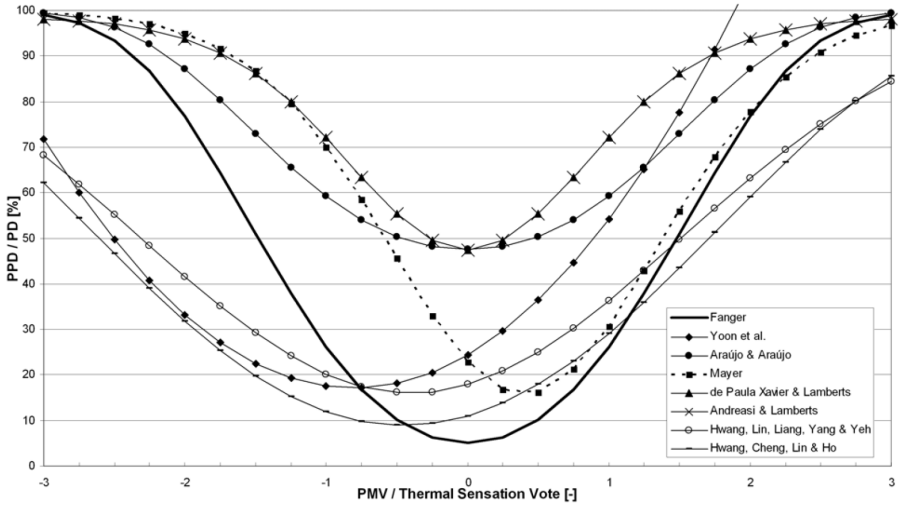

FIGURE 2.8: Image from van Hoof et al. [2010] showing the relation between PMV and PPD, and other thermal sensation indices [Andreasi and Lamberts, 2006; Araújo and Araújo, 1999; de Paula Xavier and Lamberts, 2000; Fanger et al., 1970; Hwang et al., 2009a,b; Mayer, 1997; Yoon et al., 1999].

These models do not deal with personal comfort on an individual level as they are based on averages and assumptions of personal factors from large data sets [Zhao et al., 2014]. Whilst they can account for differences in (for example) age, BMI, age and gender [Davoodi et al., 2017], they cannot deal with the fact that "different people prefer different thermal conditions" [Lee et al., 2017], as shown by Schweiker et al. [2017a]. New data-driven, machine learning based methods are emerging that require minimal input from individual users and have the potential to provide accurate personal thermal comfort predictions and energy savings [Lee et al., 2017; Zhao et al., 2014].

Despite the large variations in individuals, it is practical to design for an average occupant and PMV remains an international standard [d'Ambrosio Alfano et al., 2017] which is recognisable, extensively validated with known limitations, easily calculated and comparable.

2.3.8 Guidelines

UK law states, in section 7(1) of The Workplace (Health, Safety and Welfare) Regulations, SI 1992/3004, that "during working hours, the temperature in all workplaces inside buildings shall be reasonable". Section 7 (paragraphs 60-61) of the Approved Code of Practice (ACOP) [HSE, 2013] expands on this stating that the temperature "should normally be at least 16 °C" and that "reasonable comfort" should be achieved without the need for special clothing. An upper limit is not provided. Section 7 (paragraph 73) of the guidance [HSE, 2013] refers to Chartered Institution of Building Services Engineers (CIBSE) for

published data. The recommended temperature range for offices [CIBSE, Guide A, 2015; Clancy, 2011] is $21-23\,^{\circ}$C in winter and $22-25\,^{\circ}$C in summer. Table 2.2 sets out the official legal guidelines for air conditioned offices. The law restricting the heating of buildings via means of fuel and electricity above $10\,^{\circ}$C (The Fuel and Electricity (Heating) (Control) (Amendment) Order 1980) is due to be repealed. It was assumed that other factors within the building would provide extra heating, such as occupants, lighting and equipment [McMullan, 2012]. This law was introduced as a consequence of the energy crisis in the 1970s and is no longer policed as other policies now control energy usage.

Property	**Value**	**Reference**
Minimum winter operative	20 °C	British Standards Institute [2008]
Winter operative temperature range	20 – 24 °C	British Standards Institute [2006, 2008]
Maximum summer operative temperature	26 °C	British Standards Institute [2008]
Summer range	22 – 27 °C	British Standards Institute [2006, 2008]

TABLE 2.2: Operative temperature guidelines for air conditioned offices with medium indoor air quality.

The operative temperature (T_{op}) [CIBSE, Guide A, 2015] is the combination of the air temperature (T_{a}) and the mean radiant temperature (T_{r}) as given by

$$T_{\mathrm{op}} = H\,T_{\mathrm{a}} + (1+H)T_{\mathrm{r}}, \tag{2.15}$$

where

$$H = \frac{h_{\mathrm{c}}}{h_{\mathrm{c}}+h_{\mathrm{r}}} \sim \sqrt{10v}, \tag{2.16}$$

for surface heat transfer coefficients for convection and radiation, h_{c} and h_{r} respectively (in $\mathrm{W\,m^{-2}\,K^{-1}}$), and the air speed v (in $\mathrm{m^2\,s^{-1}}$).

Throughout the year the relative humidity should be in the region of $40-70\%$ [Clancy, 2011]. The relative humidity in summer can be taken as $60\,\%$ and $40\,\%$ in winter [British Standards Institute, 2006]. These values correspond to temperatures of $26\,^{\circ}$C and $22\,^{\circ}$C respectively and are based on the assumption that the only sources of humidity in the air-conditioned environment are the human occupants and the HVAC system [British Standards Institute, 2014].

ISO 7730 [British Standards Institute, 2006] also sets out methods to determine local thermal discomfort due to vertical air temperature gradients and radiant asymmetry (warm or cool walls, ceiling and floor) along with transient thermal environments such as temperature cycles and drifts. Table 2.3 presents the guidelines for the range of acceptable PPD, both for the thermal state of the whole body and for local discomfort due to draughts and radiant asymmetry. Table 2.4 contains the suggested temperature ranges so these dissatisfaction levels are not breached. CIBSE, Guide A [2015] quotes a more conservative value of DR less than 15% as acceptable whilst ASHRAE [2004] suggest that no more than 20% of the occupants

are thermally dissatisfied: up to 10% thermally dissatisfied generally and a further 10% who are locally thermally dissatisfied. When the air movement is faster at ankle level than over the rest of the body, CIBSE, Guide A [2015] suggest reducing temperature gradient between the ankles and head from 3 °C to a maximum of 2 °C m^{-1}.

Property	Value	Reference
Whole body PPD	< 10 %	British Standards Institute [2008]
Whole body PMV range	$-0.5 <$ PMV $< +0.5$	British Standards Institute [2008]
Local discomfort due to draught PD	< 20 %	British Standards Institute [2006]
Local discomfort due to vertical air difference PD	< 5 %	British Standards Institute [2006]
Local discomfort due to warm or cool floor PD	< 10 %	British Standards Institute [2006]
Local discomfort due to radiant asymmetry PD	< 5 %	British Standards Institute [2006]

TABLE 2.3: The predicted percentages thermally dissatisfied for air conditioned offices with medium indoor air quality.

Property	Value	Reference
Vertical air temperature difference (0.1m to 1.1m)	< 3 °C	British Standards Institute [2006]
Floor surface temperature range	$19 - 29$ °C	British Standards Institute [2006]
Warm ceiling	< 5 °C	British Standards Institute [2006]
Cool ceiling	< 14 °C	British Standards Institute [2006]
Warm wall	< 23 °C	British Standards Institute [2006]
Cool wall	< 10 °C	British Standards Institute [2006]

TABLE 2.4: Suggested temperature ranges to ensure PPD values not breached.

2.4 Computational Fluid Dynamics (CFD)

Computational Fluid Dynamics (CFD) is an amalgamation of several different and established disciplines, encompassing (but not limited to) mathematics, computer science, fluid mechanics, heat transfer and combustion [Tu et al., 2008]. It presents a viable and cost effective alternative, or complement, to physical experimentation. Frequently used as part of the design cycle, CFD is now an integral part of research and development in many industries as products can be designed and optimised before manufacture, which has potential to shorten the design cycle, improve efficiency and reduce overhead costs [Anderson, 1995; Keane and Nair, 2005; Tu et al., 2008].

Although an abundance of in-house CFD codes exist, they are usually written for specific tasks. Commercial codes are written to deal with a myriad of situations, as is the case for ANSYS Fluent [ANSYS, Inc., 2015]. A considerable benefit of commercial codes is that they are extensively tested prior to release so it can be assumed that most (if not all) of the coding errors have been ironed out, with code being implemented accurately and efficiently. The flexibility and convenience of commercial codes is also a potential flaw: whilst in many ways it may be tempting to treat a commercial code as black-box, this could be dangerous as results produced could be erroneous. As the commercial code ANSYS Fluent forms the basis of the numerical models developed in later chapters, it is important to describe the technicalities of key models which are central to accurate and reliable computer simulations.

2.4.1 Overview of CFD

Fluid Dynamics [Acheson, 2001; Bertin and Smith, 1979; Hirsch, 2007; Moran, 1984] is the study of fluid flows and the subsequent effects of that fluid on neighbouring materials it is in contact with, namely other fluids or solid bodies. These flows can be approximated numerically in a 'virtual environment' [Hirsch, 2007] by a coupled system of (usually) non-linear partial differential equations (PDEs). The very nature of these system of equations makes them exceedingly difficult (generally impossible) to solve analytically [Prasad and Ravindran, 1985]. Anderson [1995] observed that no general closed form solution had been found, a fact that remains true today.

Approximations of the solutions can be attained through exploitation of numerical methods applied to the non-linear equations. Techniques employing the original PDEs include collocation and integral methods, or expansion and perturbation methods. However, another method to obtain a numerical solution for a system of continuous time-independent Partial Differential Equationss (PDEs) is to discretise them spatially in order to obtain a system of differential algebraic equations whose solutions are subsequently approximated. Such semi-discrete equations can be represented at discrete points (nodes) and/or over discrete cells (control volumes created by connecting nodes) in the computational domain, making the construction of a grid (mesh) of nodes and cells a prerequisite for any calculation. Ever increasing computer power can be utilised to obtain quantitative predictions of these flows computationally - which is the essence of Computational Fluid Dynamics [Acheson, 2001; Anderson, 1995; Chung, 2002; Hirsch, 2007; Tu et al., 2008].

A successful simulation depends on a well posed problem [Anderson, 1995], making it essential that all aspects of the problem set-up are carefully considered. As CFD runs can be computationally expensive, time taken in the initial stages can potentially reduce the overall cost and produce more accurate results. Despite the fact that there are no universally accepted methods in applying CFD, guidelines and books [AIAA, 1998; Roache, 1998a; Tu et al., 2008] have been published to assist in the production of credible data. Credibility is established by demonstrating acceptable levels of uncertainty and error by measuring the accuracy of the simulation against benchmark model problems [Sørensen and Nielsen, 2003].

Verification and validation (V & V) is a necessary condition for credibility, however sufficient credibility is subjective and often determined by practical issues. The subsequent discussion and definitions are heavily based on the AIAA guidelines [AIAA, 1998]. Verification can be viewed as "solving the equations right" whilst validation as "solving the right equations" [Roache, 1998b]. Verification determines the fidelity of computational model to conceptual model, it does not determine whether the model is correct or even if the model is applicable to reality. Validation relies on a given model being verified *a priori* and determines the fidelity of the computational model to real world, providing evidence that the right model has been used by comparing the numerical result with experimental data [AIAA, 1998]. With the exception of trivial cases, it is impossible for the veracity and accuracy of a CFD model to be demonstrated for all conditions.

However, when it is feasible, V & V provide historical statements (such as comparison with benchmark cases) with a reproducible level of accuracy for the given situation.

Uncertainties in the solution are "potential deficiencies" [AIAA, 1998] due to lack of knowledge, for example unknown surface roughness or using an inappropriate or inadequate turbulence model. Errors in the model and simulation are defined as "recognizable deficiencies" [AIAA, 1998] and are either acknowledged (e.g. machine round-off errors) or unacknowledged (e.g. programming errors). Local errors are specific to a region of the solution domain (in either space or time, or both), whereas global errors are an accumulation of local errors such as numerical diffusion propagating through the domain.

Unacknowledged errors are usually a consequence of human faux pas [Tu et al., 2008]. These can be reduced (but not avoided) by enforcing procedural techniques, such as journal or transcript files in FLUENT. Other possibilities include oversimplification of the physical problem, uncertainty in model parameters and programming errors including numerical errors arising from discretisation of the governing PDEs or occurrence of singularities in computations [Tu et al., 2008]. Turbulence is a dominant contributor of uncertainty as currently there are no universal models applicable in every instance over all turbulent length-scales [Hirsch, 2007]. Numerical dissipation has a diffusive effect and introduces an artificial viscosity into the governing equations, reducing the effective *Re* and compromising the numerical accuracy, but increasing the stability of the solution [Anderson, 1995]. Decreasing the size of cells in the grid can reduce the dissipation [Versteeg and Malalasekera, 2007]. Numerical dispersion is apparent in the oscillations of the higher order, iterative, numerical solution schemes [Anderson, 1995].

Acknowledged errors are perhaps the easiest to address. Computer rounding errors, for instance, can be minimised using double precision arithmetic instead of single precision. Unconverged (both iterative and discretised) solutions provide further sources of errors. Inadequate iterative convergence of residuals and flow variables can be avoided with investigation into the effect of different truncation criteria on the quantities of interest [Versteeg and Malalasekera, 2007]. For any numerical method to be consistent, the truncation errors associated with the discretisation must approach zero as the spatial and temporal discretisation tends to zero. A numerical scheme is considered stable if it does not magnify errors, irrespective of their source [Tu et al., 2008]. Lax's equivalence theorem states that convergence can be implied from the presence of both consistency and stability in a numerical solution [Tu et al., 2008].

2.4.2 Spatial and numerical discretisation

The geometric domain is typically generated using a CAD (computer aided design) package such as the ANSYS Workbench software package [ANSYS, Inc., 2015]. The domain needs to be realistic whilst also allowing for flow to fully develop before entering region of interest, which may in practice mean extending the grid before an inlet for example [Tu et al., 2008]. In order to run a computational simulation of a model, both the continuous geometry and flow variables must be transformed into discrete numbers for a

computer to be able to deal with them, a process known as discretisation. For transient problems, temporal aspects of the model also require discretisation, although this is not an issue for steady-state problems.

The first part of discretisation is grid generation where the domain is subdivided into discrete control volumes, essentially a lattice of cells connected at discrete nodal points. The second stage discretises the governing flow equations which are to be solved on this grid. The discretised equations are solved in each control volume, either at cell centres or on the nodes depending on the scheme implemented, using information from the neighbouring cells. A numerical solution is obtained for the dependant variables (in the case of incompressible flow these are typically pressure and velocity) at the discrete location, generating a vast amount of data. The values between these discrete locations are obtained through interpolation and are subject to additional errors. A finer mesh gives more numerical accuracy but at a higher computational cost as the size of the algebraic systems to be solved are larger.

There are no inherent laws or governing equations for designing and generating a grid for any given domain [ed. J. F. Thompson et al., 1999]. Once a grid has been created, it is essential to ensure that there is sufficient grid density in relevant areas to capture the important flow features so that it is as accurate as necessary, whilst remaining as computationally efficient as practical. This may require *a priori* knowledge of the flow or may involve preliminary grid CFD runs. As such, obtaining an accurate and effective mesh can be extremely challenging and may be considered something of an art form. Grid generation is an important aspect of CFD and although the grid itself is only a tool in the computational simulation, the type and quality of grid used will have a profound impact on the final outcome, and on whether realistic or spurious results are obtained as the accuracy of numerical results is critically dependant on mesh quality [Hirsch, 2007; Tu et al., 2008].

The two main types of mesh are structured and unstructured, with hybrid grids containing both types. Structured grids [Chung, 2002; ed. J. F. Thompson et al., 1999] are formed by the intersections of the surfaces of curvilinear coordinate systems. If the mesh is discontinuous or excessively skewed it will impair the accuracy of the numerical solution, manifesting itself as numerical diffusion and can also lead to ill-conditioning in the algebraic systems. Unstructured grids [Chung, 2002; ed. J. F. Thompson et al., 1999] bear no relation to the coordinate system and can be created to fill any given domain.

There are various methods of spatial and temporal discretisation of the governing equations resulting in systems of algebraic equations, corresponding to the problem under investigation. Any boundary or initial conditions subsequently applied to the model must also be converted into matrix format. Several established techniques exist to discretise the governing fluid flow equations over a spatial domain. The main three are Finite Difference Methods (FDMs), Finite Element Methods (FEMs) and Finite Volume Methods (FVMs).

Once an initial solution has been found, the grid could be refined by adaptation to provide improved accuracy for additional computation. Appropriate grid refinement should reduce numerical diffusion [Sørensen and Nielsen, 2003]. Examples of grid adaptation include adapting for cell volume, boundaries, variables or their gradients [Nielsen, 2015]. Volume adaptation need not necessarily take place after a solution is sought, however it may be a required step after other adaptation methods have been used as the aim is to avoid large discontinuities in adjacent cell volume sizes [ANSYS, Inc., 2014]. Boundary adaptation seeks to ensure accurate representation at the domain boundaries. Gradient adaptation (for example in regions where shock waves occur) seeks to minimise dispersive errors and false diffusion by ensuring a fine enough grid in areas with large gradients [Nielsen, 2015].

Discretisation errors fall into two camps, spatial and temporal. With respect to spatial errors, it is preferable to show that there is monotonic reduction of discretise error on two or three successive levels of mesh refinement, from which Richardson extrapolation can be used to estimate the errors due to discretisation and in some situations a Grid Convergence Index (GCI) can be calculated [Roache, 1994, 1997, 1998a]. Increasing the density of grid points until there is no significant change in flow variables indicates that the discretisation error is at an acceptable level (the solutions are in the asymptotic region) and grid independence has been reached [Durbin and Medic, 2007]. Although the original Richardson extrapolation [Richardson, 1911] was to provide an estimate for the actual solution, it is more widely used today to provide error estimates due to the tendency to magnify errors in the solutions [Roache, 1994, 1998a]. Both the standard and generalized forms assume that the solutions f_1 and f_2 from 'fine' and 'coarse' grids respectively are in the asymptotic region. The grid refinement ratio is defined by $r = \frac{h_2}{h_1} > 1$, where h_1 and h_2 are the grid spacings. The exact solution can be estimated by

$$f_{\text{exact}} \simeq f_1 + \frac{f_1 - f_2}{r^{\rho} - 1}, \tag{2.17}$$

where ρ is the order of convergence of the solutions f_2 and f_1 to the exact solution f_{exact}. A value of $\rho = 2$ recovers the standard form of Richardson extrapolation [Roache, 1997]. Assuming monotonic convergence of the truncation error with respect to mesh spacing [Roache, 1998a], the error estimate in the fine grid is given by

$$E_{12} = \frac{f_2 - f_1}{1 - r^{\rho}}, \tag{2.18}$$

and for the coarse grid by

$$E_{21} = \frac{r^{\rho}(f_2 - f_1)}{1 - r^{\rho}}. \tag{2.19}$$

If ρ is unknown it may be estimated using a third (coarser) grid [Roache, 1994, 1998a] using constant $r = \frac{h_3}{h_2} = \frac{h_2}{h_1}$:

$$\rho = \frac{\ln\left(\frac{f_3 - f_2}{f_2 - f_1}\right)}{\ln r}. \tag{2.20}$$

When r is not constant between the three grids, ρ can be found from:

$$\frac{E_{23}}{r_{23}^{\rho}-1} = r_{12}^{\rho}\left(\frac{E_{12}}{r_{12}^{\rho}-1}\right). \tag{2.21}$$

It is not always possible to perform an exact grid refinement (or coarsening), for example when tetrahedral elements are used within the mesh. In such instances an effective values of r can be determined using the number of elements, NE, in a mesh along with the dimension D Roache [1998a]:

$$r_{\text{effective}} = \left(\frac{NE_1}{NE_2}\right)^{\frac{1}{D}}. \tag{2.22}$$

The grid convergence index (GCI) Roache [1994, 1998a] was proposed to provide a uniform method for grid refinement studies and to provide more realistic error bounds. For a two grid study, the GCI is given by

$$GCI_{12} = F_{\text{s}}E_{12}, \tag{2.23}$$

where the safety factor F_{s} should lie in the region of 1 to 3. Roache [Roache, 1998a] proposes a conservative error bound of $F_{\text{s}} = 3$ for a two grid study, and a more relaxed $F_{\text{s}} = 1.25$ for three grid where the value of ρ can be verified.

2.4.3 Modelling fluid flow

Any mathematical model of a real world phenomenon is subject to modelling assumptions and associated errors, therefore any given model will only ever be an approximation. The equations that simulate fluid flow are the Navier-Stokes equations - a coupled system of governing PDEs modelling fluid flows are fundamental to CFD, providing an empirical representation in a simulation by balancing unsteady and convection terms with diffusion and source terms. One of the main assumptions in their derivation is that the fluid is continuous. However all materials are made up at a fundamental level of discrete particles and molecules. A real fluid will also contain suspended particles and dissolved gases. Obviously the real fluid will never produce completely identical results (for all scales) as the ideal, modelled one.

The Navier-Stokes equations are derived from the basic conservation principles of mass, energy and momentum, along with a state law for the fluid (e.g. the ideal gas law). The full Navier-Stokes equations contain both convection (the transportation of a fluid property due to the flow itself) and diffusion (a transportation process due to the random motion of the fluid molecules) terms. The transportation equation is also representative of other flow variables, for instance airborne contaminants [Nielsen, 2015]. The diffusion equation is related to the viscosity of a fluid, and hence the generation of boundary layers and turbulence. The velocity and temperature components are modelled by parabolic equations whilst the pressure and density are hyperbolic [Wolfshtein, 2009].

Increasing the modelling assumptions reduces the complexity of the problem making it easier and faster to solve, but has the drawback of moving the model further away from reality, therefore a compromise should be found. For example, a simplification can be made in the case of incompressible fluids for subsonic flows where the effects associated with the compressibility of the fluid (such as shocks) are negligible. For a Newtonian fluid with velocity $\vec{u}$, density ρ, viscosity ν and pressure p, under the influence of the body force $\vec{g}= g\vec{n}$, the Navier-Stokes equations can be written as the conservation of momentum, equation (2.24), and the conservation of mass, equation (2.25):

$$\left(\frac{\partial}{\partial t}+\vec{u}\cdot\nabla\right)\vec{u}=-\frac{\nabla p}{\rho}+\nu\nabla^2\vec{u}+\vec{g}, \tag{2.24}$$

$$\nabla\cdot\vec{u}=0. \tag{2.25}$$

For an inviscid flow, the full Navier-Stokes equations can be simplified by neglecting the effects of viscosity and reduce to the Euler equations [Anderson, 1995; Euler, 2008],

$$\left(\frac{\partial}{\partial t}+\vec{u}\cdot\nabla\right)\vec{u}=-\frac{\nabla p}{\rho}. \tag{2.26}$$

Originally, the Euler equations for inviscid flow contained only the continuity and momentum equations, however today they imply the inclusion of any relevant energy equation [Anderson, 1995].

The governing fluid flow equations conform to a generic scalar transport equation [Patankar, 1980; Tu et al., 2008] for any scalar φ. The benefit of a generic equation is that it can represent a variety of quantities transported with the fluid flow. In addition to velocity components, φ could represent temperature, turbulent kinetic energy or a chemical species [Patankar, 1980]. For a diffusion coefficient Γ_φ and source term S_φ (both functions of φ) a generic scalar transport equation could be written as

$$\frac{\partial}{\partial t}(\rho\varphi)+\nabla\cdot(\rho\vec{u}\varphi)=\nabla\cdot(\Gamma_\varphi\nabla\varphi)+S_\varphi. \tag{2.27}$$

Substituting scalar terms for φ recovers the governing equations. For example, $\varphi=1, \Gamma_\varphi=S_\varphi=0$ gives the continuity equation (2.25) [Tu et al., 2008]. For the momentum equations, additional source terms are added to allow other sources of fluid motion, including pressure and non-pressure gradient terms and gravity [Tu et al., 2008]. The generic equation follows the same form as the Navier-Stokes equations, with unsteady and convection terms balancing diffusion and source terms. The diffusive term $(\Gamma_\varphi\nabla\varphi)$ does not limit φ to gradient driven diffusion as additional terms can be included in the source term [Patankar, 1980]. A small diffusion term indicates that the flow is convection driven, affecting the stability of the equation [Anderson, 1995]. The generic equation can be transformed to account for the energy E [Versteeg and Malalasekera, 2007] by specifying S_E as the energy source term and Γ_T as the thermal conductivity k. The

energy equation is then given by equation (2.28)

$$\frac{\partial}{\partial t}(\rho E) + \nabla \cdot (\rho \vec{u} E) = \nabla \cdot (k \nabla E) + S_E. \tag{2.28}$$

Similarities in flow behaviour can be observed in flows under apparently different conditions. This dynamic similarity [Tu et al., 2008] becomes clearer when the governing equations are non-dimensionalised. The Reynolds number (*Re*) is a dimensionless number, defined as the ratio of inertial to viscous forces in a given fluid which quantifies the relative importance of these forces in the given flow conditions. A high *Re* indicates that inertial forces dominate and the flow is turbulent, whereas a low *Re* indicates laminar flow. For a fluid with a mean fluid velocity $\overline{u}$, characteristic length L, dynamic viscosity μ and kinematic viscosity $\nu = \frac{\mu}{\rho}$, the Reynolds number may be defined as

$$Re = \frac{\rho \overline{u} L}{\mu} = \frac{vL}{\nu}. \tag{2.29}$$

The momentum conservation defined in equation (2.24) can be non-dimensionalised [Versteeg and Malalasekera, 2007] with respect to this characteristic length-scale L, typical flow speed U, time-scale $\frac{L}{U}$ and pressure scale $\frac{\mu U}{L}$ to produce

$$Re\left(\frac{\partial \vec{u}}{\partial t} + (\vec{u} \cdot \nabla)\vec{u}\right) = \nabla \cdot \vec{\sigma} + St\vec{n}, \tag{2.30}$$

where *St* is the non-dimensional Stokes number quantifying the significance of the gravitational and viscous forces, and $\vec{\sigma}$ is the stress tensor, given respectively for a Newtonian fluid as:

$$St = \frac{\rho g L^2}{\mu U}, \tag{2.31}$$

$$\vec{\sigma} = -p\vec{I} + \nabla\vec{u} + \nabla\vec{u}^T. \tag{2.32}$$

2.4.4 Modelling turbulence

Laminar flows are characterised by a low value of *Re* with high momentum diffusion and low momentum convection [Acheson, 2001]. These flows have a high degree of order, with exchanges in variable values due to molecular transfer. In addition, the pressure and velocity are usually independent of time. As the Reynolds number increases the flow dynamics change. Above a critical value of *Re* all flows become turbulent, characterized by statistical fluctuations of all flow variables. Turbulent flows [Davidson, 2004; ed. Thomas B. Gatski and Hussaini, 1996; Wilcox, 1994] have low momentum diffusion and high momentum convection, leading to strong and fast mixing, often defined as three dimensional unsteady random rotational motion [Wolfshtein, 2009]. The mixing of a fluid is similar to molecular diffusion, except with a much larger length-scale.

In a low viscosity fluid, there is insufficient viscosity to dissipate the smallest scales of the fluid motion, therefore they are not damped and the entire range of fluid motions exist. For flows with small Reynolds numbers, around $Re < 10^3$, viscous forces dominate and the smallest scales of motion are damped out leaving only the larger scales of motion: laminar flow. Increasing the Reynolds number will cause a transition to turbulent flow, where inertial forces dominate. As the flow passes through the transitional region towards turbulence, a state of instability is caused due to deficient damping. The exact number, Re_{crit}, at which this happens depends on the conditions of the flow and needs to be determined experimentally. In the range either side of Re_{crit}, where the flow is neither fully laminar nor completely turbulent, predicting the fluid behaviour is very difficult.

There exists a range of scales of fluid motion in turbulent flows, where a single packet of fluid moving with a bulk velocity is called an eddy. These flows exhibit a rapid, stochastic variation of velocity in both time and space and (to avoid dissipation) require a continuous supply of energy needed to maintain the turbulence as the kinetic energy is turned into heat. They can arise due to contact between the fluid and solid boundaries, or contact between two fluids which have different velocities. It is the high velocity gradients and non-linear convection terms [Hirsch, 2007] that cause disturbances in the flow and the rapid, random variations make turbulence inherently three dimensional. Consequently it should not be modelled in two dimensions.

Turbulence and boundary layer formation depends on the viscosity, therefore any models for these must include viscous terms, ruling out some simplifications of the Navier-Stokes equations (such as the Euler equations) for modelling such phenomena. At a solid boundary it is typically assumed that the flow speed is zero. A boundary layer is the thin volume connecting the stationary fluid in contact with the boundary to the free flowing fluid. The boundary layer has thickness to length ratio of order $Re^{\frac{-1}{2}}$ [Hirsch, 2007] so as the Reynolds number increases, the boundary layer gets thinner. On a boundary such as a wall, the turbulent kinematic viscosity $\tilde{\nu}$ and the Reynolds stresses vanish. For a very thin layer above the wall (the laminar sub-layer) viscous forces dominate. These need to be accommodated in any model which resolves down to a wall boundary. If the mesh is fine enough, the Navier-Stokes equations can be resolved in the laminar sub-layer. If however the mesh is too coarse, it can be assumed that the centres of the cells which lie adjacent to the walls lie within the logarithmic region of the boundary layer. Hence they can be modelled (with wall functions) using the law of the wall [Wilcox, 1994], where the velocity profile can be estimated for a dimensionless velocity u^+:

$$u^+ = \frac{1}{\kappa} \ln y^+ + c, \tag{2.33}$$

where c is a constant (≈ 5.1), κ is the von Karman constant and y^+ is a dimensionless distance from the

wall such that for a distance y and shear velocity u_τ

$$y^+ = \frac{u_\tau y}{\nu}. \tag{2.34}$$

Wall functions assume that the flow near a wall is one-dimensional and change only in the direction normal to the wall. As a general rule of thumb, wall functions are applicable for the range $11 < y^+ < 100$. Below this, in the laminar sub-layer where $y^+ = u^+$, it is assumed that the flow can be fully resolved (although this is only really the case for $y^+ \approx 1$). Above this range, the flow will be modelled inaccurately by the scheme used for the rest of the fluid. Hence it is essential that the mesh not be too coarse near a wall boundary, but coarse enough to be able to use wall functions if the mesh is not fine enough to fully resolve. It should be noted that more complicated wall functions exist [ANSYS, Inc., 2015], but they are still applicable to the same range of y^+.

The time-dependant Navier Stokes equations can in theory be solved to the smallest scales of length and time, if the grid is fine enough and the time-step small enough. This is called Direct Numerical Simulation (Direct Numerical Simulation (DNS)), [Anderson, 1995; Cant, 2002; Huser and Biringen, 1993; Ishihara et al., 2009; Moin and Mahesh, 1988; Spalart, 1988]. As it captures all relevant scales of the turbulent motion no model is needed for smallest scales. DNS is prohibitively expensive and not feasible for most engineering applications as the flow field must be very finely discretised to capture the large variation of turbulence structures [Wolfshtein, 2009]. Alternative methods involve modelling these smaller scales.

Reynolds decomposition [Chung, 2002; Wilcox, 1994] utilises statistical methods to separate the scales in a turbulent flow and resolves a scalar field, such as velocity components or pressure, into the sum of an average component and a fluctuating component. The Navier-Stokes equations are averaged over space and time. These methods are equally applicable to unsteady flows despite the time averaging so long as the changes in the mean are much greater than the time-scales of the turbulent motion, which contains most of the energy. The Ergodic Hypothesis [Wilcox, 1994] states that the time average is equivalent to ensemble average, although this cannot be proved. The Reynolds Averaged Navier-Stokes (RANS) models are the oldest form of turbulence model to govern the transport of average flow quantities. With this approach, the whole range of turbulence is modelled, thereby reducing computational cost. The ensemble version of the governing equations are solved, introducing new, apparent stresses (Reynolds stresses). This is a second order tensor of unknowns, τ_{ij} [Chung, 2002; Launder and Sandham, 2002], which must be modelled so that it vanishes on the walls of a domain.

RANS modelling can be divided into two main approaches. The first is based on the Boussinesq Hypothesis [Wilcox, 1994] which uses algebraic equations to represent the Reynolds Stresses and solve for the turbulent viscosity and transport equations for the turbulent kinetic energy and dissipation. Such models are classified by the number of transport equations they include. Using this approach yields the

turbulent viscosity, μ_t, with relatively low computational cost. However it models μ_t as an isotropic, scalar quantity which is not true - the fluctuating velocities parallel to the boundary may well be much greater than the fluctuating velocities perpendicular to it. The second approach, the Reynolds Stress Model (RSM), solves the transport equations for the Reynolds stresses and is capable of dealing with non-isotropic turbulence. This approach is more costly as it requires more transport equations to be solved.

As the name implies, zero-equation models are algebraic models which do not solve any transport equations to obtain approximations to the unknowns. These models assume that the turbulence is dissipated where it is generated and the transportation of the turbulence with the flow is ignored. A famous example is the Prandtl Mixing Length Hypothesis (MLH) [Wilcox, 1994], applicable to two dimensional boundary flows. One-equation models solve one transport equation to obtain a model for turbulence. Examples include the k-l differential stress model [Wilcox, 1994] and the Spalart-Allmaras model [Spalart and Allmaras, 1992; Versteeg and Malalasekera, 2007]. Two-equation models are called complete models as they provide a method of calculating the turbulent kinetic energy k and the length-scale l or equivalent. There are two main two-equation models, the k-ε model [Chung, 2002; Wilcox, 1994] (which in itself is split into three: the standard model, the RNG model and the Realizable model) and the k-ω model [Chung, 2002; Wilcox, 1994].

The standard k-ε model is is a well established and validated model [Versteeg and Malalasekera, 2007], commonly used for indoor flow regimes [Nielsen, 2015]. In this model, k is the turbulent kinetic energy and ε is the destruction of the turbulent kinetic energy as it is transformed into internal energy, also known as the turbulent dissipation rate. The standard $k-\varepsilon$ is more accurate for high Re flows [ANSYS, Inc., 2013, 2014]. Refining the standard model with analytical formulas replacing the constant values yields the RNG $k-\varepsilon$ model, which can account for lower Re, whilst a newer formulation of the turbulent viscosity and transport equation for ε is found in the Realizable $k-\varepsilon$ [ANSYS, Inc., 2013, 2014]. The k-ω model is capable of dealing with lower Re flows which is accurate and robust near walls [ANSYS, Inc., 2013, 2014]. Here ω is the specific dissipation rate. The SST (shear-stress transport) $k-\omega$ blends the near wall $k-\omega$ with free stream $k-\varepsilon$ making it more accurate and reliable than standard $k-\omega$ for a wider class of flows.

Reynolds Stress Models (RSM) [Launder and Sandham, 2002] are second order closure models as they close the approximation of the stress tensor at second order. They do not use the Boussinesq hypothesis, hence they can deal with non-isotropic turbulence. The transport equations are solved for all terms in the Reynolds Stress tensor. There are six transport equations to model k in three dimensions plus another transport equation to model ε, making it very computationally expensive to solve. This model can give very accurate calculations of mean flow properties and all Reynolds stresses, however as it models ε in same manner as k$-\varepsilon$, it performs poorly in similar flows [Versteeg and Malalasekera, 2007] it may not

warrant the additional computational expense.

In Large Eddy Simulations (Large Eddy Simulation (LES)) [Berselli et al., 2006; Versteeg and Malalasekera, 2007], large eddies are explicitly resolved in time dependant simulations using filtered Navier Stokes equations and a sub-grid scale model. The filtering is achieved by using a more refined mesh than a RANS model but coarser than DNS, giving a more expensive computational cost than RANS models but less expensive than DNS. By modelling less of the turbulence in the flow, less error is introduced than in a RANS model. It is also easier to model the smaller scales as they are less affected by the macroscopic boundary conditions than the large eddies and the turbulence is more likely to be isotropic.

Fluent advocate laminar-turbulence transition models over low Reynolds number versions of existing models [ANSYS, Inc., 2014] such as the low Reynolds number correction for the $k-\omega$ model. Examples of the transitional models include the Transition $k-kl-\omega$ model [Aftab et al., 2016; Walters and Cokljat, 2008] and the Transition SST model [Aftab et al., 2016; Menter et al., 2006a] which have both been developed to deal with domain that contains regions where turbulence is not fully developed. Whilst both models should yield very similar results, due to the roots in the standard SST model the Transition SST is preferred over the Transition $k-kl-\omega$ model [ANSYS, Inc., 2014]. Neither of these models have been calibrated to deal with turbulence due to buoyancy [ANSYS, Inc., 2014].

2.4.5 Natural convection

Convection occurs when heat is transferred by a moving fluid. Fluid moved by external forces is known as forced convection. When buoyancy forces dictate the fluid motion and subsequent transfer of energy this is known as natural convection. The density of a gas varies with temperature; gravity acts on the fluid pulling the colder, denser air downwards and forcing the warmer, less dense air to rise. The induced buoyant motion is opposed by drag caused by viscous diffusion in the fluid and heat loss due to thermal diffusion [Zhang et al., 2015]. Natural convection can assist (when the buoyant motion is the same direction as the forced flow) or oppose (when they are in opposite directions) the forced flow, augmenting or diminishing the heat transfer respectively [Rathakrishnan, 2012]. When they are perpendicular, fluid mixing and heat transfer are enhanced [Rathakrishnan, 2012]. Buoyant fluid motion can cause stability problems for CFD simulations [Etheridge, 2015].

CFD simulations which model convective flow require the solution of the energy transport equation subject to appropriate thermal boundary and initial conditions. Due to the nature of convection problems, very large gradients exist in the proximity of surfaces which need very fine grids to resolve the convective flow accurately [Modest, 2013]. When running CFD simulations, the density ρ must be properly specified to ensure conservation of mass. This can be achieved via the thermal expansion coefficient β (K^{-1}) which is given by equation (2.35) [ANSYS, Inc., 2013]. The Boussinesq approximation assumes that the density

variations are sufficiently small so they can be neglected except under the influence of gravity where density variations are due to temperature differences [Zhang et al., 2015]. This approximation is only valid for small temperature differences , $\beta\Delta T \ll 1$, and cannot be used with species transport equations [ANSYS, Inc., 2013]. When the Boussinesq approximation is not valid, an equation of state (such as the ideal gas law) should be used to determine the density [Demuren and Grotjans, 2009]. For an ideal gas, β is given by equation (2.36).

$$\beta \approx -\frac{1}{\rho}\frac{\Delta\rho}{\Delta T}, \tag{2.35}$$

$$\beta = \frac{1}{T}. \tag{2.36}$$

The motion of fluids due to density differences can be characterised by the Archimedes number, Ar, which is defined as the ratio of gravitational forces to viscous forces, given by equation (2.37). In mixed convection flows Ar represents the importance of natural convection relative to forced convection. For $Ar < 0.1$ natural convection is negligible, for $0.1 < Ar < 10$ both natural and forced convection are significant and for $Ar > 10$ forced convection is negligible [Rathakrishnan, 2012].

$$Ar = \frac{Gr}{Re^2} = \frac{g\beta\Delta TL}{v^2}, \tag{2.37}$$

where ΔT is the temperature difference between the supply and room air (°C), L is the height of the supply diffuser (m), v is in velocity of the supply air ($\mathrm{m\,s^{-1}}$) and Gr is the Grashof number (the ratio of buoyancy to viscous forces), given by equation (2.38) [Serth, 2007]. Flows are turbulent for $Gr > 10^9$.

$$Gr = \frac{g\beta\Delta TL^3\rho}{\mu^2}. \tag{2.38}$$

A measure of the strength of the buoyancy induced flow in pure natural convection is the Rayleigh number, Ra, given by equation (2.39). For $Ra < 10^8$ the flow is laminar buoyancy-induced flow. Transition to turbulence occurs in the range $10^8 < Ra < 10^{10}$ [Gao and Niu, 2004].

$$Ra = \frac{g\beta\Delta TL^3\rho}{\mu\alpha}, \tag{2.39}$$

for viscosity μ and thermal diffusivity α

$$\alpha = \frac{k}{\rho C_p}, \tag{2.40}$$

where C_p is the specific heat at constant pressure and k is the conductivity of the fluid.

2.4.6 Radiation

Thermal radiation is heat transfer by means of electromagnetic waves which does not require the presence of a medium, unlike both convection and conduction [Modest, 2013]. Radiative effects are comparable with convective ones in indoor air flows [Versteeg and Malalasekera, 2007] as the thermal radiation between surfaces will effect the fluid flow [Sørensen and Nielsen, 2003], becoming more important for larger temperature gradients between surfaces and the surrounding air flows [Voelker et al., 2014]. Heat transfer rates for convection and conduction are linearly proportional to temperature but varies with the fourth (or higher power) of temperature for radiation [Modest, 2013]. However, despite the low temperatures in buildings, the radiative effects are still important as they are often comparable with the convective effects [Versteeg and Malalasekera, 2007].

Due to the electromagnetic nature of radiation, it adjusts essentially instantaneously to the flow field conditions [Modest, 2013]. There is no direct coupling between radiation and the flow field as the radiation does not depend on the fluid motion [Versteeg and Malalasekera, 2007]. However, the temperature distribution and any species concentration do depend on the fluid flow field; these can effect the radiation properties of the fluid and the intensity of the radiation [Versteeg and Malalasekera, 2007]. The radiative transfer equation (RTE) does not require resolving in such fine detail in the same way as for convection, as such solving it on the existing fine grid is inefficient. However, solving on different grids and interpolating is would induce interpolation errors [Modest, 2013]. The RTE does not require solving at every iteration, instead increasing the number of energy iterations per radiation iteration could speed up the computation but would also slow convergence. As the radiation would not change over a short period of time, it could be assumed to be constant, even for short transient problems. Therefore an alternative would be to solve the RTE in isolation before running the remaining simulation. Once the RTE is suitably converged, it can be disabled without changing the influence of the radiation field in the domain [ANSYS, Inc., 2013].

There are several established methods for radiation modelling, including the P1 Radiation Model, Discrete Transfer Radiation Model, Surface to Surface, and the Discrete Ordinates Model. The Discrete Ordinates (DO) model is a discrete representation of the directional variation of the radiative intensity [Modest, 2013; Thynell, 1998]. The DO model solves the radiative transfer equation (RTE) [ANSYS, Inc., 2013; Modest, 2013; Versteeg and Malalasekera, 2007] for a finite number of discrete solid angles, which is analogous to solving the number of rays bouncing off the surface. In Cartesian coordinates, each octant of space is discretised into $N_\theta \times N_\vartheta$ solid control angles, where θ is the polar angle and ϑ is the azimuthal angle. For three dimensional problems this gives a further 8 N_θ N_ϑ transport equations. The default is $\theta = \vartheta = 2$ which is stated as a coarse value, although it requires 32 additional RTEs. The recommended values are $\theta = \vartheta =$3, 4 or 5 which gives a more reliable solution but at a far greater computational cost (up to a further 200 RTEs per iteration). Further control can be gained through dividing each control angle into $N_{\theta_p} \times N_{\vartheta_p}$

pixels. Increasing the pixelation increases the computational cost, but by less than increasing the number of angular divisions. The default 1×1 pixelation is usually sufficient for gray-diffuse radiation, rising to 3×3 for specular surfaces [ANSYS, Inc., 2013].

When the number of wavelength bands is set to zero, the DO model is a 'gray' (grey) radiation model in that it models the type of radiation that could be expected from a grey surface (as opposed to a black surface or a mirror). This is a simplification of real life problems which are not in fact all grey surfaces. The model assumes that the absorption coefficient (and wall emissivity via Kirchoff's law) is constant for the significant wavelengths in the temperature range of the problem. Kirchoff's Law states that emissivity is equal to absorptivity. The diffuse fraction, f_d, for a specular surface such as glass is $f_d = 0$ and for a purely diffuse surface is $f_d = 1$. The model also allows for fluid to be involved in absorption of radiation [ANSYS, Inc., 2013; Modest, 2013; Thynell, 1998; Versteeg and Malalasekera, 2007] via the refractive index, n, of the fluid. If the medium does not participate then $n = 1$ as the speed of light through the medium equals the speed of light in a vacuum.

2.5 Modelling indoor air flows

Traditionally experiments are carried out in the real world in laboratories or windtunnels [Barlow et al., 1999; Khattree and Rao, 2003]. However as computing power increases it is becoming more feasible to simulate these experiments computationally [Nielsen, 2015]. Clearly there are significant advantages to be gained by running certain computational simulations, especially those where experiments cannot be physically or practically performed. Such instances include simulating where economic costs of the experiment are prohibitive. In addition, computational experiments are more able to deal with larger numbers of design parameters [Santner et al., 2003].

2.5.1 Ventilation flows and turbulence

The airflow characteristics in buildings will always be incompressible and often turbulent [Sørensen and Nielsen, 2003]. Air change rates as low as $2-5$ ach can exhibit fully developed turbulence in the higher velocity areas of the room [Nielsen, 2015]. A universal model does not exist which is capable of accurately modelling all flow regimes [Wolfshtein, 2009; Zelensky et al., 2013] therefore compromises must always be made when modelling airflows [Sørensen and Nielsen, 2003]. Zhang et al. [2007] provides a table of turbulence models with suitable applications.

Using an inappropriate turbulence model can have a significant effect on the accuracy of any results obtained [Li and Nielsen, 2011]. Mixing ventilation has a more uniform turbulence intensity than displacement ventilation which may have areas of laminar flow. Most turbulence models are only suitable for fully developed turbulence, Sørensen and Nielsen [2003] recommend low Reynolds number (LRN) versions where they exist if their use can be justified by the flow regime. ANSYS, Inc. [2013] however

advocate the use of transitional turbulence models over LRN formulations which are more capable of dealing with the transition to and from turbulence. Newer models such as the transitional $k-\omega$ SST four equation model have been found to give superior results over the traditional RSM, $k-\omega$ and $k-\varepsilon$ models [Teodosiu et al., 2014] when compared to experimental data specifically for indoor airflows.

In the case of mixing ventilation, the fluid flow is driven by the momentum of the incoming supply air [Chen et al., 2015; Sørensen and Nielsen, 2003]. A supply of colder air at a higher level, or warmer air at a lower level, causes a turbulent flow to mix the air to a fairly uniform temperature throughout [Linden, 1999]. Any airborne contaminants are diluted to a uniform level [Liddament, 2000]. In contrast, displacement ventilation is characterized by large temperature variations with a stable temperature and density stratification with the cooler pool supply air near the floor and below the warmer upper layer of air [Linden, 1999]. Supply air is typically $2-3\,\mathrm{K}$ lower than the ambient room temperature, entering at $0.1-0.3\,\mathrm{m\,s^{-1}}$ [Liddament, 2000]. The warmer air exits through exhaust outlets near ceiling level [Liddament, 2000] with the aim of efficiently removing contaminants [Linden, 1999]. This latter type of ventilation generally exhibits a large variation in turbulence levels with low levels throughout the majority of the domain, higher only in areas near the supply of thermal plumes [Sørensen and Nielsen, 2003] from people, electrical equipment, windows or radiators for example.

Supply openings can present a modelling challenge, whether that be capturing the fine detail or simplifying them [Li and Nielsen, 2011; Nielsen, 2004; Nielsen et al., 2007c]. Wang et al. [2012] suggests that the boundary conditions are too complex to be described accurately in CFD simulations that seek to model real conditions.

2.5.2 Flows around people

A thermal plume is an example of natural convection where buoyancy forces dictate the fluid motion. An upward motion of warmer, less dense fluid forces the colder, denser fluid downwards [Zhang et al., 2015]. Cooler air from the supply pool is entrained into the plume, drawing the fresh air from the lower levels upwards, providing effective ventilation at heat sources [Sørensen and Nielsen, 2003]. The fluid flow surrounding the heat source has a significant impact on the nature of the plume itself, which interacts with the air flow around it [Licina et al., 2015c]. Depending on the location of the containments in the room, there is the possibility of also entraining floor level containments in the upward flow and suspending them in the breathing zone or dispersing them around the room [Salmanzadeh et al., 2012].

A considerable amount of energy is lost from a human body by way of convection [Murakami et al., 2000]. The heat transferred to the surroundings is due to the temperature gradient between the surface of the body and the surrounding air and creates a convective boundary layer (CBL) around the body, forming an ascending thermal plume over the head [Licina et al., 2015c]. There are two driving forces behind the CBL and thermal plume: the velocity of the surrounding air is responsible for convective heat release

and the magnitude of the temperature gradient between the body surface and the surrounding air drives the convection which is directly linked to the strength and speed of the plume generated [Voelker et al., 2014]. The CBL is important due to the interaction with the fluid flow in the room, IAQ and thermal comfort [Licina et al., 2015c], not only as a heat source but the human presents an obstruction to the free flow of air [Voelker et al., 2014]. Both have implications to the local turbulent intensity of the fluid flow [Voelker et al., 2014].

In physical experiments, a human can be modelled by thermal manikin, which in turn can be modelled for computational analysis by a computer simulated person (CSP), also known as a computational thermal manikin (CTM). Sørensen and Voigt [2003] for example use a thermal manikin for physical experiments and laser scanned data of this manikin created their CSP for use in the CFD simulation allowing direct comparison between the two. They used a boundary layer of extruded triangular prisms with 20 layers from the surface of the CTM, with an initial height of 5×10^{-4} m and a growth rate of 1.13 (Figure 2.9). They performed a CFD analysis (with a low Reynolds number $k-\varepsilon$ turbulence model and surface to surface radiation model) for a seated CTM in a similarly sized room, with similar surface temperatures, a much slower inlet velocity of $0.02\,\mathrm{m\,s^{-1}}$ and the entire ceiling modelled as an outlet. Shown in Figure 2.10 are the velocity and temperature profiles around the CTM which illustrate the thermal plume which is defining flow characteristic around people.

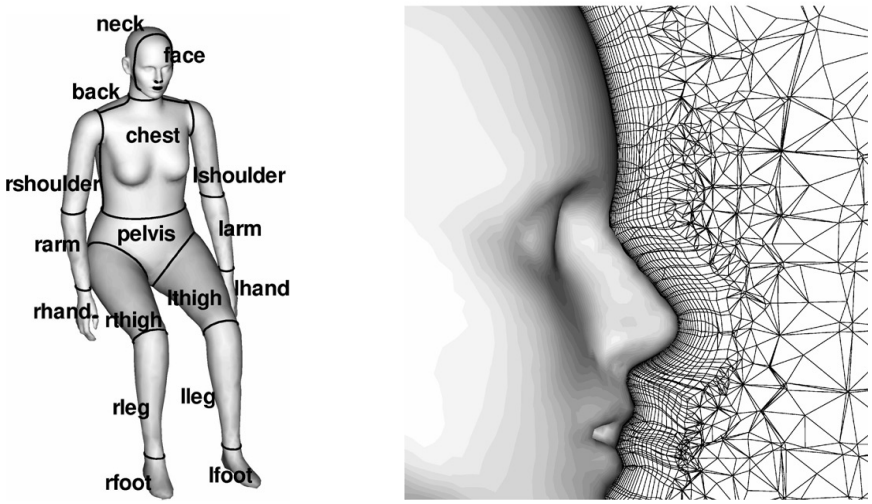

FIGURE 2.9: Left: Sectioning the CTM. Right: Inflation layer of 20 prisms. Images from Sørensen and Voigt [2003].

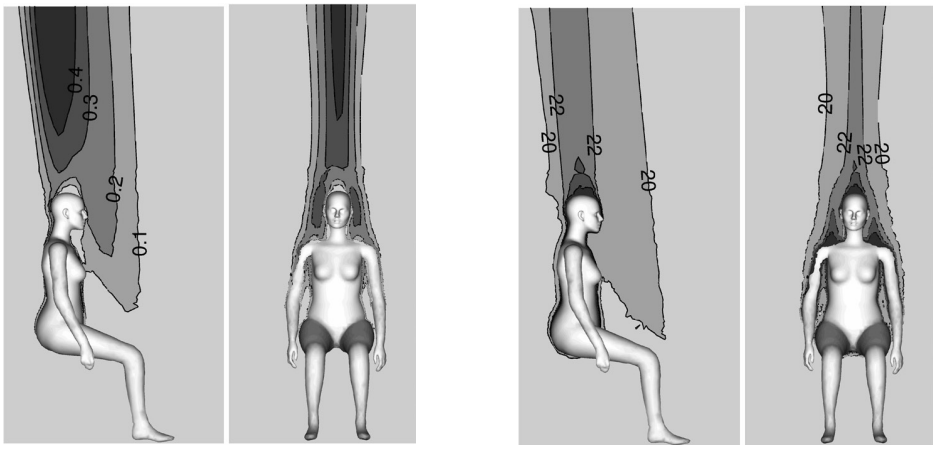

FIGURE 2.10: Left: Velocity magnitude in the thermal plume. Right: Temperature distribution for the thermal plume. Images from Sørensen and Voigt [2003]

In a recent review of thermal manikins Psikuta et al. [2017] underlined the crucial role that air layers close to the surface of humans have on heat and mass transfer. In order to capture these flow features adequately in computer simulations, high mesh resolution in the CBL is particularly important [Nielsen, 2015] and this aspect is taken forward in subsequent chapters. Related to this, Psikuta et al. [2017] also characterised the features of heat transfer mechanisms between skin and clothing with conduction, convection, radiation, evaporation and ventilation all having an influence, see Figure 2.11.

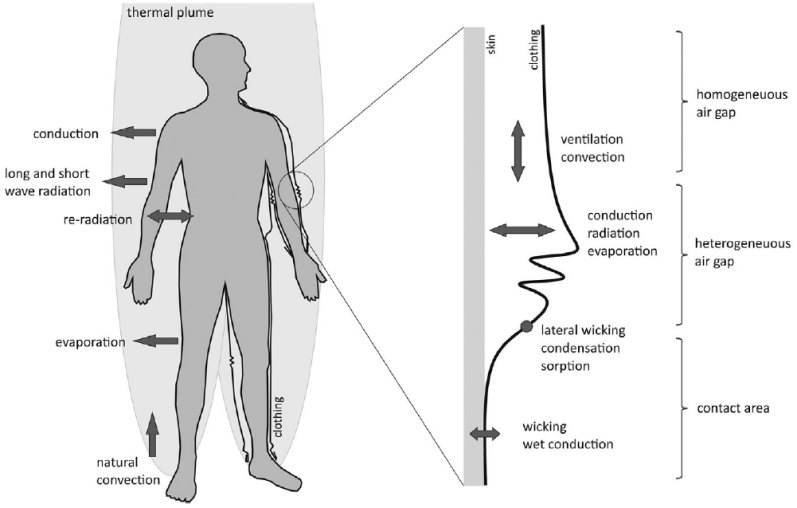

FIGURE 2.11: Image from Psikuta et al. [2017] showing heat transfer pathways at the human body surface and within the clothing layers.

Considering the shape of the object representing a person, there are many different approaches which have been adopted both experimentally and computationally. Zukowska et al. [2007a] compared four human body representations of a sitting person in a small experimental chamber. They were a cylinder,

a rectangular box, a dummy made up of boxes and cylinders and a detailed CTM. The cylinder and the box correctly simulated enthalpy and buoyancy flux but thermal plumes were much more concentrated than those generated by the dummy and the CTM. Despite being more simplified, the dummy gave almost identical results to the detailed CTM [Zukowska et al., 2007a].

From numerical modelling perspective, simplified multi-block CTMs are also used to reduce the computational complexity, however, as shown experimentally [Zukowska et al., 2007a], they are not always suitable as they do not provide adequate accuracy with significant differences in the flow field and velocity distributions around the CTM [Nielsen, 2004] and in the breathing zone [Russo and Khalifa, 2010].

Voelker et al. [2014] used a detailed thermal manikin sat on a chair with complex heating arrangements to obtain physical measurements in the micro-climate around a body under steady state conditions. They observed good agreement with published data relating to experiments with humans. At the body surface, the velocity of air is zero. Just off the surface in the boundary layer shear stresses inhibit the air velocity. Due to the heat generated by the manikin, convective forces drive the flow around the manikin and the air velocity increases with increasing distance from the body. This peaks as the influential limit is reached and the air velocity decreases to match that of the undisturbed air flow. The thickness of the CBL is found to be dependent on the geometry of the manikin. The CBL is thin around the torso, increasing in thickness as it moves up. The temperature of the CBL is bounded by that of the body surface and the undisturbed air, the highest temperatures and thickest CBL are found around the neck and head. The resulting plume above the head is as wide as the shoulders and decreases in width with height. A dead zone exists directly above the head where there is very little air movement and little turbulence. In contrast, around the thickest part of the head flow separation develops due to turbulence. Cooling the room increases the temperature difference between the room and the body thereby making the temperature gradient larger, which induces faster air velocities in the thermal plume and greater levels of turbulence. Salmanzadeh et al. [2012] found that the velocities in the thermal plume generated by a human easily reach $0.2-0.3\,\mathrm{m\,s^{-1}}$, up to a maximum of around $0.5\,\mathrm{m\,s^{-1}}$ near the surface [Sørensen and Voigt, 2003].

Deevy et al. [2008] considered the effect of a standing CTM and they allowed for a taller thermal plume with a higher ceiling and also had a larger exhaust outlet. Figure 2.12 shows their results for the velocity and temperature distributions along the centre plane for their unsteady RANS simulation using the SST $k-\omega$ model and discrete transfer radiation model. It can be seen that the displacement flow is much less disturbed by a standing CTM than by a sitting one, which forces the supply air up and over the CTM. The temperature profile is also far more stratified throughout the domain, not just behind the CTM.

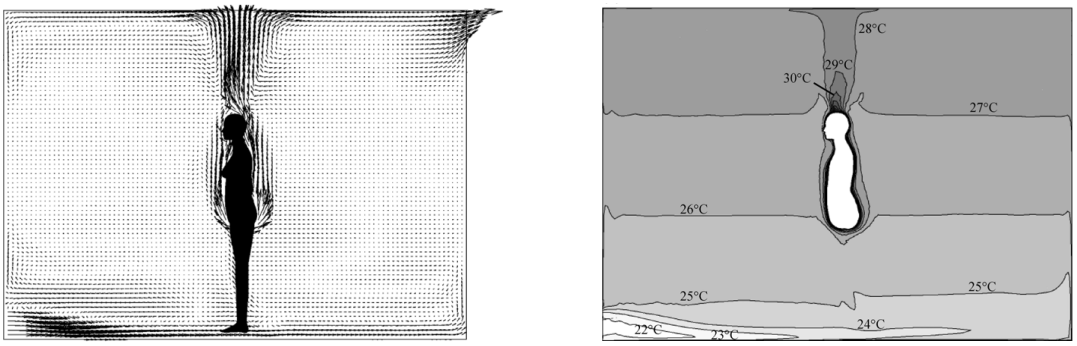

FIGURE 2.12: Left: Time averaged velocity vectors. Right: Time averaged temperature contours. Images from Deevy et al. [2008]

Deevy et al. [2008] and Sørensen and Voigt [2003] are amongst several authors to observe a better correlation between CFD and experimental data when radiation is also modelled, highlighting the importance of this modelling aspect, not only in thermal comfort calculations but also in the effect it has on convection and mixing of the flow. Deevy et al. [2008] found that inclusion of radiation terms was essential for improved CFD prediction when compared to experimental data. They postulate that the radiation from the body/thermal manikin heats the walls, leading to extra convection and mixing throughout the room. Furthermore, the mean radiant temperature is a key parameter in thermal comfort, as is asymmetric radiation. For a human or manikin, the radiative effect differs between body parts dependent on their location and size, and increasing with increasing surface temperature.

When the temperature differences are sufficiently small, $\Delta T \sim 6$ K say to account for the lower supply temperature and heat increase due to thermal sources, the Boussinesq approximation can be applied and a constant density can be assumed (see section 2.4.5). For air, $\beta \sim 3.3 \times 10^{-3}$ then $\beta \Delta T \sim 0.02 \ll 1$. For contaminants that are lighter than the surrounding air, displacement ventilation separates these contaminants from the breathing zone as they rise with the natural convection, however the Boussinesq approximation is not applicable when modelling these flows using species transport equations [ANSYS, Inc., 2013].

Breathing has little effect on the thermal plume [Salmanzadeh et al., 2012] however it can effect the concentration and location of containments in the room. The exhalation flow from both the nose and mouth is capable of infiltrating the CBL and breathing zone of another person up to 1.2 m away [Bjørn and Nielsen, 2002]. Breathing manikins indicate that air exhaled from the nose tends to flow towards the ceiling whilst air (and any contaminants it contains) exhaled from the mouth can become trapped in a thermally stratified, horizontal layer at the height of the breathing zone when the temperature gradient in that area is large enough [Bjørn and Nielsen, 2002].

Disturbances to the air flow, caused for instance by a moving manikin, effect the distribution of containments in the room [Salmanzadeh et al., 2012]. Increased movement levels lead to more mixed

conditions [Bjørn and Nielsen, 2002]. Wood [2015] found the $k-\omega$ SST turbulence model the best at capturing the wake of flow past a moving cylinder. The consequence of any such disturbance is smaller under mixing ventilation conditions than displacement ventilation, also taking less time to recover for mixing than displacement ventilation [Wu and Lin, 2015]. This is because the stratification is disturbed in displacement ventilation rooms [Bjørn and Nielsen, 2002], the vertical temperature gradients is reduced, increasing the temperature of the inhaled air and mixing the clean air close to the floor with the more polluted air at higher levels [Halvoňová and Melikov, 2010]. Disturbances closest to the displacement diffusers cause the most disruption to the flow regime [Halvoňová and Melikov, 2010].

2.5.3 State of the art knowledge in personalized ventilation in indoor and office environments

A wide range of PV methods have been considered over recent years. Irrespective of the methods used, the aims have been to improve the quality of the inhaled air, reduce risk of infection, improve thermal comfort and minimise the effect outside of the immediate environment [Melikov, 2004]. Experiments have shown a preference to moveable PV devices over fixed ones, such as those mounted at the front of a desk or in a headset [Kaczmarczyk et al., 2006]. However, PV from a headset has been shown to increase the volume of fresh air inhaled and decrease the inhalation of contaminated air [Bolashikov et al., 2013]. Other studies considered fans alternating from different directions [Kalmár and Kalmár, 2013] and fans in-built into chair arm rests to direct contaminated gases up and out of the breathing zone of a stratified air profile caused by displacement ventilation [Habchi et al., 2015].

Melikov et al. [2012] presented an experimental study using both a breathing thermal manikin and human test subjects. The personalised ventilation was provided through a seat headrest, as shown in Figure 2.13. The configuration showed a dramatic improvement in inhaled air quality and decreased risk of airborne cross-infection. Furthermore, no draught was reported.

FIGURE 2.13: Image from Melikov et al. [2012] showing the breathing thermal manikin and the placement of air terminal devices.

An alternative study utilised the fresh air at floor level and diverted this to the breathing zone [Dalewski et al., 2014], as shown in Figure 2.14. It was found that the human test subjects experienced an increase in both PAQ and thermal comfort with the PV system. Furthermore the percentage that were dissatisfied at higher temperatures decreased with the use of PV when compared to displacement ventilation alone. However, despite the ability to control the PV system they suffered with increased eye irritation.

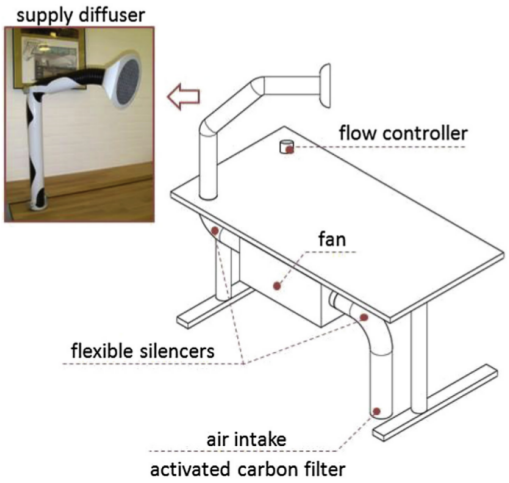

FIGURE 2.14: Image from Dalewski et al. [2014] showing the ductless personalised ventilation layout.

The effect of PV has also been studied when investigating the transmission of contaminants from one occupant to another [Nielsen et al., 2007a]. Micro-environments have been created with a controllable PV device aimed towards the face with recirculated air diffused from either side of the desk to isolate the micro-environment [Naumov et al., 2015]. One study considers an occupant under a downward ventilation jet from the ceiling with an exhaust fan mounted on the desk in front of them [Makhoul et al., 2013]. The use of the ceiling PV reduced the thermal plume, as illustrated in Figure 2.15. The desk mounted suction exhaust fan was found to control the convective flow around the body and improved the effectiveness of PV. This strategy was shown to have a significant energy reduction compared to traditional mixing ventilation alone.

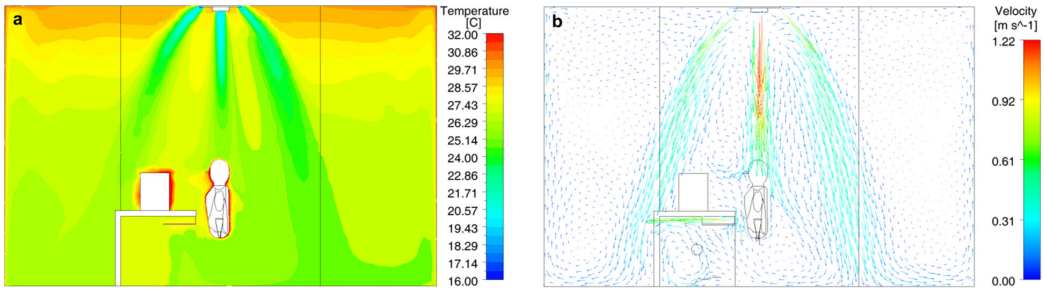

FIGURE 2.15: Image from Makhoul et al. [2013] showing a) contours of temperature and b) vectors coloured by velocity for the vertical ventilation jet.

Naumov et al. [2015] found that by maintaining an optimal micro-climate around an occupant and restricting the background climate to merely acceptable levels, substantial energy savings could be achieved. The concept of their local demand controlled ventilation is shown in Figure 2.16 with fans controlling the optimal area, along with the actual CAD showing the occupant represented by a cylinder. The micro-climate can be seen in Figure 2.17 in the velocity and temperature profiles located in a plane 0.5 m above floor level.

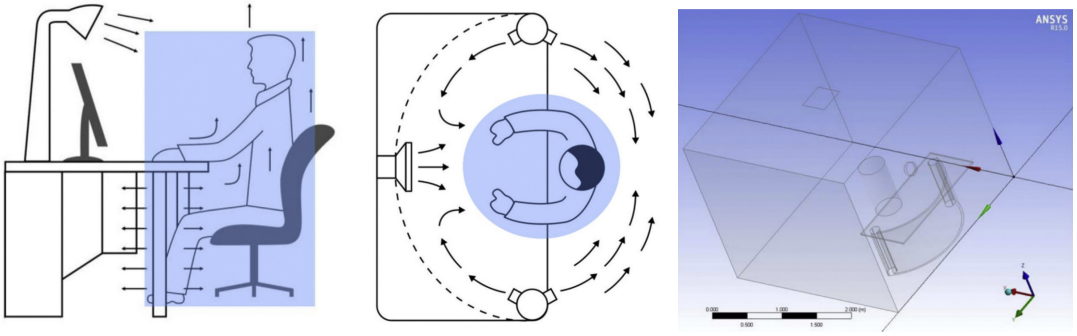

FIGURE 2.16: Images from Naumov et al. [2015] showing the concept and CAD.

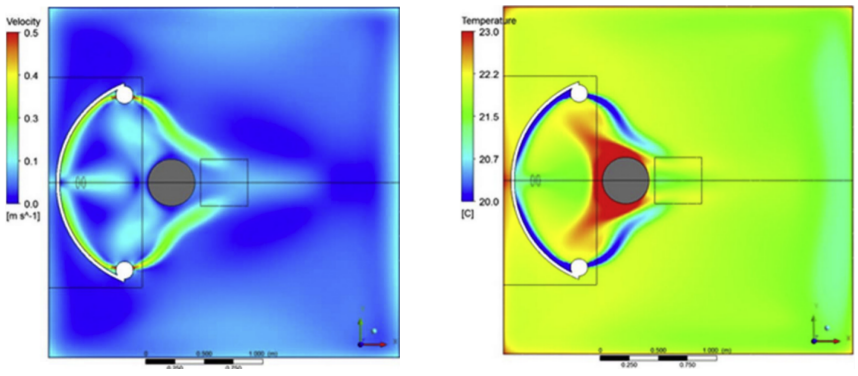

FIGURE 2.17: Images from Naumov et al. [2015] showing the velocity and temperature 0.5 m above floor level.

Junjing et al. [2014] mounted exhaust fans directly in the chair of a breathing thermal manikin to minimise the risk of contamination spreading to the rest of the room, the set up is shown in Figure 2.18. Both displacement and mixing ventilation were considered. The study concluded that a personalised ventilation strategy coupled with a personalised exhaust system provided more fresh air to the breathing zone than a PV system alone.

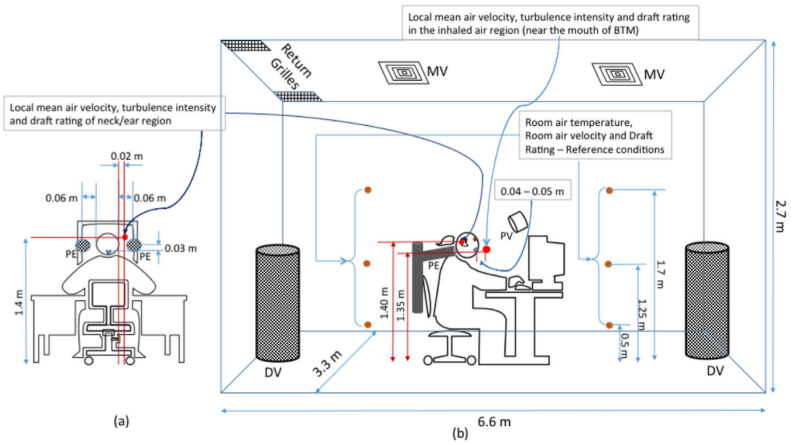

FIGURE 2.18: Image from Junjing et al. [2014] showing the experimental set-up.

Mazej and Butala [2012] found that a PV mounted on the desk surface with air supplied upward towards the face increases the chances of contaminated air moving around the room, as illustrated in Figure 2.19. It was found that the highest quantity of clean air from PV was associated with the greatest thermal discomfort. Furthermore, the PV system dominated the dispersal of exhaled air into the room, increasing risk of airborne infection.

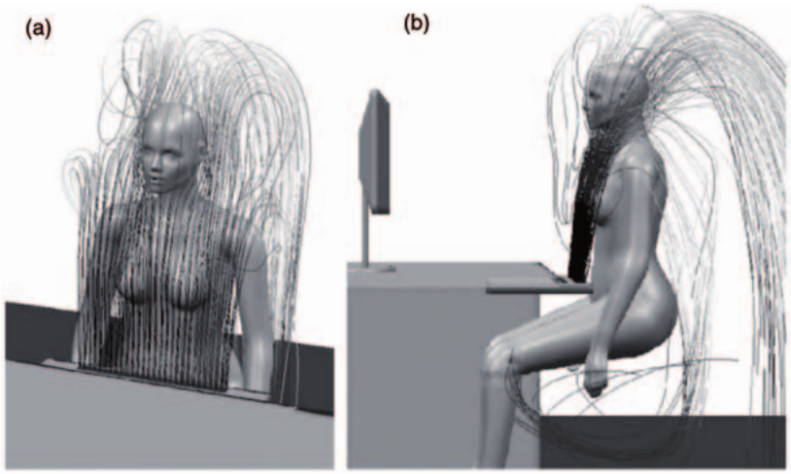

FIGURE 2.19: Image from Mazej and Butala [2012] showing the pathlines of the air from the PV system.

There are some situations where contaminant dispersal should be actively avoided, such as hospital wards, operating theatres and other healthcare environments. Nielsen et al. [2007b] found that there is merit in adding PV systems to the pillows and/or mattresses of beds in hospital wards, for example. King et al. [2013] found the RSM to be the best turbulence model for tracking particles (to represent bioaerosols) in one and two bed hospital rooms.

Horikiri et al. [2015] found that the presence of furniture did not significantly effect the overall temperature

in an unoccupied room, although it did cause recirculation zones. The presence of a chair had a strong interaction with the ventilation flow from floor level [Licina et al., 2015c], whilst the presence of a desk blocks the thermal plume from the legs of a sitting CTM and redirects it towards the body [Mazej and Butala, 2012].

Licina et al. [2015c] performed experiments using thermal manikin to investigate the effects of assisting, opposing and transverse flow on the human convective boundary layer (CBL). The non-breathing, clothed, female thermal manikin was sat on a chair in a test chamber and released $65\,\mathrm{W\,m^{-2}}$ giving a surface temperature in the range $30.5-34.5\,^{\circ}\mathrm{C}$. The opposing flow was released from above the manikin in a downwards vertical direction, whilst for transverse flow the air was released directly in front of the manikin. In the case of assisting flow was released from directly below the manikin but in this instance the manikin was standing as previous experiments had shown that the geometry of the chair significantly impacted the airflow patterns in the breathing zone. The flow field around the manikin was recorded using a particle image velocimetry (PIV) system. An opposing flow of $0.175\,\mathrm{m\,s^{-1}}$ had an insignificant effect on the CBL in the breathing zone, barely changing the flow characteristics from that with no flow. However the height of the plume was reduced to 0.4 m above the top of the head and horizontally stratified. The opposing flow of $0.3\,\mathrm{m\,s^{-1}}$ reduced the peak velocity in the CBL by almost half, with disturbances in the breathing zone where the CBL and opposing flow met creating a vortex and a very high local turbulent intensity. The height of the plume was reduced to 0.15 m above the top of the head. The opposing flow of $0.425\,\mathrm{m\,s^{-1}}$ destroyed the thermal plume entirely. With the exception of the area under the chin and mouth which benefited from head being a physical obstacle to the flow, the remainder of the flow directly in front of the face was in a downwards direction. High turbulence levels were observed in the area in front of the mouth where the flow changed direction due to the collision of the CBL and opposing flow. The transverse flow penetrated the CBL at $0.175\,\mathrm{m\,s^{-1}}$, completely replacing the upward flow with a horizontal one for both $0.3\,\mathrm{m\,s^{-1}}$ and $0.425\,\mathrm{m\,s^{-1}}$. For a seated manikin, the assisting flow of $0.175\,\mathrm{m\,s^{-1}}$ increased the air velocity in the breathing zone, but decreased it for $0.3\,\mathrm{m\,s^{-1}}$ and $0.425\,\mathrm{m\,s^{-1}}$ flows due to the formation of a vortex with a downwards flow in front of the abdominal region, which was caused by interactions between the assisting flow and the chair. When the manikin was standing, the chair was not present to block the air flow and increasing the velocity of the assisting flow increased the velocities in the breathing zone.

Melikov and Pokora [2014] studied the seat occupancy rate and body movements of eleven occupants in an office over one working day. They found that the occupants were seated at their desks for 70 % of the time. There was an average of 0.63 m between the PC monitor and the occupant, varying between 0.48 m and 0.72 m. For the majority of the time, the occupants' moved an average 0.225 m to either side, with a maximum of 0.75 m, changing position several times a minute. They suggest that a PV unit should be designed to take these movements into consideration so that the occupant may benefit from inhaling the highest quality air. An area of width 0.7 m with a core penetrating to a depth of 0.8 m from the diffuser is

proposed. To achieve this depth would require a diffuser diameter of around 0.2 m as they state that the length of the core of fresh air is typically four to five times that of the diffuser diameter. To achieve the proposed width, they suggest the possibility of a rotating diffuser that moves with the occupant.

Mazej and Butala [2012] considered two cases of a breathing CTM, nostrils only and mouth only with a PV system located at waist level directed up towards the breathing zone. They found that breathing had little impact on the airflow in the room however it had significant impact on airflow near the breathing zone. Inhaled air was drawn from below the jaw where the PV interacted with the thermal plume. Exhalation from the mouth was horizontal and penetrated the thermal plume without recirculation. Exhalation from the nose interacted with the rising plume and the PV flow, becoming entrained in the upwards flow. This supports previous research which found that air and contaminants exhaled from the nose moves towards the ceiling whilst exhaled gases from the mouth can become thermally stratified [Bjørn and Nielsen, 2002]. Whilst manikins can mimic the respiratory frequency and general airflow patterns, the levels of contaminants will differ due to the simplified mouth structure and other modelling constraints [Xu et al., 2015]. Actual human breathing is far more complicated with variations in exhaled airflow directions with a higher scattering of contaminants and greater turbulence levels [Xu et al., 2015].

Kalmár [2015] varied the direction of the airflow within the PV micro-environment to avoid occupant adaptation to a steady state. This strategy could potentially lower energy usage compared to more traditional ventilation systems. It was found that women preferred smaller time intervals between the changes in airflow direction than men.

Fans can be used to increase mixing and complement ventilation for higher temperature ranges, whilst also lowering energy costs by minimising the reliance on HVAC units [Pasut et al., 2014]. Zhai et al. [2015] performed experimental tests in warm and humid environments with ceiling fans on human test subjects. Due to the nature of the overhead fans and the variation in airflow despite constant fan speeds, these experiments were transient in nature. The occupants had no control over the fans located directly overhead. It was found that increased thermal comfort and PAQ was often found at fan speeds over an above the recommended limit of $0.8\,\mathrm{m\,s^{-1}}$. Pasut et al. [2014] found that for both fixed and oscillating fans at several locations all directed towards the occupants face, PAQ was improved and thermal comfort was unaffected.

The graphs in Figures 2.20, 2.21, 2.22 and 2.23 below are representative fixed PV nozzles cases found in literature: Bogdan et al. [2016]; Bolashikov et al. [2013]; Cermak et al. [2006]; Gao and Niu [2004]; Makhoul et al. [2013]; Mazej and Butala [2012]; Nielsen et al. [2007a]; Russo et al. [2009]; Yang et al. [2010]. Figure 2.20 shows the spatial location of the PV nozzles with respect to the breathing zone, located at (0,0). It can be seen that vast regions of this parameter space is unexplored. Part of this can be explained by the practicality of the location, such as directly over the head of a seated occupant may

provide an obstacle to a standing occupant. Furthermore, a wide range exists in the size (area) of the PV nozzle exit (Figure 2.21) and the associated PV velocity required to reach the breathing zone (Figure 2.22). The thermal parameter space is covered more comprehensively that the spatial one. Figure 2.23 shows the ambient and PV temperatures used. The literature covers the extremes of summer and winter indoor temperatures for various locations around the world.

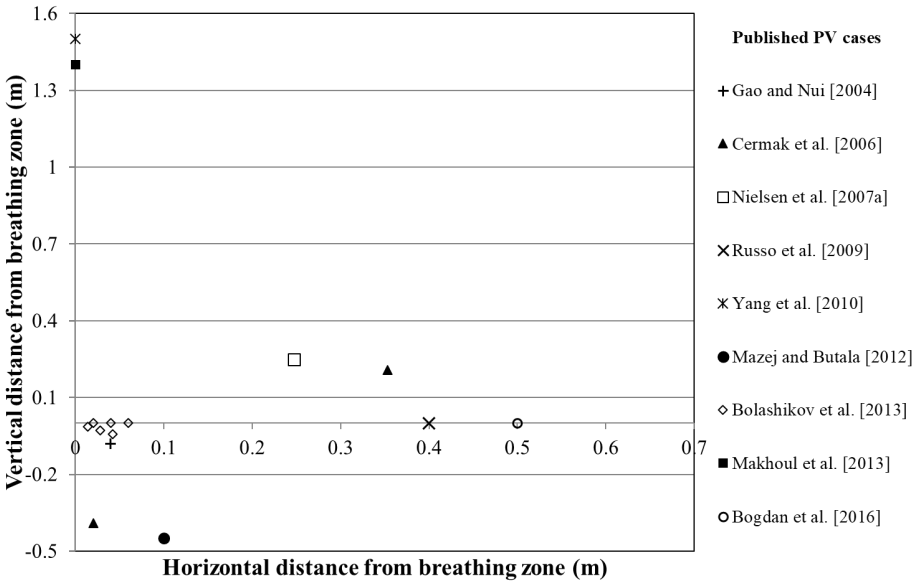

FIGURE 2.20: Spatial location of PV nozzles in literature.

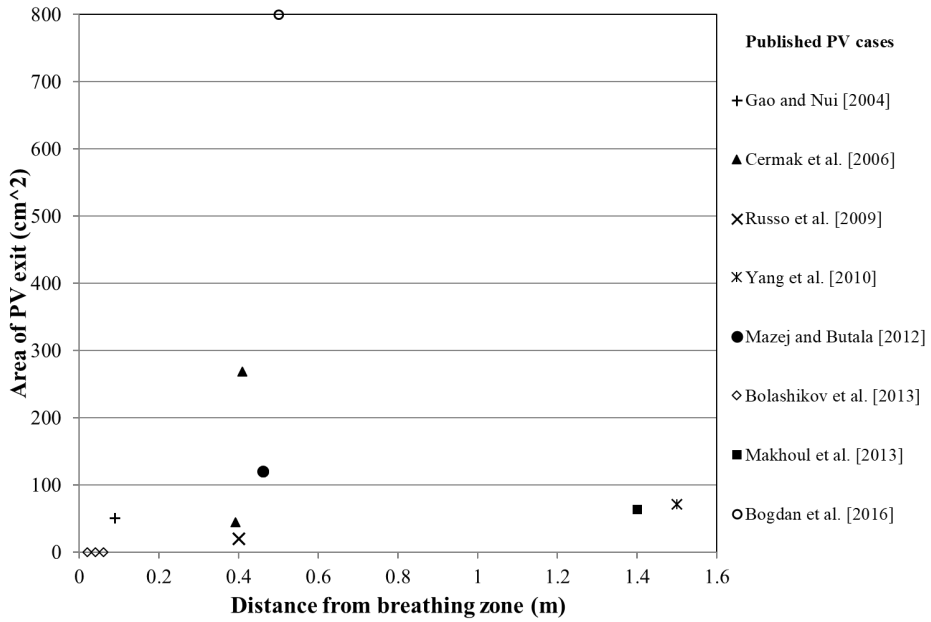

FIGURE 2.21: Areas of the PV nozzle used in literature for different PV distances from the BZ.

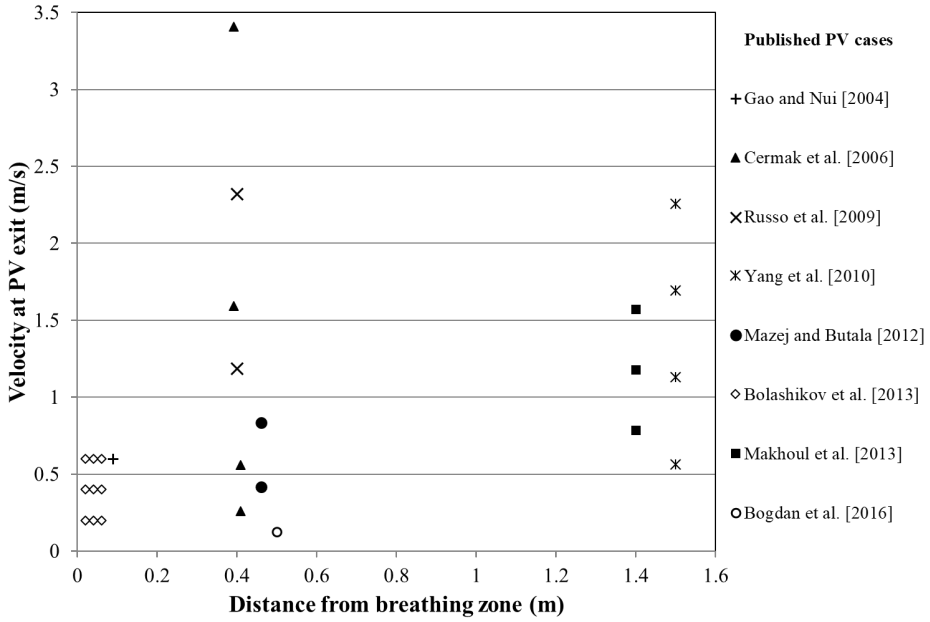

FIGURE 2.22: Air velocities at the PV nozzle used in literature for different PV distances from the BZ.

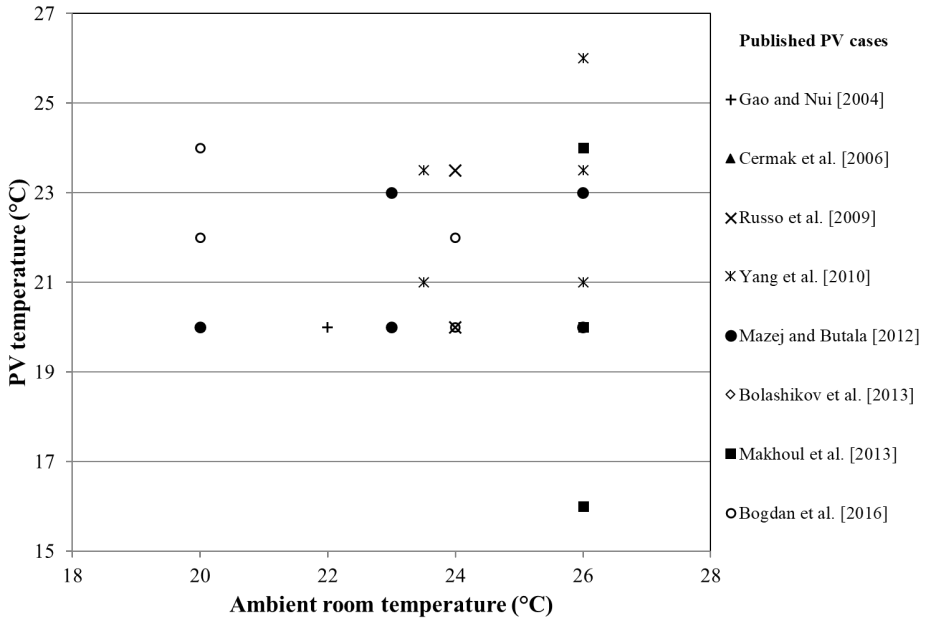

FIGURE 2.23: Ambient air and PV air temperatures used in literature.

2.6 Knowledge gaps

Following a review of the relevant literature, it is apparent that there is no systematic exploration of the factors involved in numerically modelling PV systems. Whilst CFD modelling has been applied to PV, it has been relatively simple and there has been no detailed consideration of the factors involved in PV placement and usage, nor aspects such as radiation modelling, turbulence models and the level of detail needed to represent a thermal manikin. These are the gaps in knowledge that will be addressed in this thesis.

The research presented here will cover:

- The impact of distance between the PV nozzle and the breathing zone of an occupant.
- The influence of room and PV temperature on ventilation patterns, indoor air quality and thermal comfort.
- The impact of two occupants on ventilation performance and thermal comfort.

These aspects have not, to the authors knowledge, been studied in detail in this context. The outcomes of the research presented in this thesis fall into two broad categories, namely the simulation process and the results generated. Successfully addressing these gaps in knowledge should lead to a valuable contribution to knowledge in the form of useful and practical guidelines, for both simulations and, ultimately, PV deployment.

3. Developing a computational strategy

Contents

The central theme of this thesis is concerned with computational modelling of personalised ventilation systems. It is therefore essential to establish a robust modelling approach, demonstrating the reliability and accuracy of the CFD predictions under known conditions in order to have confidence in the results in related scenarios. The aim of this chapter is to implement the theory and methods from §2.4, detailing a number of stages in the development of establishing a computational strategy upon which the remainder of the research in this thesis will be based.

Due to the importance of accounting for radiation in occupied indoor environments, analytical test case is used to identify the most suitable settings to accurately represent the radiation field (§3.1). This is followed by a number of fluid flow test simulations, based around an experimentally validated benchmark test case, to verify the most appropriate numerical models, mesh parameters and boundary conditions which are taken forward in subsequent chapters (§3.2, §3.3 and §3.4). A summary of all the CFD settings is presented in Table 3.15 at the end of this chapter in section 3.4.10.

3.1 Validation of radiation modelling in CFD

Thermal radiation is an integral part of determining the indoor environment, comparable with convection [Versteeg and Malalasekera, 2007] on the impact on the flow field [Sørensen and Nielsen, 2003] and used in the calculation of the thermal comfort metrics; namely the operative temperature (as defined in equation (2.15)) and PMV (equation 2.8). The aim of this section is to determine the appropriate settings for the CFD solver Fluent, to be used in the remainder of the thesis.

3.1.1 The analytical solution

An analytical test case was used to verify the Discrete Ordinates (DO) radiation model discussed in § 2.4.6 and to determine the appropriate model settings. The computational domain considered was a closed cube of dimension $(1 \times 1 \times 1)$ m filled with air, with one hot wall, as shown in Figure 3.1a. One wall (on the yz-plane) was heated to 32°C and the five remaining walls heated to 22°C. An analytical solution was used as a direct comparison for the results obtained through simulations. The mean radiant temperature T_r at a point p is given by

$$T_r = \sum F_{ap} T_s, \tag{3.1}$$

where T_s is the temperature of the surface and

$$F_{ap} = \frac{1}{4\pi} \sin^{-1}(\sin\alpha \sin\beta) \tag{3.2}$$

is the angle factor used to determine the relative area of that surface seen at point p. Figure 3.1b shows the mean radiative temperature inside the domain given by equation (3.1). The heated wall is not shown in this image in order to allow the contours on the xy and xz planes. It can be seen that the radiation field is rotationally symmetric about the x-axis.

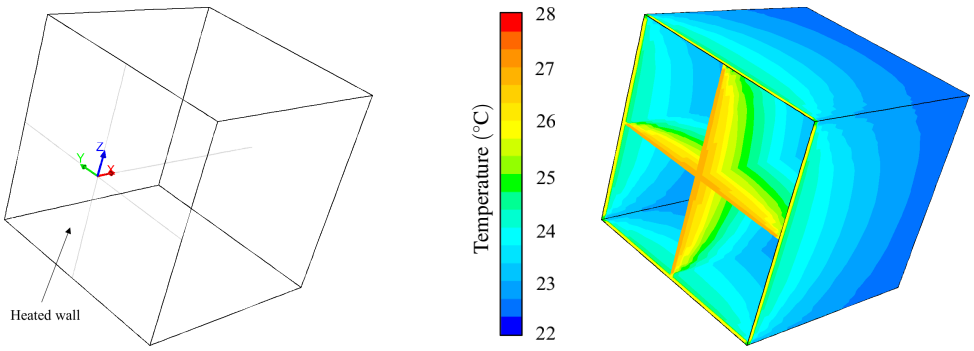

(a) Computational domain.

(b) Analytical solution for mean radiant temperature (°C).

FIGURE 3.1: Analytical radiation field inside a cube.

3.1.2 Computational modelling

Air movement occurs due to natural convection achieved through heating of the closed domain with no inlets or outlets present. Simulations were run in Fluent and modelled with laminar flow, gravity activated with buoyancy forces modelled using the Boussinesq approximation. Each wall was set as constant temperature with no heat generation and an internal emissivity of 1 (thereby making it a perfect absorber with nothing reflected). The walls were modelled as opaque to radiation. Thermal simulations were run to convergence with the Discrete Ordinates (gray) radiation model. In 3D Cartesian coordinates, each octant is divided into $N_\theta \times N_\vartheta$ control angles. For this validation, $N_\theta = N_\vartheta = 2$ (coarse) to $N_\theta = N_\vartheta = 5$ (fine) were investigated, making it computationally expensive as each iteration requires $8N_\theta N_\vartheta$ radiative transport equations (RTEs). This equates to 32 RTE's per iteration for the coarsest DO model and 200 RTE's for the finest. Further control can be obtained by subdividing the control angles into pixels (N_{θ_p} and N_{ϑ_p}), at less computational expense than increasing number of control angles. $N_{\theta_p} = N_{\vartheta_p} = 1,\ldots,5$ were considered, noting that Fluent recommendation is $N_{\theta_p} = N_{\vartheta_p} = 1$ for diffuse surfaces and $N_{\theta_p} = N_{\vartheta_p} = 3$ for specular ones. The simulations were run for both first and second order upwind discretisation of the RTE's.

3.1.3 Analysis

Figures 3.2 and 3.3 show contours of the mean radiant temperature on the walls and the centre planes for $N_\theta = N_\vartheta = 2$ and 5 respectively. Simulations were run for all the cases stated and the same general trends were found. Qualitatively, all the radiation fields are in the same range as the analytical solution, although none exhibit rotational symmetry about the x-axis. Increasing the number of control angles, N_θ and N_ϑ, from 2 to 5 sees the radiation fields approach the expected analytical solution. There appears to be negligible improvement for increasing the number of pixels, N_{θ_p} and N_{ϑ_p}. Distinct and consistent differences between first and second order discretisation of the RTE's is apparent, with the first order cases producing smoother, more realistic fields, despite requiring considerably less computational expense than second order discretisation simulations.

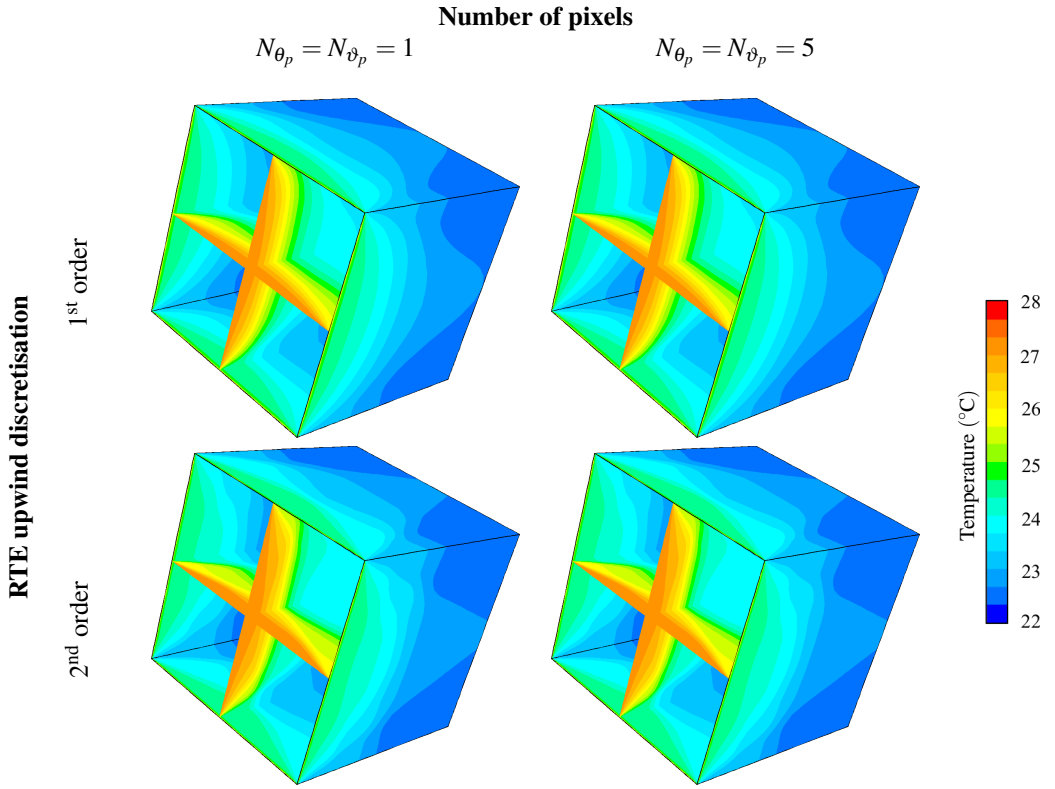

FIGURE 3.2: Contours of mean radiant temperature (°C) for $N_\theta = N_\vartheta = 2$ control angles.

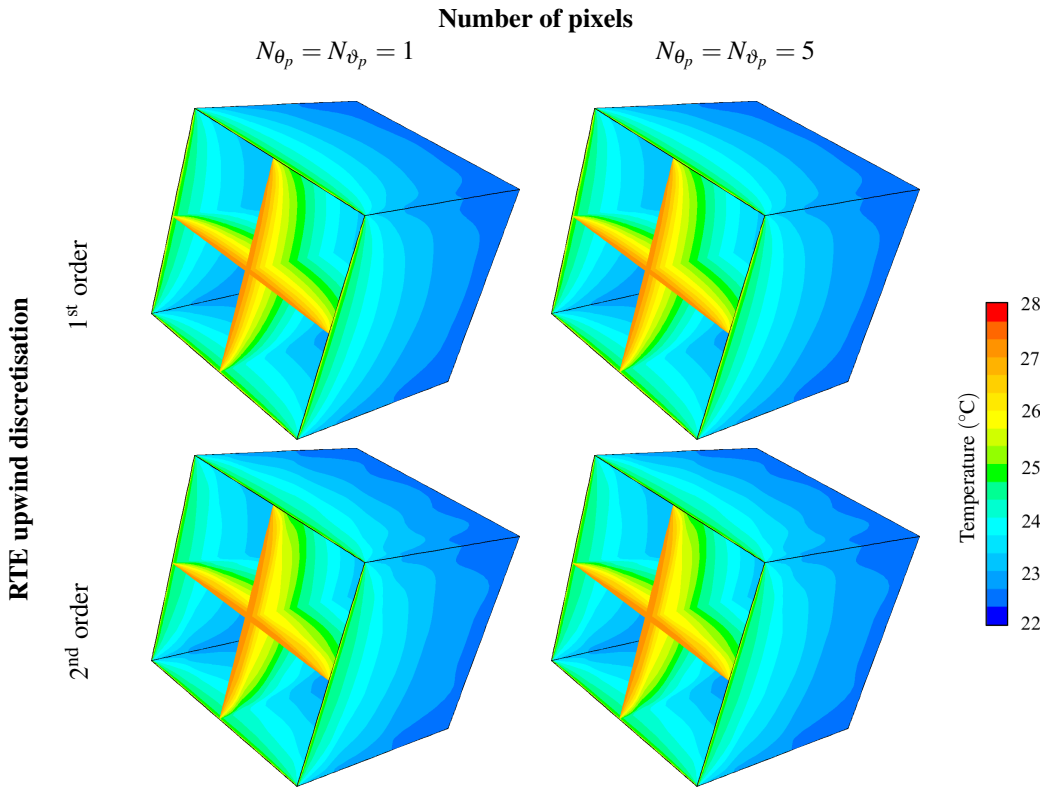

FIGURE 3.3: Contours of mean radiant temperature (°C) for $N_\theta = N_\vartheta = 5$ control angles.

A direct, quantitative, comparison between the radiation simulations and the analytical data was made at $27,000$ locations in the domain using a $30 \times 30 \times 30$ data cloud of equally spaced points exported from Fluent. To ensure values from inside the computational domain, the extents of this data cloud were specified to be 1mm inside each wall boundary. Data was processed using the statistical programming language R, comparing the simulated values at the data cloud locations with the analytical ones. To assess the accuracy of the simulations, several statistical measures were considered: Pearson's product moment correlation (r), root mean square error (RMSE), mean absolute deviation (AD) and maximum AD. These measures consider the computational domain as a whole and compress the data output from the $27,000$ locations into single statistical numbers for ease of comparison.

The Pearson's product moment correlation is a measure of linear correlation between the variables, namely the analytical solution and the CFD prediction. A value of 0 means there is no correlation whilst -1 and $+1$ imply a negative or positive correlation respectively. A correlation value close 1 means that the CFD prediction is close to the analytical solution. However, the measurements of errors (RMSE, mean AD and max AD) should tend to 0 for a good prediction. These statistical measures of accuracy of the CFD predictions with different control angles ($N_\theta = N_\vartheta = 2 \ldots 5$) are shown (to 4 signifcant figures) in Table 3.1. Values were found to be constant for any given control angle ($N_\theta = N_\vartheta$) irrespective of pixelation, so only values of $N_{\theta_p} = N_{\vartheta_p} = 2$ are presented.

RTE	Control angles ($N_\theta = N_\vartheta$)			
Discretisation	2	3	4	5
1st order	0.9910	0.9974	0.9987	0.9992
2nd order	0.9812	0.9939	0.9972	0.9988

(a) Pearson's product moment correlation

RTE	Control angles ($N_\theta = N_\vartheta$)			
Discretisation	2	3	4	5
1st order	0.2117	0.1208	0.0938	0.0824
2nd order	0.2923	0.1701	0.1230	0.0966

(b) RMSE (°C)

RTE	Control angles ($N_\theta = N_\vartheta$)			
Discretisation	2	3	4	5
1st order	0.1647	0.0948	0.0761	0.0691
2nd order	0.2274	0.1345	0.0974	0.0782

(c) Mean AD (°C)

RTE	Control angles ($N_\theta = N_\vartheta$)			
Discretisation	2	3	4	5
1st order	0.6201	0.4202	0.3287	0.2822
2nd order	0.9763	0.5451	0.4100	0.3496

(d) Max AD (°C)

TABLE 3.1: Statistical measures of accuracy of CFD prediction (with $N_{\theta_p} = N_{\vartheta_p} = 2$ pixels) for the radiation in a cube.

It can be seen from Table 3.1a that there is a better correlation between the analytical solution and the CFD prediction using the 1st order discretisation of the radiative transport equation (RTE) than with the 2nd order discretisation. Similarly, in the errors in Tables 3.1b, 3.1c and 3.1d are all smaller for the 1st order discretisation than they are for the 2nd order. This could be because 1st order discretisation is more diffusive and therefore more representative of the inverse square law underpinning radiation fields.

In all the measures, the accuracy of the prediction can be seen to improve by increasing the number of

control angles. The correlation in Table 3.1a increases, very close to a perfect correlation of $r = 1$ for $N_\theta = N_\vartheta = 5$. Tables 3.1b, 3.1c and 3.1d show that the RMSE, mean AD and max AD all decrease for increasing control angles, although the step changes observed are smaller after $N_\theta = N_\vartheta = 3$. The maximum absolute deviations are four times larger than the mean AD, with variations of up to 1 °C for the second order discretisation simulations, almost twice that of the first order ones.

These tables reaffirm the qualitative findings discussed above: pixelation is inconsequential, second order discretisation of the RTE's causes higher errors than first order and increasing the control angles improves the CFD prediction.

3.1.4 Summary

The aim of this section was to gain an understanding of the processes and challenges involved in numerically modelling radiation. From this test case, the following observations and conclusions can be drawn:

1. Even the largest errors found are, for practical purposes, not that significant.
2. Whilst there is a case for requiring a physically realistic radiation field, especially for more complex geometries (such as around a computational thermal manikin), the extra computational cost for finer angular control (and the corresponding increase in number of radiative transport equations to be solved) is warranted.
3. The extra computational cost inured by increasing from 1st to 2nd order discretisation of the radiative transport equations is not justified as all results indicate that the errors are significantly higher.
4. Given the negligible effect of increasing the pixelation, the value of 2 has been chosen arbitrarily as the midpoint between the values stated by Fluent.

Table 3.2 shows a summary of the radiation settings for the CFD solver used for the remainder of the thesis.

Radiation settings

Radiation model	Discrete Ordinates (gray)
Control angles	$N_\theta = N_\vartheta = 5$
Pixels	$N_{\theta_p} = N_{\vartheta_p} = 2$

Discretisation schemes

Discrete Ordinates	First order upwind

TABLE 3.2: CFD solver radiation settings.

3.2 The benchmark test case

This benchmark test case simulates personalised ventilation delivered to a computational thermal manikin (CTM) and follows Khalifa et al. [2009] and Russo et al. [2009] throughout this section (§3.2). The purpose of this work was to gain understanding of the processes, challenges and physics involved in such simulations. This test case serves as a precursor to the main work on developing a research strategy detailed in §3.4.

3.2.1 The computational model

The CTM (for this test case and future work) was generated from STL data provided online [CFD Benchmarks, 2014]. The STL was generated from a laser scan of a real, asymmetric, thermal manikin and required several iterations of cleaning and smoothing to convert it into an IGES file suitable for importing into ANSYS DesignModeler to generate the CAD. This was achieved with the aid of Geomagic Studio [Geomagic Studio, 2014] and Meshlab [MeshLab, 2014]. The next challenge was to obtain an adequate mesh on the surface of the CTM. A coarse mesh was generated using ANSYS Mesh, sufficient in this instance as no detail was required on the CTM. The inflation layer around the CTM contained 10 layers with a first cell height of 5×10^{-4} m and growth rate of 1.13, based on Sørensen and Voigt [2003], although 20 layers in the inflation layer could not be generated. This was in part down to the limitation of the software used, but also the surface mesh and geometry of the CTM. Figure 3.4 shows the CTM, a close up of the surface mesh on the CTM face and the inflation layer from the nose and mouth.

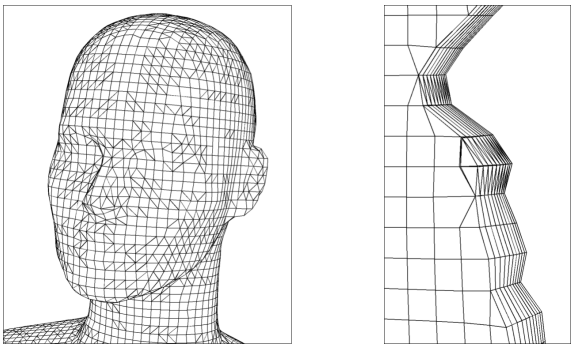

(a) Surface mesh on CTM face.

(b) Slice showing boundary layer from CTM nose and mouth.

FIGURE 3.4: Personalised ventilation test case: Meshing the initial computational thermal manikin.

As described in Khalifa et al. [2009] and Russo et al. [2009], an unclothed thermal manikin was seated within a room of size 2.03 m wide, 2.64 m long and 2.49 m high; the computational domain is shown in Figure 3.5a. A predominantly structured hexahedral mesh of 2.1 million cells was generated, clustered around the inlets, outlets, CTM and thermal plume (Figure 3.5b).

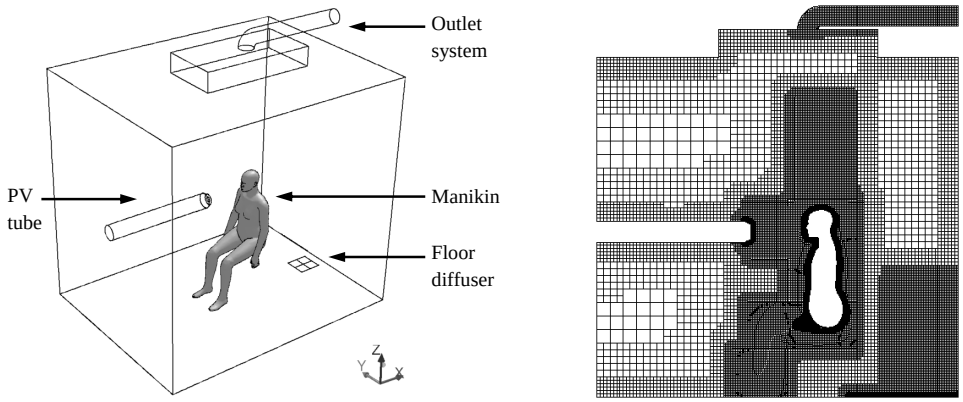

(a) Computational domain.

(b) Mesh on slice through centre plane.

FIGURE 3.5: Personalised ventilation test case: The computational domain and mesh.

Following Russo et al. [2009] for all the boundary conditions, air was supplied to the room through a diffuser in the floor and a personalised ventilation tube. The floor diffuser had a total area of $0.23 \times 0.24\,\mathrm{m}$ with a four way directional grill. The diffuser as a whole supplied air at a rate of $16.51\,\mathrm{s}^{-1}$ at a temperature of $20.5\,^{\circ}\mathrm{C}$ with a turbulent intensity of 10%.

The PV supply was modelled as a velocity inlet from the circular face of diameter $5.08 \times 10^{-2}\mathrm{m}$ at the end of the PV tube, located 0.406 m directly in front of the nose of the CTM. Air was projected normal to this circular face, towards the CTM, at a rate of $2.41\,\mathrm{s}^{-1}$ at a temperature of $23.5\,^{\circ}\mathrm{C}$ with a turbulent intensity of 1.7%. The air was exhausted through the ceiling outlet which had an area of $0.58 \times 1.17\,\mathrm{m}$ located directly above the CTM. Room air was modelled at $24.5\,^{\circ}\mathrm{C}$. Remaining boundaries were modelled as walls with a no-slip condition applied. The CTM had a surface temperature of 305.15 K, the walls and ceiling were set at $23.5\,^{\circ}\mathrm{C}$ and the floor at $22\,^{\circ}\mathrm{C}$.

The case was assumed to be steady-state and was run in 3D using a double precision solver with ANSYS Fluent [ANSYS, Inc., 2015]. A SIMPLE pressure-velocity coupling was employed, with gradients were computed using a Green-Gauss cell based method. The $k-kl-\omega$ turbulence model was used in this instance to deal with the transition from laminar to turbulent flow within the domain. Buoyancy forces acted on by gravity were modelled with the Boussinesq approximation. Second order discretisation schemes were used for the pressure, momentum, turbulent kinetic energy, laminar kinetic energy, specific dissipation rate and energy equations.

Simulations were run until convergence was reached. This was deemed to be when the residuals had dropped several orders of magnitude and were no longer falling. The average wall y^+ on the CTM was found to be well under 1. Once the flow had converged, the flow equations were turned off and a user defined function (UDF) with a scalar transport equation was used to calculated the local residence time in each cell and hence the local air exchange rate. A low diffusivity $\left(1 \times 10^{-5}\,\mathrm{m}^2\,\mathrm{s}^{-1}\right)$ was required for this.

3.2.2 Analysis

Contours of velocity magnitude in a slice through the centre plane of the domain and 0.1 m above the floor are shown in Figure 3.6. The velocity in the contour plot is capped at $1.2\,\mathrm{m\,s^{-1}}$ to show definition for the flow field for the lower speeds, which means that the red regions are $1.2\,\mathrm{m\,s^{-1}}$ or greater. These images highlight that the air velocities were highest in the vicinity of the inlets and outlet. The remainder of the domain was typically lower than $0.15\,\mathrm{m\,s^{-1}}$. Flow rotation, mixing and asymmetry caused by the four way floor diffuser can be seen not only in the contours of velocity magnitude just above the floor (Figure 3.6b), but also in the pathlines released from the wall inlet diffuser and PV inlet, shown in Figure 3.7. The results presented support the assertion that this is a three dimensional problem, in contrast to the assumption made by Russo et al. [2009] who use a symmetry plane.

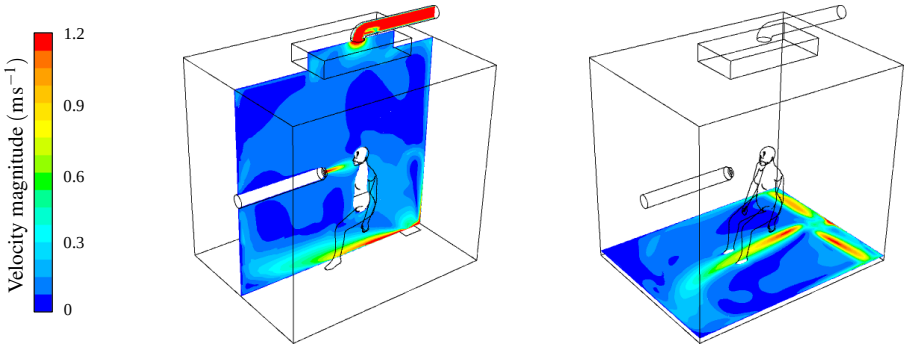

(a) Centre plane of domain. (b) 0.1 m above the floor.

FIGURE 3.6: Personalised ventilation test case: Contours of velocity magnitude.

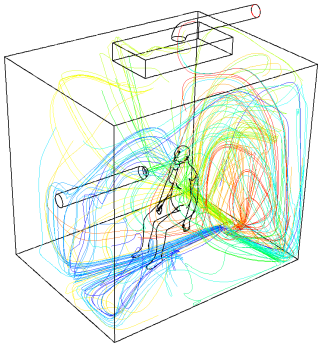

FIGURE 3.7: Personalised ventilation test case: Pathlines from inlets, coloured by particle ID.

Experimental results are presented in Khalifa et al. [2009], with additional data found online at CFD Benchmarks [2014]. Data is provided for the normalised velocity magnitude and normalised turbulent intensity profiles at the nozzle exit. Figure 3.8 shows a comparison of the CFD with these data sets. Both graphs show good agreement (within experimental error) for the majority of the nozzle, with increasing disagreement close to the edges. This indicates that the mesh is too coarse in this area, indicating a need to refine in this area [Russo et al., 2009].

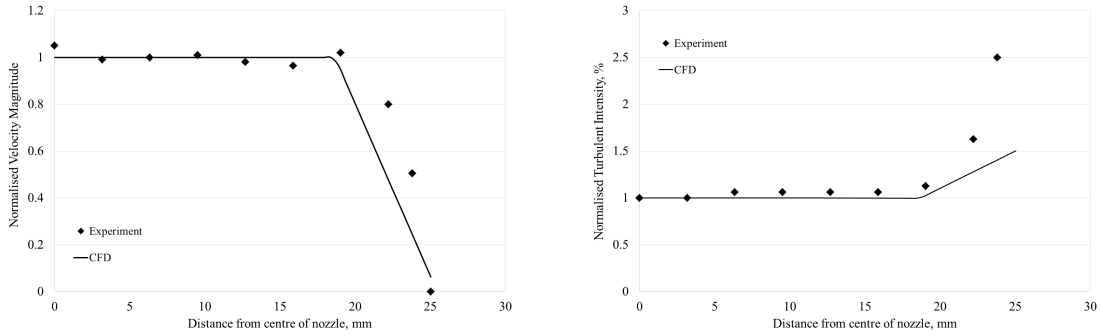

(a) Normalised velocity magnitude.

(b) Normalised turbulent intensity.

FIGURE 3.8: Personalised ventilation test case: Comparison with experimental data at the nozzle exit.

Further experimental data is provided for vertical profiles of a model contaminant SF_6 (Sulfur hexafluoride) along the centre plane on lines 10 mm and 25 mm from the CTM's nose [CFD Benchmarks, 2014]. Since SF_6 is not contained within the standard Fluent chemical database ANSYS, Inc. [2014], this was modelled by a scalar transport equation. Values of 46.56 ppm and 0.69 ppm were specified for the SF_6 concentration at the floor diffuser and PV nozzle respectively [Khalifa et al., 2009; Russo et al., 2009]. Experimental data is provided either as a concentration in ppm or as a normalised air-quality index, AQI [Khalifa et al., 2009; Russo et al., 2009], given by

$$\mathrm{AQI} = \frac{C_{\mathrm{bz}} - C_{\mathrm{ex}}}{C_{\mathrm{pv}} - C_{\mathrm{ex}}}, \tag{3.3}$$

where the concentrations are given by C_{bz} in the breathing zone, C_{ex} at the exhaust and C_{pv} at the PV nozzle. An AQI of 0 represents perfectly mixed air, whilst a value of 1 indicates clean air in the breathing zone. For clean air at the PV nozzle, $C_{ex} = 0$, the AQI can be negative if $C_{bz} > C_{ex}$.

No experimental data is provided for the concentration at the exhaust. Using the specified value at the nozzle inlet and rearranging equation (3.3) for C_{ex} does not give a consistent answer for the experimental data, although it does suggest that it is lower at the exhaust than several areas near the breathing zone. The specified concentrations were normalised for the Fluent user defined scalar (UDS) and specified for small volumes over the inlets. The scalar transport equation was run with a second order discretisation scheme on a steady flow field. The values for C_{ex} and C_{pv} were calculated respectively by a surface integral for the vertex average at the exhaust boundary and a volume integral for the volume average of cells in front of the PV inlet. Different diffusivities were investigated as these were found to have a significant impact on the AQI. Figure 3.9 shows the AQI curve for a scalar of diffusivity $2 \times 10^{-3}\,\mathrm{m^2\,s^{-1}}$ which produced the closest match to data at both the 10 mm and 25 mm lines. The ordinate axis is scaled with respect to the PV nozzle radius (R), centred in line with the tip of the CTM's nose.

The CFD generated AQI curves (Figure 3.9) are in good agreement with the experimental data in the region of interest, matching both the peaks and the gradients of the curves within a region of $\pm$3R from the PV jet centreline at $y/R = 1$. The peaks are in line with the flow from the PV nozzle and show that the PV

improves the air quality in the breathing zone. The AQI from the experimental data tends towards zero, or becomes negative, either side of the PV jet flow as the measured value of the pollutant is less at the exhaust than it is in the domain. Furthermore, there are uncertainties in how measurements are made at the PV nozzle and exhaust as neither Russo et al. [2009] nor Khalifa et al. [2009] explicitly state their methods.

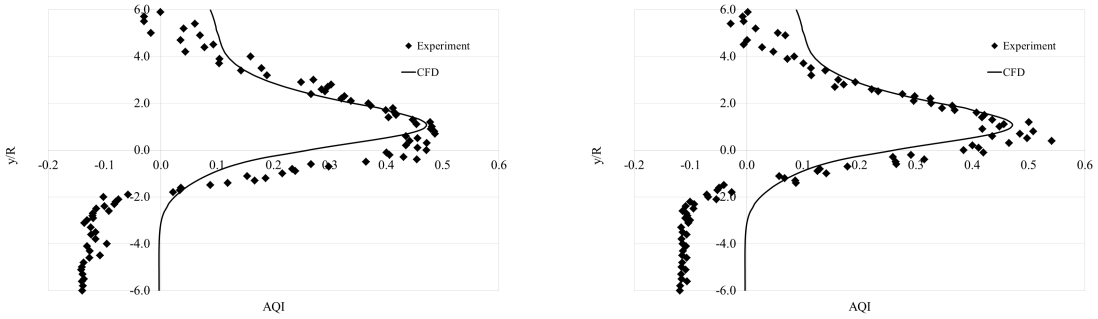

(a) 10 mm in front of CTM face.

(b) 25 mm in front of CTM face.

FIGURE 3.9: Personalised ventilation test case: AQI on lines in centre of domain in front of CTM nose using a UDS.

3.2.3 Summary

The aim of this section was to gain an understanding of the processes and challenges involved in numerically modelling an indoor airflow with a personalised ventilation system. From this benchmark test case, the following observations and conclusions can be drawn:

1. Physically realistic flows can be modelled numerically using a steady state CFD simulation.
2. A transitional turbulence model is capable of capturing the flow field.
3. The exhaust system caused unwarranted computational expense due to the fine mesh required when in fact it is not needed as it does not affect the flow field in the regions of interest.
4. The four way floor diffuser caused asymmetry in the flow field, with unnecessary mixing and flow rotation detracting from the investigation into the benefit of a PV system.
5. The surface mesh on the CTM and the resulting inflation layers require refining.
6. Such a refined mesh over the top of the CTM is not necessary and causes extra computational expense as the PV displaces the thermal plume.
7. The surface mesh on the PV nozzle would benefit from refinement around the edges.
8. Scalar transport is capable of determining AQI in the breathing zone of a CTM in the presence of a PV system.

3.3 PV jet flow

In this research, the personalised ventilation is delivered to the computational thermal manikin via a jet flow. This section considers jet flows in further detail. Following §3.2.3, steady state CFD simulations with a transitional turbulence model are used to model the PV jet flow on a simplified domain with a refined nozzle mesh.

3.3.1 An introduction to jets

Jets of fluid that are released from a circular orifice with a top-hat (constant) velocity profile will decay in speed as they propagate into their surroundings as a direct result of the turbulence at the boundaries of the flow [Albertson et al., 1950]. If the surrounding fluid is the same as that of the jet, statistically stationary and ambient, then the flow will be antisymmetric [Pope, 2000] about the jet central axis. Figure 3.10a shows a schematic of how the velocity profiles decay as entrained local fluid is drawn in to the jet flow. In the case of a circular orifice, the zone of flow establishment generates a cone of pure jet fluid which posses the same velocity as the fluid entering the domain at the jet orifice. Once beyond this cone, the velocity decays as the jet fluid mixes with the surrounding, entrained fluid.

In an environment where the density of the fluid changes, as with buoyancy, the jet axis does not remain perpendicular to the orifice, as illustrated in Figure 3.10b.

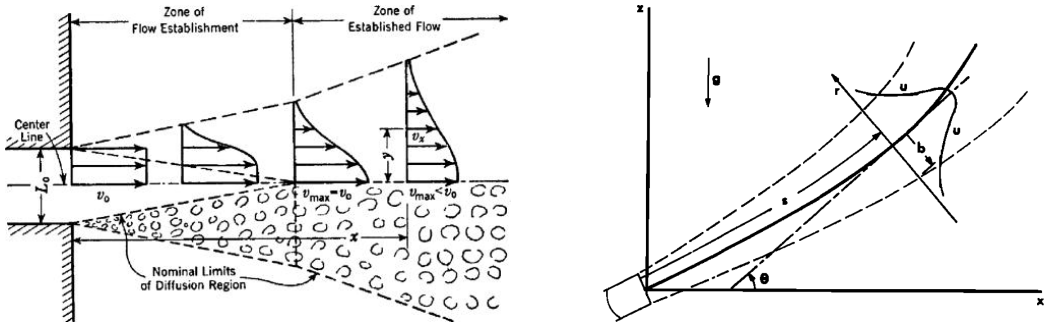

(a) Image from Albertson et al. [1950] showing jet velocity profiles and jet diffusion.

(b) Image from Hirst [1971] showing the coordinate system for a buoyant jet.

FIGURE 3.10: Images from Albertson et al. [1950] and Hirst [1971] describing jet flow.

From the perspective of providing clean air with a PV jet, the clean air will be contained within the cone of establishment. The zone of flow establishment will propagate a maximum distance of x_{ZFE} from the orifice along the jet axis, irrespective of Reynolds number. For a jet fluid with a large enough Re, entering an ambient and statistically stationary fluid, from a circular orifice of diameter d, a simple estimate is given by Albertson et al. [1950]

$$x_{ZFE} \leq 6.2d. \tag{3.4}$$

3.3.2 Simulation description

The baseline test case was modified by removing the CTM and moving the PV nozzle close to the wall to allow jet development. The outlet system was replaced by a simpler pressure outlet and the four-way floor diffuser was replaced with a wall inlet diffuser, as shown in Figure 3.11. A primarily hexahedral mesh containing 3.6 million cells was generated using Fluent Meshing, refined around the wall inlet and the PV jet flow. Simulations were run with the Transition SST turbulence model. As in §3.2, the boundary conditions followed Russo et al. [2009], with the exception of the new wall inlet which was set with a velocity of $0.2\,\mathrm{m\,s^{-1}}$ in order to maintain the same flow rate as Russo et al. [2009]. The PV remained unchanged at $1.184\,\mathrm{m\,s^{-1}}$ ($Re \approx 4 \times 10^3$).

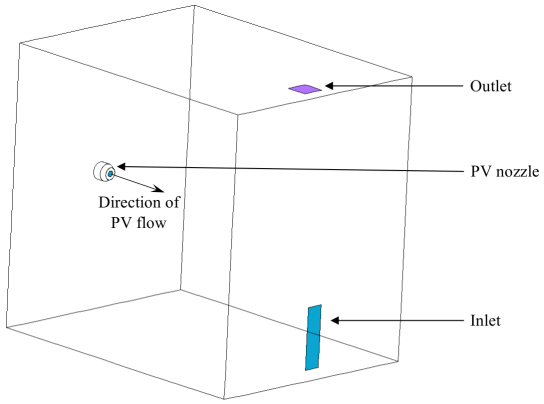

FIGURE 3.11: Computational domain for PV jet flow without the CTM.

3.3.3 Isothermal jet flow

An initial isothermal simulation was run to establish a baseline. Figure 3.12 shows contours of the velocity magnitude on planes perpendicular to the PV jet axis. It can be seen in the side view (Figure 3.12a) that the opposing flow from the wall diffuser has a small. but significant, impact on the PV jet which is not symmetric in the plane about the jet axis. The jet axis curves first upwards, then downwards. When viewed from above (Figure 3.12b), the jet is symmetric.

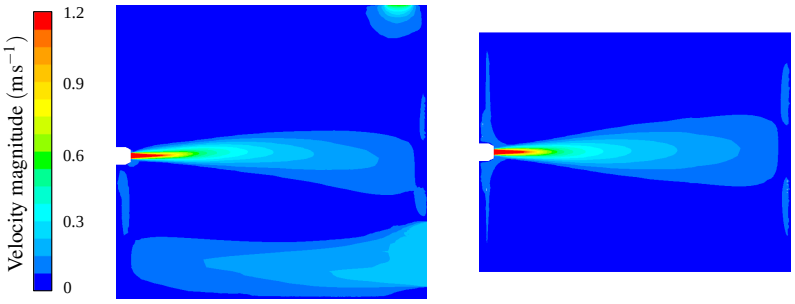

(a) Vertical plane. (b) Horizontal plane.

FIGURE 3.12: Contour plots of velocity magnitude for isothermal PV jet flow in planes perpendicular to the jet axis.

The velocity decay along the jet axis (in the x-direction), Figure 3.13, can be seen to follow the expected profile: constant velocity within the zone of flow establishment (ZFE), followed by a steep decay which levels off [Khalifa et al., 2009; Xu et al., 2018]. The end of the ZFE is 0.22 m from the nozzle, which equates to $4.3d$, less than the maximum empirical value of $6.2d$ in equation (3.4) [Albertson et al., 1950]. That empirical relation is based on the jet flow entering a statistically stationary fluid. That is not the case here as there is an opposing flow from the wall inlet. It is also for a large enough Re number, here $Re \approx 4 \times 10^3$ which is quite small.

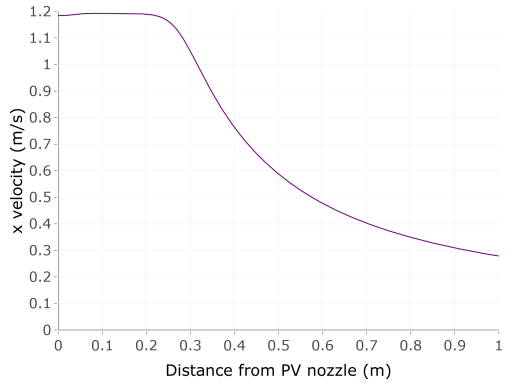

FIGURE 3.13: Graph of the velocity decay along the PV jet axis.

This axial asymmetry observed in Figure 3.12 can also be seen in the velocity profiles taken at several locations along the jet axis. The vertical and horizontal planes are shown in Figures 3.14a and 3.14b respectively. The first line is taken at the PV nozzle orifice ($x = 0.0$m) and exhibits the 'top-hat' profile expected in both planes [Albertson et al., 1950].

The zero velocity areas either side of the 'top-hat' correspond to the solid annulus surrounding the PV nozzle where there is no fluid flow. Above and below this annulus can be seen to asymmetric (Figure 3.14a), due to the flow from the wall inlet reaching the wall below the PV nozzle and recirculating back into the domain. Either side of the annulus (Figure 3.14b), however, is symmetric. As are all the other velocity profiles in this plane. The velocity profiles are taken at equally spaced distances from the PV nozzle to one third of the way into the domain ($x = 0.88$m). The reduction in the maximum velocities can be seen to reduce with increasing distance from the nozzle, with the profiles spreading outwards as they entrain the surrounding fluid.

The same broadly holds for Figure 3.14a, except the flow is not symmetric and in this region of the computational domain the jet axis is forced upwards. This can be seen as the maximum velocities in each profile shifts up the ordinate axis. Even the profile at the end of the ZFE shows a maximum velocity slightly above the line assumed to be the PV jet axis, perpendicular to the PV nozzle. In light of this, the values at the turning point in Figure 3.13 slightly under-predict the values as they do not follow the true jet axis.

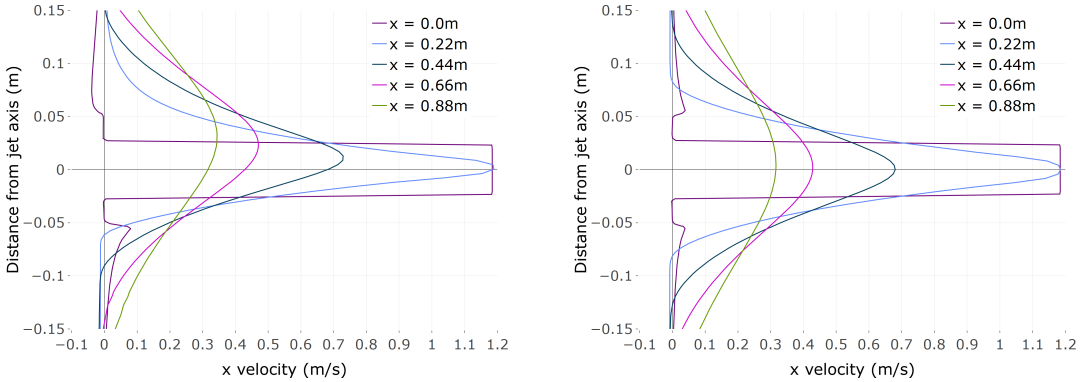

(a) Profiles in the vertical plane.

(b) Profiles in the horizontal plane.

FIGURE 3.14: Velocity decay profiles in the planes perpendicular to the jet axis.

3.3.4 Small variations in the temperature of the PV jets

Building on the isothermal case in §3.3.3, the thermal boundary and flow conditions from Russo et al. [2009] were imposed. Further simulations were run without the PV flow (wall inlet only, using the same parameters) and for a closed domain without any inlets or outlets in order to ascertain the effect of the inlet flows on the temperature in the domain. Two further cases with small perturbations of $\pm 2.5\,^{\circ}$C to the PV temperature were also considered to investigate the effects of buoyancy on the PV jet flow.

The volume average temperature in the closed domain (no flow in or out) was calculated to be 23.30 °C. This was found to be almost a degree lower at 22.25 °C with the presence of the flow from the wall inlet. Table 3.3 shows the volume averages of the total temperature in the domain for the three different PV temperatures. It can be seen that the volume average temperatures for all three PV jet temperatures is very similar and the dominant cooling effect is from the wall inlet flow. The coolest PV jet has a very slight cooling effect whilst the warmer two bring the volume average temperature back a very small amount. The volume of the domain influenced by the PV jet is small in comparison to that altered by the wall inlet flow and their effect is imperceptible.

PV jet	**Room temperature**
21 °C	22.20 °C
23.5 °C	22.42 °C
26 °C	22.43 °C

TABLE 3.3: Volume average room temperatures with different PV jet temperatures.

Plotting the velocity decay along the jet axis (in the x-direction), it can be seen in Figure 3.15 that the thermal PV jets closely follow the isothermal case. The ZFE is similar in all cases. The small differences that are observed are due to the curving of the jet axis where the PV velocity slows down.

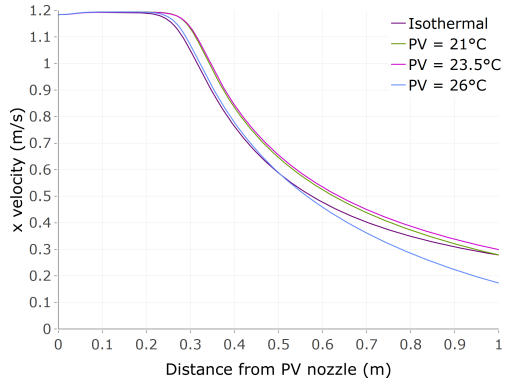

FIGURE 3.15: Graph of the velocity decay along the PV jet axis.

In the central vertical plane, perpendicular to the jet axis at the nozzle, stratified temperature contours can be seen for all PV jet temperatures (Figure 3.16). The stratification is very similar for the PV at 23.5 °C and 26 °C, as are the volume average temperatures for the domain (Table 3.3). The flow can be seen to adhere to displacement ventilation in the absence of the four-way floor diffuser mixing the flow. The coolest air enters from the wall inlet and quickly falls towards the floor. Meiss et al. [2013] showed the same effect when their inlet flow (albeit close to ceiling height) was cooler than their computational domain. The PV jet at 21 °C also enters the domain at a lower temperature than the surrounding fluid (Figure 3.16a) and is directed downwards. At 23.5 °C, the PV flow can be seen to be marginally warmer than the surrounding fluid (Figure 3.16b). As observed in Meiss et al. [2013], when the incoming flow is warmer than the fluid it enters, the incoming flow rises with buoyancy, which is the case for the PV flow at 26 °C (Figure 3.16c).

(a) PV jet 21 °C. (b) PV jet 23.5 °C. (c) PV jet 26 °C.

FIGURE 3.16: Contour plots of total temperature (°C) on the central vertical plane to illustrate effect of PV temperature.

Figures 3.17 and 3.18 show the contours of velocity magnitude with the different PV jet temperatures on the vertical and horizontal planes perpendicular to the jet axis at the PV nozzle, Whilst large differences are apparent in the shape of the jets, they are all consistent around the cone of establishment. The direction of the jet flow is a function of both the jet velocity and the temperature difference between the jet and the ambient fluid (Figure 3.17). Whilst the fluid is moving faster in the zone of flow establishment, it is less influenced by buoyancy forces. As it decays into the established flow, buoyancy forces dominate the jet direction.

When the PV jet is viewed from above (Figure 3.18), it can be seen that the cooler two PV jet temperatures remain in the plane perpendicular to the jet axis a the PV nozzle for longer than the warmest PV jet, as this is influenced more as it has the greatest temperature difference between the PV jet temperature and the ambient fluid.

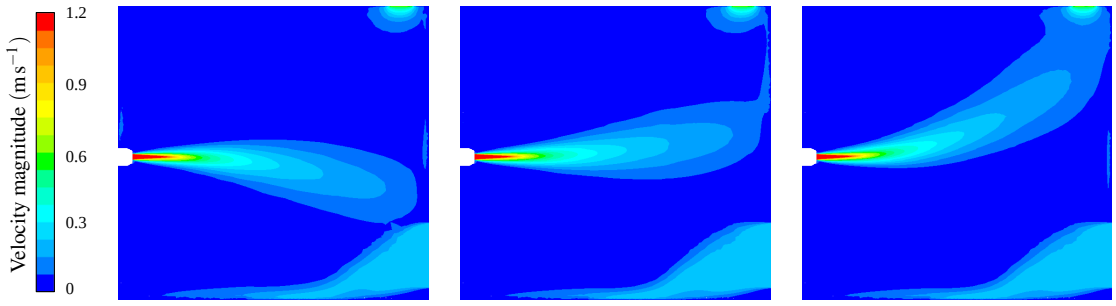

(a) PV jet 21 °C. (b) PV jet 23.5 °C. (c) PV jet 26 °C.

FIGURE 3.17: Contour plots of velocity magnitude (m s^{-1}) on the central vertical plane to illustrate effect of PV temperature.

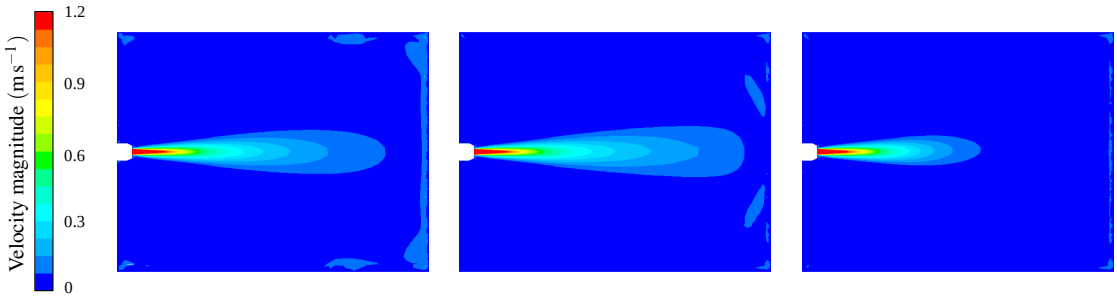

(a) PV jet 21 °C. (b) PV jet 23.5 °C. (c) PV jet 26 °C.

FIGURE 3.18: Contour plots of velocity magnitude (m s^{-1}) on the horizontal plane to illustrate effect of PV temperature.

3.3.5 Summary

The aim of this section was to ensure that the PV jet flows are physically realistic. The computational domain was based on a simplified version of the benchmark test case presented in §3.2. The following observations and conclusions can be drawn from these PV jet simulations:

1. A simple wall inlet and ceiling pressure outlet on the ceiling allowed the establishment of displacement ventilation.

2. Refining the surface mesh on the PV nozzle ensured a more physically realistic velocity profile for the flow leaving the PV nozzle.

3. The velocity profiles show that the PV jet flow develops and decays as expected, with the zone of flow establishment within the empirically anticipated region.

4. Under the influence of buoyancy forces, the PV jet axis curves due to temperature and density changes.

3.4 The computational domain

The aim of this section is to build on the insight gained in §3.2 and §3.3 with a view to continuing to develop a methodology from which the remainder of the research in the thesis will be based. To this end, the domain is simplified, the CTM is refined, a new meshing strategy is employed and solver settings are determined.

3.4.1 Simplification of the benchmark case

The original benchmark test set out in Khalifa et al. [2009] and Russo et al. [2009] induced undesirable factors into simulations. For example, the four-way floor diffuser caused a rotational swirl in the room flow, detracting from the effects of the PV flow under investigation. To isolate the PV flow, the floor diffuser was replaced in favour of a simple wall diffuser, thus making the main ventilation strategy displacement based rather than mixing. The outlet system located at the top of the computational room caused many issues with convergence due to poor cell quality. One method of resolving this was to drastically refine and increase the mesh in this area, which came with a significant computational cost. Therefore, the entire outlet system was removed in favour of a simple pressure outlet. Both of these changes were successfully implemented for the PV jet flows in §3.3 and allowed displacement ventilation to form. Figure 3.19 shows the resulting simplified domain with the CTM. Further modifications to this domain (location of the outlet and inlet wall diffuser orientation) are discussed in §3.4.6.

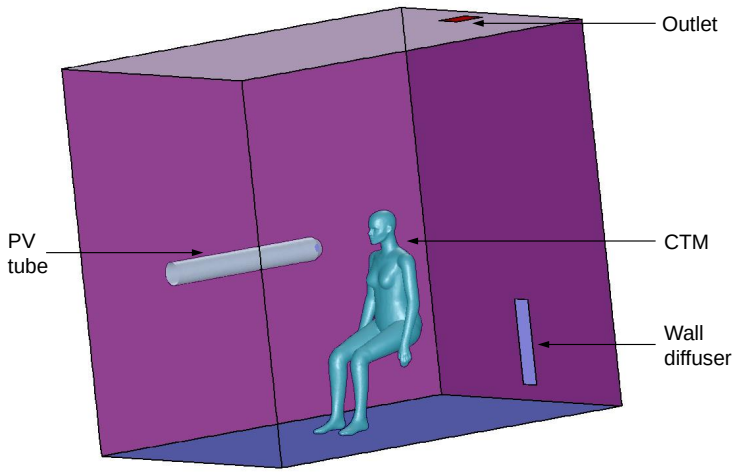

FIGURE 3.19: Simplified computational domain.

The flow rate was kept at the same value as the benchmark case Khalifa et al. [2009], with the inlet area determined by an inlet velocity of $0.2\,\mathrm{m\,s^{-1}}$. Table 3.4 sets out the inlet conditions. The thermal boundary conditions on the walls, floor and ceiling were specified at a constant temperature, as shown in Table 3.5. The CTM could either be specified as a constant heat flux (of $58.1\,\mathrm{W\,m^{-2}}$) or a constant temperature (of

32 °C). The effect of these boundary conditions is discussed in §3.4.5. The following simulations used a constant temperature on the CTM unless otherwise specified.

	Diffuser	PV
Flow rate	$16.51\,s^{-1}$	$2.41\,s^{-1}$
Temperature	20.5 °C	23.5 °C
Turbulent intensity	5%	1.7%

TABLE 3.4: Inlet conditions for simplified test case.

	Temperature
Walls & ceiling	23.5 °C
Floor	22 °C
CTM	$58.1\,W\,m^{-2}$ or 32 °C

TABLE 3.5: Thermal boundary conditions.

3.4.2 Improving the CTM

The original method of importing and meshing the CTM generated substandard and inconsistent meshes. A new strategy was employed by importing the STL of the CTM directly into Fluent Meshing. Figures 3.20a and 3.20b show the original geometry before and after joining the constituent parts. Considerable work went into smoothing the surface of the CTM, details of which can also be seen in Figure3.22. This smoother surface to allowed the generation of a better quality surface mesh and inflation layers. Following [Sørensen and Voigt, 2003], the CTM was split into body parts (Figure 3.21), including mouth and nostrils for breathing zone calculations. Once complete, the CTM surface mesh remained unchanged throughout the simulations, therefore ensuring consistency in that area of the simulations. A total of 1.66×10^5 cells were generated and the maximum skewness refined to a value below 0.46.

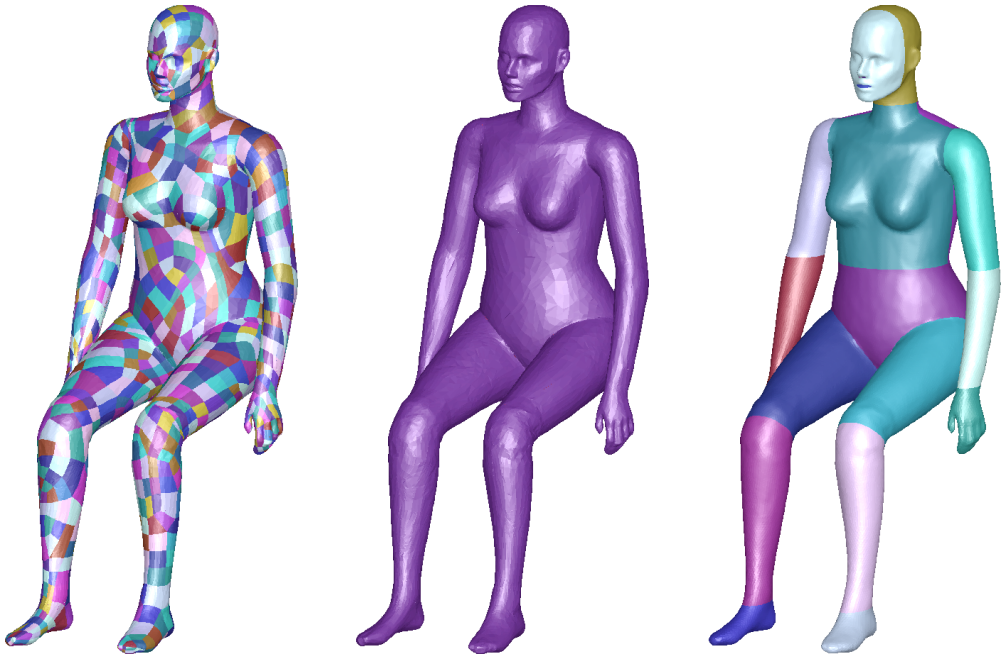

(a) CTM STL as provided. (b) CTM combined parts. (c) CTM surface smoothed and split into coherent parts.

FIGURE 3.20: Evolution of the CTM surface and mesh.

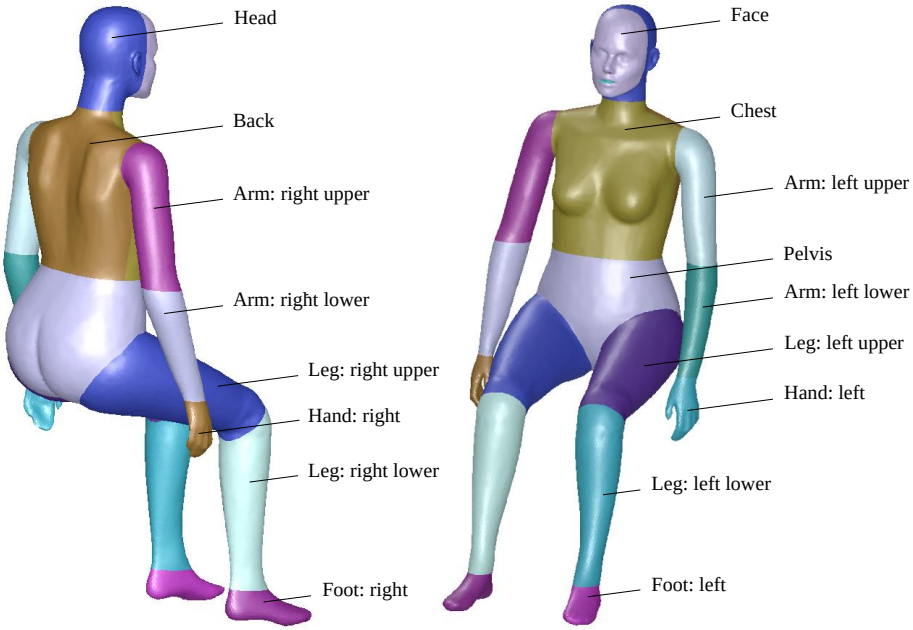

FIGURE 3.21: The CTM model detailing sections.

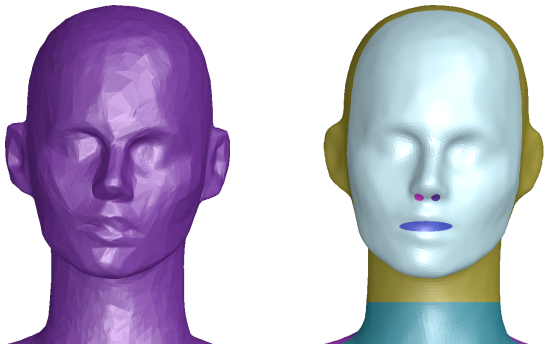

(a) Orginal CTM STL face.

(b) Smoothed CTM face with mouth and nostrils.

FIGURE 3.22: CTM face before and after smoothing process.

3.4.3 Meshing the domain

The domain was split into a predominantly hexahedral mesh of 5.4 million cells, using Fluent Meshing, to enable it to be aligned with the flow from the PV and wall diffuser inlets for greater accuracy. A slice through the centre of the domain is shown in Figure 3.23a. The mesh was refined around the inlets and the CTM, these refinement zones are shown in Figure 3.23b. The refined surface mesh on the PV nozzle in §3.3 was used to ensure a physically realistic PV jet flow. Table 3.6 details the breakdown of the surface area of the constituent CTM body parts, the number of cells and element size. To ensure accuracy in the simulated results in the breathing zone, the mesh on the surface of the mouth and the nostrils was refined in greater detail than the rest of the CTM. Figure 3.24 shows the clustering of cells on the CTM face and breathing zone, whilst Figure 3.25a relates this to the inflation layer, which contained 10 layers, the first cell height being 3×10^{-4} m with a growth rate of 1.13, shown in for the breathing zone

in Figure 3.25b. Attempts to increase the thickness of the inflation layer failed due to the complexity of the underlying geometry. All surface meshes and generation settings were saved in Fluent which meant that any modifications required only minor adjustments. This allowed for efficient and consistent mesh generation. Minor mesh refinements using the Fluent meshing tools brought the typical max skew down to under 0.8.

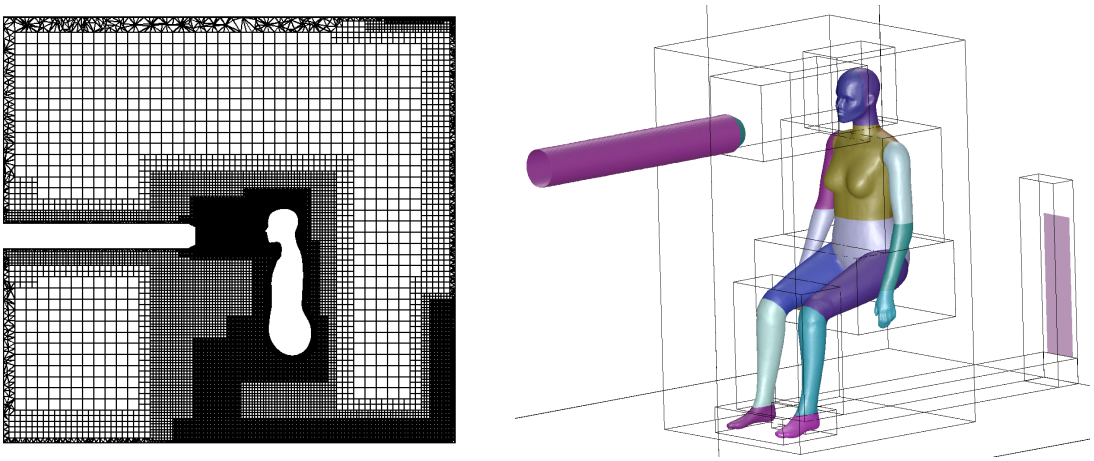

(a) Mesh on the centre plane.

(b) Mesh refinement zones around the CTM and inlets.

FIGURE 3.23: Images of the mesh and refinement zones.

CTM section	**Area (m^2)**	**Number of cells**	**Max cell length (m)**
Head	0.0728	18,838	0.003
Face	0.0432	15,150	0.003
Mouth	0.0003	3,006	0.0005
Nostril: left	4.89×10^{-05}	493	0.0005
Nostril: right	5.39×10^{-05}	552	0.0005
Back	0.1327	19,261	0.004
Chest	0.1503	21,971	0.004
Pelvis	0.1845	17,240	0.005
Arm: left upper	0.0752	7,066	0.005
Arm: right upper	0.0772	7,269	0.005
Arm: left lower	0.0558	3,621	0.006
Arm: right lower	0.0574	3,732	0.006
Hand: left	0.0269	1,824	0.006
Hand: right	0.0239	1,632	0.006
Leg: left upper	0.1965	12,726	0.006
Leg: right upper	0.1956	12,695	0.006
Leg: left lower	0.1088	7,013	0.006
Leg: right lower	0.1088	7,011	0.006
Foot: left	0.0404	2,584	0.006
Foot: right	0.0406	2,618	0.006
Whole CTM	1.5908	161,100	

TABLE 3.6: Details of CTM surface mesh.

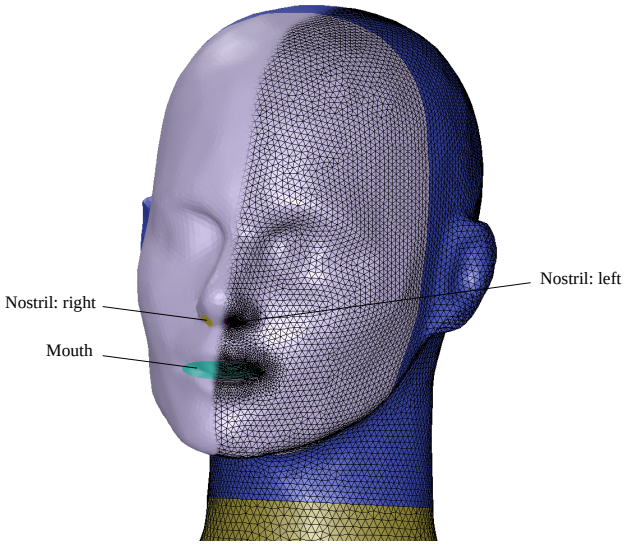

FIGURE 3.24: Close up view of the CTM face showing mesh clustering.

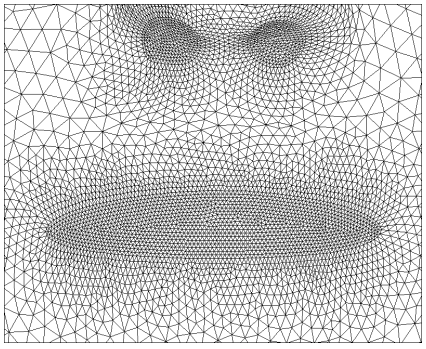

(a) Front view of surface mesh on CTM face.

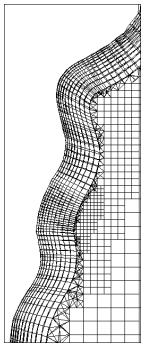

(b) Corresponding side view of inflation layer on CTM mouth and nose.

FIGURE 3.25: Close up of mesh and inflation layer in CTM breathing zone.

3.4.4 Effect of PV flows on simulated flow field

In order to establish whether a PV system provides an improvement to a ventilation set-up, it is first necessary to establish a baseline with pure displacement ventilation and to ascertain whether this is a physically representative model. Furthermore, it is prudent to establish whether the the presence of the PV tube has any discernible effect on the flow features. Simulations were conducted to this end.

Displacement ventilation with a CTM and no PV flow

Schlieren photography captures the changes in density of a fluid. In the thermal boundary layers and plumes, the effect of increasing temperature decreases the density of the fluid (air) as it gains energy and expands. Figure 3.26 shows the front and side views of the thermal plume of a human volunteer using Schlieren imaging techniques. Here the person is male, clothed and breathing. These are three

distinguishing features differing from the CTM in the CFD simulations. The act of breathing can be seen to interact with the thermal plume; different postures alter the behaviour of the thermal boundary layer and plume [Licina et al., 2015b]; clothed areas insulate the body but reduce the boundary temperature in contact with the surrounding air [Craven and Settles, 2006] (therefore reducing the magnitude of the plume). Noting these points, it can be seen that the thermal plume rises from the shoulders and head of the person, slightly expanding before coalescing above the head.

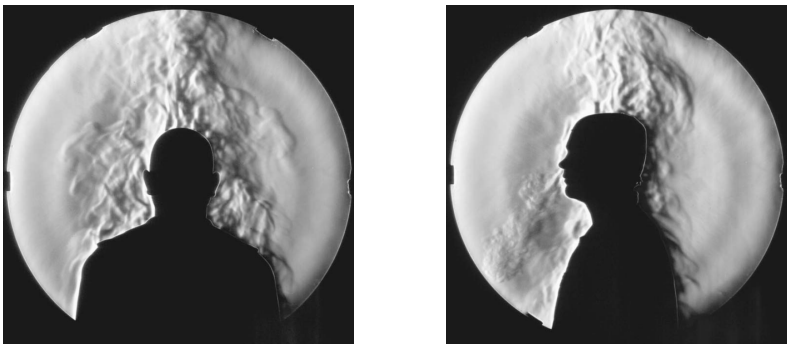

(a) Front view. (b) Side view.

FIGURE 3.26: Images from Craven and Settles [2006]: Schlieren photography of human thermal plume.

Liua et al. [2009] obtained experimental data under three ventilation strategies: no ventilation (NV), mixing ventilation (MV) and displacement ventilation (DV). Figure 3.27a shows (to scale) the location of the measurement line, 25 cm above the CTM head. Experimental data was digitally obtained from the graph presented in Nielsen [2015]. The CFD prediction from the simulation with no PV tube or PV flow is compared with the experimental data in the graph in Figure 3.27b.

It can be seen that the location of the peak velocity was a good match with the experiment for no ventilation and mixing ventilation. The experiment showed effectively no plume for displacement ventilation. It can also be seen that the magnitude of the velocity at the peak was greater for the CFD simulation than for the experiment. This may be down to the CFD over-predicting the velocity, which could be due to a modelling assumption or over-simplification. The mesh in the area of the plume was not particularly refined as this was not of primary interest in the research. However, it should be noted that this is not a like-for-like comparison. The experiment was for a standing thermal manikin, very much simpler in shape than the CTM and emitting energy at a lower level (just over half the heat flux at 30 W). Furthermore, no information was provided for the experimental ventilation (for instance rate or temperature) or indeed any boundary conditions in the room. All of these factors affect the resultant plume and add to the modelling uncertainties. Given that it is generally accepted that the maximum velocity magnitude of the thermal plume above a person is $0.25\,\mathrm{m\,s^{-1}}$, located 25 cm above the head [Nielsen, 2015], and the CFD for an unclothed CTM predicts $\sim 0.3\,\mathrm{m\,s^{-1}}$ in the correct location, this would indicate that it is a physically realistic prediction.

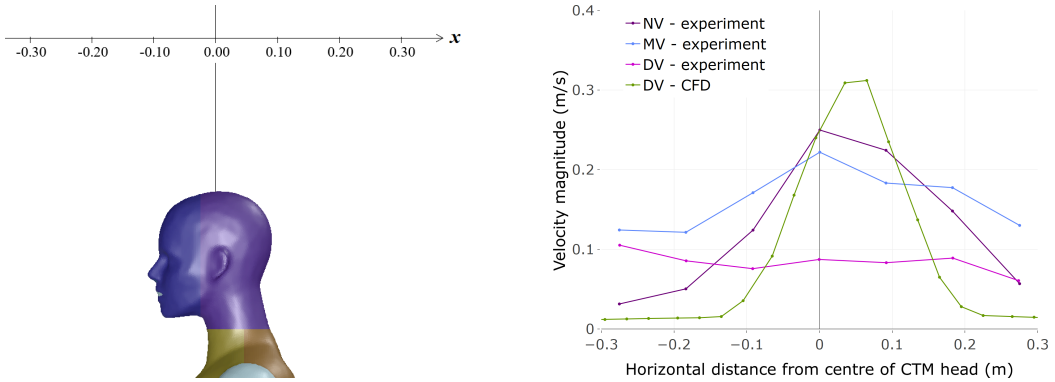

(a) Location of measurement line.

(b) Velocity magnitude $(\mathrm{m\,s^{-1}})$

FIGURE 3.27: Comparison of velocity magnitude in the thermal plume from CFD with experimental data 25 cm above CTM head.

The simulated thermal plume can be seen in Figure 3.28a which shows the pathlines (coloured by velocity magnitude) following the trajectories of fluid particles leaving the CTM surface. More particles can be seen leaving body parts which were closer to a horizontal inclination than a vertical one, such as the upper legs and shoulders. The dominant force was convection, acting in an upwards direction, therefore particles leaving the CTM from vertically inclined surfaces tended to travel up along the surface until they are able to leave a horizontal surface. This is consistent with literature, for example Licina et al. [2015b] who quote that there are additional convective flows from the thighs and lower legs of a seated person. The pathlines coalesced over the CTM head, as in the Schlieren images in Figure 3.26. Pathlines can also be used to visualise the flow from the wall inlet, as in Figure 3.28b, where it can be seen that the cooler air entered and quickly pooled at floor level (surrounding the feet of the CTM), dispersed and slowed down. It can be seen that the air was forced upwards when it reached the walls of the domain. This is also evident in Figure 3.29, which shows the pathlines coloured by particle ID (a direct comparison to Figure 3.7).

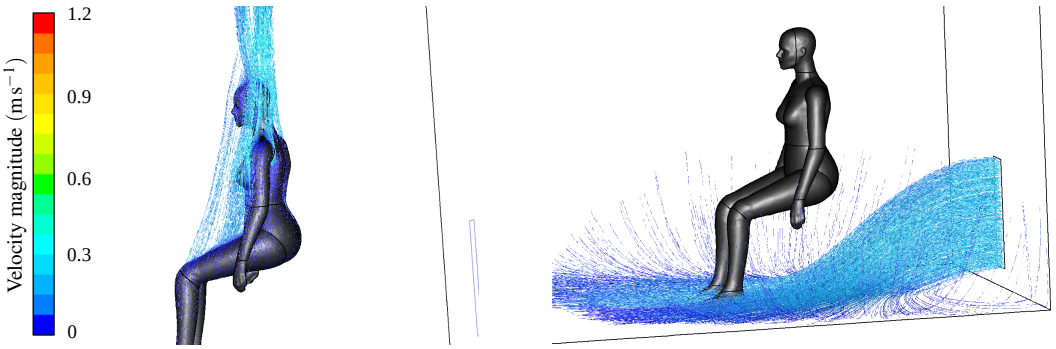

(a) Pathlines from CTM surface.

(b) Pathlines from wall inlet.

FIGURE 3.28: Displacement ventilation and no PV tube: pathlines coloured by velocity magnitude $(\mathrm{m\,s^{-1}})$ released from the CTM surface and the wall inlet.

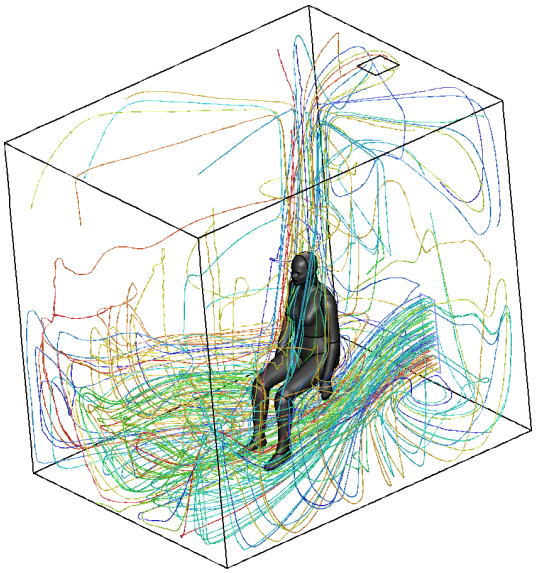

FIGURE 3.29: Displacement ventilation and no PV tube: pathlines coloured by particle ID released from the wall inlet.

Contours of velocity magnitude are shown on four planes in the domain in Figures 3.30 and 3.31 for no PV tube and no PV flow respectively. The first vertical plane is a slice through the centre of the domain, coincident with the PV jet axis (when modelled) and parallel to the direction of flow entering from the wall inlet. There are two further vertical planes perpendicular to the inlet flows, these are located 5mm in front of the CTM nose and behind the CTM head. The final horizontal plane is coincident with the PV jet axis (when modelled) and cuts through the middle of the breathing zone. With the exception of the presence of the PV tube in Figure 3.31, the flow fields were virtually indistinguishable and they indicate that the flow field was not significantly effected by the presence of the PV tube.

These images highlight that the air movement was fastest when entering the room through the diffuser, in the thermal plume located directly over the CTM and when exiting through the outlet. The dominant features in the room with no PV were the flow from inlet diffuser and the thermal plume from the CTM. These both played important roles in determining the flow field. The flow from the wall inlet can be seen to enter the domain perpendicular to the wall then fall towards the floor as it was cooler and denser air than the surrounding fluid (Figures 3.30a and 3.31a). As this flow reduced in height, it increased in width and decreased in velocity (Figures 3.30c and 3.31c). Further from the inlet, the cooler air formed a pool of fresher air at floor level (Figures 3.30b and 3.31b). The thermal plume rose from the lower limbs of the CTM (Figures 3.30a, 3.31a, 3.30b and 3.31b), gathered speed and rose vertically from the shoulders and head of the CTM (Figures 3.30a, 3.31a, 3.30c, 3.31c, 3.30d and 3.31d). The plume was comparable in size and velocity magnitude as found by Sørensen and Voigt [2003] in a similar scenario. Furthermore, exhibited the same properties around the shoulders and head as captured in the Schlieren photography around a real person (Figure 3.26).

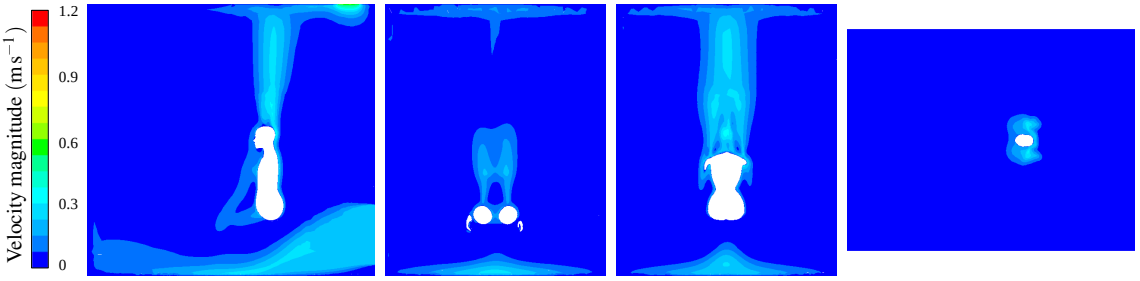

(a) Centre plane. (b) In front of face. (c) Behind head. (d) Horizontal plane in BZ.

FIGURE 3.30: Displacement ventilation and no PV tube: contour plots of velocity magnitude (m s^{-1}) on several planes in the domain.

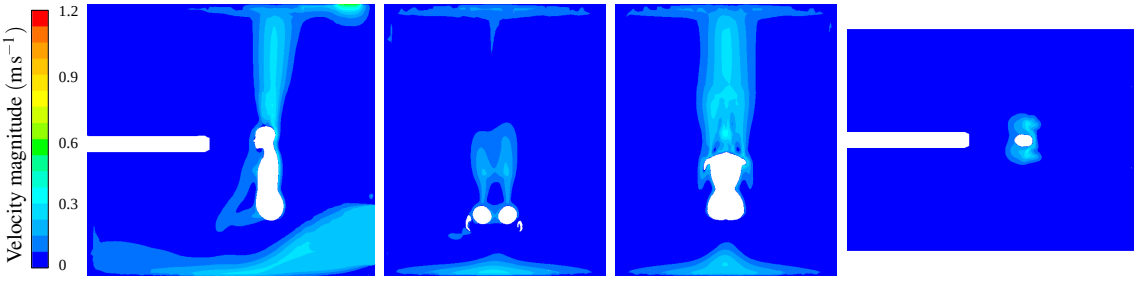

(a) Centre plane. (b) In front of face. (c) Behind head. (d) Horizontal plane in BZ.

FIGURE 3.31: Displacement ventilation with PV tube but no PV flow: contour plots of velocity magnitude (m s^{-1}) on several planes in the domain.

As the contour plots for the case with a PV tube and no PV flow are essentially identical barring the presence of the PV tube, only the plots without the tube are presented here for total temperature and radiative temperature (Figures 3.32 and 3.33 respectively). The thermal stratification was constant throughout the domain, with the cool inlet air dropping to the floor and pooling (Figures 3.32a, 3.32b and 3.32c). The thermal plume rose off the lower limbs of the CTM (Figure 3.32b), shoulders (Figures 3.32c and 3.32d) and head (Figure 3.32a), with the highest temperatures on and close to the CTM surface. Comparable plumes and stratification are observed in Li et al. [2013] under displacement ventilation.

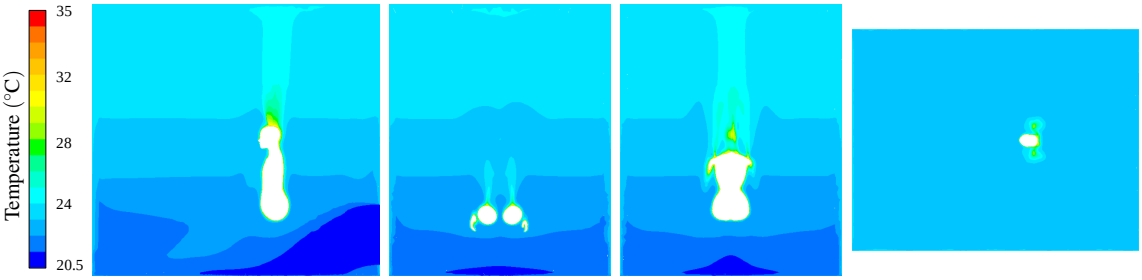

(a) Centre plane. (b) In front of face. (c) Behind head. (d) Horizontal plane in BZ.

FIGURE 3.32: Displacement ventilation and no PV tube: contour plots of total temperature (°C) on several planes in the domain.

The contours of radiative temperature (Figure 3.33) appear physically realistic in nature, coolest near the floor, constant throughout the domain expect near the thermal mass of the CTM. Here they were warmest closest to the CTM surface, with a smooth but rapid reduction with distance.

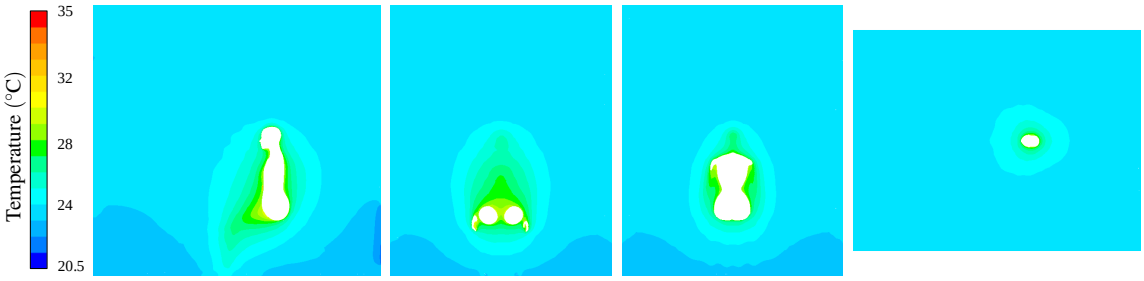

(a) Centre plane. (b) In front of face. (c) Behind head. (d) Horizontal plane in BZ.

FIGURE 3.33: Displacement ventilation and no PV tube: contour plots of radiative temperature (°C) on several planes in the domain.

Displacement ventilation with a CTM and PV flow

The PV jet flow can be seen in Figure 3.34 with pathlines (coloured by velocity magnitude) from the PV nozzle. The cone of flow establishment is the fastest air (red) (Figure 3.34a), whilst the volume of the jet increases as surrounding air is entrained into the jet flow. A closer view of the PV jet impinging on the CTM (Figure 3.34b) shows the PV flow slowed down rapidly as it passed around the CTM face. In a physical scenario, this would depend on details including the orientation of the face with respect to the PV jet, the topology of the face, hairstyle, facial hair or glasses. The air behind the CTM slowed significantly, but increased in temperature (therefore more buoyant), and moved in an upwards trajectory.

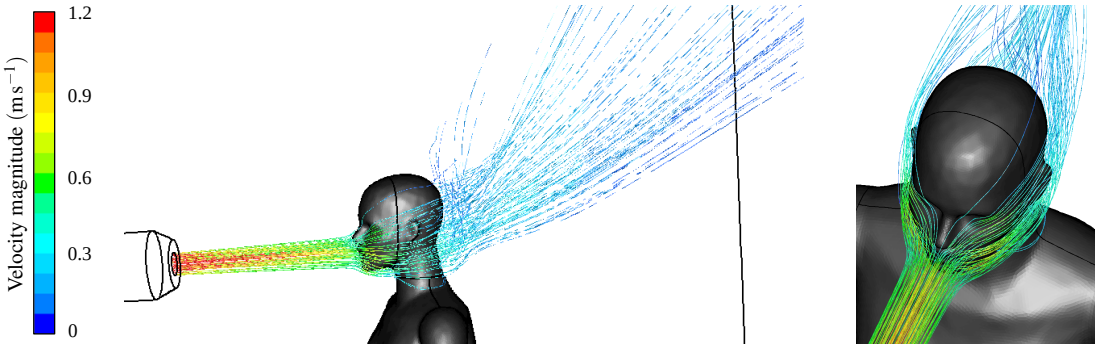

(a) View from the side. (b) View from above.

FIGURE 3.34: Displacement ventilation and PV jet flow: pathlines coloured by velocity magnitude (ms^{-1}) released from the the PV nozzle.

The effect of the PV jet aimed at the CTM face serves to redirect the thermal plume backwards, as seen in Figure 3.35 which shows the pathlines from the surface of the CTM without and with the PV. The thermal plume under the influence of the PV jet was spread over a greater volume. This was partly due to the change in the flow characteristics of the plume itself, and partly due to the addition of the fluid flow from the PV jet (Figure 3.34a).

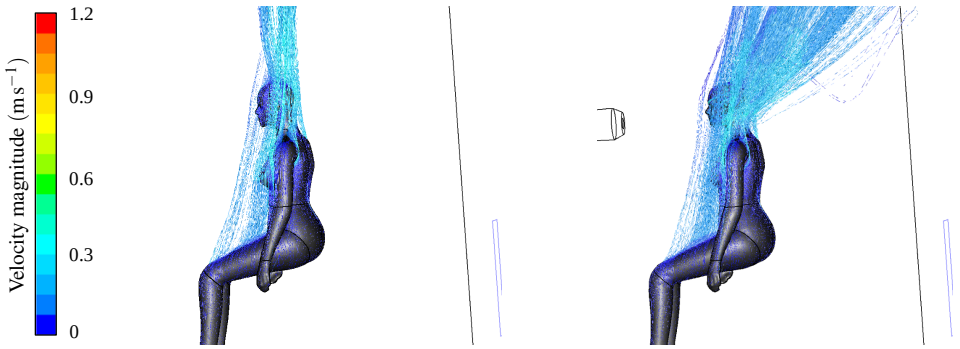

(a) Without PV. (b) With PV.

FIGURE 3.35: Displacement ventilation with and without PV jet flow: pathlines coloured by velocity magnitude (m s^{-1}) released from the the CTM surface, side view.

Without PV flow, the convective boundary layer (CBL) rose vertically, leaving the CTM in three distinct plumes from the shoulders and head (Figure 3.36a). The PV flow forced through this, redirecting the CBL around the jet, widening it (Figure 3.36b). The general plume direction was altered backwards, as noted above (Figure 3.35), and the dispersed air moved slightly slower than the focused vertical plume did without the PV jet. The PV jet disrupted the CBL on the CTM face, head and neck. Vertical flows were redirected radially by the impinging jet. The CBL rising from the torso didn't reach the neck as it interacted with the PV jet and formed regions of recirculation, travelling backwards in a helical motion around the CTM collar (Figure 3.36b). The CBL around the breathing zone was directed around the cheeks, jaws and under the ears (Figure 3.36b). The CBL that passed around and over the nose (Figure 3.36a) was split apart into two directions over the eyes, eyebrows and ears regions (Figure 3.36b).

The combination of these flows led to the change in the location and flow pattern of the plume leaving the CTM's head (Figure 3.37). Without the PV flow, the CBL merged from all directions with minimal swirl and was convected vertically from the top of the CTM head (Figure 3.37a). With PV however, the varying velocities of the flows merging from different directions caused the plume to leave the CTM head further back, with a stagnation point between two opposing vortices, which travelled upwards at a slower speed than the baseline plume (Figure 3.37b).

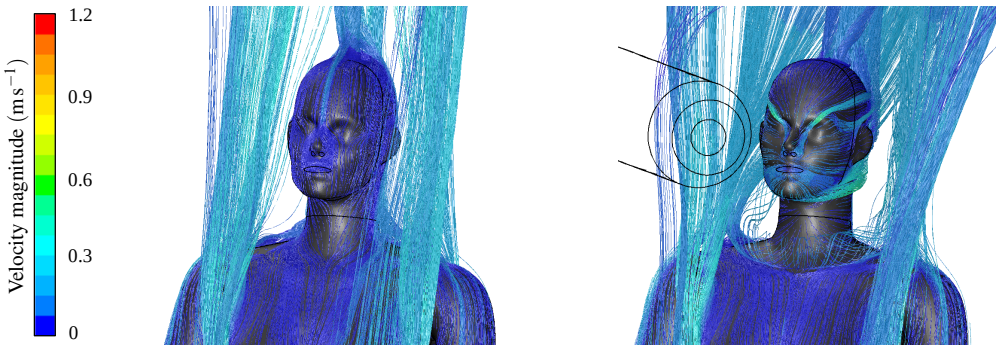

(a) Without PV. (b) With PV.

FIGURE 3.36: Displacement ventilation with and without PV jet flow: pathlines coloured by velocity magnitude (m s^{-1}) released from the the CTM surface, side view.

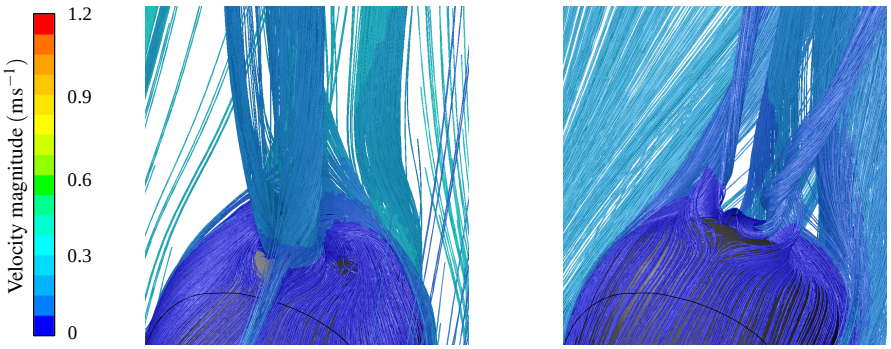

(a) Without PV. (b) With PV.

FIGURE 3.37: Displacement ventilation with and without PV jet flow: pathlines coloured by velocity magnitude (m s^{-1}) released from the the CTM surface, top view.

As seen in the PV jet flow in §3.3.4, the ventilation from the wall inlet is not effected by the PV jet. The addition of the PV flow serves to redirect the thermal plume behind the CTM (Figures 3.38a and 3.38d). The PV jet can be seen to pierce through the convective plume rising from the lower limbs of the CTM (Figure 3.38b), splitting the plume from the CTM head and shoulders into three distinct directions (Figure 3.38c) and reducing the momentum.

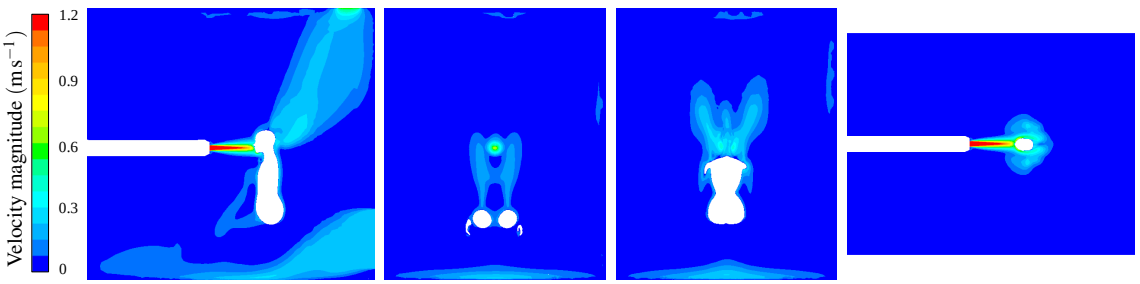

(a) Centre plane. (b) In front of face. (c) Behind head. (d) Horizontal plane in BZ.

FIGURE 3.38: Displacement ventilation and PV flow: contour plots of velocity magnitude (m s^{-1}) on several planes in the domain.

These observations are also evident in the contours of total temperature (Figure 3.39), where it can also be seen that the thermal stratification occurs at lower levels due to the addition of warmer air. The radiation field remains unaffected (Figure 3.40).

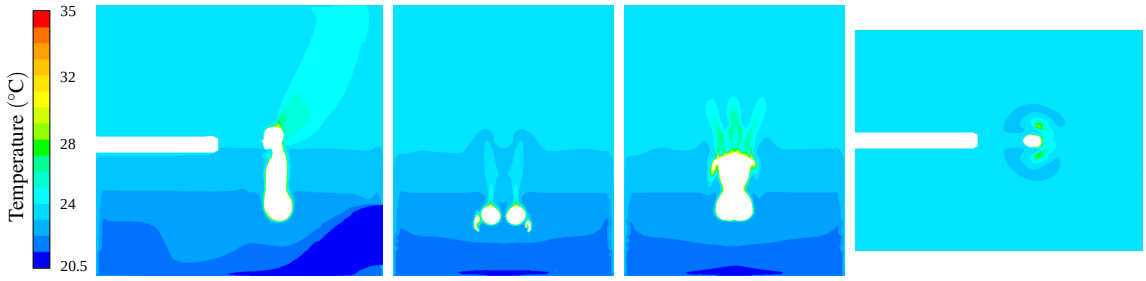

(a) Centre plane. (b) In front of face. (c) Behind head. (d) Horizontal plane in BZ.

FIGURE 3.39: Displacement ventilation and PV flow: contour plots of total temperature (°C) on several planes in the domain.

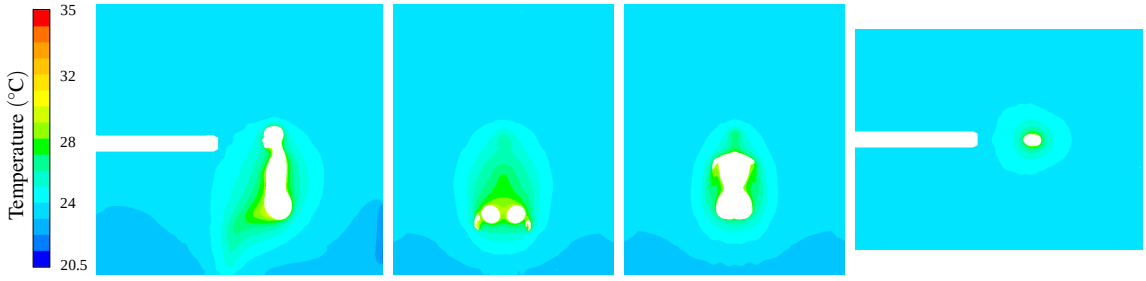

(a) Centre plane. (b) In front of face. (c) Behind head. (d) Horizontal plane in BZ.

FIGURE 3.40: Displacement ventilation and PV flow: contour plots of radiative temperature (°C) on several planes in the domain.

Quantitative comparison of the effect of the PV tube and PV flow

Three data clouds, each containing 30^3 equally spaced sampling locations, were specified around the CTM. Two were $1\,m^2$ cubes around the CTM and one was a $0.4\,m^3$ cube around the head. Figure 3.41 shows the outline of the data clouds. Coordinate values that were located within the CTM body, or PV tube, did not produce data output. The lower cube contained 25.7k sampling points, with 26.7k in the upper cube and 25.4k in the head cube. The data clouds allowed for direct comparisons of the CFD simulated variables at the same spatial locations, irrespective of features in the domain (for instance the PV tube) and mesh.

Pearson's product moment correlation (r) was used as a measure of linear correlation between the simulated variables, with data processed using the statistical programming language R, as in §3.1.3. Here, a value of 1 indicates identical flow variables, whilst a value of 0 means no correlation. Simulated values of velocity magnitude ($m\,s^{-1}$) and temperature (°C) were compared for the three scenarios, with the correlations shown in Table 3.7. The baseline case for the correlations was with no PV tube (and hence no PV flow). It can be

seen that the presence of the PV tube (with no flow) has very little impact on both the velocity magnitude and temperature surrounding the CTM. However, whilst there is very little impact in the lower data cloud for either the velocity magnitude or temperature, there is almost no correlation in the velocity magnitude in the data clouds around the head and upper CTM when there is a PV flow. The temperature is also effected, but to a lesser degree. This can be seen qualitatively in contour plots.

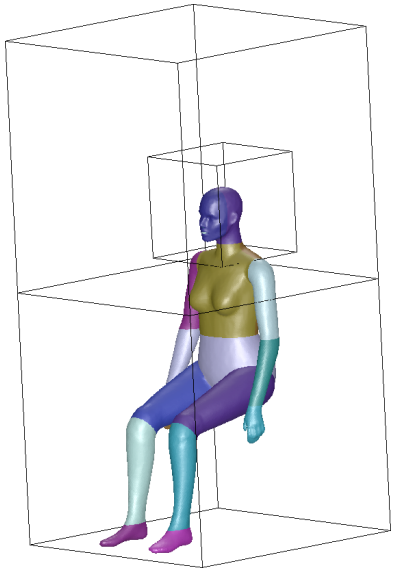

FIGURE 3.41: Outline of data clouds surrounding the CTM.

Data cloud	PV tube, no PV flow		With PV flow	
	Velocity magnitude	Temperature	Velocity magnitude	Temperature
Head	0.9946	0.9954	0.2875	0.6437
Upper	0.9982	0.9975	0.3738	0.7623
Lower	0.9981	0.9994	0.9488	0.9743

TABLE 3.7: Pearson's product moment correlation (4 s.f.) for velocity magnitude and temperature in the data clouds, comparing the effect of PV tube and PV flow with no tube or flow.

3.4.5 Thermal boundary conditions on the CTM

The thermal boundary conditions on the CTM provided in Table 3.5 specify either a constant heat flux or a constant temperature. The effect of the boundary conditions on thermal comfort and when they may be appropriate to use is explored further in chapter 4. To ascertain what, if any, impact these boundary conditions have on the flow in the domain, simulations were run in order to compare and contrast the CFD output. Both simulations were initially run with just thermal effects, then solved for radiation and continued running taking into account the radiation field. The constant temperature boundary condition

sets the surface to be constant whilst the constant heat flux allows for greater temperatures in areas where there is another close heat source, such as the CTM armpit, as illustrated in Figure 3.42.

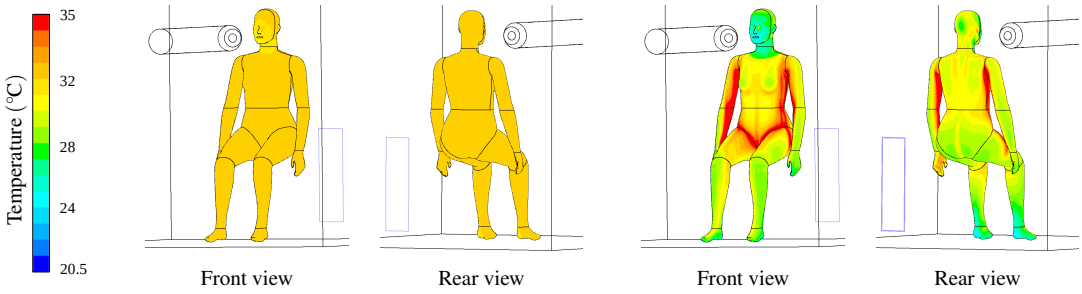

(a) Constant temperature BC. (b) Constant heat flux BC.

FIGURE 3.42: Displacement ventilation and PV flow: contours of surface temperatures (°C) on the CTM surface for different thermal boundary conditions on the CTM.

The constant temperature gives an over-simplified and non-physical profile as it is almost unaffected by air movement. This can be seen on the face, feet, lower legs and hands of the CTM which are cooled by the PV and wall inlet flows. Considering the surface values quantitatively, Figure 3.43 shows the minimum, mean and maximum values of the temperature on the surface of the CTM. It is clear from these graphs that the constant temperature boundary condition is just that - very nearly constant over all the body parts, with only a very slight deviation on the face under the influence of the PV flow (Figure 3.43a). Overall, the mean values on the CTM are quite similar for the different boundary conditions, with the exception of the hands, lower legs, feet and face which are cooler with the heat flux boundary condition (Figure 3.43b), with lower minimum temperatures (Figure 3.43a), due to the air flows they experience. The maximum values for the temperature on the CTM with the heat flux boundary condition occurs in areas that are close to other body parts and subject to radiative heat transfer, such as the armpits. The maximum value on the face is considerably lower than the rest of the CTM due to the PV flow (Figure 3.43c)

For the CTM body parts unaffected by air flows, the mean values (Figure 3.43b) are comparable to the values published by Licina et al. [2015b] for a nude, breathing thermal manikin in a 23 °C room (see the green line in Figure 3.44). Unlike the computational simulations, the measurements made by Licina et al. [2015b] were in an environment with the thermal manikin shielded from the ventilation (to protect the convective boundary layer form the manikin) and seated on a chair (subject to thermal losses due to conduction). In addition to the manikin being a slightly different shape and size, segmented into body parts differently, details of the thermal boundary conditions for the thermal manikin were not provided, adding to numerical uncertainties.

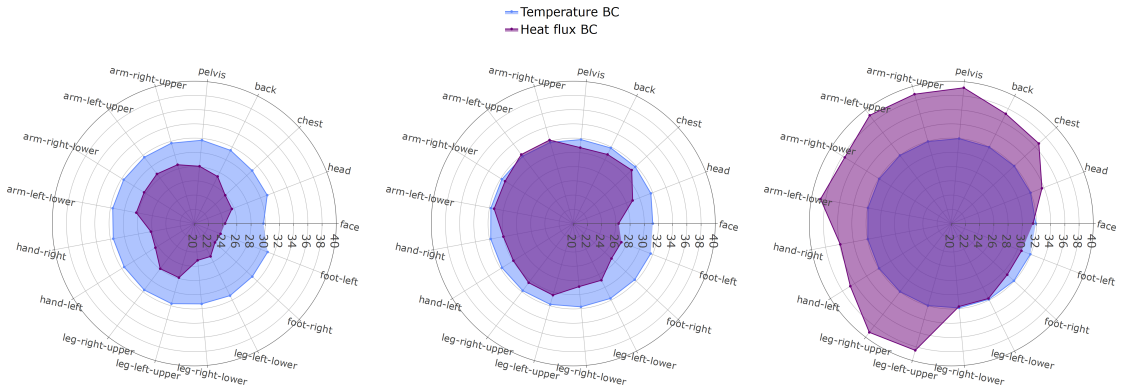

(a) Minimum value. (b) Mean value. (c) Maximum value.

FIGURE 3.43: Radar charts of the minimum, mean and maximum values of total temperature (°C) on the CTM surface for different boundary conditions.

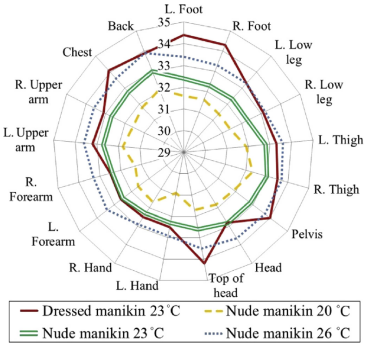

FIGURE 3.44: Image from Licina et al. [2015b] showing example experimental temperatures on a breathing thermal manikin in different conditions.

Qualitative comparison of the effect of the CTM thermal boundary conditions

Comparisons of the velocity magnitude are shown for the constant temperature and constant heat flux boundary conditions on the CTM in Figures 3.45 and 3.46 respectively. The case with the constant temperature boundary condition can be seen to have a stronger and warmer thermal plume, with greater air movement around the CTM body (Figures 3.45a and 3.46a) and a stronger plume from the lower limbs (Figures 3.45b and 3.46b). The constant heat flux boundary condition causes a smaller plume from the CTM head (Figures 3.45c and 3.46c) as more of it is directed towards the rear of the domain by the PV jet (Figures 3.45d and 3.46d). This can also be seen in the total temperature contours (Figures 3.47 and 3.48), where the constant heat flux boundary condition transfers less energy into the thermal plume from the CTM (Figures 3.47a, 3.48a, 3.47b and 3.48b) but influences a wider volume of the domain (Figures 3.47d and 3.48d). The contours of radiative temperature (Figures 3.49 and 3.50) show that the constant heat flux boundary condition is considerably higher on the surface of the CTM and influences a far greater volume of the domain than the constant temperature boundary condition.

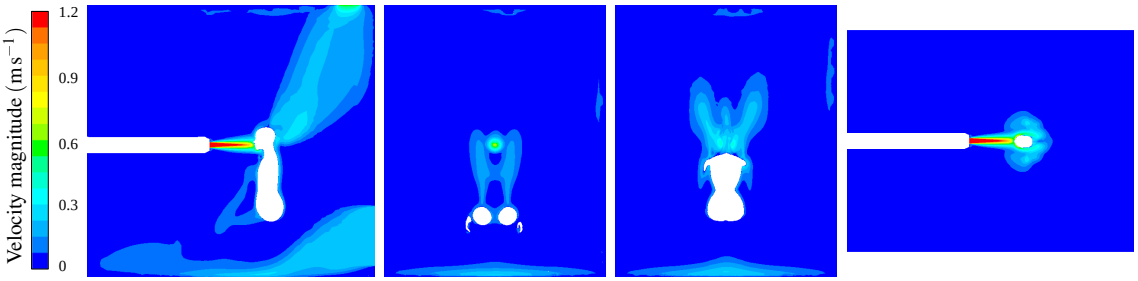

(a) Centre plane. (b) In front of face. (c) Behind head. (d) Horizontal plane in BZ.

FIGURE 3.45: Displacement ventilation and PV flow: contour plots of velocity magnitude (m s^{-1}) on several planes in the domain with the constant temperature BC on the CTM.

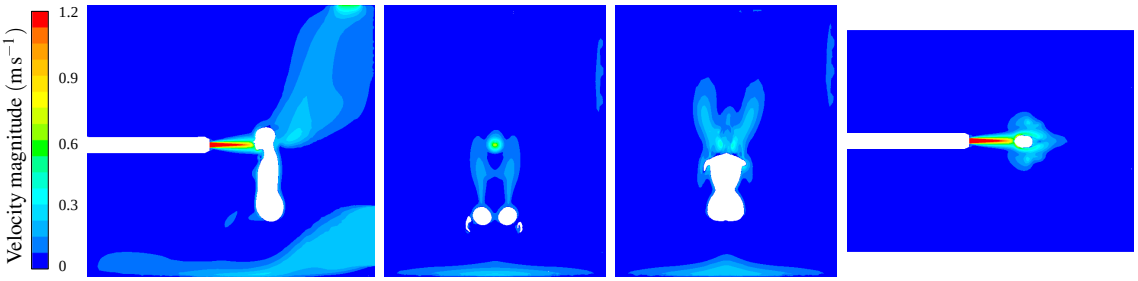

(a) Centre plane. (b) In front of face. (c) Behind head. (d) Horizontal plane in BZ.

FIGURE 3.46: Displacement ventilation and PV flow: contour plots of velocity magnitude (m s^{-1}) on several planes in the domain with the constant heat flux BC on the CTM.

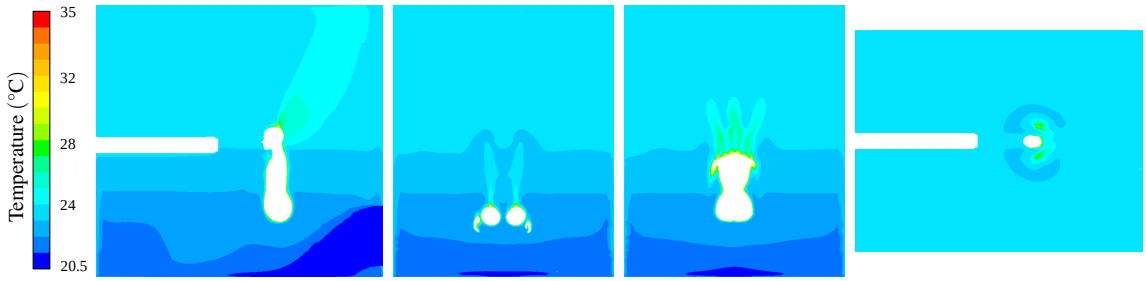

(a) Centre plane. (b) In front of face. (c) Behind head. (d) Horizontal plane in BZ.

FIGURE 3.47: Displacement ventilation and PV flow: contour plots of total temperature (°C) on several planes in the domain with the constant temperature BC on the CTM.

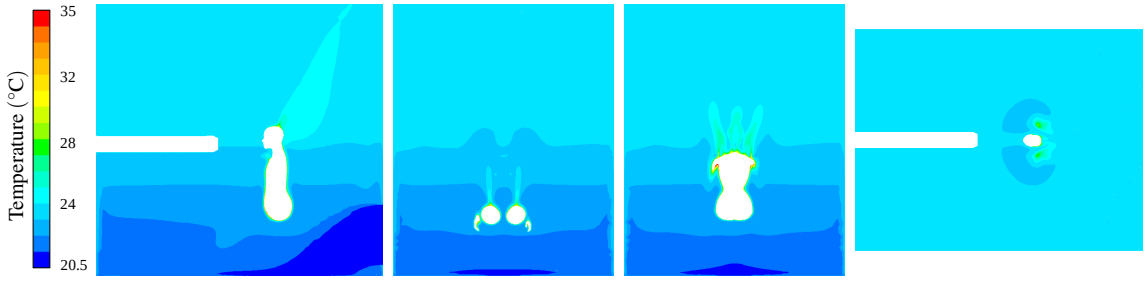

(a) Centre plane. (b) In front of face. (c) Behind head. (d) Horizontal plane in BZ.

FIGURE 3.48: Displacement ventilation and PV flow: contour plots of total temperature (°C) on several planes in the domain with the constant heat flux BC on the CTM.

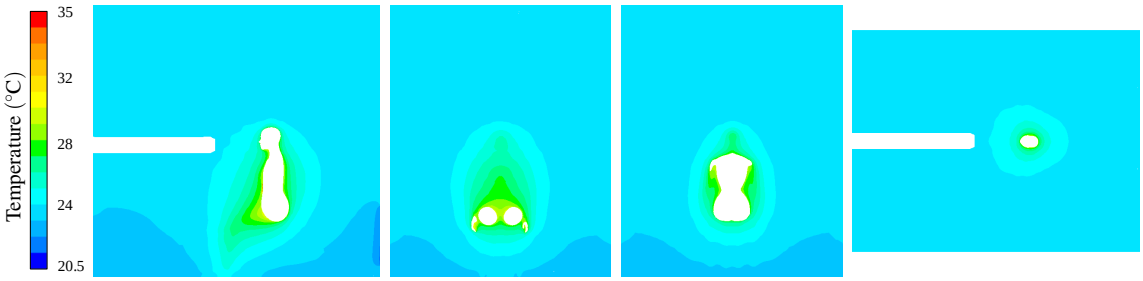

(a) Centre plane. (b) In front of face. (c) Behind head. (d) Horizontal plane in BZ.

FIGURE 3.49: Displacement ventilation and PV flow: contour plots of radiative temperature (°C) on several planes in the domain with the constant temperature BC on the CTM.

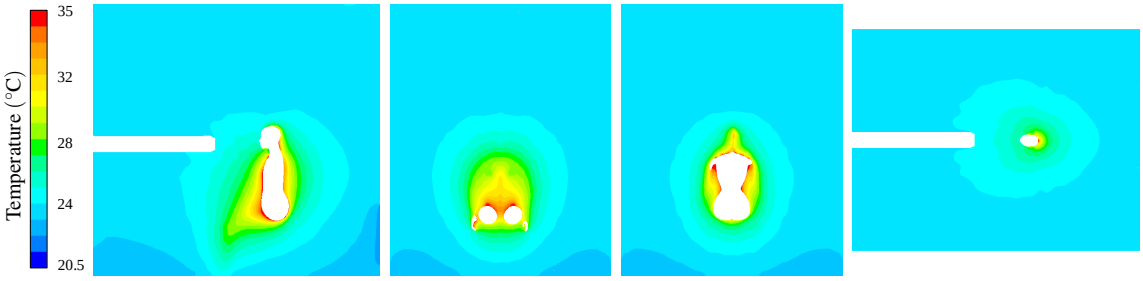

(a) Centre plane. (b) In front of face. (c) Behind head. (d) Horizontal plane in BZ.

FIGURE 3.50: Displacement ventilation and PV flow: contour plots of radiative temperature (°C) on several planes in the domain with the constant heat flux BC on the CTM.

Quantitative comparison of the effect of the CTM thermal boundary conditions

To compare the effect of the CTM thermal boundary conditions on the surrounding flow field, using the data clouds introduced in §3.4.4 (Figure 3.41), Table 3.8 shows Pearson's product moment correlation for velocity magnitude and temperature in the data clouds. It can be seen that generally there is very little difference in either of the fields. The thermal boundary conditions on the CTM have slightly less influence in the lower data cloud as this has a higher correlation (closer to 1). The correlations for the data clouds around the head and the upper data cloud are very similar, for both the velocity magnitude and the temperature. These areas are affected more by the boundary condition than the lower data cloud, with the temperature more affected than the velocities, as observed qualitatively in contour plots.

Data cloud	**PV tube, no PV flow**	
	Velocity magnitude	**Temperature**
Head	0.9787	0.9495
Upper	0.9751	0.9498
Lower	0.9839	0.9850

TABLE 3.8: Pearson's product moment correlation (4 s.f.) for velocity magnitude and temperature in the data clouds, comparing the effect of thermal boundary conditions on the CTM.

3.4.6 Effect of outlet location

In order to ascertain whether the location of the outlet had any significant bearing on either the thermal plume or flow field within the domain, a comparison was made between simulations with the outlet at the front and rear of the domain. The Pearson's product moment correlation (r) is shown in Table 3.9 for values of velocity magnitude and temperature in both domains in the three data clouds. It can be seen that there is negligible effect on the temperature in any of the data clouds or the velocities in the lower data cloud around the CTM head. The upper data cloud, however, shows that there are slight variations in the velocity magnitude. This can be seen in of the contours of velocity magnitude shown in Figure 3.51. The thermal plume appears to be stronger close to the rear outlet than it is for the domain with the front outlet. However, this is outside of the region of interest and makes very little difference to the overall flow field in the domain.

Data cloud	**PV tube, no PV flow**	
	Velocity magnitude	**Temperature**
Head	0.9971	0.9938
Upper	0.9739	0.9932
Lower	0.9992	0.9996

TABLE 3.9: Pearson's product moment correlation (4 s.f.) for velocity magnitude and temperature in the data clouds, comparing the effect of the outlet location.

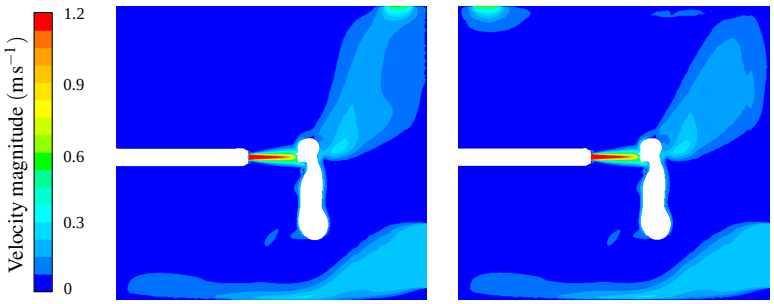

(a) Rear outlet. (b) Front outlet.

FIGURE 3.51: Contour plots of velocity magnitude (m s^{-1}) on the centre plane for the different outlet locations.

3.4.7 Reynolds and Rayleigh numbers

The Reynolds (Re) and Rayleigh (Ra) numbers are dimensionless numbers, discussed in sections 2.4.3 and 2.4.5 respectively. They are useful parameters for characterising the properties and relative importance of different kinds of forces which govern flows. A high Re indicates that inertial forces dominate and the flow is turbulent, whereas a low Re indicates laminar flow with viscous forces dominating. The critical values that determine whether the flow is turbulent, laminar or transitioning between the two are dependent on the geometry that bounds the flow. In the case of natural convection, the flow is characterised as

buoyancy-induced and is laminar when $Ra < 10^8$, with transition to turbulence occurring in the range $10^8 < Ra < 10^{10}$ [Gao and Niu, 2004].

To investigate the properties and forces involved in the baseline test case proposed in §3.4, a thermal simulation (with radiation) was run using the Transitional SST model. The values of several flow parameters were exported for two sets of data clouds, both with equally spaced intervals. The first (small) set contained $30 \times 30 \times 30$ locations, which, accounting for the locations within the CTM and PV tube, resulted in 23k data points. Similarly, the large set had 865k data points within the computational domain from a specified 100^3 data cloud.

Violin plots are a handy visual aid as they are a composite of a box plot whilst also showing the rotated kernel density plot indicating how the data is distributed. Violin plots of the velocity magnitude for these data sets are shown in Figure 3.52. Given that the velocity of air from the PV tube was $1.18\,\mathrm{m\,s^{-1}}$, it is clear from the range of velocities that the data locations from the small data set were too widely spaced to adequately sample the small section of the domain containing the PV flow (despite having 23k points). The range of velocities found in the significantly larger data set indicates that it does capture this area of PV flow sufficiently.

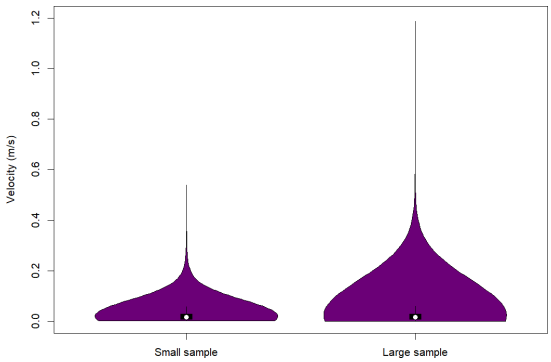

FIGURE 3.52: Distributions of the velocity magnitude comparing the small and large data sets.

The width of a violin plot indicates the probability of the distribution. It can be seen in Figure 3.52 that both data sets show that the majority of the computational domain contains very low velocity air. Violin plots also show the same information as a boxplot, with the black box representing the interquartile range and the white circle denoting the median value. The 95% confidence intervals are not easy to see in this plots as they are so close to the interquartile range.

Statistical analysis was also performed on the data sets, shown in Table 3.10. Similar values are found for the mean, median, modes and standard deviations. Skewness is descriptive indicator of the shape of a distribution. Both data sets are positively skewed as their means are greater than their medians and modes. The mean values for both data sets are both a tenth of the wall inlet velocity, which is the main mechanism

for ventilating the domain. The mean values are both an order of magnitude larger than the mode value, with the majority of the flow in the domain moving with a velocity magnitude of $\sim 0.006\,\mathrm{m\,s^{-1}}$. Significant differences can be seen in the minimum and maximum values, with the larger data set capturing the greatest range. Not only does it capture the PV flow but also the areas of minimal air movement. Standard deviation and variance are typically used to describe the spread of data. Another descriptor is the kurtosis, which is a unit-less number which describes the shape of the central peak and tails of the distribution, shown graphically in Figure 3.53. For distributions with the same variance (as seen here), the kurtosis provides a measure of the relative height of the distribution and is more sensitive to values further than the mean than the variance. In these data sets, the larger sample has a greater concentration of lower values of velocity close to the mode value than the small sample. This is not obvious from the graphs as each violin plot is the same width. Therefore it is essential to consider the numerical distribution data alongside the graphical presentation.

	Small sample	**Large sample**
mean	0.0236	0.0244
median	0.0157	0.0160
mode	0.00625	0.00667
min	0.000821	0.00000968
max	0.539	1.19
std dev	0.0289	0.0299
skewness	4.53	5.60
kurtosis	37.2	87.0

TABLE 3.10: Distribution data for the velocity magnitude of small and large data sets.

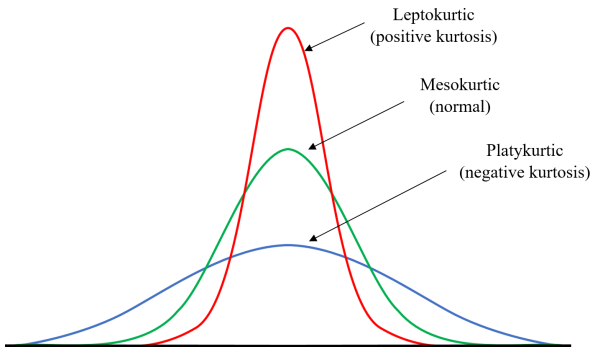

FIGURE 3.53: Graphical explanation of kurtosis.

Calculating the Reynolds and Rayleigh numbers requires a characteristic length-scale to be set, see equations (2.29) and (2.39) respectively. As the majority of the flow enters through the wall diffuser, its width of 0.15 m is chosen as the characteristic length. It should be noted that in reality, flows entering through diffusers pass though small holes which would then determine the characteristic length, but this is not modelled here. Figure 3.54 shows the violin plots for the Reynolds and Rayleigh numbers calculated

for the data sets. Corresponding statistical data is presented in Table 3.11. It is clear that *Re* is highly sensitive to the size of the data sample, which is not the case for *Ra*. The reason for this lies in *Re* requiring values for velocity, which has already been shown to be sensitive to the size of the sample set as the smaller set fails to capture the PV flow.

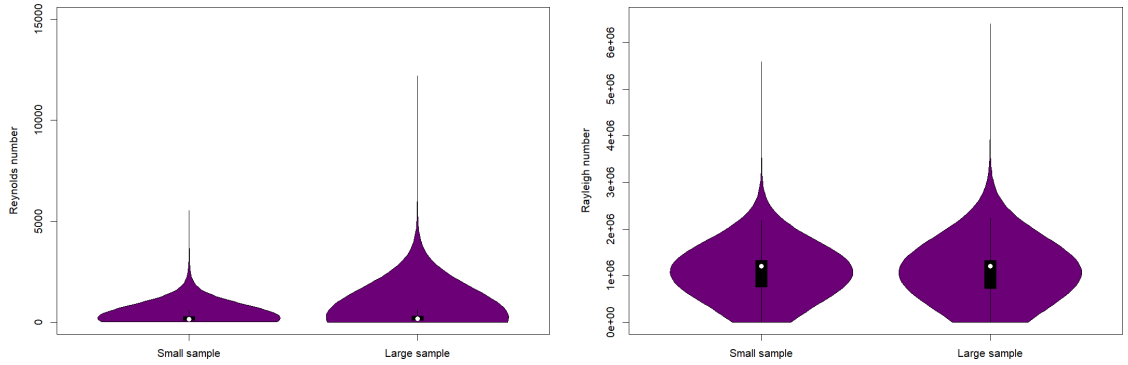

(a) Reynolds number. (b) Rayleigh number.

FIGURE 3.54: Distributions of Reynolds and Rayleigh numbers comparing the small and large data sets.

	Small sample	**Large sample**
mean	243	250
median	161	164
mode	64.2	68.5
min	8.43	0.0994
max	5,530	12,200
std dev	297	308
skewness	4.53	5.60
kurtosis	37.2	87.0

(a) Reynolds number.

	Small sample	**Large sample**
mean	1,040,000	1,030,000
median	1,200,000	1,200,000
mode	1,330,000	1,340,000
min	0	0
max	5,590,000	6,400,000
std dev	341,000	347,000
skewness	-0.440	-0.451
kurtosis	4.40	3.61

(b) Rayleigh number.

TABLE 3.11: Distribution data for the Reynolds and Rayleigh numbers comparing the small and large data sets.

A brief inspection of these graphs and data indicate that only a very small part of the domain may exhibit fully turbulent flow. However, the characteristic length-scale was chosen arbitrarily connected to the size of the wall diffuser. The air entering here is only at $0.2\mathrm{m\,s}^{-1}$. Different length-scales may be appropriate in different regions of the domain, which can present a challenge when considering the domain as a whole. More flow enters into the domain from wall inlet which is most important for the majority of the domain, however the region of greatest interest is dominated by the PV flow. Air enters at a much faster pace from the PV nozzle, which has a diameter of 0.0508m. Figure 3.55 and Table 3.12 compare the distributions using these different length-scales. Vast differences are be observed for the smaller PV length-scale, with both *Re* and *Ra* drastically smaller. Even only considering the wall inlet length-scale, the 95% confidence interval for *Re* is well under 10^3 with a maximum of 1.2×10^4. Similarly for *Ra*, the 95% confidence interval is around 2×10^6 with a maximum of 6×10^6. Increasing the number of data locations is, up to

a finite point, likely to see a similar trend of capturing more of the flow. From the numbers generated, none of the domain appears to be fully developed turbulent flow, at most it is in a transitional phase. This supports the usage of a transitional turbulence model in the simulations.

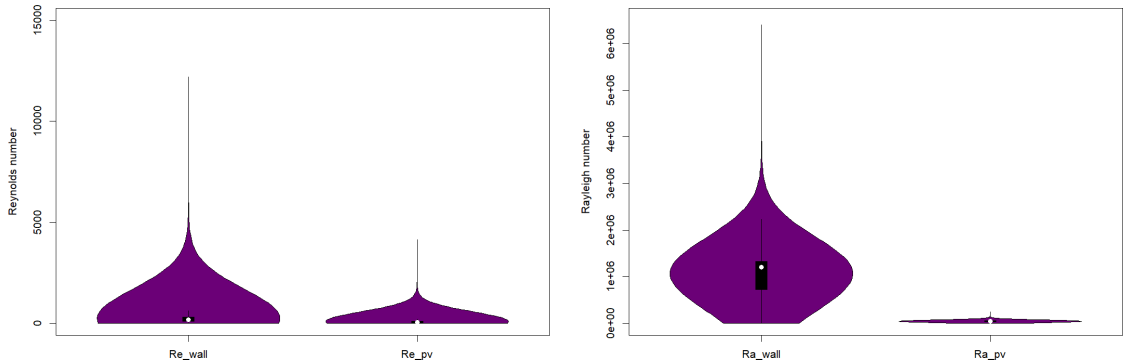

(a) Reynolds number. (b) Rayleigh number.

FIGURE 3.55: Distributions of Reynolds and Rayleigh numbers comparing the characteristic length-scales.

	L_{wall}	L_{pv}
mean	250	84.7
median	164	55.6
mode	68.5	23.2
min	0.0994	0.0337
max	12,200	4,130
std dev	308	104
skewness	5.60	5.60
kurtosis	87.0	87.0

(a) Reynolds number.

	L_{wall}	L_{pv}
mean	1,030,000	40,200
median	1,200,000	46,800
mode	1,340,000	52,200
min	0	0
max	6,400,000	249,000
std dev	347,000	13,500
skewness	-0.451	-0.451
kurtosis	3.61	3.61

(b) Rayleigh number.

TABLE 3.12: Distribution data for the Reynolds and Rayleigh numbers comparing the characteristic length-scales.

3.4.8 Grid independent solutions

The purpose of this study was to conduct a grid independence study to ascertain a suitable grid density for the computational domain. The baseline case described above will be referred to as the fine mesh, containing 5.4 million cells. Effectively doubling the average cell size on each surface and in the hexcore specifications yielded the medium mesh, containing 1.3 million cells. Repeating this procedure gave a coarse mesh with 382k cells. The results are analysed qualitatively and quantitatively for global and local measures. Volume average total temperature is a quantitative global parameter, used here for GCI (Grid Convergence Index) calculation. Small improvements can be seen with increasing grid density. This is a standard quantitative comparison, however it gives no indication of whether a flow field is suitably refined in regions of interest.

	Cell count	Effective grid refinement ratio	Total temperature (°C)	GCI
Fine	5,410,052	1.60	23.11	0.0043
Medium	1,327,860	1.51	23.05	0.0122
Coarse	382,123		22.93	

TABLE 3.13: Grid convergence index using the volume average total temperature with the three mesh densities.

On a more local level, using the three data clouds around the CTM defined in §3.4.4, the CFD predictions for velocity magnitude and temperature for the medium and coarse meshes were compared with those from the fine mesh. Table 3.14 shows the Pearson's product moment correlation (r). Generally, the medium mesh gave a closer prediction to the fine mesh than the coarse one. This method of analysis can add to overall discussions of the mesh accuracies but still does not highlight any areas which may need refining.

Data cloud	Fine / medium		Fine / coarse	
	Velocity magnitude	Temperature	Velocity magnitude	Temperature
Head	0.9939	0.9846	0.9557	0.9294
Upper	0.9864	0.9930	0.9491	0.9562
Lower	0.9927	0.9994	0.9488	0.9743

TABLE 3.14: Pearson's product moment correlation (4 s.f.) for velocity magnitude and temperature in the data clouds, comparing the different grid densities.

Contours of velocity magnitude on the central plane (see Figure 3.56) qualitatively show an example of one variable in locations of interest. The coarsest mesh captures most of the essential flow physics but the mesh can be seen in the contours and the PV jet is ill-defined with most of the thermal plume is missing. The medium mesh captures more of the flow physics yet is still dependent on mesh density, but still does not capture the flow as well as the fine mesh.

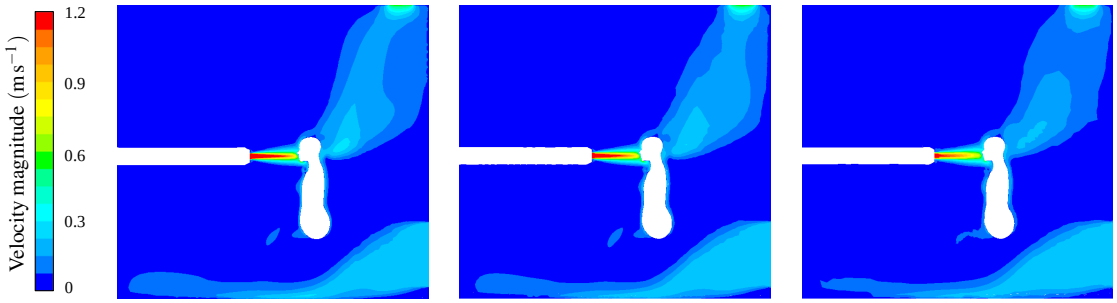

(a) Fine mesh. (b) Medium mesh. (c) Coarse mesh.

FIGURE 3.56: Contour plots of velocity magnitude $(\mathrm{m\,s^{-1}})$ on the centre plane for the different mesh densities.

The x-velocity component of air leaving the PV nozzle along the jet (x) axis (the location of which is shown in red in Figure 3.57a) is plotted against distance from the PV nozzle in Figure 3.57b. The silhouette of the CTM head is superimposed onto the graph to highlight the location. The graphs shows the velocity of the air remaining constant in the jet core before reducing in an area of established flow before impinging on the CTM face. There is a small area of recirculation behind the CTM head.

All meshes capture the flow leaving the PV nozzle and again in the CTM inflation layer. The velocity decay for the finest mesh remains constant in the zone of flow establishment (ZFE) before decaying into established flow, with a sharp deceleration before the CTM. The medium mesh under-predicts the length of the ZFE slightly. However there is a marked difference with the coarsest mesh failing to capture the correct jet flow physics, it merely decays from leaving the PV nozzle until it reaches the CTM, which is physically unrealistic. The medium mesh performed better as it was much closer to the fine mesh prediction with a more realistic physical profile.

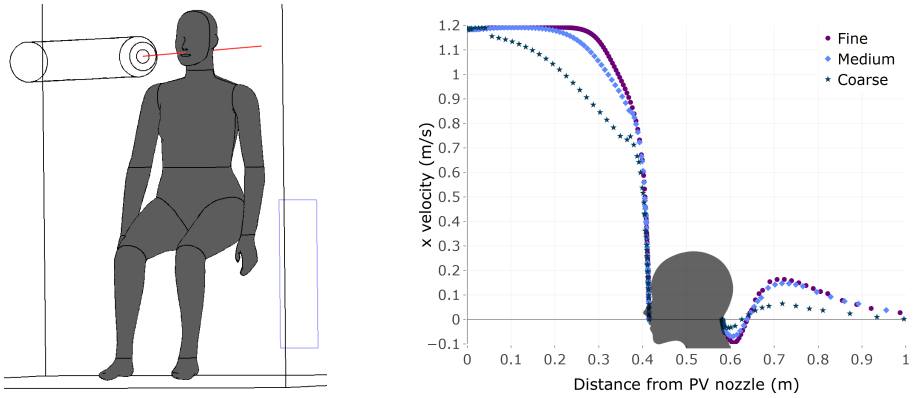

(a) PV jet axis (red).

(b) Graph of x-velocity ($\mathrm{m\,s^{-1}}$) along the PV jet axis against distance from the PV nozzle.

FIGURE 3.57: Location of PV jet axis and x-velocities along the jet axis for the different mesh densities.

Several different measures have been used to asses the quality of the CFD solution and the mesh dependence. The finest mesh has been shown to be the most accurate globally and locally, capturing the flow physics and making physically realistic predictions. Therefore this is the mesh density that will be used for the remainder of this work.

3.4.9 Comparison of modified domain with experimental data

In §3.2 the personalised ventilation benchmark test case of Khalifa et al. [2009] and Russo et al. [2009] was presented and validated. Based on the observations drawn, the domain was simplified and refined. Although the new domain configuration changed the main ventilation from mixing to displacement, the corresponding experimental data is situated in the breathing zone of the CTM, an area dominated by the PV jet flow and less influenced by the main ventilation strategy. Therefore, the same experimental data is used to further validate this new baseline case.

Figure 3.58 shows the AQI on the vertical lines, normalised with respect to the PV nozzle radius, R (as in Figure 3.9). The Air Quality Index (AQI) given by equation (3.3) was calculated on vertical lines 10 mm and 25 mm in front of the CTM nose. A Fluent UDS (User Defined Scalar) was used for a scalar transport equation with the diffusivity of the scalar was set at $2 \times 10^{-3}\,\mathrm{m^2\,s^{-1}}$, as in the benchmark case.

The CFD predictions for the AQI on both vertical lines in the CTM breathing zone are a good match with the experimental data in the PV jet regions. Moving further afield, the UDS is more diffuse than the physical experiments using SF_6 as a tracer. Neither of the CFD predictions for this domain are as close to the experimental data as the predictions using the benchmark domain, which is unsurprising given that the main mechanism for ventilating the domain has been changed. However, in the region of interest, where the PV jet flow dominates, the CFD prediction is physically realistic.

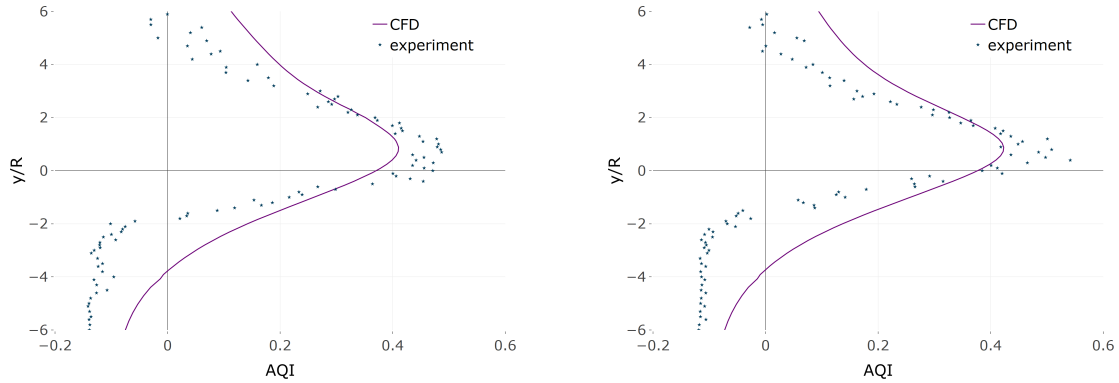

(a) 10 mm in front of CTM face.

(b) 25 mm in front of CTM face.

FIGURE 3.58: Simplified PV test case: AQI on lines in centre of domain in front of CTM nose using a UDS.

3.4.10 Summary

The aim of this section was to bring together, and build upon, the knowledge acquired in previous sections in order to develop a robust and reliable simulation strategy with physically realistic variable predictions. The following observations and conclusions can be drawn:

1. Implementing the CFD solver settings for radiation modelling determined in §3.1 gives a physically realistic thermal radiation field in the domain and around the CTM.

2. An improved meshing strategy allowed for better quality meshes of consistent quality, easily refined in areas of interest. Refining the mesh on the PV nozzle ensured a more realistic velocity profile.

3. Simplification of the benchmark domain does not affect the PV flow in the breathing zone. The location of the outlet has little impact on flow within the domain, negligible in regions of interest in the breathing zone.

4. Fluid flow around a CTM in displacement ventilation behaved as expected, with dominant flow structures from the wall inlet and the thermal plume. The addition of the PV tube (with no flow) had negligible effect on the flow in the domain.

5. The addition of the PV jet pierced the convective boundary layer around the CTM face, redirecting and splitting the thermal plume behind the CTM.

6. The constant temperature boundary condition on the CTM surface gave an over-simplified and non-physical temperature profile on the CTM, whereas the constant heat flux was more physically realistic. There was little difference on the flow field and overall temperature fields in the domain for either boundary condition, however the heat flux condition had a much larger influence in the radiation field in the domain.

7. In the majority of the computational domain, the air movement is very slow. Only a small portion may experience fully developed turbulent flow. In order to be applicable, traditional turbulence models require that turbulent flow be established, which is not the case here. Simulation software guidelines advise newer models with the ability to deal with regions transitioning from laminar to turbulent flow over low Reynolds number formulations of traditional models.

Table 3.15 lists the CFD solver settings identified for use in the remainder of this thesis (unless specified otherwise).

General CFD settings

Space	3D
Precision	Double
Thermal	Yes
Turbulence model	Transitional SST
Steady state	Yes

Radiation settings

Radiation model	Discrete Ordinates (gray)
Control angles	$N_\theta = N_\vartheta = 5$
Pixels	$N_{\theta_p} = N_{\vartheta_p} = 2$

Thermal boundary conditions

CTM	Constant heat flux
Walls	Constant temperature

Solver settings

Pressure or density based	Pressure
Pressure-velocity coupling	Coupled
Pseudo transient	Yes

Discretisation schemes

Pressure	PRESTO!
Discrete Ordinates	First order upwind
All other variables	Second order upwind

TABLE 3.15: CFD solver simulation settings.

4. Development of numerical modelling approach to simulate air quality and thermal comfort

Contents

The previous chapter introduced a baseline simulation strategy involving a seated CTM contained in small room. Key aspects were considered including radiation modelling, mesh design and the general model setup. The aim of this chapter is to explore important modelling assumptions and their applicability for simulating air quality and thermal comfort which are taken forward in subsequent chapters. There are two central themes presented here, of which the first is a detailed investigation into the effect of the boundary condition imposed on the simulated thermal mass (introduced in §3.4.5) and the second is a comparison of a detailed computational thermal manikin (CTM) and a simple heated cylinder (defined in §4.1) which is a common alternative in the literature to a detailed CTM. These are considered in detail with respect to the airflow within the domain (§4.2) and effect on the air quality (§4.3). Building on this work, the final section considered the selection of thermal comfort metrics, including the operative temperature and different methods for calculating PMV (§4.4).

4.1 Simulation descriptions

Three different computational domains were used in this study. The first was the PV jet flow in an empty room which provides a useful baseline with reduced computational expense (introduced in §3.3.2, Figure 3.11). The second was the simplified benchmark case, described in §3.4.1 (Figure 3.19), which included the CTM and was used with and without the PV flow. The third, with a heated cylinder as a surrogate for a thermal manikin, is introduced in §4.1.1 below. Unless explicitly stated otherwise, all boundary conditions remained as set out in Tables 3.4 and 3.5, using the solver settings in Table 3.15.

4.1.1 Computational domain for the cylinder

With the exception of the CTM replaced by a heated cylinder, the computational domain size and shape was kept the same (Figure 4.1a) with inlets and outlets in the same locations. The cylinder was constructed to have an identical surface area as the CTM, set at the same height above the domain floor (to avoid conduction) and reaching the same height as the top of the CTM head. These parameters determined the radius of 0.166 m. The front face of the cylinder was located so that it was coincident with the vertical line that passed through the CTM top lip. Figure 4.1b shows a superimposed image of the CTM on top of the cylinder for a direct comparison of size, shape and location.

The cell sizes of the surface mesh on the cylinder was comparable to that on the CTM torso. Due to the simplified geometry, this resulted in a total of 7.54×10^4 cells on the surface of the cylinder. The inflation layers (of which there were ten) and refinement zones were also comparable to the CTM mesh, resulting in a computational grid of 3.6 million cells, a slice through the centre plane is shown in Figure 4.1c.

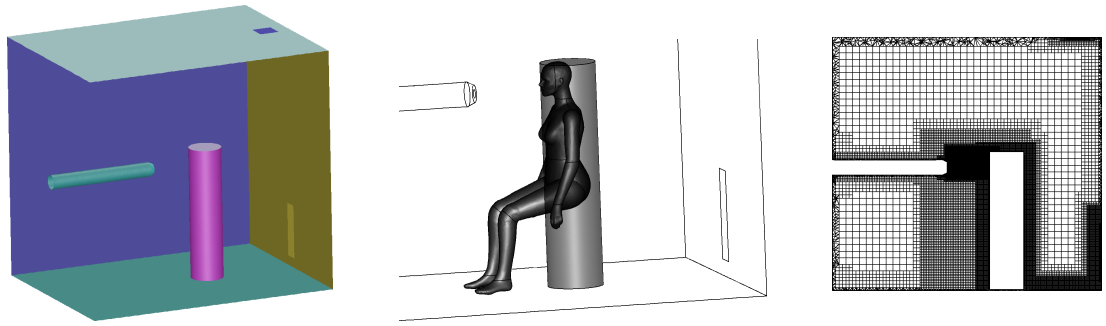

(a) Computational domain. (b) Cylinder and CTM placement. (c) Mesh on the centre plane.

FIGURE 4.1: Computational domain and mesh for the cylinder.

4.2 Room airflow

This section serves to illustrate the differences in flow within the computational domain due to the different thermal occupant geometries and computational boundary conditions. Simulated flows with no thermal mass and with the CTM were discussed in §3.3.4 and §3.4.4 respectively, whilst the effect of thermal boundary conditions on the CTM were introduced in 3.4.5. As in the previous sections, the baseline case with no PV is shown first to highlight the effect of PV jet flow.

4.2.1 No PV jet flow

Clearly the CTM and cylinder differed in shape and therefore interacted with the flow fields differently. The CTM, for example, had more horizontal surfaces, whilst the cylinder had a larger horizontal surface at the top, somewhat dwarfing the CTM head (Figure 4.1b). Also the base of the cylinder was much closer

to the wall inlet flow than the lower limbs of the CTM, which were slightly parted and therefore allowed the flow from the wall inlet to pass through with less obstruction. The cylinder created a barrier to the inlet flow, causing more disruption.

For the case with no PV flow, Figure 4.2 shows the pathlines (coloured by velocity magnitude) released from the surface of the cylinder and wall inlet respectively - a direct comparison with the equivalent flow field for the CTM is shown in Figure 4.3 (which is a duplicate of 3.28 in §3.4.4). Pathlines released from the surface of the cylinder (Figure 4.2a) shows that the velocity magnitude of the resultant plume was of similar magnitude to that of the CTM (Figure 3.28a). However, the plume left the surface of the cylinder towards the front of the body whilst it left the CTM closer to the rear. The pathlines on the cylinder were redirected around the sides of the body as it blocked the incoming flow from the wall inlet. Figure 4.2b shows the flow from the wall inlet being hindered by the presence of the cylinder, forcing it to spread either side of it at floor level, whereas the inlet flow moves more freely for the CTM case and is hindered to far lesser extent.

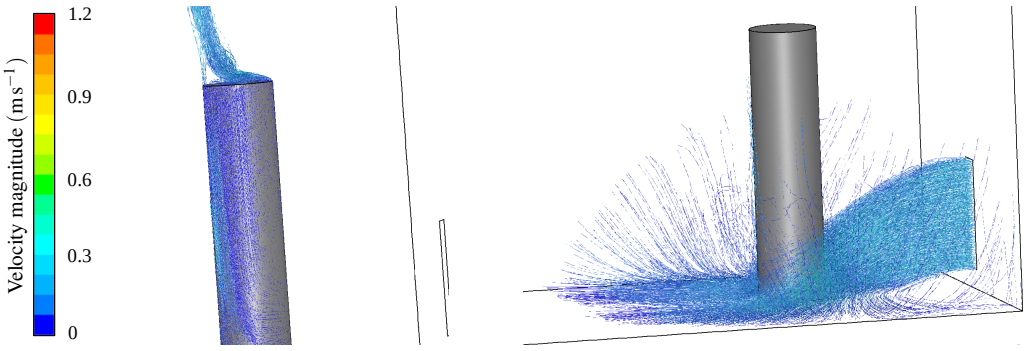

(a) Pathlines from CTM surface. (b) Pathlines from wall inlet.

FIGURE 4.2: Pathlines coloured by velocity magnitude (m s^{-1}) released from the cylinder surface and the wall inlet with no PV tube or PV flow.

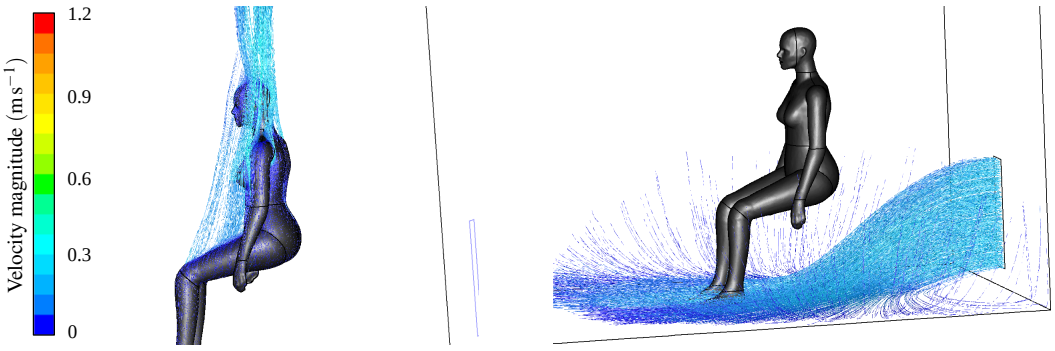

(a) Pathlines from CTM surface. (b) Pathlines from wall inlet.

FIGURE 4.3: Displacement ventilation and no PV tube: pathlines coloured by velocity magnitude (m s^{-1}) released from the CTM surface and the wall inlet (duplicate of Figure 3.28).

These flow features can be seen in the contours of velocity magnitude on the planes defined around the CTM in §3.4.4. Contours of velocity magnitude for the cylinder are shown in Figure 4.4, as described above. The cylinder formed an obstacle blocking the flow from the wall inlet (Figure 4.4a), forcing it around the sides of the cylinder close to the floor (Figure 4.4c). The thermal plume can be seen to be smaller, slightly slower and narrower than that of the CTM (Figures 4.4a and 4.4c), although the CBL (convective boundary layer) travelled up the entirety of the front face of the cylinder (Figure 4.4b) remaining close to the surface (Figure 4.4d). The flow structures are also evident in the contours of temperature in Figure 4.5, where the coolest air temperature abruptly stopped upon reaching the cylinder (Figure 4.5a) and the thermal plume pierces the thermal stratification (Figures 4.5a, 4.5b and 4.5c). As shown for the CTM, the heat flux boundary condition was sensitive to the air flow interacting with the surface. This is evident in the radiative temperature which was coolest in the path of the inlet flow and warmest on the diagonally opposite surface.

The constant temperature boundary condition shown in Figure 4.6a generated a larger thermal plume than the equivalent heat flux boundary condition (Figure 4.4a). Slightly lower thermal stratification layers where also evident for the constant temperature boundary condition (Figure 4.6b) indicating a small increase in the domain temperature, compared to constant heat flux (Figure 4.5a).

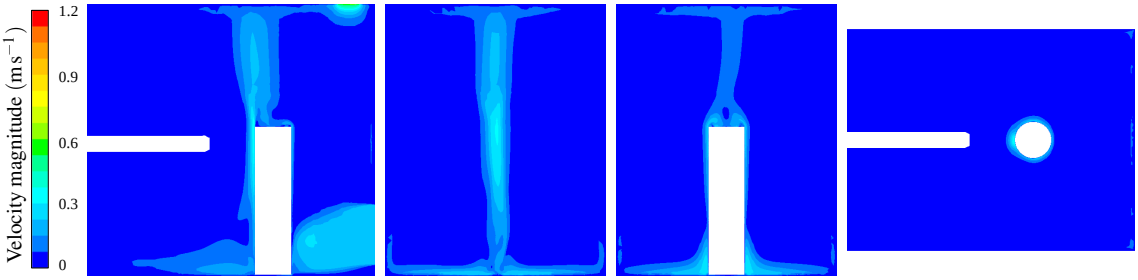

(a) Centre plane. (b) In front of "face". (c) Behind "head". (d) Horizontal plane in BZ.

FIGURE 4.4: Contour plots of velocity magnitude (ms^{-1}) on several planes in the domain for the constant heat flux boundary condition on the cylinder with PV tube but no PV flow.

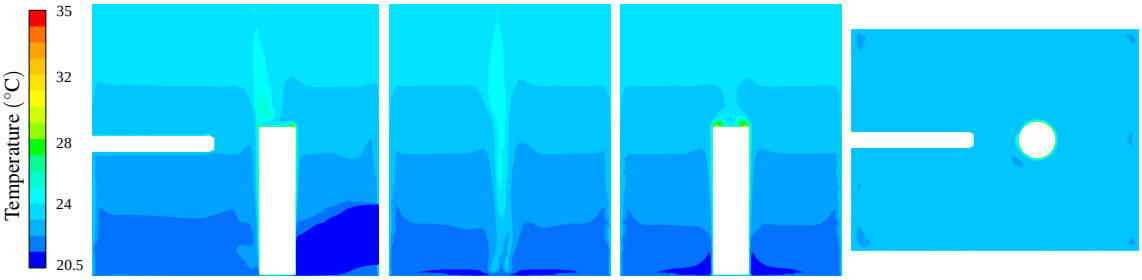

(a) Centre plane. (b) In front of "face". (c) Behind "head". (d) Horizontal plane in BZ.

FIGURE 4.5: Contour plots of total temperature (°C) on several planes in the domain for the constant heat flux boundary condition on the cylinder with PV tube but no PV flow.

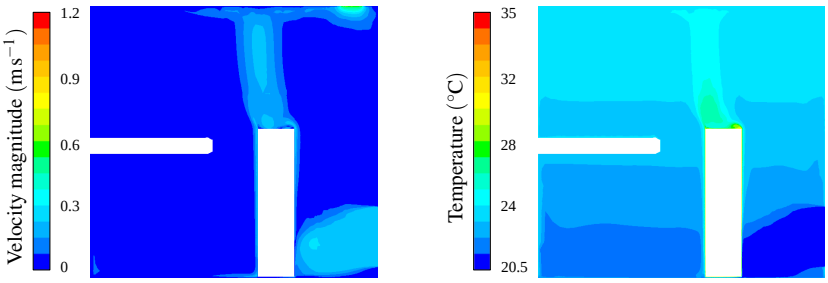

(a) Velocity magnitude (ms^{-1}). (b) Total temperature (°C).

FIGURE 4.6: Contour plots on the planes in the domain for the constant temperature boundary condition on the cylinder with PV tube but no PV flow.

To put the temperatures observed in the ventilated room into perspective, consider a closed room with no inlet flow containing no thermal mass. The volume average room temperature was 23.30 °C. This was reduced by over a degree to 22.25 °C with the flow from the wall inlet. As expected, Table 4.1 shows that the addition of the CTM and cylinder both increase the room temperature when compared to no thermal mass. It is worth noting that these single numbers encompass the air volume in the entire room, most of which remains unchanged. The volumes surrounding the thermal masses change under the different conditions and it is these changes which cause the variations in the overall volume average for the rooms. Despite having the same surface area and the same thermal boundary conditions, the overall room temperature was less with a heated cylinder than for the CTM. The heat flux boundary condition caused lower room temperatures in both cases, but less so for the CTM than the cylinder.

	CTM	**Cylinder**
Temperature BC	22.98 °C	22.89 °C
Heat flux BC	22.92 °C	22.79 °C

TABLE 4.1: Volume average room temperatures for the different boundary conditions on the CTM and cylinder with PV tube but no PV flow.

The small differences in the room temperatures can be explained by considering the interaction between the flow field and the cylinder. The constant temperature boundary condition specifies a constant temperature irrespective of the surrounding flow field, whilst the constant heat flux boundary condition is sensitive to it. Figure 4.7 shows the surface temperature of the cylinder for both boundary condition types, with heat flux generating a lower surface temperature, especially in the path of the cooler inlet flow.

Table 4.2 shows that the range and mean of the surface temperatures on the CTM and cylinder is almost identical for the constant temperature boundary condition, which is expected given the boundary condition type. However the heat flux boundary condition had a greater range, largest for the CTM which also had a higher mean than the cylinder. This is down to the geometry and heat gains due to radiation from close

body parts (such as the limbs on the CTM) which was not applicable in the case for the cylinder. The temperature range for the cylinder was unrealistic, for instance the maximum was too low, whereas the range for the CTM was more physically representative.

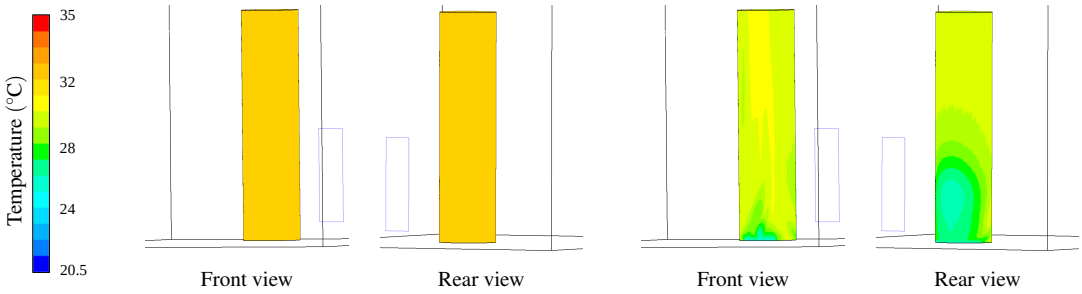

(a) Constant temperature BC. (b) Constant heat flux BC.

FIGURE 4.7: Contours of surface temperatures for the different boundary conditions on the CTM and cylinder with PV tube but no PV flow.

	CTM			Cylinder		
	Min	**Mean**	**Max**	**Min**	**Mean**	**Max**
Temperature BC	30.95 °C	31.81 °C	31.99 °C	31.48 °C	31.81 °C	31.98 °C
Heat flux BC	23.57 °C	30.33 °C	38.96 °C	24.71 °C	29.03 °C	31.48 °C

TABLE 4.2: Surface temperatures for the different boundary conditions on the CTM and cylinder with PV tube but no PV flow.

4.2.2 With PV jet flow

Next, the effect of adding the PV jet flow to the baseline displacement ventilation regime is considered. Pathlines from the PV nozzle show that the PV jet impinged on the surface of the cylinder (Figures 4.8a and 4.8b). The flow stagnated in the very centre, but spread outwards in a radial direction. At the top and around the sides, the pathlines generally travelled around the surface of cylinder before joining the thermal plume. However, the lower half of the PV jet interacted with the rising convective boundary layer, which had been concentrated towards the front of the cylinder by the incoming displacement ventilation flow from the wall diffuser.

The interaction with the CBL caused the PV jet to recirculate as it spiralled around the cylinder, carried with the momentum of the local bulk flow. This is in stark contrast to the pathlines observed for the PV jet interacting with the CTM (Figure 3.34) where they stayed attached to the streamlined CTM head, coalescing at the rear as they began to interact with the thermal plume. Here, the cylinder was much wider than both the CTM head and the PV jet and also had a much stronger CBL at the front of the cylinder.

However, for the CTM, it was the rising CBL that was caught in recirculation spirals caused by the PV flow (Figure 3.35a).

Pathlines from the cylinder surface show the CBL, which was punctured by the PV jet (Figure 4.8c), redirecting the upwards flow radially outwards to around the zone of flow establishment. Whilst some of the CBL passed around the sides of the cylinder, the rising flow that interacted with the lower part of the PV jet was moved away from the surface and forced into regions of recirculation before rejoining the combined jet flow and thermal plume.

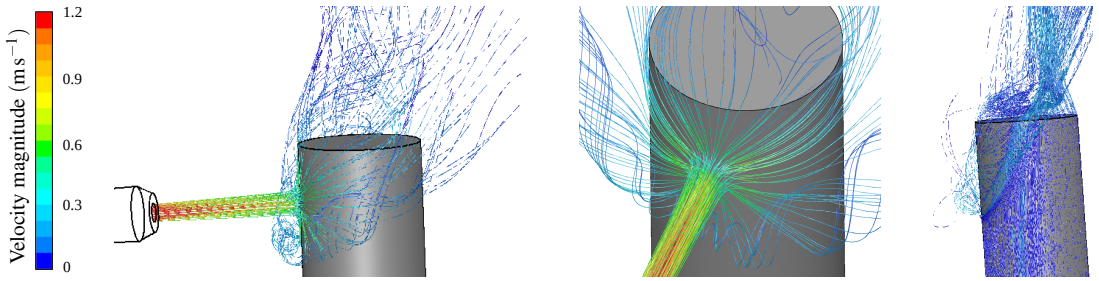

(a) View from the side. (b) View from above. (c) CBL.

FIGURE 4.8: Pathlines coloured by velocity magnitude (m s^{-1}) released from the the PV nozzle (a and b) and cylinder surface (c).

These flow features can be seen in the contour plots in the domain on vertical and horizontal planes. Figures 4.9 and 4.10 show contours of velocity magnitude and temperature on regions of the vertical and horizontal planes perpendicular to the PV jet axis, for the constant temperature and heat flux boundary conditions on the cylinder. The constant temperature boundary condition generated a stronger thermal plume from the cylinder (Figures 4.9a and 4.9c) as was the case with the CTM (Figures3.45a and 3.47a).

Recirculation regions can be seen below the PV jet in Figures 4.9a and 4.10a, with a stronger CBL for the heat flux boundary condition. Similarly, the recirculation regions observed around the sides of the cylinder can be see in Figures 4.9b and 4.10b, again stronger and redirected further backwards with the heat flux boundary condition, as was the case with the CTM (Figures 3.45d and 3.46d). With the exception of the thermal plumes, the overall thermal stratification patterns were almost identical whether the constant temperature or heat flux was used either the cylinder or the CTM.

Table 4.3 shows the volume average temperatures in the room, as for the case with no PV flow (Table 4.1) there is very little difference overall. The room temperature increased slightly with the addition of the PV jet at 23.5 °C.

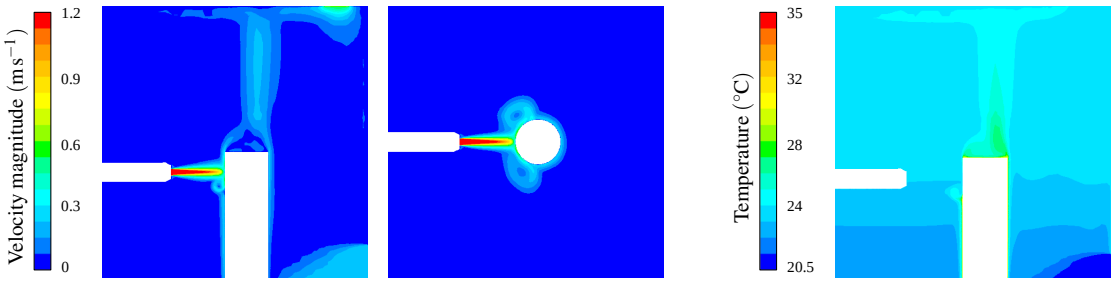

(a) Centre plane. (b) Horizontal plane. (c) Centre plane.

FIGURE 4.9: Contour plots of velocity magnitude (m s^{-1}) and total temperature (°C) on regions of the vertical and horizontal planes in the domain for the constant temperature boundary condition on the cylinder.

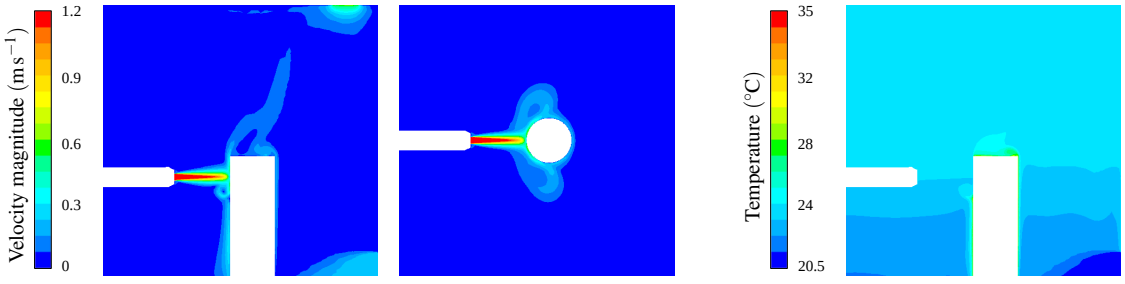

(a) Centre plane. (b) Horizontal plane. (c) Centre plane.

FIGURE 4.10: Contour plots of velocity magnitude (m s^{-1}) and total temperature (°C) on vertical and horizontal planes in the domain for the constant heat flux boundary condition on the cylinder.

	CTM	**Cylinder**
Temperature BC	23.15 °C	23.12 °C
Heat flux BC	23.11 °C	22.99 °C

TABLE 4.3: Volume average room temperatures for the different boundary conditions on the CTM and cylinder.

As shown previously for the CTM (Figure 3.42), the surface of the cylinder with the heat flux boundary condition cooled under the influence of the PV jet more than that with the constant temperature boundary condition. This is shown Figure 4.11 where surface temperatures in line with the PV tube are around 25 °C with constant heat flux which would be expected. However, a temperature of $\sim$ 32 °C is observed with the constant temperature boundary condition. These findings correlate with those for the CTM (Figure 3.42).

Due to the geometry, the cylinder had a larger area cooled than the CTM. Despite this, the mean surface temperature remained almost unchanged with the PV flow (Tables 4.2 and 4.4). The minimum on the cylinder was lower for the temperature BC as this was affected more by the warmer, but faster, PV jet flow than the cooler, slower, wall inlet flow. The range of temperatures for the heat flux BC on both the CTM and the cylinder was very similar with and without the PV flow as these ranges were determined by the wall inlet (cool flow) and the radiative heat transfer.

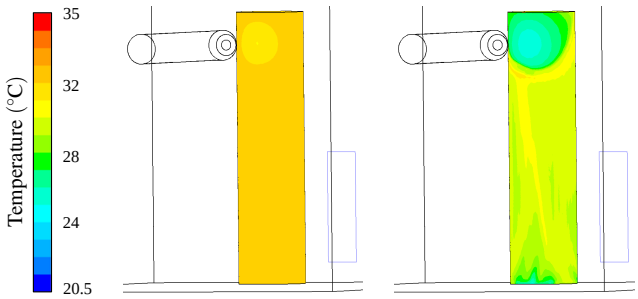

(a) Constant temperature BC. (b) Constant heat flux BC.

FIGURE 4.11: Contours of surface temperatures (°C) on the cylinder surface for different thermal boundary conditions on the cylinder.

	CTM			Cylinder		
	Min	**Mean**	**Max**	**Min**	**Mean**	**Max**
Temperature BC	29.75 °C	31.79 °C	31.99 °C	30.64 °C	31.80 °C	31.97 °C
Heat flux BC	23.95 °C	30.23 °C	39.15 °C	24.93 °C	28.93 °C	31.95 °C

TABLE 4.4: Surface temperatures for the different boundary conditions on the CTM and cylinder with PV flow.

Using the data clouds introduced in §3.4.4 (Figure 3.41), Pearson's product moment correlation, *r*, was calculated to directly compare the velocity magnitude and temperature fields generated as a result of the different thermal boundary conditions on the CTM and cylinder (Tables 4.5 and 4.6). It can be seen in Table 4.5 that there is a good correlation between the boundary conditions for the CTM in the velocity magnitudes simulated for both with and without PV flow, better in fact with the PV flow. This is also the case for the cylinder, but the correlations are significantly weaker due to the wider range of velocities cited earlier. As noted for Table 3.8, the thermal boundary conditions have less influence lower in the domain. The Tables show the marked difference in velocity flow fields observed around the "head" area of the cylinder with no PV flow (Figures 4.4 and 4.6). Better correlations around the cylinder were found for the temperature field than with the velocities, with the exception of the "head" area subjected to PV flow. Generally, the flow fields surround the CTM were less sensitive to the thermal boundary conditions applied to the CTM than for the cylinder.

Data cloud	**No PV flow**		**With PV flow**	
	CTM	**Cylinder**	**CTM**	**Cylinder**
Head	0.9357	0.6293	0.9787	0.8709
Upper	0.9752	0.8498	0.9751	0.8027
Lower	0.9798	0.8376	0.9839	0.8691

TABLE 4.5: Pearson's product moment correlation (4 s.f.) for velocity magnitude in the data clouds, comparing the effect of thermal boundary conditions on the CTM and cylinder, with and without PV flow.

Data cloud	No PV flow		With PV flow	
	CTM	Cylinder	CTM	Cylinder
Head	0.9573	0.9369	0.9495	0.8117
Upper	0.9672	0.9603	0.9498	0.8971
Lower	0.9803	0.9572	0.9850	0.9699

TABLE 4.6: Pearson's product moment correlation (4 s.f.) for the temperature in the data clouds, comparing the effect of thermal boundary conditions on the CTM and cylinder, with and without PV flow.

4.2.3 Summary

The aim of this section was to illustrate the differences of the flows in the room due to differences in shape of the thermal mass (namely a complicated and detailed thermal manikin and a simple cylinder) and the boundary condition applied for the simulation. Results from the simulations involving the cylinder were compared to previously presented results for the CTM (in §3.4.4 and §3.4.5). The following key observations were made:

1. In general, the room flow was quite different for the CTM and cylinder. The different geometries interacted with the room flow in different ways, both through the spatial location and their influence on temperature distributions.

2. Flow from wall inlet diffuser was blocked by the cylinder, whereas it could mostly flow between the legs of the CTM. The effect of this on the CBL was minimal on the CTM, however it redirected most of the CBL flow towards the front of the cylinder.

3. A larger thermal plume was generated by the CTM than cylinder. The convective boundary layer for the CTM was dependant on the seated position, specifically rising heat from the horizontal areas such as the legs, shoulders and top of head. For the cylinder, the CBL rose mainly up the front of the body after being displaced close to the floor level by the flow from the wall inlet. The maximum velocities were comparable, however less air moved at that speed for the cylinder.

4. The PV flow was less disturbed by the more streamlines CTM face which notably reduced flow stagnation and a greater air mass flow rate passing round the sides of the head unhindered. For the cylinder, the combination of the interaction with the strong CBL and the wider shape of the obstacle caused regions of recirculation and flow mixing directly below the jet. This occurred at a lower level for the CTM.

5. The constant temperature boundary condition was unrealistic in the presence of localised airflows, such as the ventilation from the wall inlet and the PV flow. It therefore created larger thermal plumes.

6. A realistically shaped thermal mass (like the CTM) with natural thermal boundary conditions (i.e. heat flux) is essential if the general flow regime in the domain is required.

4.3 Air quality

For the benchmark case detailed in §3.2, based on the work of Russo et al. [2009] and Khalifa et al. [2009], a model contaminant, SF_6 (Sulfur hexafluoride), was used to determine the air quality and the relative improvement gained through using a PV system. The air quality index (AQI) was calculated using Equation (3.3), where an AQI of 0 represents perfectly mixed air, whilst a value of 1 indicates clean air in the breathing zone. In the CFD simulation presented in §3.2.2, SF_6 was modelled as a Fluent user defined scalar (UDS) and compared with experimental data [CFD Benchmarks, 2014] in (Figure 3.9).

Computational simulations afford the luxury of the ability to directly measure variables of interest, something that can be limited in physical experiments. To directly ascertain any improvements made, or deteriorations caused, by the use of a PV system, the mean age of air can be simulated as a proxy for air quality. As stated in §2.2.4, local mean age of air (MAOA) is, statistically, the average time taken for fresh supply air to reach a spatial location [Chanteloup and Mirade, 2009; Meiss et al., 2013] and is effectively a direct measure of air quality [Simons et al., 1999]. MAOA was calculated as a post-process to the simulations, as a user defined scalar (UDS) in a user defined function (UDF). This is provided in Appendix A.1. Air was specified with a low diffusivity ($2.88 \times 10^{-5} m^2 s^{-1}$), with a zero age at the inlets. The MAOA predictions were directly compared across the cases and also used to determine an AQI for direct comparison with the experimental data.

4.3.1 The effect of PV jet flow on MAOA

The purpose of a PV system is to improve on the baseline case (without any PV) and deliver fresher, cleaner air to the breathing zone. To that end, the baseline must first be established so that comparisons can be made.

The baseline case - no PV jet flow

Comparisons of contour plots of MAOA for the CTM and cylinder (Figures 4.12 and 4.13) indicate the underlying fundamental differences in the velocity flow field (Figures 3.45, 3.46, 4.9 and 4.10). In all cases, the air was fresher when it entered the domain through the wall inlet, rising with the thermal plume and exiting. The contours also highlight large regions of recirculation and stagnating air within the room (in front and behind the plume) that contain very old air with little or no air movement (yellow and orange in the contour plots).

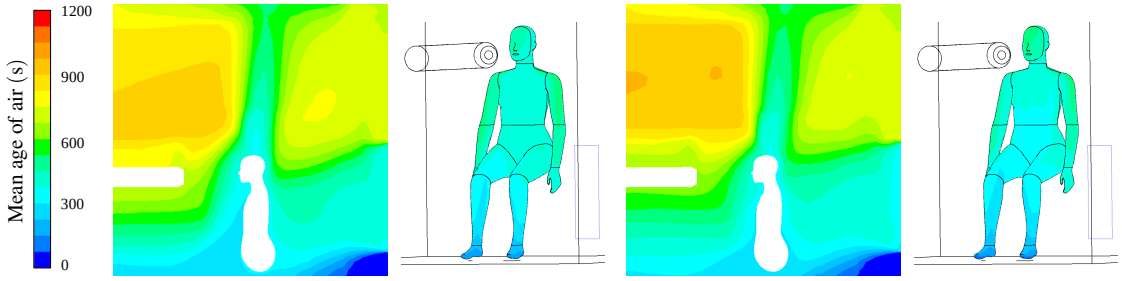

(a) Constant temperature BC. (b) Constant heat flux BC.

FIGURE 4.12: Contours of mean age of air (s) on a region of the centre plane and CTM surface with no PV flow.

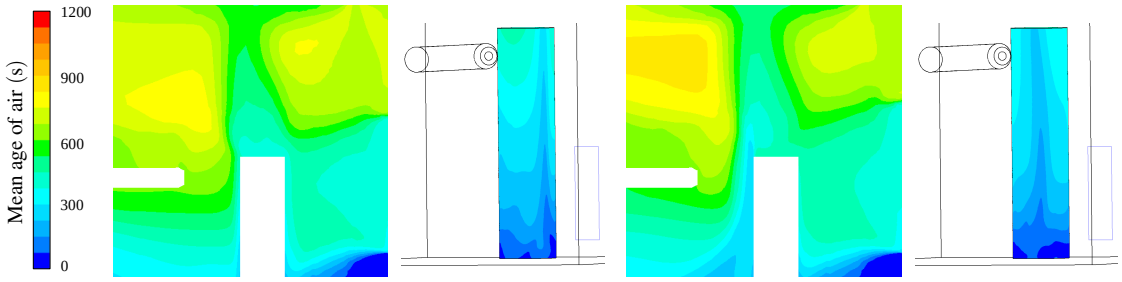

(a) Constant temperature BC. (b) Constant heat flux BC.

FIGURE 4.13: Contours of mean age of air (s) on a region of the centre plane and cylinder surface with no PV flow.

Considering the maximum values of MAOA in the domain (Table 4.7) indicates that the shape of the thermal mass (and hence the room flow and thermal plume) has more of an effect than the type of thermal boundary conditions applied; for the CTM cases, air became trapped in the domain for much longer than the cylinder cases. The heat flux boundary conditions appear to cause a marginal increase in the oldest age of air.

	CTM	**Cylinder**
Temperature BC	967	876
Heat flux BC	971	898

TABLE 4.7: Maximum MAOA (s) in the computational domain for the different boundary conditions on the CTM for no PV flow.

For the CTM cases, surface area mean values of MAOA were taken at the mouth and nostrils to determine the baseline MAOA in the breathing zone (Table 4.8). The air flow took slightly longer to reach to the nostrils than it did the mouth. This is in steady state conditions with no other movement or breathing, so in reality these values would differ. However, they are beneficial for the purposes of establishing the impact of PV in the breathing zone. A 10 % difference between the thermal boundary condition types was found in the values in the breathing zone, with the heat flux condition causing the air to take longer to reach the face.

	Mouth	Nostrils
Temperature BC	344	353
Heat flux BC	384	393

TABLE 4.8: Mean MAOA (s) at the CTM mouth and nose for the different boundary conditions on the CTM with no PV flow.

With PV flow

In all cases the presence of the thermal plume blocked the flow of the air over the PV tube, essentially trapping it inside the domain for longer. The top front of the domain (above the PV tube) was found to contain very slow moving, recirculating air (Figures 4.14 and 4.15). Due to the large extent of the recirculating region, there was an overall rise in the MAOA despite the presence of the PV flow. It can be seen from Tables 4.7 and 4.9 that this air was older with the CTM than for cylinder, and contained for longer with use of the PV system. The contours on the CTM and cylinder surfaces show that the MAOA was older on the forehead and top of head of the CTM than on the top of the cylinder. Inspection of the contour plots on the planes reveals that the blunt shape of the cylinder isolated the older recirculating air (above the PV tube), preventing it from entering the breathing zone.

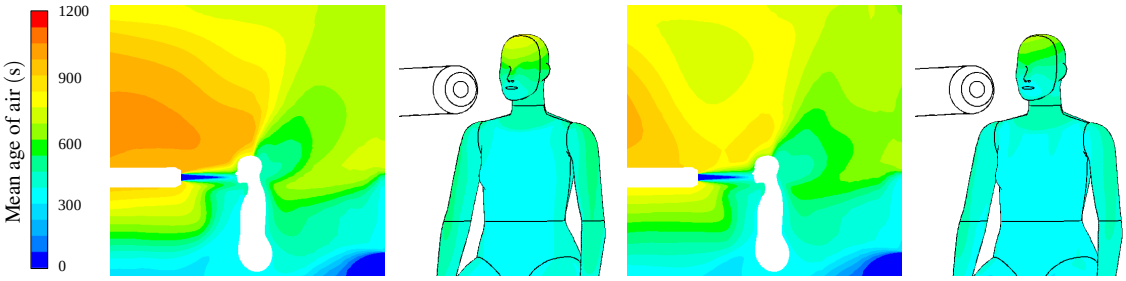

(a) Constant temperature BC. (b) Constant heat flux BC.

FIGURE 4.14: Contours of mean age of air (s) on a region of the centre plane and CTM surface with PV flow.

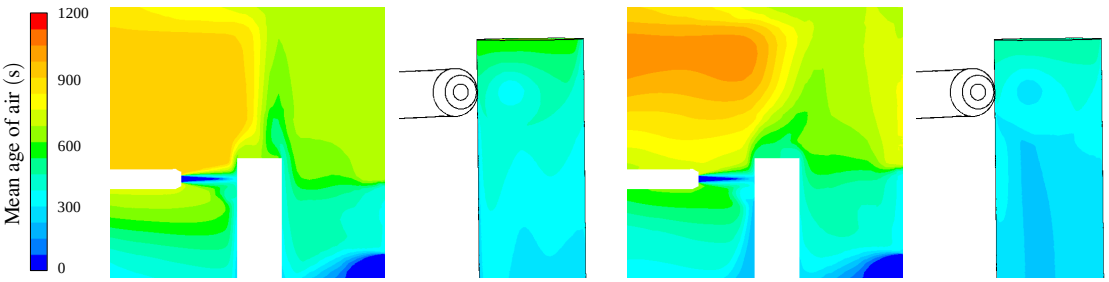

(a) Constant temperature BC. (b) Constant heat flux BC.

FIGURE 4.15: Contours of mean age of air (s) on a region of the centre plane and cylinder surface with PV flow.

	CTM	Cylinder
Temperature BC	1082	962
Heat flux BC	1015	1119

TABLE 4.9: Maximum MAOA (s) in the computational domain for the different boundary conditions on the CTM with PV flow.

The purpose of a PV system is to deliver clean air to the breathing zone. Comparing the mean MAOA at the mouth and nostrils with and without PV (Tables 4.8 and 4.10) it can be seen that the MAOA at the nostrils is older with the PV than without. It is also older at the mouth with the PV using the constant temperature boundary condition. These (perhaps initially counter-intuitive) findings highlight that a PV system does not necessarily guarantee that better air quality will be attained through its use. The flow features of the PV jet and the surrounding entrained air, along with the topology of any physical barriers (such as a CTM or cylinder) and dominant sources of thermal loads are all crucial factors involved in the determination of quality of the air. An essential element of beneficial PV usage is correct placement of the device with respect to the breathing zone. This is discussed in more detail in Chapter 5.

	Mouth	Nostrils
Temperature BC	373	423
Heat flux BC	333	370

TABLE 4.10: Mean MAOA (s) at the CTM mouth and nose for the different boundary conditions on the CTM for with PV flow.

Placement of a jet flow PV system, and it's efficacy, is dependant on the flow features of the jet (as described in §3.3). Figure 4.16a shows the velocity decay on the PV jet axis (the location of which is shown in Figure 3.57a) for both the CTM and the cylinder compared with the no thermal mass case (Figure 3.15). It can be seen that both the CTM and the cylinder followed the no thermal mass case very well, where the velocity remained constant from the PV nozzle exit until the end of the zone of flow establishment ($x \sim 0.3\text{m}$), until the rapid descent at the CTM or cylinder surface where the PV jet stagnated and impinged. A region of recirculation can be seen in the graph behind the CTM head (indicated by the negative x-velocity) whereas the air is still in the wake behind the cylinder. The depth of the cylinder is also larger than that of the CTM, leaving a larger gap in the graph.

The simulated MAOA value along the PV jet axis (Figure 4.16b) followed the expected physical profile. Namely that it was fresh, young air in the zone of flow establishment (where the velocity along the jet axis remained constant) and aged rapidly in the established jet flow as it entrained older air. The MAOA can be seen from the graphs to be more sensitive to the end of the jet flow establishment than the velocity, with an earlier inflection point. The lines for both the CTM and the cylinder match closely to the no thermal mass case throughout the jet flow establishment, however the CTM line can be seen to diverge and age faster,

although following the same trend. This fits with the observations of the contours in Figure 4.15 where it was clear that the topology of the thermal mass influenced the MAOA distribution. Given the closeness of the predictions, both the no thermal mass and the simplified cylinder shape are capable of providing a meaningful estimation of the MAOA. Furthermore, these results suggest that simply modelling the PV jet without a thermal mass can give an indication of the location for the ideal PV system deployment.

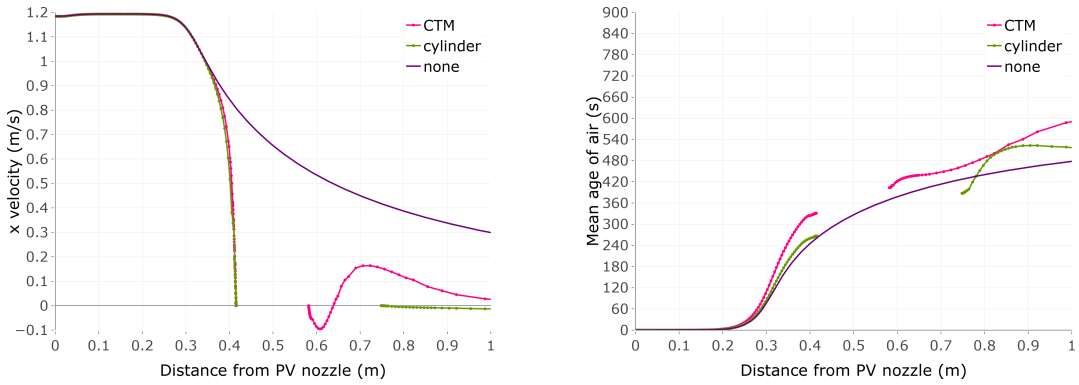

(a) x-velocity ($\mathrm{m\,s^{-1}}$) of air with distance from PV nozzle.

(b) Mean age of air (s) with distance from PV nozzle.

FIGURE 4.16: Graphs of x-velocity of air and mean age of air along the PV jet axis comparing CTM and cylinder with no thermal mass.

4.3.2 MAOA as a measure of AQI

Modifying Equation (3.3) to reflect MAOA replacing contaminant concentrations, the AQI equation becomes

$$\mathrm{AQI} = \frac{\mathrm{MAOA_{bz}} - \mathrm{MAOA_{out}}}{\mathrm{MAOA_{pv}} - \mathrm{MAOA_{out}}}, \tag{4.1}$$

where $\mathrm{MAOA_{bz}}$ was the value in the breathing zone, $\mathrm{MAOA_{out}}$ was the value taken at the exhaust and $\mathrm{MAOA_{pv}}$ was the value specified (0) at the PV nozzle. All MAOA values were calculated in seconds. Given that the MAOA at the PV nozzle was specified to be 0, the only scenario in which the AQI would be negative would be if the air in the BZ was older than that at the outlet.

The AQI was calculated on the vertical lines 10 mm and 25 mm in front of the CTM and cylinder and compared with the experimental data using a tracer gas [CFD Benchmarks, 2014] used by Russo et al. [2009] and Khalifa et al. [2009]. As noted in §3.4.9, the experimental data was obtained under mixing ventilation conditions (§3.2.1, Figure 3.5a), however a good match was obtained for the simplified domain (§3.4.1, Figure 3.19) in the region of the PV jet (Figures 3.58a and 3.58b).

The graphs generated using the MAOA for AQI in Figure 4.17 are a direct comparison with those in Figure 3.58 obtained using a UDS for the AQI as they are calculated on the same domain, the only difference being the measure of air quality. As with the UDS, a good match was obtained in the region of interest, namely the flow governed by the PV jet (with the range $\pm\, y/\mathrm{R} = 1 \sim 5\,\mathrm{cm}$). The MAOA gave a better match for the AQI higher in the domain than the UDS, however the MAOA predicted a significantly better air quality lower in the domain. The reason for this was that the wall inlet also provided MAOA specified to be clean and fresh, unlike the UDS case which specified only the PV flow. Comparing the experimental data with the cylinder gives a reasonable approximation despite the differences in the room flows due to the different shaped thermal masses discussed in §4.2.2.

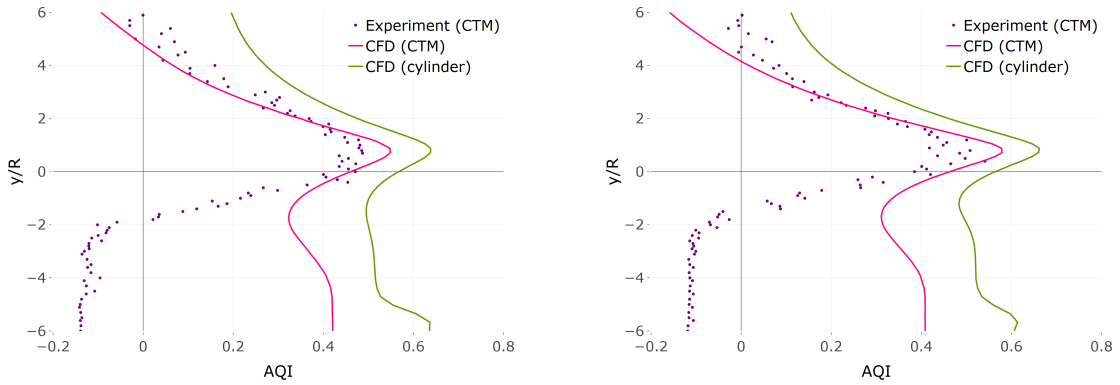

(a) 10 mm in front of CTM and cylinder face.

(b) 25 mm in front of CTM and cylinder face.

FIGURE 4.17: AQI on lines in centre of domain in front of CTM nose (with constant heat flux boundary condition) using MAOA compared to experimental data with a tracer gas.

The AQI calculation is heavily reliant on the value taken at the outlet. A benefit of CFD simulations is the ability to easily determine an average value. This might not be the case in physical experiments and any value obtained may be spatially or temporally dependant, as was the case with the experimental data for this benchmark case [CFD Benchmarks, 2014]. Table 4.11 shows the range of values at the outlet for the different cases. The mean values were consistent for all four cases, however the heat flux boundary condition generated a larger range for both the CTM and the cylinder, further highlighting the dependency of the flow field on both the shape and boundary conditions of the thermal mass used.

	CTM			**Cylinder**		
	Min	**Mean**	**Max**	**Min**	**Mean**	**Max**
Temperature BC	684	704	746	676	700	726
Heat flux BC	644	705	806	649	701	762

TABLE 4.11: Values of MAOA (s) at the outlet for the different boundary conditions on the CTM and cylinder with PV flow.

Comparison of the predicted AQI at the CTM mouth and nostrils, with and without PV flow (Table 4.12) with the raw MAOA values (Tables 4.8 and 4.10 respectively) show that the AQI also predicts better air quality at the mouth than nostrils in all cases, with a higher AQI analogous to a lower MAOA.

	No PV flow		**With PV flow**	
	Mouth	**Nostrils**	**Mouth**	**Nostrils**
Temperature BC	0.505	0.492	0.470	0.399
Heat flux BC	0.448	0.435	0.528	0.475

TABLE 4.12: AQI using MAOA at the CTM mouth and nose for the different boundary conditions on the CTM for no PV flow and with PV flow.

4.3.3 Summary

This section discussed the application of MAOA as a proxy for air quality.

1. The MAOA flow field is highly dependent on the velocity flow field, highlighting sensitive areas not necessarily apparent from just considering the velocity fields alone.
2. MAOA can accurately represent air quality in regions of interest, such as a PV jet and BZ.
3. Using a simplified shape such as a cylinder can give an indication of the air quality in the BZ.
4. Calculating MAOA along a PV jet axis (in the absence of any thermal mass) can be used to determine the suitable placement of a PV system for improved air quality.

4.4 Modelling thermal comfort

This section considers the impact of a thermal mass in the room on the effect on thermal comfort predictions. Following the earlier sections of this chapter, two separate variables were investigated; namely the choice (and presence) of a thermal mass (CTM or cylinder), the choice of boundary condition type applied to the thermal mass (constant temperature or constant heat flux). In this section, the selection of thermal comfort metrics is considered, which includes the operative temperature and two forms of PMV/PPD calculations. Thermal comfort was determined as a post-process step with a UDF to determine the operative temperature, PMV and PPD values, shown in Appendices A.2 and A.1 respectively. The volume averaged relative humidity of 50 % was specified via a constant mass fraction of water vapour. All other conditions were kept constant, the PV flow remained at 23.5 °C at a distance of 0.406 m from the breathing zone of the thermal mass. Clothing and activity were modelled as consistent with office attire (1 Clo) and energy expenditure (1 Met) for a sedentary person.

Section 2.3 discussed at length different factors involved in thermal comfort, an inherently individual and problematic metric to quantify (Figure 2.5) because "different people prefer different thermal conditions" [Lee et al., 2017]. The PMV/PPD model does not deal with personal comfort on an individual level, instead based on averages and assumptions of personal factors from large data sets [Zhao et al., 2014] in a steady-state environment [Djamila, 2017; Fanger, 1972]. Despite the large variations observed in individuals, it is practical to design for an average occupant and PMV remains an international standard [d'Ambrosio Alfano et al., 2017] which is recognisable, extensively validated with known limitations, easily calculated and comparable. Whilst it is acknowledged that there are other more sophisticated methods for measuring thermal comfort (as discussed in Chapter 2), this is not the focus of this research, as will be discussed in more detail in Chapter 7.

Two different forms of PMV calculation were compared. The first form ("original") used the calculated radiation field at every location whilst the second form ("modified") replaced these values with the volume average radiation in the domain. Specifically, the original UDF ran with line 205 and the modified replaced this with line 206 in the UDF in Appendix A.1. The rationale behind the modification was that the Fanger's original thermal comfort equations (Equations 2.8 and 2.13) were based on single values of temperature and radiation in the room. CFD calculations, however, discretise the domain into (in these cases) millions of cells and determines the value for every cell. It has already been shown in Chapter 3 (§3.4.4) that the radiation field was a lot warmer near the CTM surface. Averaging the radiation throughout the room made the prediction more in-line with Fanger's original predictions rather than using a disproportionately high value near a thermal mass.

Both versions of the UDF used the value of the temperature calculated at every location in the computational domain. Similarly, the air velocity determined at every location was also used. On the surfaces a no slip boundary condition set the velocity to be 0, meaning that the air velocity was not directly part of the thermal comfort calculation on the surface of the CTM. With the constant temperature boundary condition applied on a surface, the temperature was constant over the entire surface. However, the constant heat flux boundary condition applied to a surface allowed for variations in surface temperature due to the influence of local air flows and therefore indirectly accounted for their effects. The UDFs required that the relative humidity had been calculated throughout the domain, achieved through modelling a constant mass fraction of water vapour and solving with a species transport simulation. The clothing (and hence thermal insulation of the clothing) was assumed constant with a fixed value of Clo over the surface of the CTM. CIBSE, Guide A [2015] specifies the method of calculating single values of PMV and PPD for a given room, using an iterative loop to calculate the expected surface temperature of clothing, followed by calculation of heat loss components to determine the thermal comfort metrics. The UDFs used this method to determine the values of PMV and PPD at every location in the computational domain.

4.4.1 PV flows with no thermal mass

The computational set-up described in §3.3.2, Figure 3.11 with PV flow but no thermal mass was used to establish a baseline thermal comfort prediction. Figure 4.18 shows contours on the central vertical plane to illustrate the differences in the total temperature, radiative temperature and operative temperature for the case with the PV flow at 23.5 °C. The total temperature was mainly stratified according to the airflow, the radiation field was determined by the surface temperatures of the walls and floor in the domain whilst the operative temperature combined the two, providing a more uniform environment except in areas of faster air movement. There was very little difference in the volume averages of these in the domain, with 22.42 °C, 23.26 °C and 22.99 °C observed for the total, radiative and operative temperatures respectively. Without the presence of a thermal mass, there was negligible difference in the predictions made by either UDF for PMV in the domain (Figure 4.19a) and hence the PPD (Figure 4.19b). The domain was predicted to be marginally cooler than thermal neutrality, with a volume averaged mean PMV value of -0.1736 and PPD of 5.87 % with the original UDF (and -0.1731 for PMV, 5.79 % for PPD with the modified UDF), except in the areas of inlet and PV flow which were slightly cooler still. In the case of the wall inlet, the reduced PMV value was due to the lower temperature of the slow moving inlet air, whilst for the PV it was the faster movement of the air.

(a) Total temperature. (b) Radiative temperature. (c) Operative temperature.

FIGURE 4.18: Contour plots of temperatures (°C) on the central vertical plane for the case with PV flow at 23.5 °C and no thermal mass.

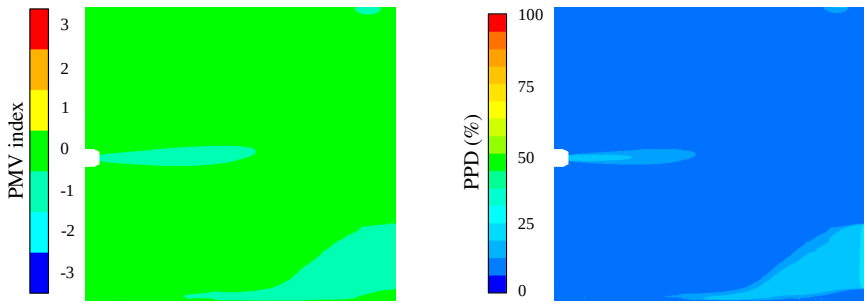

(a) Original UDF. (b) Total temperature (°C).

FIGURE 4.19: Contours of PMV index and PPD on the central vertical plane for no thermal mass using the original UDF with PV flow at 23.5 °C.

4.4.2 PMV with the CTM and cylinder

As shown for the case with no thermal mass, the operative temperature (Table 4.13) was slightly warmer than the volume average temperature in the room (Table 4.1) by between 0.5 °C and 0.8 °C. Due to the inclusion of radiation in the calculation, the heat flux boundary condition cases generated marginally higher overall operative temperatures. The shape of the thermal mass (which had identical surface areas) had a negligible effect on these values.

	CTM	**Cylinder**
Temperature BC	23.43 °C	23.43 °C
Heat flux BC	23.56 °C	23.58 °C

TABLE 4.13: Volume average operative room temperatures for the different boundary conditions on the CTM and cylinder.

Contours of PMV index are shown on the centre plane and on the CTM, for both thermal boundary conditions, in Figures 4.20 and 4.21 for the original and modified UDFs respectively. Similarly, for the cylinder in Figures 4.22 and 4.23. It can be seen in the contours that regions close to the thermal mass, for the heat flux boundary condition especially, were dominated by the heat generated, whilst further afield the values were comparable to the no thermal mass case (Figure 4.19a). The field values indicate that the PMV was higher in the room overall with the heat flux boundary conditions. This is confirmed in Table 4.14 which shows that the heat flux boundary condition generated marginally higher volume average PMV indices than for the temperature boundary condition, irrespective of shape of thermal mass or UDF used. The domain as a whole was more sensitive to the type of thermal boundary condition used on the thermal mass than either the shape of the thermal mass or the UDF calculation employed.

Whilst the average values of PMV in the domain were slightly cooler than thermally neutral (with small negative values of PMV), the values on the surface of the CTM and cylinder were warmer. The contour plots show values on the CTM and cylinder were very similar for the respective boundary condition and UDF, for example Figures 4.20a and 4.22a, or Figures 4.21b and 4.23b. The surface values were more sensitive to the UDF than the boundary condition type (Table 4.15). The heat flux boundary condition allowed for variations in surface temperature (as shown previously in §3.4.5, Figure 3.42) due to proximity of other heat sources or air movement.

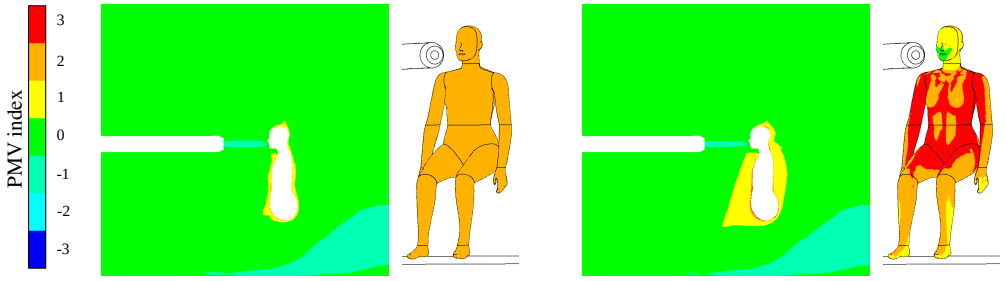

(a) Constant temperature BC. (b) Constant heat flux BC.

FIGURE 4.20: Contours of PMV index on the central vertical plane and CTM surface using the original UDF.

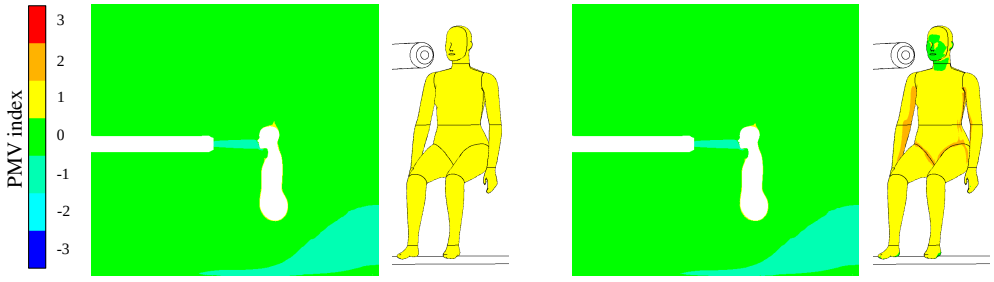

(a) Constant temperature BC. (b) Constant heat flux BC.

FIGURE 4.21: Contours of PMV index on the central vertical plane and CTM surface using the modified UDF.

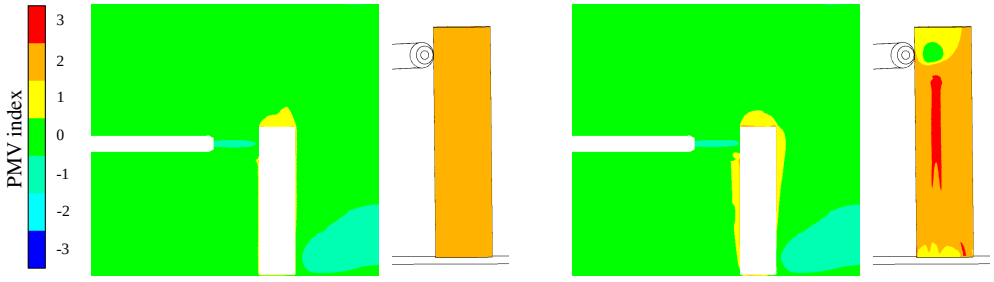

(a) Constant temperature BC. (b) Constant heat flux BC.

FIGURE 4.22: Contours of PMV index on the central vertical plane and cylinder surface using the original UDF.

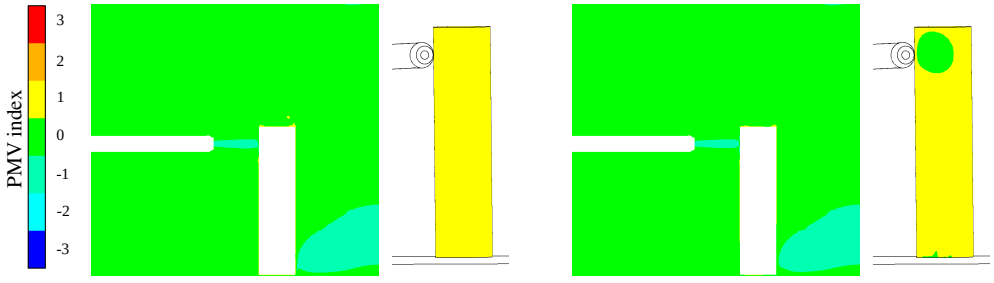

(a) Constant temperature BC. (b) Constant heat flux BC.

FIGURE 4.23: Contours of PMV index on the central vertical plane and cylinder surface using the modified UDF.

	Volume average PMV index in domain			
	Temperature BC	**Heat flux BC**	**Temperature BC**	**Heat flux BC**
CTM	-0.0412	-0.0211	-0.0406	-0.0206
Cylinder	-0.0417	-0.0315	-0.0410	-0.0245
	(Original UDF)		(Modified UDF)	

TABLE 4.14: Volume average PMV index in the domain for the different boundary conditions and UDFs on the CTM and cylinder.

	Surface average PMV index on thermal mass			
	Temperature BC	**Heat flux BC**	**Temperature BC**	**Heat flux BC**
CTM	1.60	1.94	0.92	0.81
Cylinder	1.48	1.69	0.92	0.68
	(Original UDF)		(Modified UDF)	

TABLE 4.15: Surface average PMV index for the different boundary conditions and UDFs on the CTM and cylinder.

Variations in the mean PMV index on the individual body segments (Figure 4.24) highlights the importance of the choice of UDF and boundary condition. When the heat flux boundary condition is used, these simulation results show that PMV predictions on the CTM are closer to thermal comfort (particularly the face and feet) in the presence of the PV jet and the wall inlet. The constant temperature boundary condition leads to predictions which are further away from thermal comfort. In each case, the PMV values on the surface of the thermal mass are lower with the modified UDF, more realistic and closer to that in the domain as a whole.

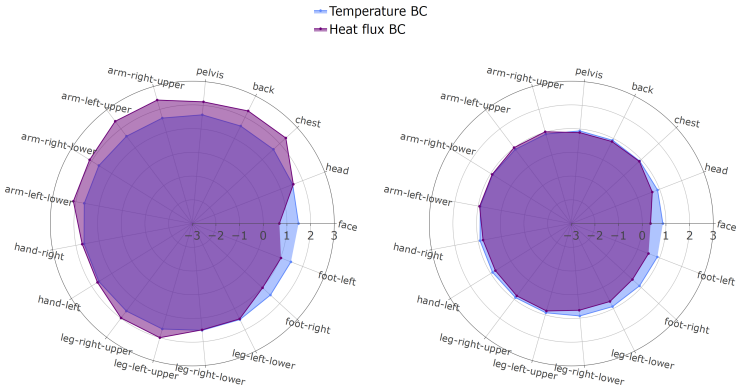

(a) Original UDF. (b) Modified UDF.

FIGURE 4.24: Radar charts of the PMV index on the CTM surface for different boundary conditions.

Comparing the CTM and cylinder with no thermal mass, the predicted value of PMV along the PV jet axis, is shown for both thermal boundary condition types using the original UDF and modified one in Figures 4.25 and 4.26 respectively. In all cases, the predicted values can be seen to follow the expected case with no thermal mass as the jet approached the thermal mass, until it reached the thermal boundary layer when the index increased rapidly, giving identical values for the CTM and cylinder. As seen in Figure 4.16, the

cylinder was larger than the CTM at the PV jet level, leaving a wider gap in the graphs. The predicted PMV index remained elevated in the thermal boundary layer behind the CTM and cylinder. Beyond this, the predicted levels dropped to those in the bulk flow, outside of the influence on the PV jet and in line with the volume average for the domain as a whole. For both UDF methods, the constant heat flux BC (Figures 4.25b and 4.26b) gave a lower level of predicted PMV under the influence of the PV (until the jet impinged on the CTM) than the constant temperature BC (Figures 4.25a and 4.26a) due to the lower temperature (from the PV jet) experienced in this region with the heat flux method. The original UDF allowed disproportionately high increases in the prediction (such as behind the CTM head) due to the elevated radiation field close to a thermal mass. This was mitigated by the averaging approach taken for the modified UDF.

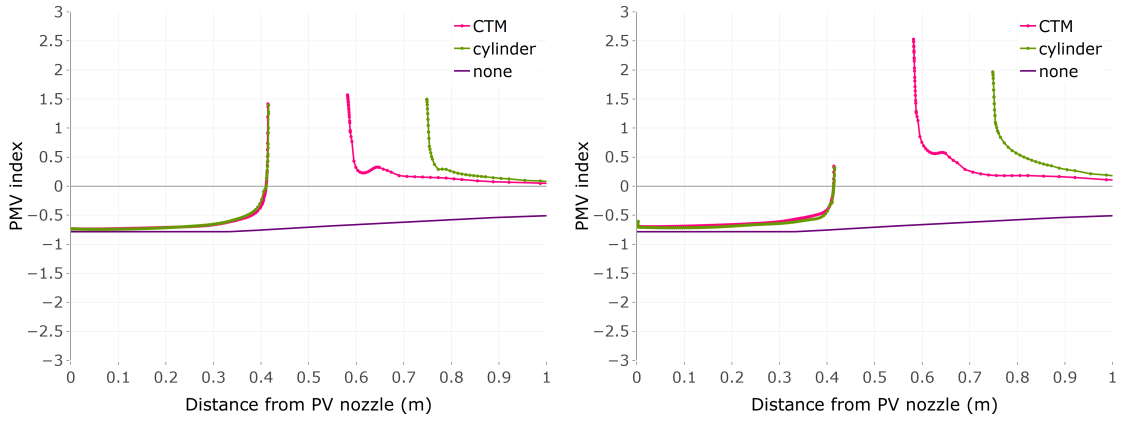

(a) Constant temperature BC. (b) Constant heat flux BC.

FIGURE 4.25: Graphs of PMV index along the PV jet axis comparing CTM and cylinder with no thermal mass, using the original UDF.

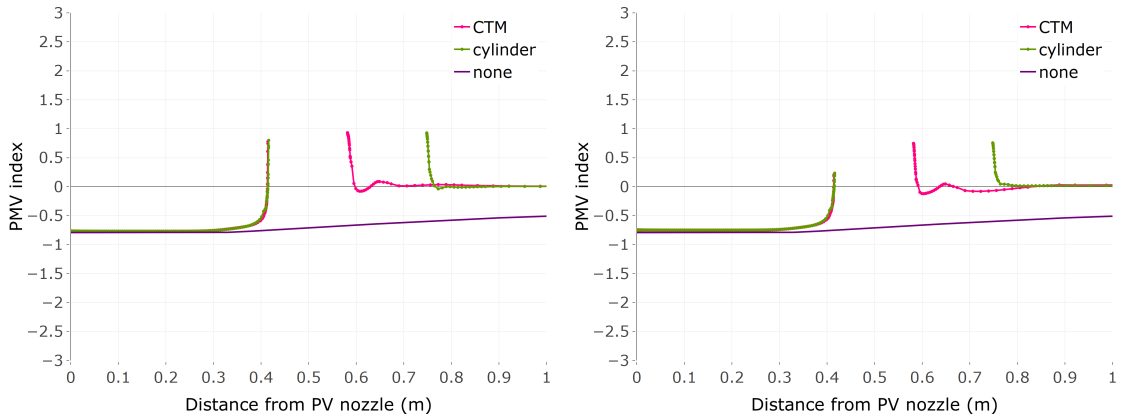

(a) Constant temperature BC. (b) Constant heat flux BC.

FIGURE 4.26: Graphs of PMV index along the PV jet axis comparing CTM and cylinder with no thermal mass, using the modified UDF.

4.4.3 PPD with the CTM and cylinder

It was shown that in Figures 4.20, 4.21, 4.22 and 4.23, the primary differences from the no thermal mass case (Figure 4.19a) were most evident in the regions close to the thermal mass. The differences occurred on the surface of the thermal source, due to either the shape, boundary condition type or UDF implementation. The same was true for the PPD calculation, for which the PMV index was the only variable. Table 4.16 shows the negligible differences in the volume averaged PPD values in the domain, which were slightly higher for the original UDF than the modified one.

	Volume average PPD (%) in domain			
	Temperature BC	**Heat flux BC**	**Temperature BC**	**Heat flux BC**
CTM	5.45	5.53	5.35	5.35
Cylinder	5.46	5.48	5.38	5.32
	(Original UDF)		(Modified UDF)	

TABLE 4.16: Volume average PPD (%) in the domain for the different boundary conditions and UDFs on the CTM and cylinder.

	Surface average PPD (%) on thermal mass			
	Temperature BC	**Heat flux BC**	**Temperature BC**	**Heat flux BC**
CTM	56.1	68.4	22.9	19.9
Cylinder	49.6	61.2	23.0	15.0
	(Original UDF)		(Modified UDF)	

TABLE 4.17: Surface average PPD (%) for the different boundary conditions and UDFs on the CTM and cylinder.

There were similarities between the values generated by CTM and cylinder for each instance. This can be seen more clearly in the mean values on the surfaces (Table 4.17), which also highlight the unrealistically high values generated with the original UDF, especially with the heat flux BC (Figures 4.27 and 4.28). Furthermore, the differences in the PMV index observed on the individual sections of the CTM (Figure 4.24) become more distinct when using the PPD metric (Figure 4.29).

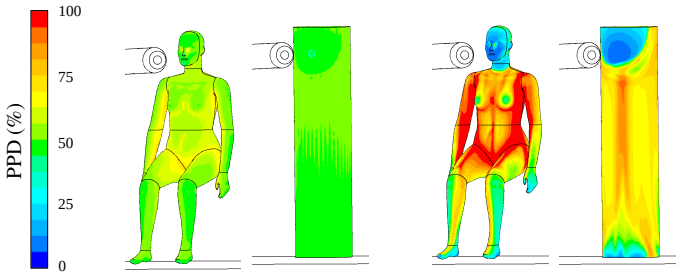

(a) Constant temperature BC. (b) Constant heat flux BC.

FIGURE 4.27: Contours of PPD (%) on the CTM and cylinder surface using the original UDF.

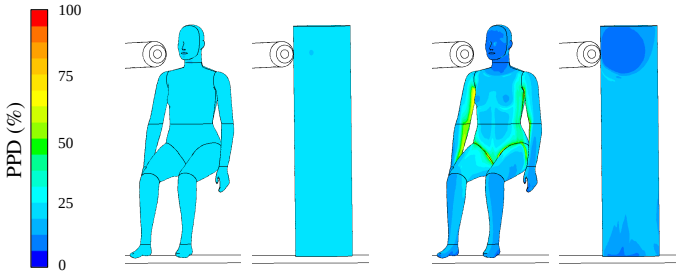

(a) Constant temperature BC. (b) Constant heat flux BC.

FIGURE 4.28: Contours of PPD (%)on the CTM and cylinder surface using the modified UDF.

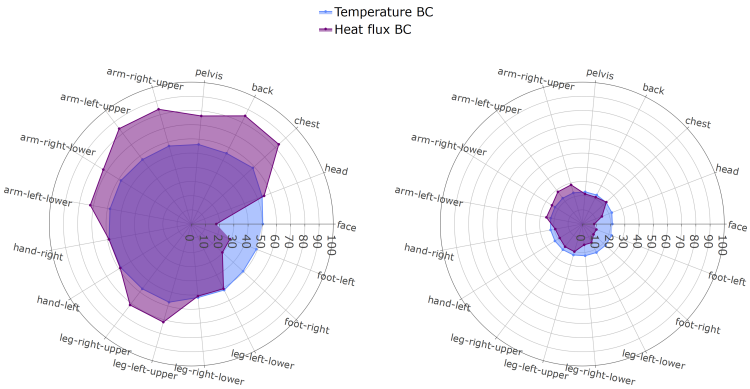

(a) Original UDF. (b) Modified UDF.

FIGURE 4.29: Radar charts of the PPD (%) on the CTM surface for different boundary conditions.

4.4.4 Sensitivity to perturbations in relative humidity and PV temperature

In order to ascertain the importance of relative humidity (RH) in the thermal comfort calculations, simulations were run using the CTM with the heat flux boundary condition and the modified UDF for a range of relative humidities. In addition, to ensure that these results were not temperature specific, they were also simulated at several PV temperatures (23.5 °C $\pm$ 2.5 °C). Figure 4.30 shows the PMV index on the PV jet axis for RH of 40 %, 50 % and 60 % with PV temperatures of 21 °C and 26 °C. It can be seen that, for a given temperature, there is a slight effect from these large variations in RH at these temperatures ($\pm$2 % in PPD on the surface of the CTM), both within the PV jet and the room in general

(behind the CTM). A significant difference is seen, however, in the PMV prediction in the jet and at the CTM surface for the variation in PV temperature. This shows that the PMV index is much more sensitive to temperature than relative humidity. The variations in PV temperature will be explored in greater detail in Chapter 5 .

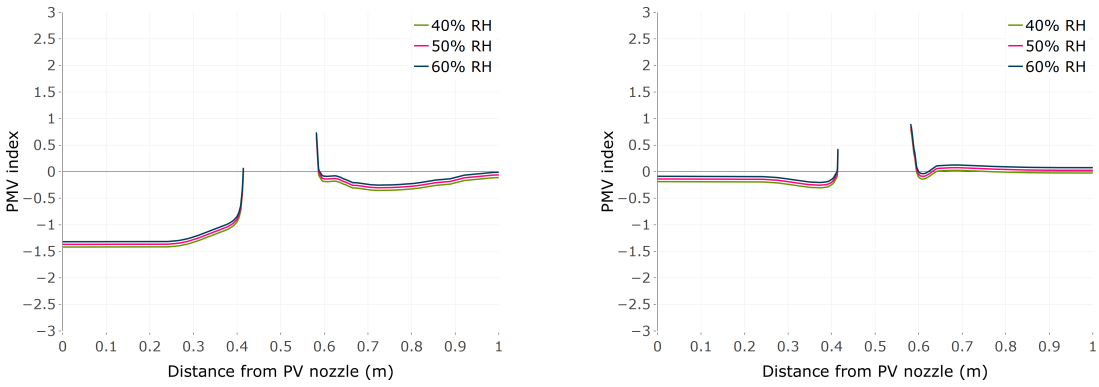

(a) PV at 21 °C

(b) PV at 26 °C.

FIGURE 4.30: Graphs of PMV index along the centreline comparing different relative humidities for the different PV temperatures.

4.4.5 Summary

This section was concerned with the presence and complexity of a thermal mass (CTM or cylinder), the choice of boundary condition type applied to the thermal mass (constant temperature or constant heat flux) and the selection of thermal comfort metrics. Based on the results presented in this chapter, the important observations are listed below.

1. The operative temperature metric combines the temperature and radiation fields, offering no further information pertaining to comfort levels.

2. There is little or no difference between the original and modified UDF's when there is no thermal mass present, or in the surrounding domain.

3. The presence of a single thermal mass makes a small difference to the overall predicted thermal comfort metrics. An accumulative effect could reasonably be expected for further thermal sources.

4. Irrespective of choice of thermal boundary condition or UDF, regions not dominated by the presence of thermal mass predict same thermal comfort metric as those without a thermal mass.

5. The original UDF over-predicts the thermal comfort metrics in the thermal boundary layer, which is exacerbated by the constant heat flux boundary condition, giving physically unrealistic predictions which propagate into the volume averaged values for the domain.

6. The constant temperature boundary condition gives an indication of thermal comfort in ambient conditions but cannot be used to investigate the effects of air flow or draughts, unlike the constant heat flux boundary condition which is more physically realistic.

7. The cylinder can give an indication of the thermal comfort at the surface of a CTM as the thermal comfort metrics are more sensitive to the thermal boundary conditions than either the shape of the thermal source or the choice of UDF.

8. The no thermal mass PMV profiles on the PV jet axis follow both the CTM and cylinder profiles closely until the thermal boundary layer is reached.

9. For the temperature range of interest, variations in the relative humidity had little effect on the thermal comfort metrics.

10. If thermal comfort is required, and local flows are involved, the heat flux boundary condition is the most suitable.

11. A realistically shaped thermal source is required if local information is needed, for instance the values of thermal comfort metrics on a face.

12. The modified UDF provides a compromise between the original PMV thermal comfort equation (with limited information) and the CFD calculations (with an abundance of information) and brings the PMV/PPD metrics into a more realistic range.

13. Perturbations to PV temperature effects predicted thermal comfort.

5. Temperature and placement of personalised ventilation with breathing zone analysis

Contents

The work in this chapter is a logical extension of the results from Chapter 4 with the important aspects carried forward. Outside of the zone of flow establishment (ZFE) of the PV jet, the air quality drops rapidly (as illustrated in the graphs in Figure 4.16), with the use of a PV system not guaranteeing enhanced air quality (Tables 4.8 and 4.10). It was shown in §4.4.4 that for the temperature range of interest, variations of 10 % in the relative humidity (from the baseline of 50 %) had little effect on the thermal comfort metrics. However, perturbations to the temperature of the PV air flow of $\pm 2.5\,^{\circ}\mathrm{C}$ had a significant effect.

The aim of the work contained within this chapter was to consider the effect of alterations to the PV air temperature and locations. Simulations were run using modifications to the simplified benchmark test case [Russo et al., 2009]. The heat flux boundary condition was used on the CTM. The PMV and PPD were calculated using the modified UDF for a relative humidity of 50 %. With the CTM fixed, the PV tube was moved to six equally spaced horizontal locations from the CTM breathing zone and perturbations made to the PV temperature to evaluate it's sensitivity.

As in Chapter 4, general room airflow is presented (§5.1) followed by air quality (§5.2) and thermal comfort (§5.3). The sensitivity of the results to small perturbations to the wider boundary conditions is considered in each section. Some of the findings presented in this chapter were published in two conference papers Gilkeson et al. [2018b] and Gilkeson et al. [2018a].

5.1 Room airflow

This section serves to illustrate the differences in flow within the computational domain due to the different temperatures of the PV flow and distances of the PV nozzle from the CTM breathing zone. Using the domain introduced in §3.4 (Figure 3.19), the PV tube was moved to six equally spaced horizontal locations in the range 0.086 m to 0.636 m from the CTM breathing zone and simulations run for PV temperatures of 21 °C, 23.5 °C and 26 °C (i.e. baseline ± 2.5 °C, [Yang et al., 2010]) from the benchmark case. In all cases the PV jet velocity was kept constant at $1.184\,\mathrm{m\,s^{-1}}$ which is consistent with the benchmark case [Khalifa et al., 2009; Russo et al., 2009].

All simulations were carried out using the CTM with the heat flux thermal boundary condition; both of these aspects were identified as being more realistic for room airflows in the previous chapter. All other meshing and computational parameters remained unchanged to ensure consistent results.

The rationale for these PV placements was to systematically explore parameter space in a way that hasn't been done before. Several other studies tend to fix the PV location without necessarily considering where to correctly position it, for example whether the CTM breathing zone is situated within or outside of the ZFE (zone of flow establishment), see for example Figure 2.20 in §2.5.3. Figure 5.1 superimposes these new locations (in red) onto the spatial locations presented in literature.

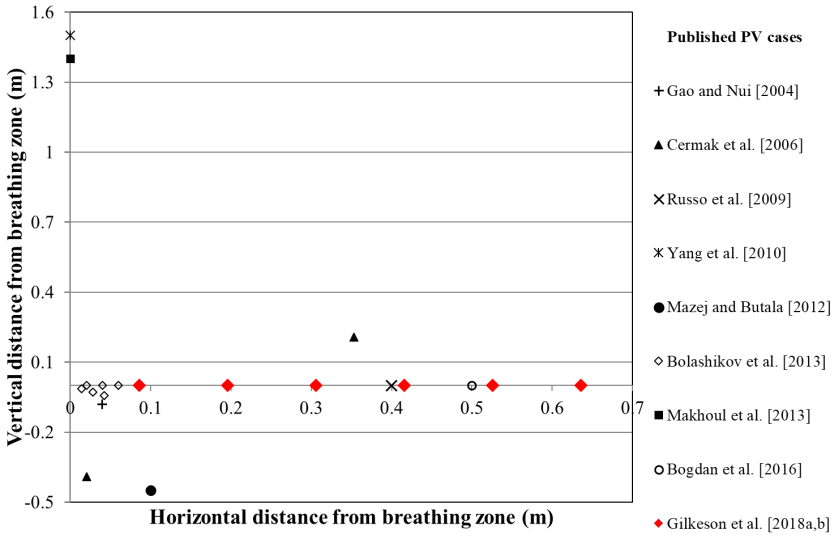

FIGURE 5.1: Spatial location of PV nozzles in literature.

Similarly, the PV temperatures were chosen to correspond to those in literature, which (as seen in Figure 2.23, §2.5.3) covered a wider range of the parameter space for both the ambient room temperature and corresponding PV temperature.

5.1.1 Pathlines of PV jet flow and the convective boundary layer

Pathlines from the PV nozzle (Figure 5.2) show that the PV jet caused more disruption to the flow behind the CTM when the nozzle was closer to the face. When the PV flow was warmer than the ambient temperature in the domain (at 26 °C), this extra heat energy fed the convection current behind the CTM and rose with the naturally occurring buoyant plume. Conversely, the cooler, denser PV air (at 21 °C) lowered the plume behind the CTM head.

All PV flows curved downwards as they entered the warmer thermal boundary layer at the CTM face, this was more prominent for the slower moving air. As with the jet only flow in §3.3.4, the PV jet axes curved up or down depending on the relative temperature of the jet to the ambient conditions. This became more apparent with increasing distance between the PV nozzle and the CTM breathing zone. A direct consequence of this was that the PV jet flow impinged on the CTM face at different locations depending on the PV temperature and distance (Figure 5.3).

It can be seen that at 0.636 m, the PV jet curves down towards the chin for 21 °C whilst it tends towards eye level for 26 °C. This has ramifications not only in terms of thermal comfort and air quality, but also wider implications such as dry, irritable eyes [Dalewski et al., 2014].

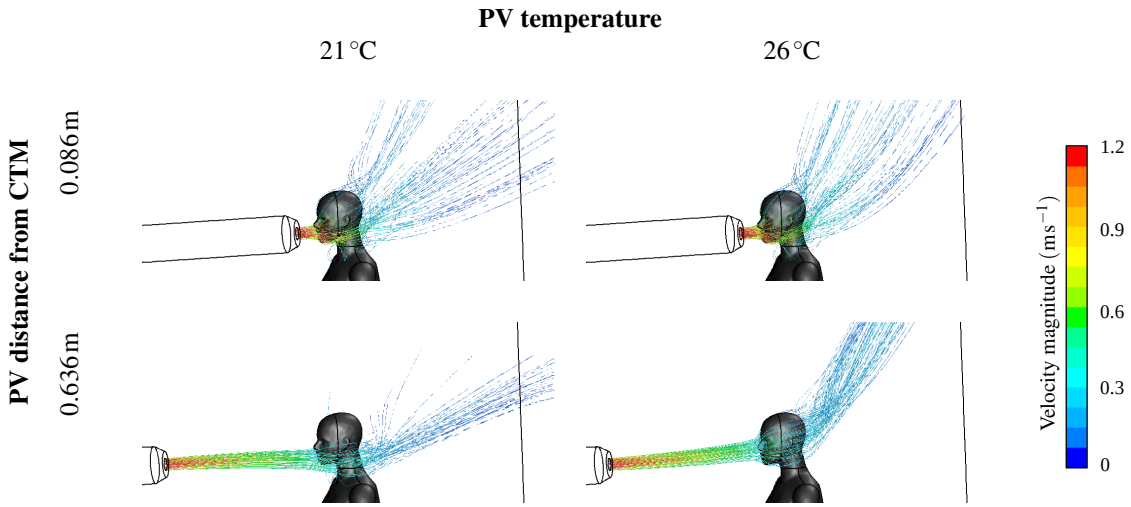

FIGURE 5.2: Pathlines coloured by velocity velocity magnitude $(\mathrm{m\,s^{-1}})$ released from the PV nozzle for the extreme PV distances and temperatures, side view.

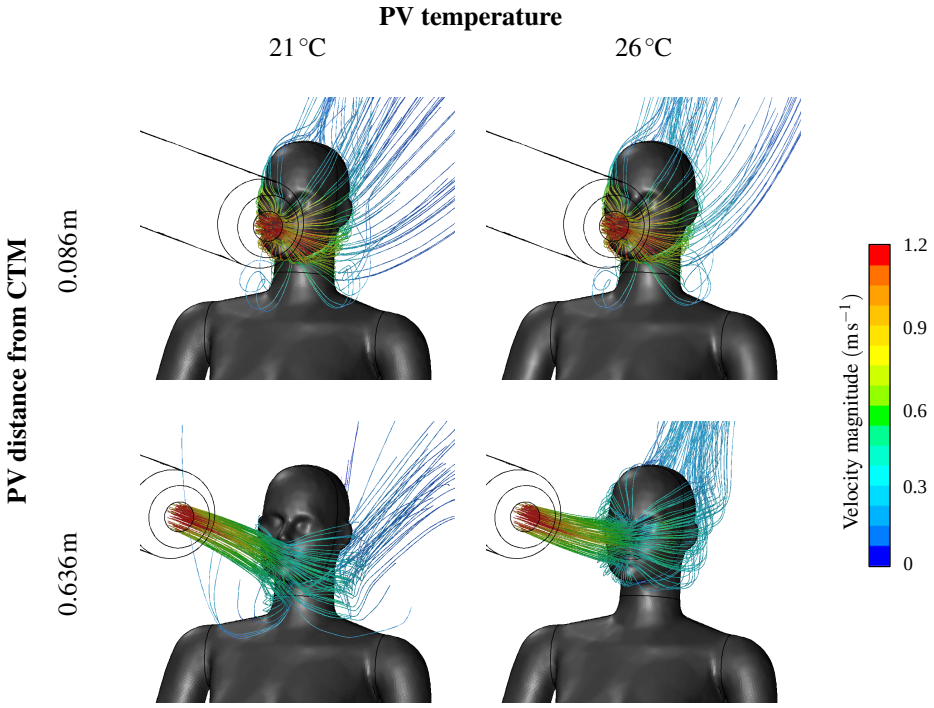

FIGURE 5.3: Pathlines coloured by velocity velocity magnitude $(\mathrm{m\,s^{-1}})$ released from the PV nozzle for the extreme PV distances and temperatures, front view.

Analysis of the pathlines of particles released from the PV nozzle showed that in all cases, after reaching the CTM, the flow from the PV jet was entirely contained within the volume of the thermal plume generated by the CTM (under the influence of the jet). This was not true for the cylindrical thermal mass considered in the previous chapter (Figure 4.8c). Pathlines of particles released from the surface of the CTM (Figure 5.4) show that the cooler PV flow disrupted the air behind the CTM more than the warmer PV, which generated a stronger and more compact plume. This is in contrast to the findings from the PV flow (Figure 5.2) where the primary disruption was related to the proximity of the jet. Combining the two flow structures shows that closer and cooler PV jets disrupt the thermal plume (and hence room airflow) more than warmer jets located further away.

As described in §3.4.4, without a PV jet the convective boundary layer (CBL) on the CTM rose with buoyancy and departed in vertical plumes from the CTM head and shoulders (Figure 3.36a). The baseline PV case (located 0.416 m from the breathing zone, set at 23.5 °C) punctured the CBL, causing regions of recirculation around the front of the neck and shoulders (Figure 3.36b). Figure 5.5 shows that this happened irrespective of PV temperature when the PV nozzle was close to the CTM, with similar flow features on the CTM face. When the PV nozzle was located further away, and more importantly the PV flow was slower, these regions of recirculation did not occur. For the higher PV temperature, the regions of the CTM surface affected by the flow were similar, however the effect of the jet on the CBL in general was very different. With the PV nozzle further from the breathing zone, the jet accumulated increasing amounts of entrained air, thereby increasing the size of the jet flow.

As noted for Figures 5.2 and 5.3, the temperature of the PV flow relative to the ambient room temperature dictated its trajectory. The interaction of the jet with the CBL differed depending not only on the speed of the jet but also the topology of the surface it impinged on. It can be seen that the cooler PV flow reached the CTM at a lower level than the warmer jet, blowing the CBL off a larger portion of the CTM neck and shoulders. The effect of this on the wider room flow was that the air flow in the thermal plume curved around the entrained air of the jet, unlike the plume for the warmer flow which was split into three distinct directions.

The flow over the CTM face was dependant on the distance and temperature of the PV. All PV flows resulted in air speeding up as it passed under the jaw and around the ears. When the PV was closer to the face (and therefore faster moving air) the flow features were similar across the different PV temperatures. As the PV distance was increased, the jet was slower and the temperature (and direction) of the flow became more important factors. Despite the centre of the jet arriving at a lower point on the CTM for the cooler PV, the flow features on the face were similar with increasing distance for the different temperatures, with the notable exception of the flow around the nose being directed over the eyes for the cooler PV and under the eyes for the warmer flow.

Another factor that influenced how the thermal plume interacted with the room air was how and where the plume departed from the top of the CTM head. It was observed that with no PV, the pathlines following the CBL travelled up the head of the CTM, amalgamating at the top and leaving the surface vertically due to convection (Figure 3.37a). The addition of the baseline PV flow tilted the plume, moved the location of departure from the CTM further back on the head and changed the properties, making it slower moving with two opposing vortices (Figure 3.37b). Whilst the location and structure of the base of the thermal plume was similar for the different temperatures when the PV nozzle was close to the CTM, the plume was faster for the higher temperature PV (Figure 5.6). The plume with the higher temperature PV was faster irrespective of PV distance. In all cases, the CBL from the back of the CTM contained faster moving air as this was warmer having not been cooled by any PV flow.

The interaction between the flows due to the PV and the rising CBL at the rear of the head caused the observed vortices. The magnitude of which was dependant on not only the PV temperature but also how, where and how fast the PV jet arrived at the CTM. The cooler PV located further away, for instance, was directed downwards due to buoyancy and the jet flow mainly impinged on the lower face of the CTM (Figure 5.3) resulting in smaller and slower opposing vortices in the thermal plume (Figure 5.6). The warmer jet from the same location impinged on the entire face (Figure 5.3) which resulted in a pair of larger and faster vortices (Figure 5.6). These flow features described were very sensitive to the topology of the CTM, therefore they would result in potentially very different local flow structures in the presence of variations of clothes, hair, hairstyles, furniture, size and shape of a person, for example.

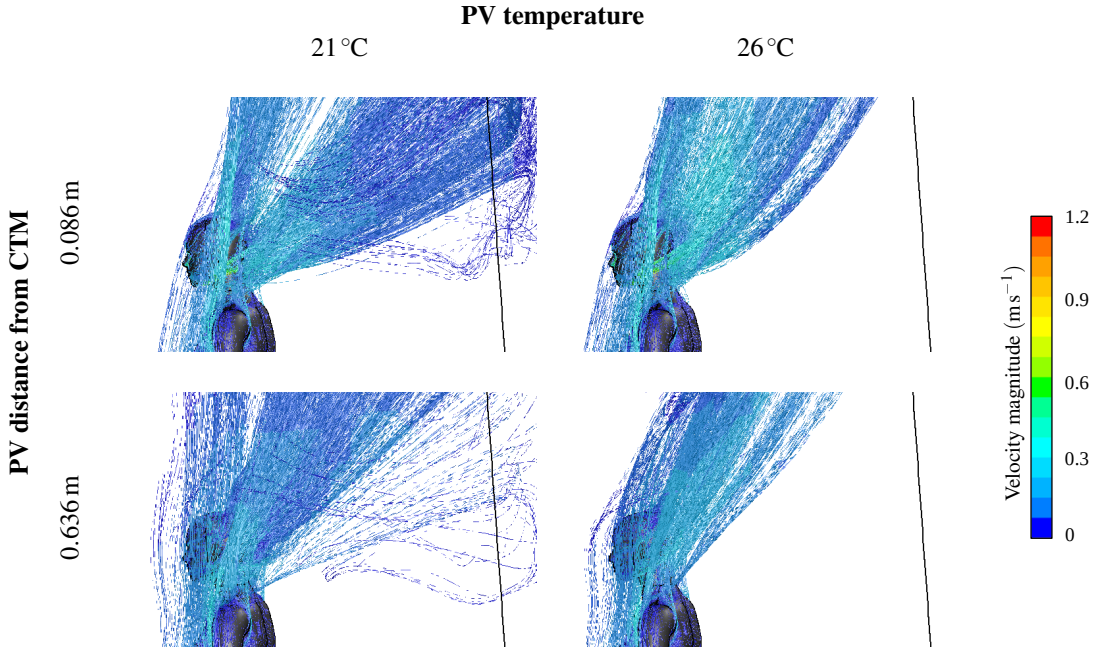

FIGURE 5.4: Pathlines coloured by velocity velocity magnitude $(\mathrm{m\,s^{-1}})$ released from the CTM surface for the extreme PV distances and temperatures, side view.

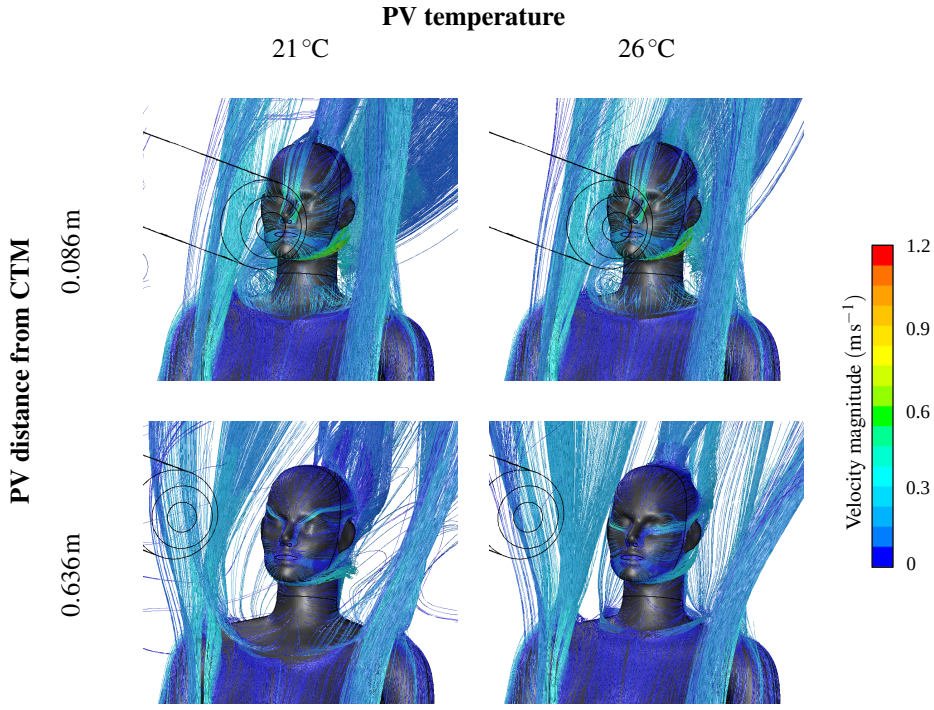

FIGURE 5.5: Pathlines coloured by velocity velocity magnitude $(\mathrm{m\,s^{-1}})$ released from the CTM surface for the extreme PV distances and temperatures, front view.

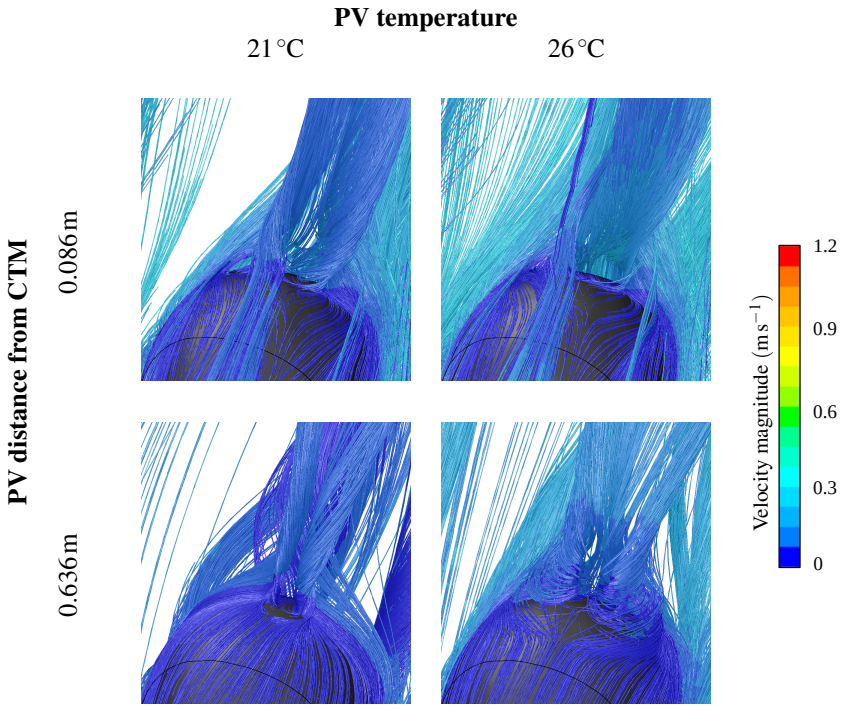

FIGURE 5.6: Pathlines coloured by velocity velocity magnitude $(\mathrm{m\,s^{-1}})$ released from the CTM surface for the extreme PV distances and temperatures, top view.

5.1.2 Qualitative comparison of flow features

The flow features described above (§5.1.1) can also be seen in the contour plots of velocity magnitude in the domain on vertical and horizontal planes (Figures 5.7, 5.8 and 5.9). The plume can be seen to leave the CTM head at different points, with faster airflow directly behind the CTM neck for close PV jets (Figure 5.7). Areas of recirculating flow are indicated on the CTM chest (Figure 5.7) and around the head and shoulders (Figure 5.9). As would be expected, faster air was found in the thermal plume for the warmer PV cases (Figures 5.7 and 5.8) with increases of around 20 % seen compared to the cooler cases. The plumes under the influence of the closer PV jets had a stronger vertical trajectory closer to the CTM than those further away, which were split into three directions by the jet, wider for the warmer jet which impinged on the CTM at a higher spatial location (Figure 5.8). There was more disruption to the flow in the horizontal plane in the breathing zone for the jets which had travelled the larger distances, more so for the cooler jet than the warmer one which rose out of the plane due to convection forces (Figure 5.9).

Contours of temperature show consistent thermal stratification created by the displacement flow across the range of simulations in the majority of the computational domain, with the exception of the regions affected by the PV jet and thermal plume (Figure 5.10). The cooler PV lowered the temperature behind the CTM irrespective of PV distance. The thermal plume emanating from the CTM was significantly cooler with the cooler PV temperature than with the warmer one. A larger volume of warmer air in the thermal plume was found for closer PV jets.

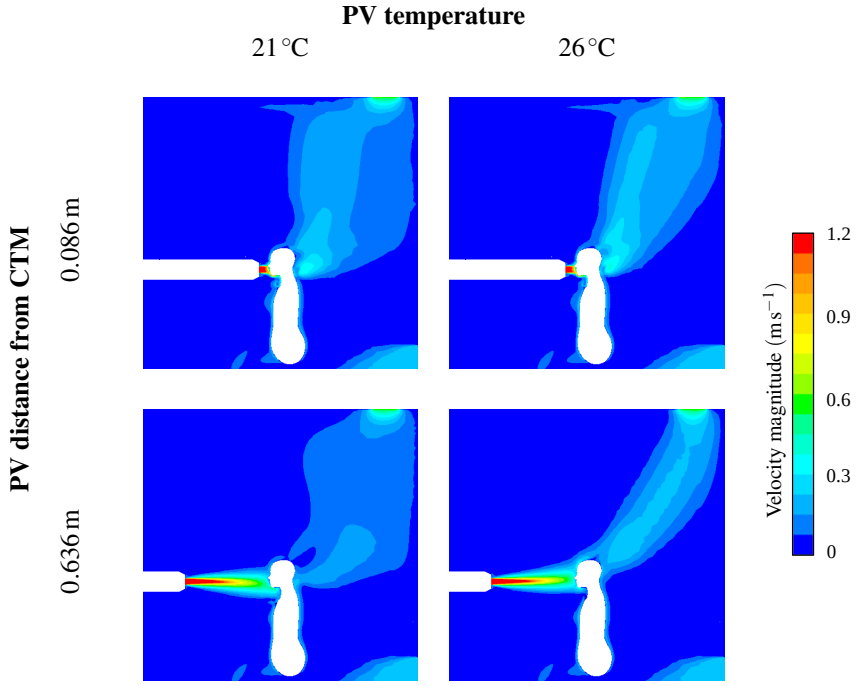

FIGURE 5.7: Contours of velocity magnitude $(\mathrm{m\,s^{-1}})$ on the central vertical plane for the extreme PV distances and temperatures.

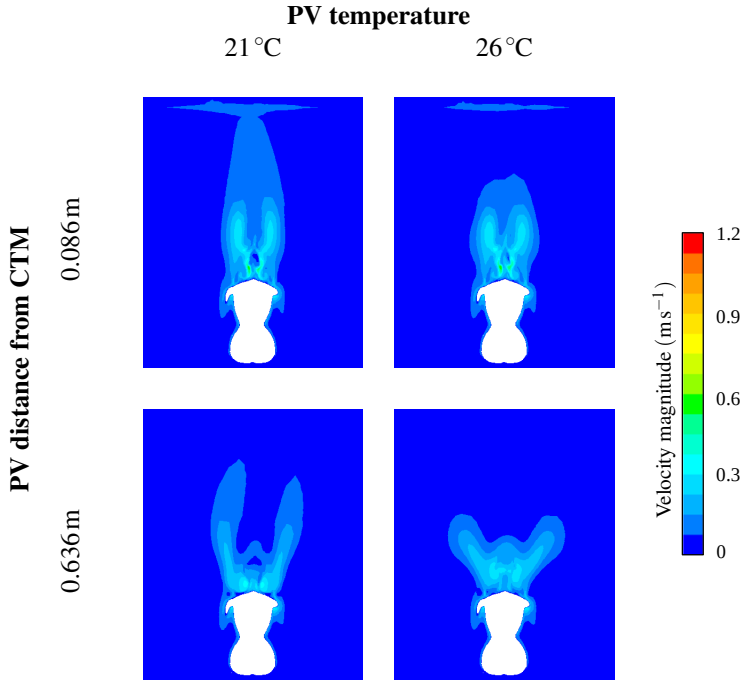

FIGURE 5.8: Contours of velocity magnitude $(\mathrm{m\,s^{-1}})$ on the vertical plane behind the CTM head for the extreme PV distances and temperatures.

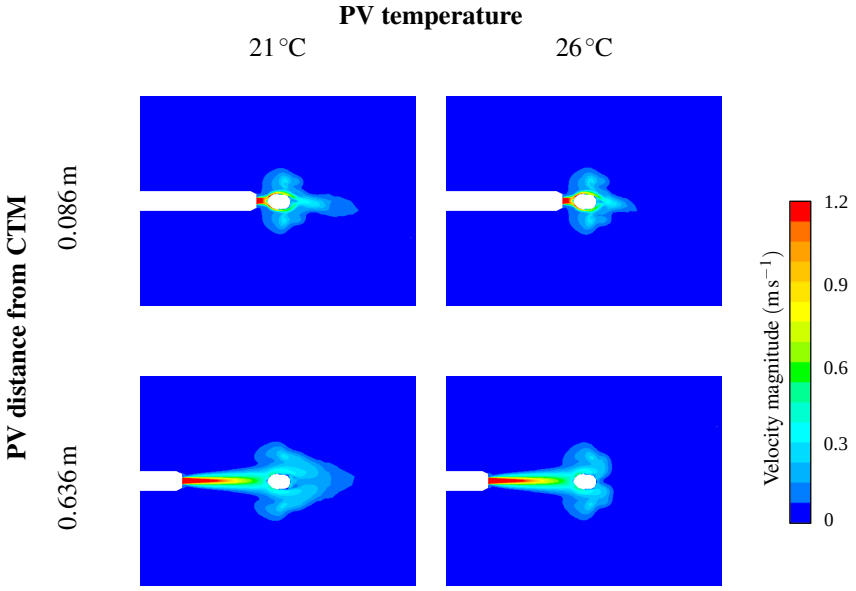

FIGURE 5.9: Contours of velocity magnitude $(\mathrm{m\,s^{-1}})$ on the horizontal plane in the breathing zone for the extreme PV distances and temperatures.

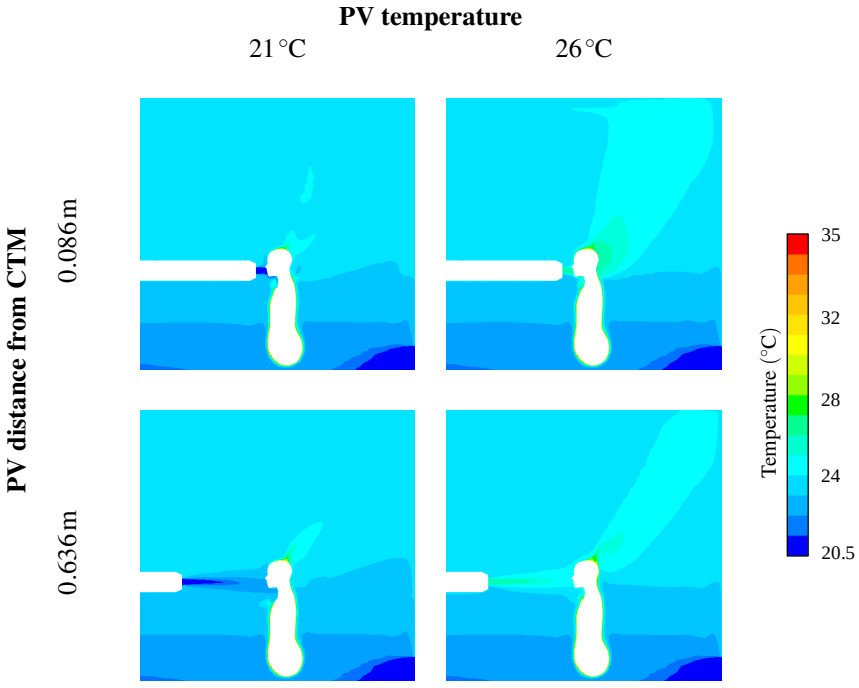

FIGURE 5.10: Contours of temperature (°C) on the central vertical plane for the extreme PV distances and temperatures.

5.1.3 Quantitative comparison of flow around the CTM

As seen in Figure 5.10, the thermal stratification in the computational domain is sensitive to the temperature of the PV jet but not to the distance it travels to reach the CTM. Table 5.1 shows the volume average temperatures in the room which confirms this sensitivity. It should be noted that although the PV temperature sensitivity may appear small with a room temperature range of 0.1 °C, the PV jet has much more of an influence locally.

PV distance	**PV temperature**		
from CTM	**21** °C	**23.5** °C	**26** °C
0.086 m	23.06 °C	23.11 °C	23.16 °C
0.636 m	23.06 °C	23.12 °C	23.16 °C

TABLE 5.1: Volume average room temperatures for the PV distances from the CTM breathing zone and PV temperatures.

Using the data clouds introduced in §3.4.4 (Figure 3.41), Pearson's product moment correlation, r, was calculated to directly compare the velocity magnitude and temperature fields generated as a result of the different PV temperatures. For all PV distances, the baseline temperature was with the PV jet set at 23.5 °C as this was close to the ambient temperature in the room. The correlations were determined between the data clouds from the 21 °C and 23.5 °C jets, and also for the 26 °C and 23.5 °C jets, to ascertain the impact of a cooler and warmer than ambient PV jets respectively. For all the PV temperatures and distances simulated, the correlations between the lower data clouds were virtually 1 (with very minor, statistically insignificant variations), meaning that the lower part of the domain around the CTM was insensitive to the PV flows directed at the CTM head.

Figures 5.11 and 5.12 contain graphs of the correlations over the PV distances from the breathing zone, for the higher two data clouds of velocity magnitude and temperature respectively. It can be seen that that in all the simulations, the warmer PV jet was closer to the ambient PV flow and temperature fields than the cooler jet. The correlations all decrease with distance, with the gradients tending to become larger past the end of the zone of flow establishment ($\sim$ 0.3 m), especially for the cooler PV jet. Within the ZFE, the velocity fields around the CTM head were very similar for all PV temperatures (Figure 5.11a) despite there being significantly less correlation in the temperature fields in the same volume (Figure 5.12a). This indicates that temperature (and convection) was not the main driving force of the flow in this volume, it was the momentum of the PV jet. As seen in the pathlines and velocity contours above, there was a greater range of velocities and temperatures around the CTM head with increasing distance in the established flow region. The larger volume contained within the upper data cloud contained not only the differences in the flow fields due to the PV jet (temperature and location) and the flows of the thermal plume, but also a large volume of unaffected flow field in front of the CTM. The effect of this was to bias the correlation, effectively making the larger data clouds less sensitive to the changes observed in the breathing zone

(Figures 5.11b and 5.12b).

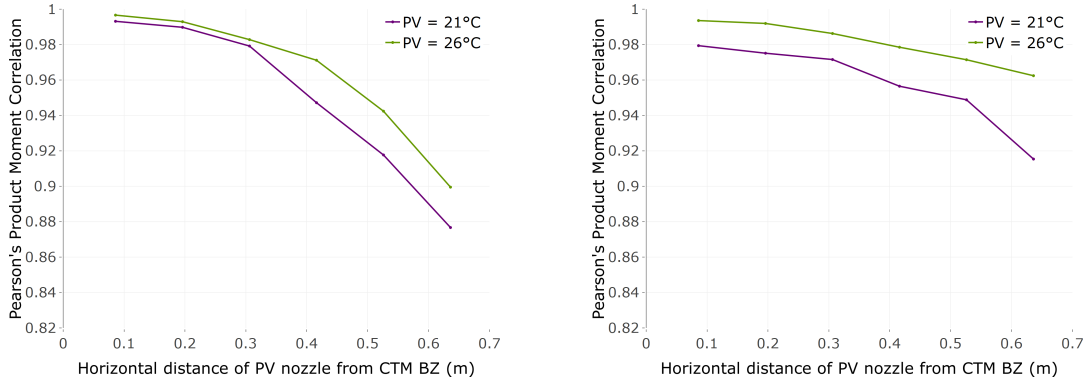

(a) Data cloud around CTM head. (b) Upper data cloud.

FIGURE 5.11: Graphs of Pearson's Product Moment correlation comparing the velocity flow fields around the CTM head and upper body at 21 °C and 26 °C with the baseline at 23.5 °C for increasing PV distance from the CTM breathing zone.

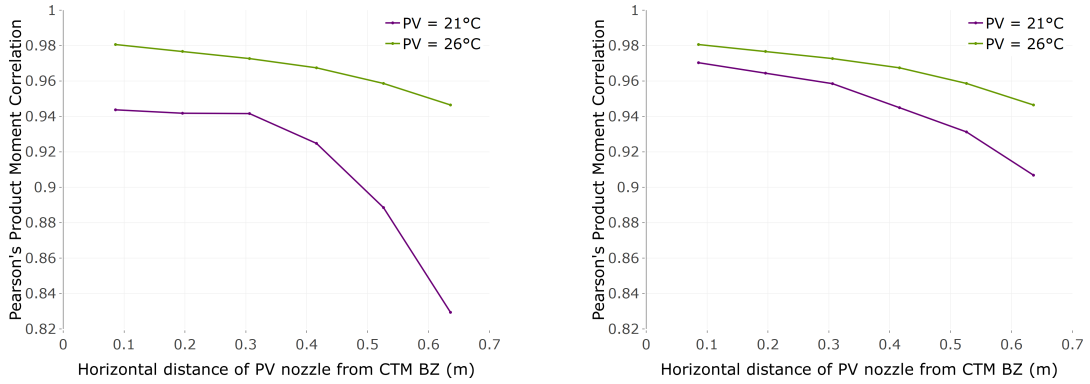

(a) Data cloud around CTM head. (b) Upper data cloud.

FIGURE 5.12: Graphs of Pearson's Product Moment correlation comparing the temperature flow fields around the CTM head and upper body at 21 °C and 26 °C with the baseline at 23.5 °C for increasing PV distance from the CTM breathing zone.

5.1.4 Sensitivity to perturbations in domain thermal boundary conditions

To ascertain whether the room conditions or the PV jet dominated the simulations, small perturbations of $\pm 0.5\,^{\circ}\mathrm{C}$ were made to all the thermal boundary conditions. These boundary conditions included the walls, ceiling, floor and wall inlet flow. They excluded the PV jet and the CTM. Table 5.2 shows the volume averaged room temperature for a representative case with the PV at 0.306 m from the CTM breathing zone; this distance is where the ZFE just reached the CTM. Decreasing the thermal boundary conditions by half a degree also decreased the room temperature by half a degree. However, increasing it by the same amount only increased the room temperature by a third of a degree.

Thermal BCs	PV temperature 21 °C	23.5 °C	26 °C
-0.5 °C	22.6 °C	22.6 °C	22.7 °C
Baseline	23.1 °C	23.1 °C	23.2 °C
+0.5 °C	23.4 °C	23.4 °C	23.5 °C

TABLE 5.2: Volume average room temperatures for the perturbations in thermal boundary conditions, with the PV at 0.306 m from the CTM breathing zone.

Contours of temperature are shown on the central plane for the thermal boundary perturbations with PV at 21 °C and 26 °C (0.306 m from the breathing zone) in Figures 5.13 and 5.14 respectively. The thermal levels for stratification were slightly lower for the cooler boundary conditions, with cooler inlet air from the wall pooling more at floor level. Increasing the thermal boundary conditions with respect to the PV at 21 °C effectively made the PV jet cooler, whilst decreasing the boundary conditions with respect to the PV at 26 °C effectively made the PV jet warmer compared to the ambient room temperature. This had more effect in regions surrounding the PV jet. However, the room conditions had more effect on the thermal plumes, with warmer rooms having warmer plumes.

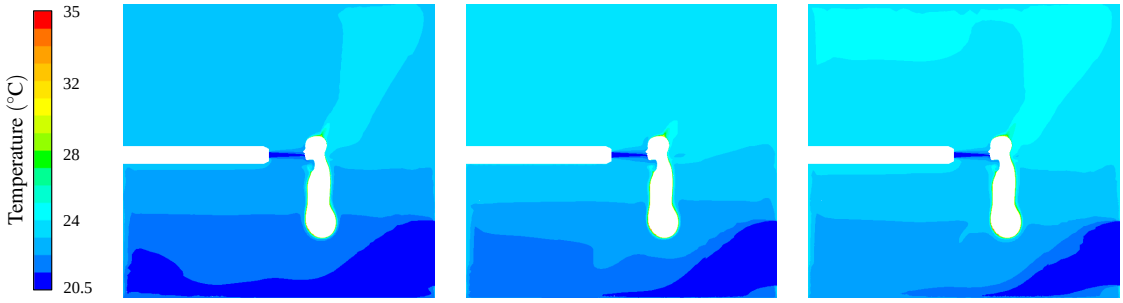

(a) BCs −0.5 °C. (b) Baseline BCs. (c) BCs +0.5 °C.

FIGURE 5.13: Contour plots of total temperature (°C) on the central vertical plane to illustrate the effects of the perturbations to thermal boundary conditions for PV = 21 °C, 0.306 m from the CTM breathing zone.

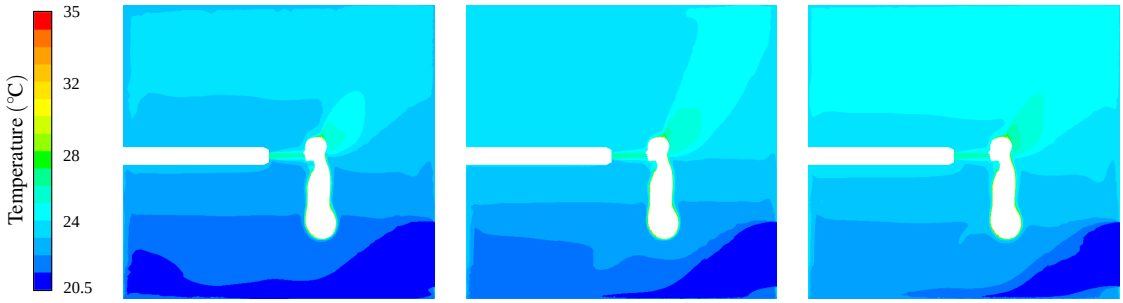

(a) BCs −0.5 °C. (b) Baseline BCs. (c) BCs +0.5 °C.

FIGURE 5.14: Contour plots of total temperature (°C)) on the central vertical plane to illustrate the effects of the perturbations to thermal boundary conditions for PV = 26 °C, 0.306 m from the CTM breathing zone.

The corresponding contours of velocity magnitude are shown in Figures 5.15 and 5.16 respectively. As expected, the thermal plume was slower for the effectively cooler PV jet in a warmer room. It departed the CTM head further behind the CTM and contained more horizontal flow in the lower regions of the domain (Figure 5.15c). A faster thermal plume was found in a cooler room with a warmer PV jet (Figure 5.16a). The same trends observed for the PV temperatures above also applied for these perturbations, demonstrating that the important parameter was the relative difference between the ambient room temperature and the PV jet. Fundamentally, the flow fields were predominantly unaffected by the 0.5 °C perturbations to the thermal boundary conditions.

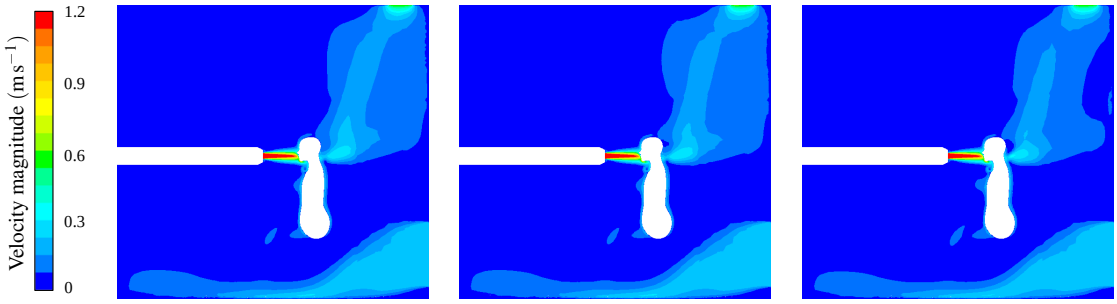

(a) BCs −0.5 °C. (b) Baseline BCs. (c) BCs +0.5 °C.

FIGURE 5.15: Contour plots of velocity magnitude (m s^{-1}) on the central vertical plane to illustrate the effects of the perturbations to thermal boundary conditions for PV = 21 °C, 0.306 m from the CTM breathing zone.

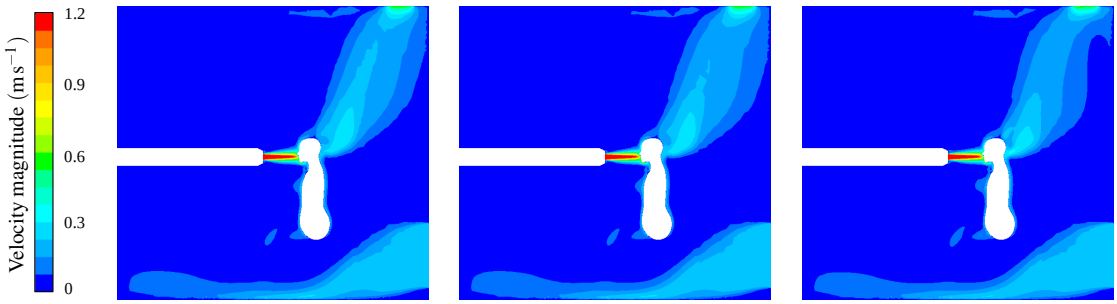

(a) BCs −0.5 °C. (b) Baseline BCs. (c) BCs +0.5 °C.

FIGURE 5.16: Contour plots of velocity magnitude (m s^{-1}) on the central vertical plane to illustrate the effects of the perturbations to thermal boundary conditions for PV = 26 °C, 0.306 m from the CTM breathing zone.

5.1.5 Summary

This section discussed the impact of PV temperature and location on the effect airflow patterns in the room and around the CTM.

1. Irrespective of PV temperature or distance from breathing zone, a PV system significantly altered the thermal plume and therefore the overall flow in the room.

2. The temperature of the PV jet with respect to the ambient room temperature was the dominant

thermal parameter.

3. Warmer jets increased the energy in the plume and enhanced the resulting buoyancy forces, whereas cooler jets kept the jet lower in the room with denser air.

4. PV jets placed in close proximity to the front of the CTM led to enhanced recirculation due to the interaction with the CBL.

5. The relative PV temperature became more important with PV distance, influencing the trajectory of the jet and hence location of jet impingement on the CTM.

6. Relative temperature and speed of the PV jet affected the interaction with the convective boundary layer.

7. A PV system located too far from the breathing zone can disrupt a displacement ventilation strategy, such as the one considered here, causing a change towards mixed ventilation for the entire domain.

5.2 Air quality

As in §4.3, local mean age of air (MAOA) was used as a proxy for air quality. This was achieved as a post process step to the main simulation, as a scalar variable in a UDF (Appendix A.1). The scalar transport equation was solved on a fixed velocity field, with the flow equations turned off. The MAOA was found to be highly dependent on the velocity flow and could accurately represent air quality in regions of interest, such as a PV jet and BZ. The values along the PV jet axis with and without a thermal mass suggested that the jet flow alone could provide a useful indication of where to locate a PV system in relation to the breathing zone, as the air quality outside of the ZFE could in fact be worse than no PV system. The work presented in this section extends that of previous chapters, considering the air quality over a range of distances and PV temperatures.

5.2.1 MAOA sensitivity to PV temperature and distance

As seen in §4.3.1 (Figures 4.14 and 4.15), the maximum MAOA in the domain was due to large volumes of slow moving recirculation over the PV tube caused by the thermal plume. The more vertical the orientation of the plume, the older the maximum MAOA. As discussed above, the shape and strength of the plume was dependant on both the PV distance from the CTM and the temperature of the PV jet. The same relationship between MAOA and velocity was found for variations in PV temperature and distance. Figure 5.17 shows contours of MAOA on the central plane, whose properties are directly relatable to the contours of velocity magnitude (Figure 5.7).

The air was freshest within the cone of establishment of the flow. Outside the cone, the entrained air that moved with the flow was older, notably at the top front of the domain over the PV tube (red and orange

contours). As the PV is moved further from the BZ, the air became more mixed and the cone of fresh air moves further from the breathing zone.

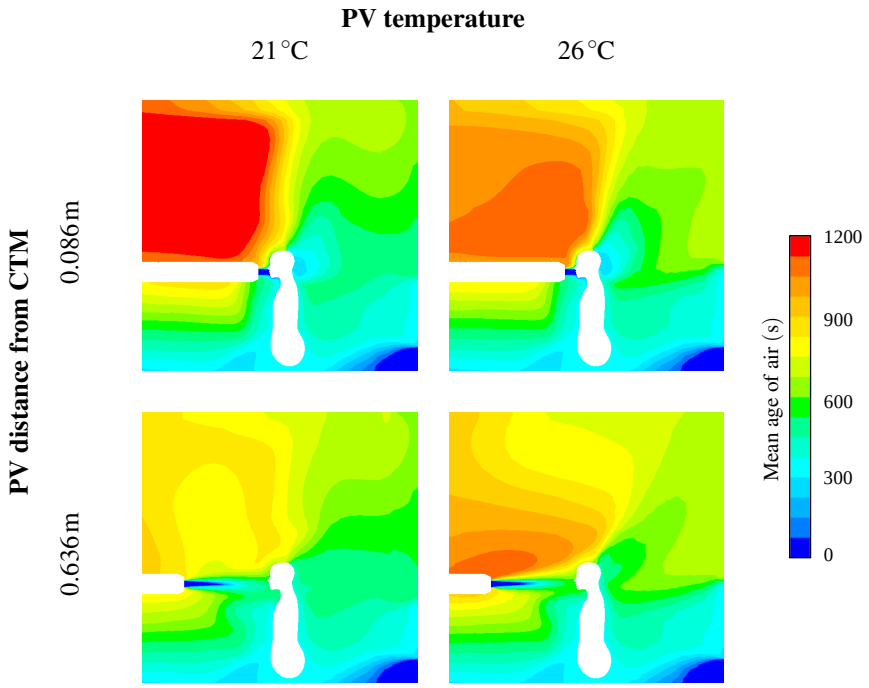

FIGURE 5.17: Contours of MAOA (s) on the central vertical plane for the extreme PV distances and temperatures.

5.2.2 MAOA analysis in the breathing zone

In all cases, the MAOA in the breathing zone was younger than the air on the rest of the face due to the PV jet. As stated in §4.3.1 (Table 4.8), with no PV system the mean MAOA at the CTM mouth and nostrils was 384 s and 393 s respectively (around 6 minutes). Considering the MAOA with the PV active, the mean (area weighted) values at the CTM mouth and nostrils (Table 5.3) are practically the same with the PV close to the BZ for all PV temperatures and notably reduced compared to the no PV case. This trend only held within the PV jet cone of establishment. Even with the end of the cone touching the CTM between the nose and mouth, the MAOA was close to 2 minutes old at the mouth and nostrils. This rose rapidly outside of the ZFE to close to 10 minutes for the furthest PV distance simulated, meaning that a poorly placed PV can almost double the MAOA at the CTM breathing zone compared to no PV system. Instances where the PV system performed worse than no PV are indicated in red text in Table 5.3.

PV distance from CTM BZ	Mean MAOA (s)					
	Mouth	Nostrils	Mouth	Nostrils	Mouth	Nostrils
0.086 m	0.18	39	0.18	43	0.18	40
0.196 m	5	119	3	112	3	101
0.306 m	123	283	107	276	104	220
0.416 m	344	401	333	370	366	393
0.526 m	441	475	476	501	498	508
0.636 m	501	521	572	593	565	572
	(PV = 21 °C)		(PV = 23.5 °C)		(PV = 26 °C)	

TABLE 5.3: Mean MAOA (s) values at CTM mouth and nostrils for all PV distances and temperatures.

Contours of MAOA on the CTM face are shown in Figure 5.18. It can be seen that the closer the PV nozzle was, the fresher (younger) the air reaching the CTM face was, irrespective of PV temperature. In all cases, the freshest air was found on the lower part of the CTM face, with older air higher up the face. For the larger PV distances, the trajectory of the jet flow (due to temperature and thus buoyancy of the jet) determined the location on the CTM face where the PV flow impinged and stagnated. This trajectory, along with the extensive interaction with the room flow due to the thermal plume, governed the age of the air surrounding (and entrained into) the jet. Despite the jet impacting higher on the CTM face for the warmer PV, older air was entrained into the PV jet flow, making the MAOA older at larger distances.

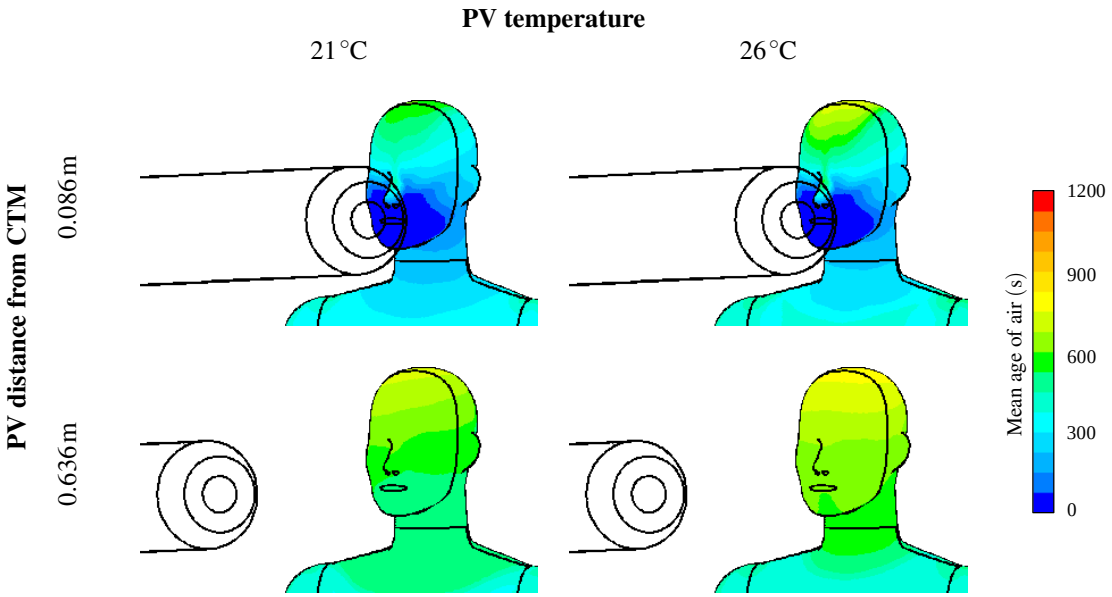

FIGURE 5.18: Contours of MAOA (s) on the CTM face for the extreme PV distances and temperatures.

The distributions of MAOA on the face of the CTM under the different simulated conditions was found using the probability density function of the values at the cell surface (weighted according to cell size). Integrating these functions (the area under the curve) gives a value of 100% probability that all the data is contained within that interval $(-\infty, \infty)$. The differences observed in the contours of MAOA on the

face under the conditions simulated (Figure 5.18) can be seen graphically in Figure 5.19. When the PV nozzle was close to the face (Figure 5.19a), the most likely age of air was very fresh, however there was a range of almost 15 minutes (900 s). All three PV temperatures gave very similar MAOA results, with no statistically significant differences. The range of the distributions on the face have halved by the maximum PV distance (Figure 5.19b), with all distributions shifted towards the older air. The effect of differences in PV temperature are far more pronounces in this graph, with the freshest air being the coolest. The distributions changed from uni-modal to bi-modal for intermediate PV distances, either side of the zone of flow establishment (Figure 5.20). The range of MAOA reduced and the modal values became more distinct outside of the cone, in the established jet flow regions. The PV temperature became more important outside of the cone, with warmer air more likely to be older than cooler air.

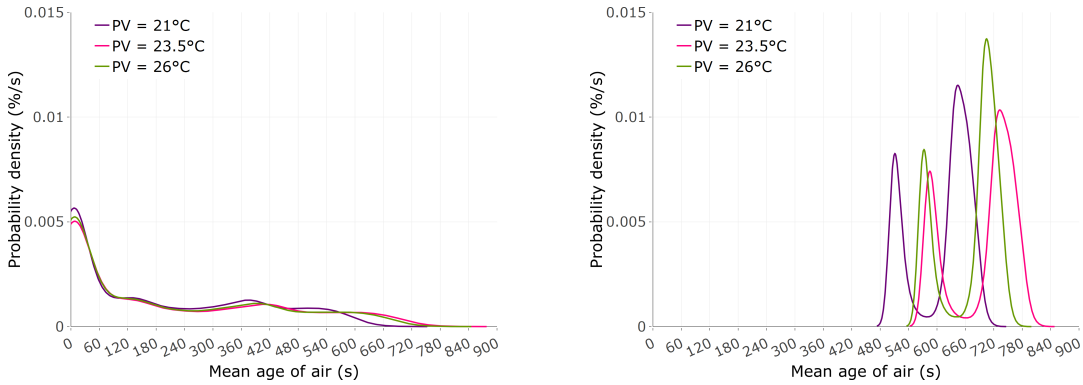

(a) PV at 0.086m from face.

(b) PV at 0.636m from face.

FIGURE 5.19: Graphs of the probability density functions of MAOA (s) on the CTM face for the different PV temperatures at PV distances 0.086 m and 0.636 m from the breathing zone.

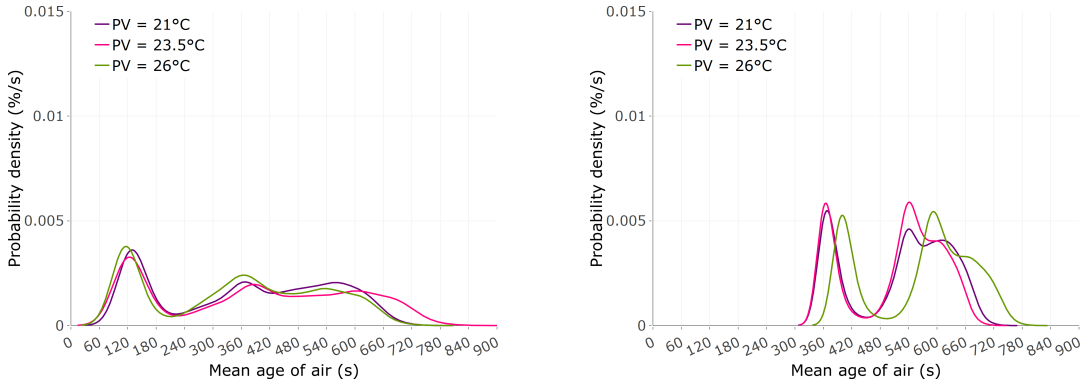

(a) PV at 0.306m from face.

(b) PV at 0.416m from face.

FIGURE 5.20: Graphs of the probability density functions of MAOA (s) on the CTM face for the different PV temperatures at PV distances 0.306 m and 0.416 m from the breathing zone.

Probability density distributions of the MAOA on the CTM mouth (Figures 5.21 and 5.23) and nostrils (Figures 5.22 and 5.24) are shown for the extremities of the PV distances simulated. Each graph is

displayed in two scales, global (as with Figures 5.19 and 5.20) and locally to show their differing the properties. The distributions of MAOA on the CTM mouth and nostrils show that very close to the CTM (where the breathing zone is located well inside the cone of establishment of the PV jet), the three PV temperature configurations exhibited very similar distribution functions, with air much younger (fresher) at the mouth than the nostrils and a larger range of age of air at the nostrils. With the PV slightly further away, the cooler air was more likely to be older and the warmer air had a slightly smaller range of air ages. This trend continued until the end of the cone. Outside of the jet cone, the profiles of the distribution functions for each PV temperature became more distinct and their range of air ages reduced. The difference between the age of air at the mouth and nostrils becomes less pertinent as the PV jet flow became established and entrained local air from the bulk flow.

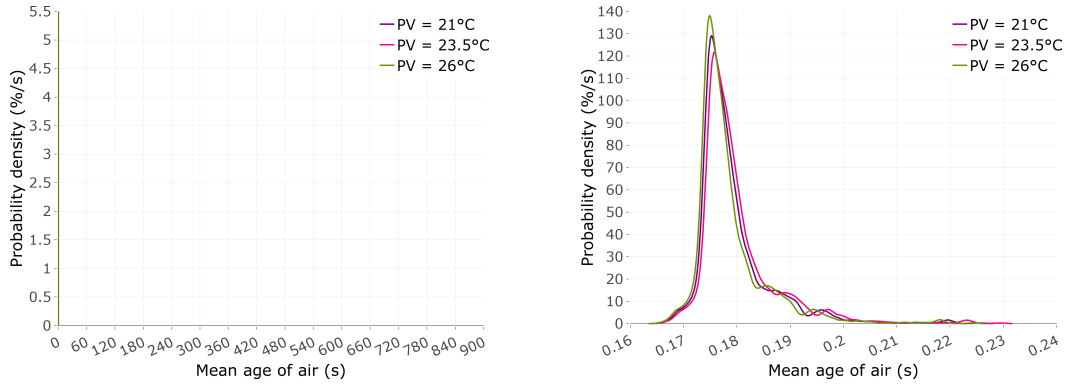

(a) Global scale. (b) Local scale.

FIGURE 5.21: Graphs of probability density function distribution for MAOA on the CTM mouth for the different PV temperatures at 0.086m, global and local scales.

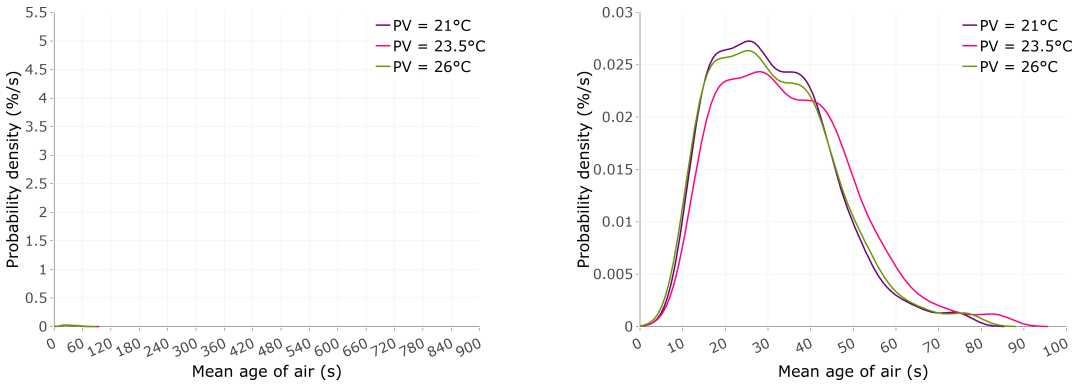

(a) Global scale. (b) Local scale.

FIGURE 5.22: Graphs of probability density function distribution for MAOA on the CTM Nostrils for the different PV temperatures at 0.086m, global and local scales.

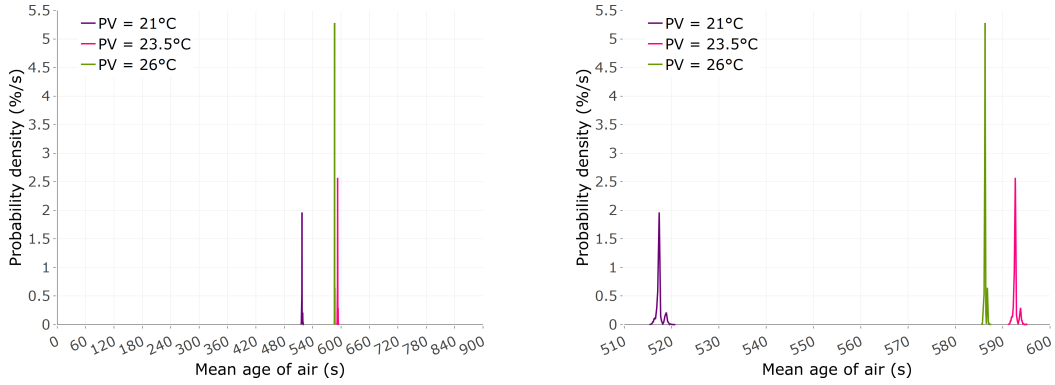

(a) Global scale. (b) Local scale.

FIGURE 5.23: Graphs of probability density function distribution for MAOA on the CTM mouth for the different PV temperatures at 0.636m, global and local scales.

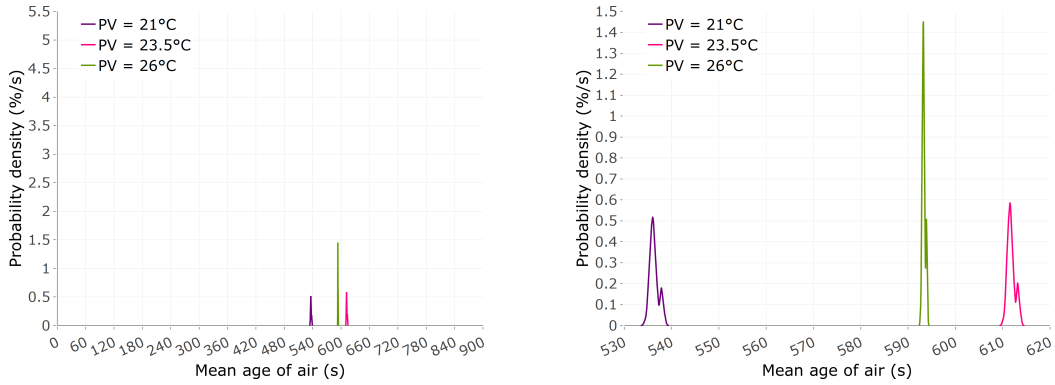

(a) Global scale. (b) Local scale.

FIGURE 5.24: Graphs of probability density function distribution for MAOA on the CTM nostrils for the different PV temperatures at 0.636m, global and local scales.

In §4.3.1 (Figure 4.16) it was noted that both the CTM and the cylinder followed the no thermal mass case very well for the velocity decay on the PV jet axis (the location of which is shown in Figure 3.57a). For the simulated MAOA value along the PV jet axis, the CTM and the cylinder matched closely to the no thermal mass case throughout the jet flow establishment, however the CTM line diverged and aged faster, although following the same trend. The graphs in Figures 5.25 and 5.26 show that these relationships hold for the CTM over the PV distances and PV temperatures simulated. The lines are only present from the PV nozzle to the CTM head and not behind the head (as in Figure 4.16) for clarity.

For all cases, the velocity decay of the PV jet with no thermal mass in the domain matches well with the different PV nozzle locations until the jet impinges on the CTM surface (Figures 5.25a and 5.26a). The cooler jet very slightly over predicts air velocity, whereas a slight under prediction occurs for the warmer jet. The differences in these cases are insignificant and comparable with experimental error. For substantial differences between the jet and the ambient room temperature, the impact on velocity may be

more pronounced.

As found previously, the MAOA of the PV jet with no thermal mass in the domain matched well with the cases for the CTM and cylinder until close to the end of the zone of flow establishment. This trend held over the simulated distances and PV temperatures (Figures 5.25b and 5.26b), although the highest PV temperature followed the no thermal mass case for slightly longer. The jet axis is defined to meet the CTM between the mouth and nostrils. Whilst the MAOA along this axis can give an indication of where to place a PV system (and where not to), the values along this line are significantly lower than the actual predictions at the CTM mouth and nostrils (Table 5.3). In reality, people move, breath and have different facial features, for example, which would all affect the age of air and air quality reaching their mouth and nose.

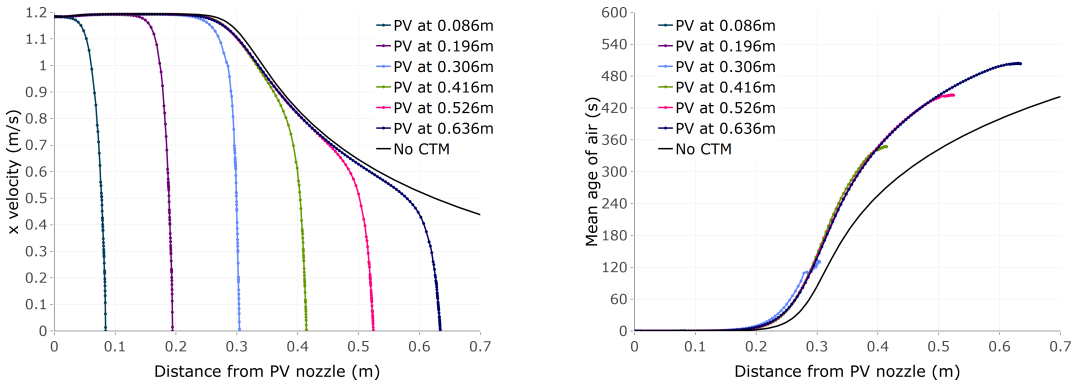

(a) x-velocity ($\mathrm{m\,s^{-1}}$) of air with distance from PV nozzle.

(b) Mean age of air (s) with distance from PV nozzle.

FIGURE 5.25: Graphs of x-velocity of air and mean age of air along the centreline comparing the different PV locations for PV = 21 °C.

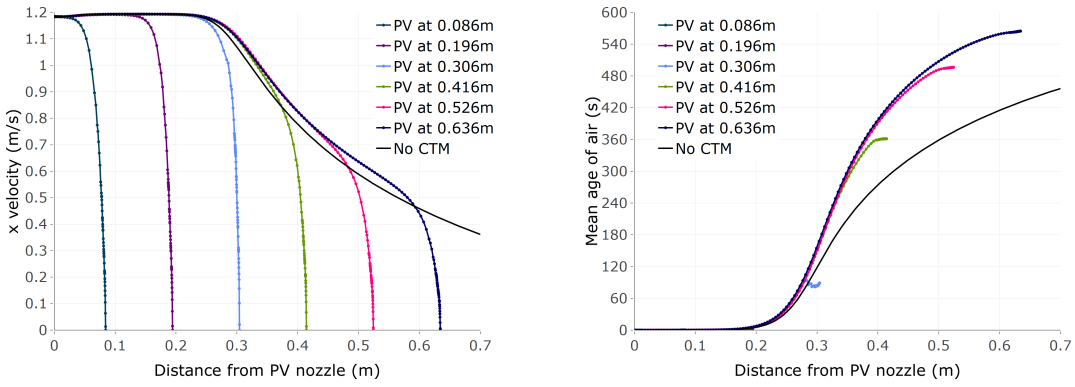

(a) x-velocity ($\mathrm{m\,s^{-1}}$) of air with distance from PV nozzle.

(b) Mean age of air (s) with distance from PV nozzle

FIGURE 5.26: Graphs of x-velocity of air and mean age of air along the centreline comparing the different PV locations for PV = 26 °C.

5.2.3 Effect of sample size

It can reasonably be expected that the values of MAOA taken from sample volumes within the breathing zone provided a more representative measure than the single data point at the end of the jet axis. Three data clouds of $2\,cm^3$, $4\,cm^3$ and $6\,cm^3$, each containing 10^3 uniformly distributed data points, were specified in the breathing zone of the CTM, centred on the plane coincident with the PV jet axis at the nozzle exit (Figure 5.27). The smallest, BZ2 (shown in red), encompassed the majority of the mouth. The middle sample, BZ4 (shown in blue), also included the nostrils. The largest, BZ6 (shown in green), had larger dimensions than the PV nozzle.

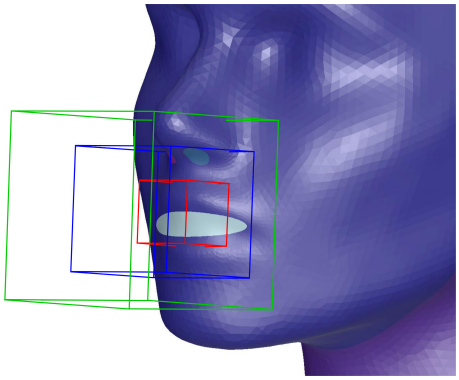

FIGURE 5.27: The three data cloud sample sizes in the breathing zone (red = BZ2, blue = BZ4 and green = BZ6).

Statistical analysis on the data cloud samples highlighted a wide variety in the mean, median and mode for the smaller PV distances within the cone of establishment, corresponding to the wide range of velocities found in these regions. Increasing the sample volume exacerbated this. The sample volume had less influence on the MAOA values (with the mean, median and mode becoming similar) as the airflow became relatively uniform (established) outside of the jet core. Within the jet cone there was little difference in MAOA due to PV temperature, however this began to have an influence outside of the jet cone with warmer air generally.

Figure 5.28 shows the mean values of the data cloud sample volumes (BZ2, BZ4 and BZ6) along with the area weighted mean values on the CTM mouth and nostrils for the extremes of the PV temperature. BZ0 is the projection of the centre of the PV nozzle on the CTM face, located at the midpoint between the mouth and nostrils. Within the jet cone ($< 0.306\,m$), mean BZ6 over-predicts MAOA, but mean BZ4 is a good predictor for nostrils and mean BZ2 for the mouth for all PV temperatures. By increasing PV distance, the sample size had less influence on the MAOA values as the airflow became more uniform outside of the ZFE. Outside of the jet cone ($> 0.416\,m$), all the sample volumes predict the mean values found at the CTM mouth and nostrils well (the mean and mode at this distance are very similar).

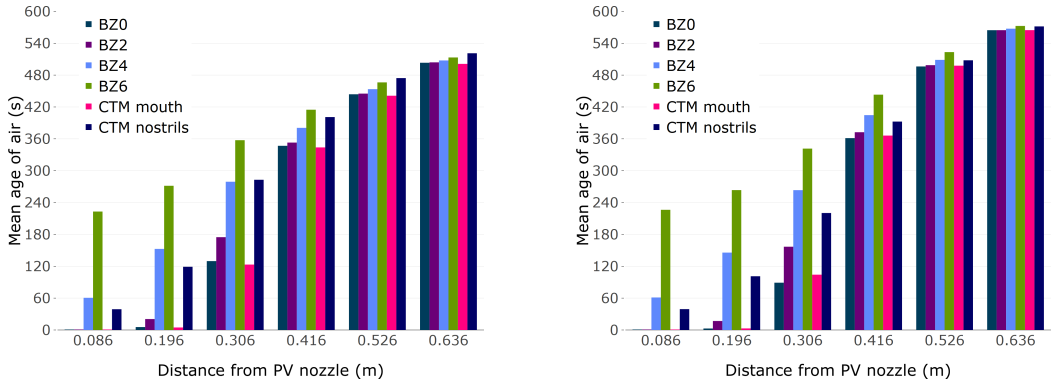

(a) PV = 21°C (b) PV = 26°C

FIGURE 5.28: Bar charts comparing the mean MAOA values at the three sample sizes with values at mouth and nostrils at the different PV distances for the different PV temperatures.

From a practical design perspective, Figure 5.26 suggests that simulations for a PV jet without a CTM can provide an indication of where to place a PV system in relation to the breathing zone and the zone of flow establishment containing the clean, fresh air. However, the bar charts in Figure 5.28 show that the value of MAOA on the jet axis (BZ0) bears little relation to the actual values at the mouth and nostrils within the flow establishment region. The graphs in Figure 5.29 show comparisons of the mean MAOA in the sample volumes BZ2 and BZ4 at distances from the PV nozzle with and without the CTM present for the case with PV = 23.5°C. In the region of established flow ($>$ 0.416 m), none of the sample sizes for the no CTM case predicted the values at the CTM mouth and nose. Within the flow establishment, BZ2 gave a good prediction of the values of mean MAOA at the mouth whilst BZ4 gave a good prediction of the values at the nostrils. This is significant as it represents a simple method at the design stage to predict air quality using a PV system without the complication of fully modelling the scenario with a CTM. Furthermore, within the zone of flow establishment, it has been shown that the jet flow form and structure varies very little between the isothermal case and small thermal variations (§3.3.4, Figure 3.15), such simulations could be simplified further without the necessity of modelling the thermal environment.

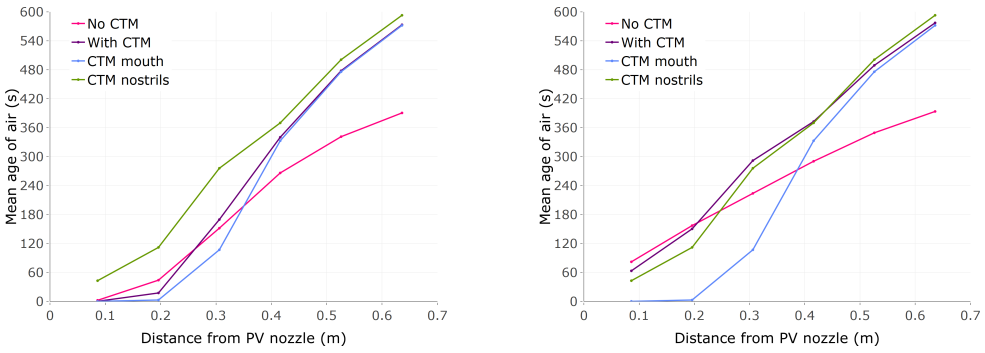

(a) BZ2 (b) BZ4

FIGURE 5.29: Graphs comparing the values of mean MAOA in different sample sizes at different PV locations, with and without a CTM, for the PV at 23.5°C.

5.2.4 Sensitivity to perturbations in domain thermal boundary conditions

It was shown in §5.1.4, by using small perturbations of $\pm 0.5\,°C$ in the domain thermal boundary conditions, that the temperature of the PV jet with respect to the ambient room temperature was the dominant thermal parameter governing the jet flow field. Furthermore, the thermal boundary conditions themselves dictated the remainder of the flow structures within the domain. Contours of velocity magnitude on the centre plane were shown for a representative case (Figures 5.15 and 5.16). The corresponding contours for MAOA are shown in Figures 5.30 and 5.31 respectively. As already shown, the MAOA was very sensitive to changes in the velocity field, with the large areas of recirculation at the front of the domain controlled by the thermal plume from the CTM. This area was more sensitive to the cooler PV jet than the warmer one.

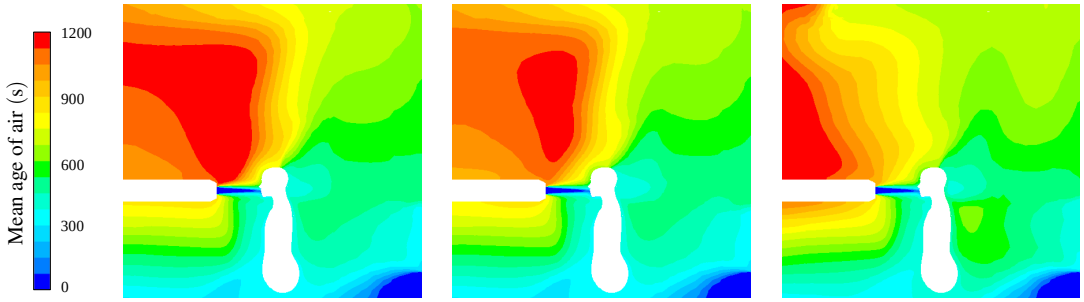

(a) BCs $-0.5\,°C$. (b) Baseline BCs. (c) BCs $+0.5\,°C$.

FIGURE 5.30: Contour plots of MAOA (s) on the central vertical plane to illustrate the effects of the perturbations to thermal boundary conditions for PV = 21 °C, 0.306 m from the CTM breathing zone.

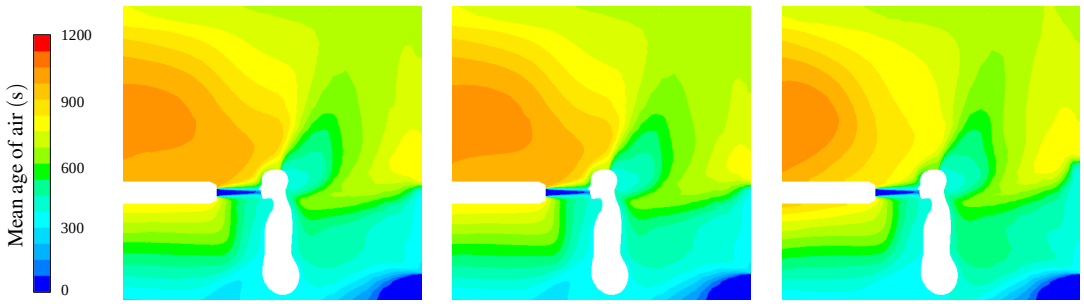

(a) BCs $-0.5\,°C$. (b) Baseline BCs. (c) BCs $+0.5\,°C$.

FIGURE 5.31: Contour plots of MAOA (s) on the central vertical plane to illustrate the effects of the perturbations to thermal boundary conditions for PV = 26 °C, 0.306 m from the CTM breathing zone.

The corresponding mean MAOA values at the mouth and nostrils are shown in Table 5.4. Small perturbations to the thermal boundary conditions in the room have a negligible effect in the areas dominated by the PV flow, such as values near the mouth, with more impact in areas affected by the entrained room air, such as the nostrils. It should be noted that this analysis does not account for breathing and the expected changes to the local flow structure, however, this beyond the scope of this research.

PV	Mean MAOA (s)					
Temperature	**Mouth**	**Nostrils**	**Mouth**	**Nostrils**	**Mouth**	**Nostrils**
21 °C	129	308	123	283	122	272
26 °C	108	214	104	220	103	197
	(BCs - 0.5 °C)		(Baseline BCs)		(BCs + 0.5 °C)	

TABLE 5.4: Mean MAOA values at CTM mouth and nostrils to illustrate the effects of the perturbations to thermal boundary conditions for different PV temperatures, 0.306 m from the CTM breathing zone.

This is also evident upon inspection of the contours of MAOA on the CTM face, where the regions surrounding the mouth and nostrils remained constant for the respective PV temperatures whilst higher up the CTM face was exposed to older air (Figure 5.32).

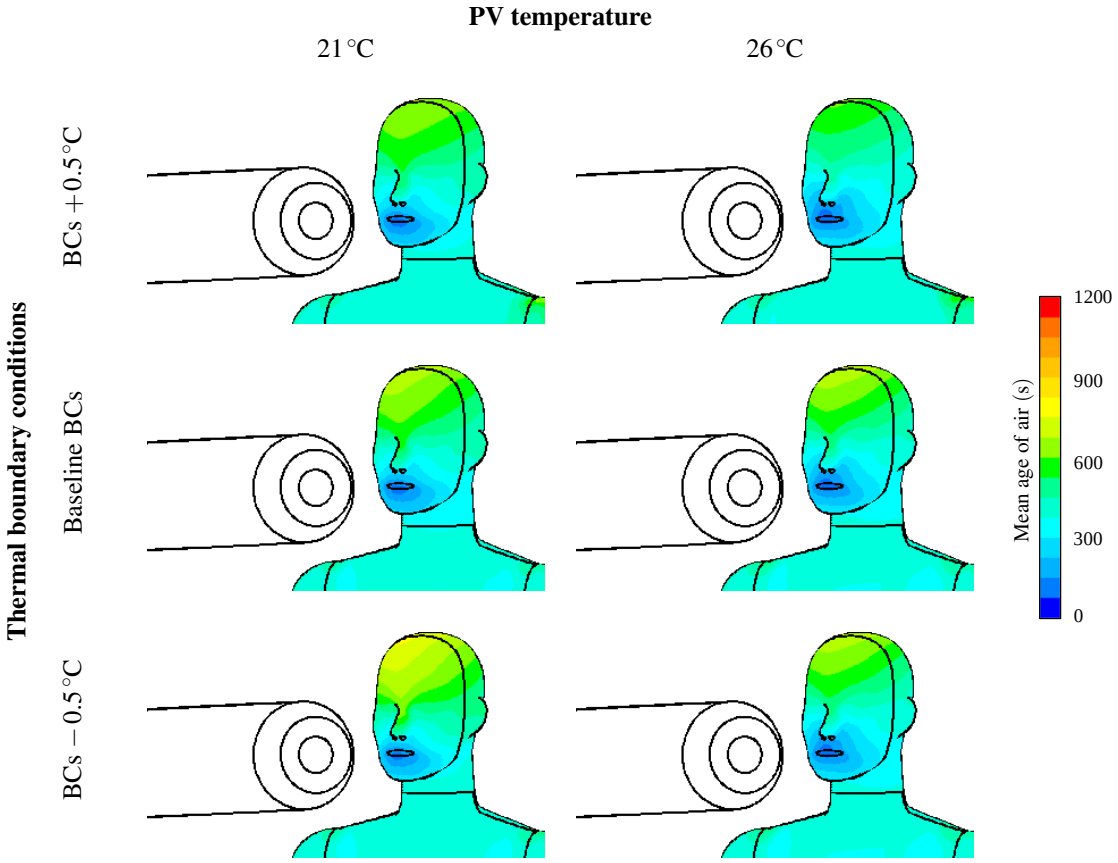

FIGURE 5.32: Contours of MAOA (s) on the CTM face to illustrate the effects of the perturbations to thermal boundary condition with the PV at 21 °C and 26 °C, 0.306 m from the breathing zone.

Within the zone of flow establishment, the values for the smaller two sample volumes (BZ2 and BZ4) varied very little with either perturbations to the thermal boundary conditions or PV temperature (Table 5.5). In the established jet flow regions, however, values of mean MAOA were effected by both variations in the thermal boundary conditions and the PV temperature, as these regions also included more of the older, entrained air (Table 5.6).

PV	Mean MAOA (s)			
Temperature	BZ2	BZ4	BZ2	BZ4
21 °C	0.164	46.8	0.151	41.4
23.5 °C	0.161	46.2	0.165	47.7
26 °C	0.159	45.3	0.160	45.9
	(BCs - 0.5 °C)		(BCs + 0.5 °C)	

TABLE 5.5: Values of mean MAOA in two different sample sizes for the different PV temperatures, 0.086 m from the breathing zone with perturbations to the thermal boundary conditions.

PV	Mean MAOA (s)			
Temperature	BZ2	BZ4	BZ2	BZ4
21 °C	502	505	498	502
23.5 °C	578	582	558	562
26 °C	559	562	572	575
	(BCs - 0.5 °C)		(BCs + 0.5 °C)	

TABLE 5.6: Values of mean MAOA in two different sample sizes for the different PV temperatures, 0.636 m from the breathing zone with perturbations to the thermal boundary conditions.

5.2.5 Summary

This section presented the air quality in the domain in terms of the mean age of air.

1. The MAOA was found to be more sensitive to the distance between the PV nozzle and breathing zone than small variations in temperature.

2. A poorly located PV jet placed in a displacement flow can cause a significant deterioration in air quality compared to no PV.

3. The local flow physics can have an impact on variations in sample volume and hence incomplete statistical analysis may be misleading.

4. Small perturbations to the thermal boundary conditions in the room have negligible effect in the areas dominated by the PV flow.

5. A PV jet without a thermal mass can be used to give an indication of the air quality in the ZFE at a breathing zone using the mean values in sample volumes of 2 cm^3 and 4 cm^3 for the mouth and nostrils respectively.

5.3 Thermal comfort

In this work, as in §4.4, thermal comfort is presented in terms of the PMV and PPD, calculated as a post-process to the simulations utilizing the modified UDF (Appendix A.1). Volume average radiation temperature was used in the calculations; with volume average relative humidity set at 50 %; clothing and activity modelled as consistent with office attire (1 clo) and energy expenditure (1 met).

Preliminary simulations (in §4.4.4) highlighted that small variations in the temperature of the air in the PV jet had an impact on the thermal comfort in regions affected by the PV jet, which is explored further in this section.

5.3.1 Thermal comfort in the domain

As discussed in §5.1.3, for the small changes in PV temperature, the overall room temperature only experienced minimal change (Table 5.1). Similarly, the PMV index in the domain did not change significantly with the variations in PV temperature or distance from the breathing zone (Table 5.7). The contours on the central vertical plane (Figure 5.33) show slight differences from the no thermal mass case (§4.4.1, Figure 4.19a), the only differences are attributable to the CTM and its impact on the PMV locally.

PV distance	**PMV index**		
from CTM	**21** °C	**23.5** °C	**26** °C
0.086 m	-0.029	-0.021	-0.015
0.636 m	-0.027	-0.019	-0.013

TABLE 5.7: Volume average PMV index in the domain for the PV distances from the CTM breathing zone and PV temperatures.

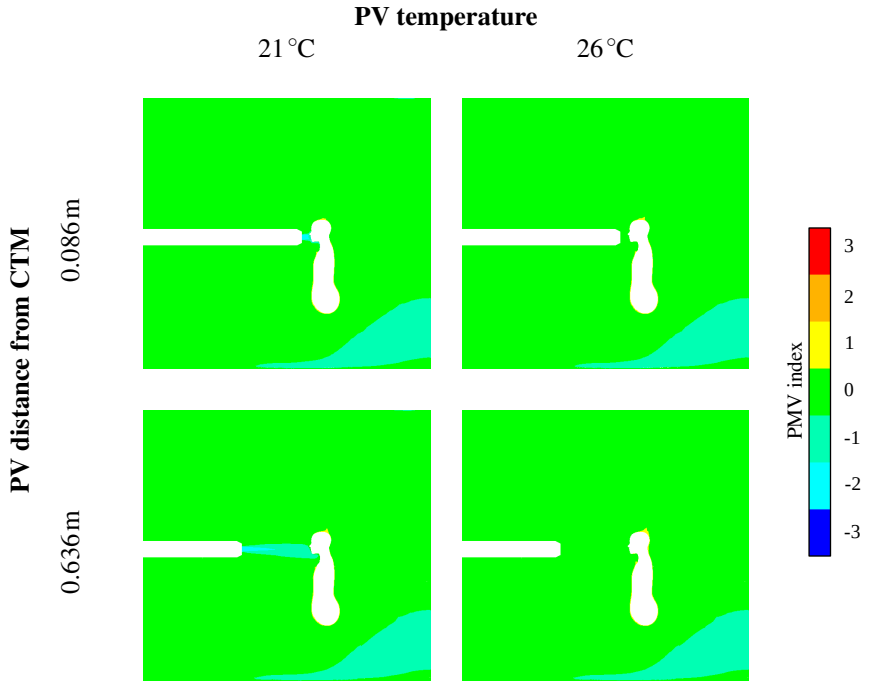

FIGURE 5.33: Contours of PMV index on the central vertical plane for the extreme PV distances and temperatures.

The same held for the PPD, as the PMV is the only variable. The contours in Figure 5.34 highlight that the only notable variations in PPD occur due to the air movement from the wall inlet and PV tube. The overall variations in PPD due to the changes in PV temperature (Table 5.8) are negligible compared to the no PV case which gave a PPD of 5.34%.

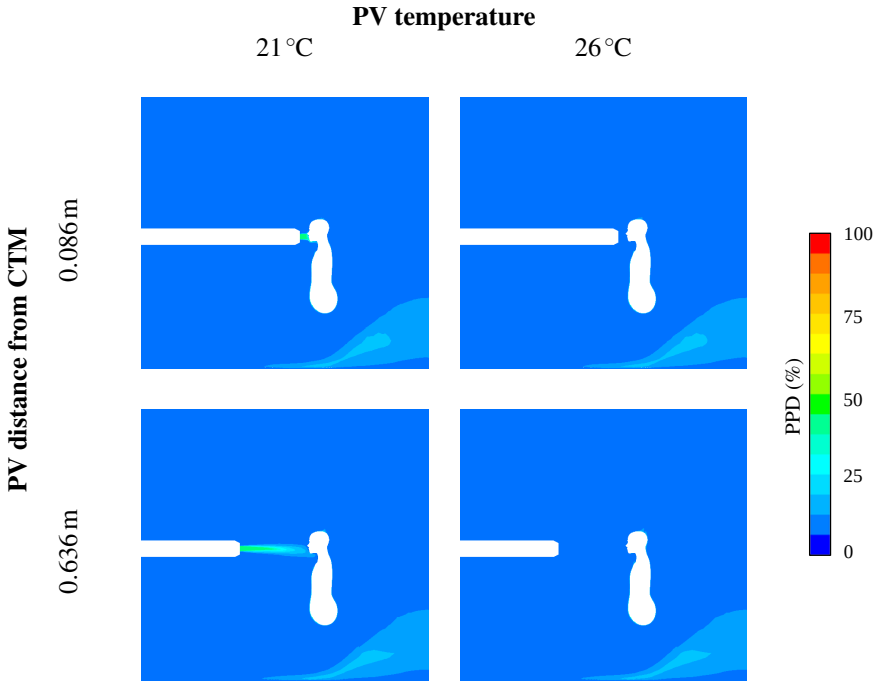

FIGURE 5.34: Contours of PPD (%) on the central vertical plane for the extreme PV distances and temperatures.

PV distance from CTM	PPD (%)		
	21 °C	**23.5** °C	**26** °C
0.086 m	5.33	5.35	5.37
0.636 m	5.34	5.35	5.37

TABLE 5.8: Volume average PPD (%) in the domain for the PV distances from the CTM breathing zone and PV temperatures.

5.3.2 Thermal comfort measurements on the CTM

Considering the CTM surface as a whole, the surface area weighted PMV values (Table 5.9) did not appear to vary much over the PV temperature and distance ranges simulated. The maximum overall change was a reduction of 3.5 % from the no PV case (PMV = 0.817) which occurred with the coolest PV flow (21 °C) at the closest distance to the breathing zone (0.086 m). The improvements to the thermal comfort reduced with both increasing PV temperature and PV distance.

PV distance from CTM BZ	Whole body PMV Index					
	PMV	% change	PMV	% change	PMV	% change
0.086 m	0.789	-3.5	0.8	-2.1	0.81	-0.9
0.196 m	0.793	-3.0	0.802	-1.9	0.811	-0.8
0.306 m	0.797	-2.5	0.805	-1.5	0.812	-0.6
0.416 m	0.798	-2.4	0.805	-1.5	0.812	-0.6
0.526 m	0.801	-2.0	0.807	-1.2	0.815	-0.3
0.636 m	0.803	-1.7	0.81	-0.9	0.817	0.0
	(PV = 21 °C)		(PV = 23.5 °C)		(PV = 26 °C)	

TABLE 5.9: Whole body PMV index and percentage change from the no PV case for the different PV distances and PV temperatures.

It was shown in §3.4.5 (Figure 3.42b) that the only areas on the CTM that changed temperature due to the PV system were those in the path of the PV flow. Contours of temperature on the surface of the CTM (Figure 5.35) show that the biggest reduction in surface temperature occurred for the coolest PV flows, more so for closer PV flows.

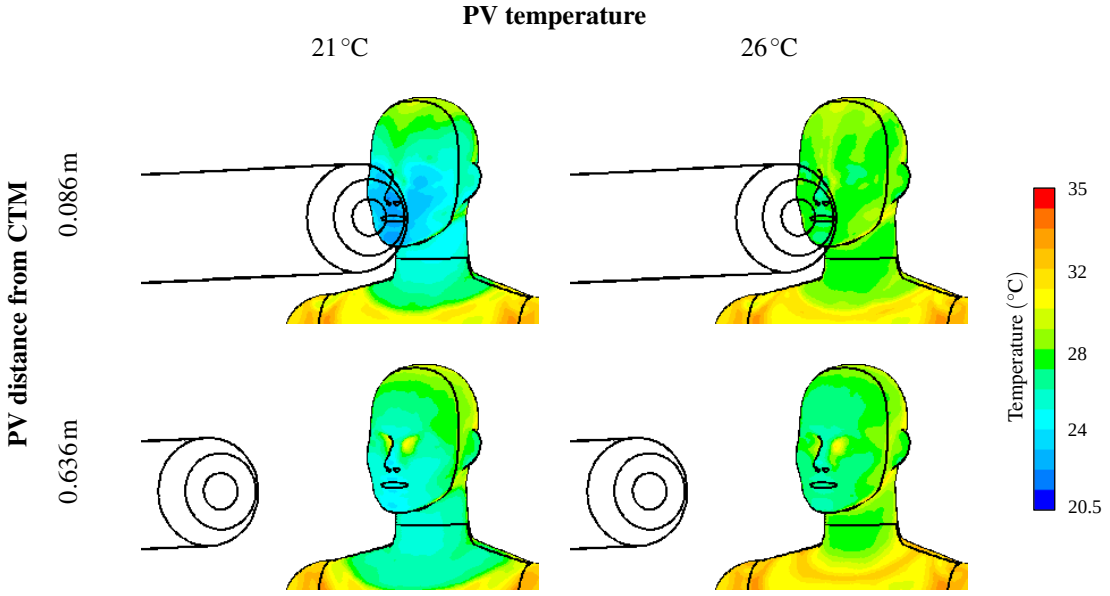

FIGURE 5.35: Contours of temperature (°C) on the CTM face for the extreme PV distances and temperatures.

Inspection of the PMV values on the constituent CTM parts (Tables 5.10 and 5.11) show that the thermal comfort metrics barely changed on the majority of the CTM body for variations in PV temperature or PV distance. Tables 5.10 and 5.11 show extremes of PV temperatures and distances to highlight the consistency in the thermal comfort metrics outside of the PV jet affected regions. As expected, the greatest variations were found around the face and head, shown in red in the tables. Lower minimum PMV values were found for the coolest PV flows, indicating that PMV is most sensitive to the PV air temperature in this environment.

	Mean	Min	Max
face	0.2	-0.8	0.7
head	0.5	-0.1	0.9
chest	0.9	0.1	1.6
back	0.8	0.4	1.7
pelvis	0.8	0.6	1.9
arm-right-upper	1.0	0.7	1.9
arm-left-upper	1.0	0.7	1.9
arm-right-lower	0.9	0.6	1.7
arm-left-lower	0.9	0.6	1.8
hand-right	0.8	0.4	1.5
hand-left	0.8	0.4	1.6
leg-right-upper	0.8	0.6	1.9
leg-left-upper	0.8	0.6	1.8
leg-right-lower	0.7	0.3	0.9
leg-left-lower	0.7	0.3	0.9
foot-right	0.5	0.1	0.8
foot-left	0.5	0.1	0.8

TABLE 5.10: PMV index on CTM. PV at 0.086m at 21°C.

	Mean	Min	Max
face	0.5	0.2	1.1
head	0.7	0.4	1.1
chest	0.9	0.5	1.6
back	0.9	0.7	1.7
pelvis	0.9	0.6	1.9
arm-right-upper	1.0	0.7	1.9
arm-left-upper	1.0	0.7	1.9
arm-right-lower	0.9	0.6	1.7
arm-left-lower	0.9	0.6	1.8
hand-right	0.8	0.4	1.5
hand-left	0.8	0.4	1.6
leg-right-upper	0.8	0.6	1.9
leg-left-upper	0.8	0.6	1.8
leg-right-lower	0.7	0.3	0.9
leg-left-lower	0.7	0.3	0.9
foot-right	0.5	0.1	0.8
foot-lefts	0.5	0.1	0.8

TABLE 5.11: PMV index on CTM. PV at 0.636m at 26°C.

Contours of PMV index on the CTM (Figure 5.36) show that there was more change in comfort due to variations in PV temperature than there was with variations in PV distance. Again, this underlines the importance of PV temperature which as greater influence on thermal comfort that the proximity of the face to the flow. The changes observed were concentrated around the face, neck, shoulders and chest, depending on the trajectory of the PV jet.

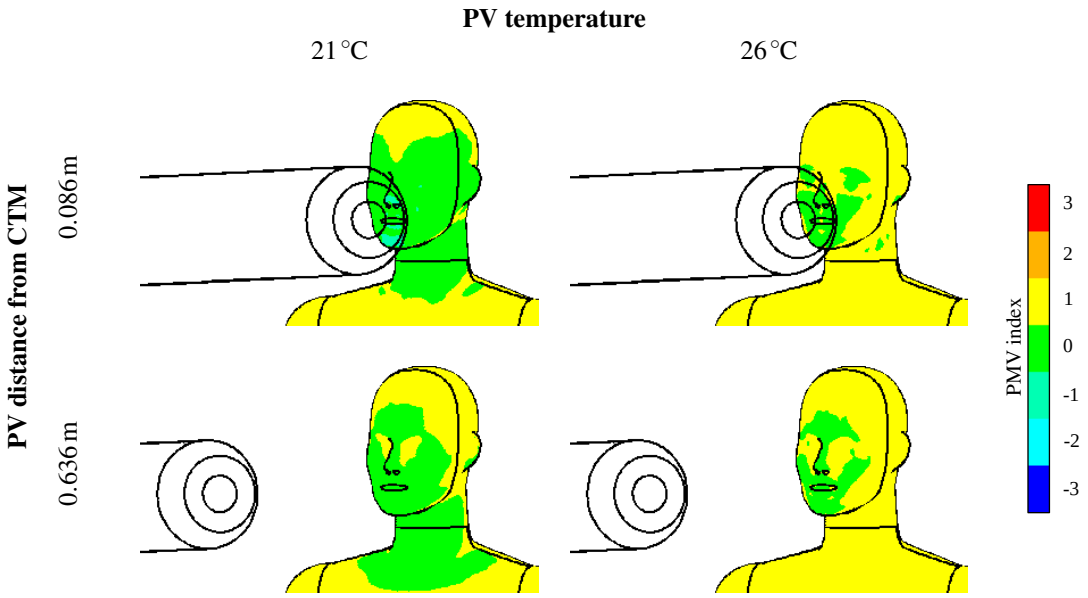

FIGURE 5.36: Contours of PMV Index on the CTM face for the extreme PV distances and temperatures.

Table 5.12 shows the improvements made in the surface PMV value on the CTM face through use of the PV. The no PV case had a PMV value of 0.759 on the face. Improvements of up to 73% can be seen for the facial PMV values. The coolest PV had a greater influence at closer ranges, however even the warmest PV generated consistent improvements of around 30 % across the PV range of distances considered. This is reflected in the lower (darker blue) PPD values predicted on the CTM surface shown in Figure 5.37.

		Facial PMV Index					
		PMV	**% change**	**PMV**	**% change**	**PMV**	**% change**
PV distance from CTM BZ	**0.086 m**	0.203	-73	0.379	-50	0.549	-28
	0.196 m	0.241	-68	0.390	-49	0.537	-29
	0.306 m	0.295	-61	0.405	-47	0.521	-31
	0.416 m	0.355	-53	0.428	-44	0.515	-32
	0.526 m	0.403	-47	0.451	-40	0.521	-31
	0.636 m	0.442	-42	0.478	-37	0.533	-30
		(PV = 21 °C)		(PV = 23.5 °C)		(PV = 26 °C)	

TABLE 5.12: Facial PMV index and percentage change from the no PV case for the different PV distances and PV temperatures.

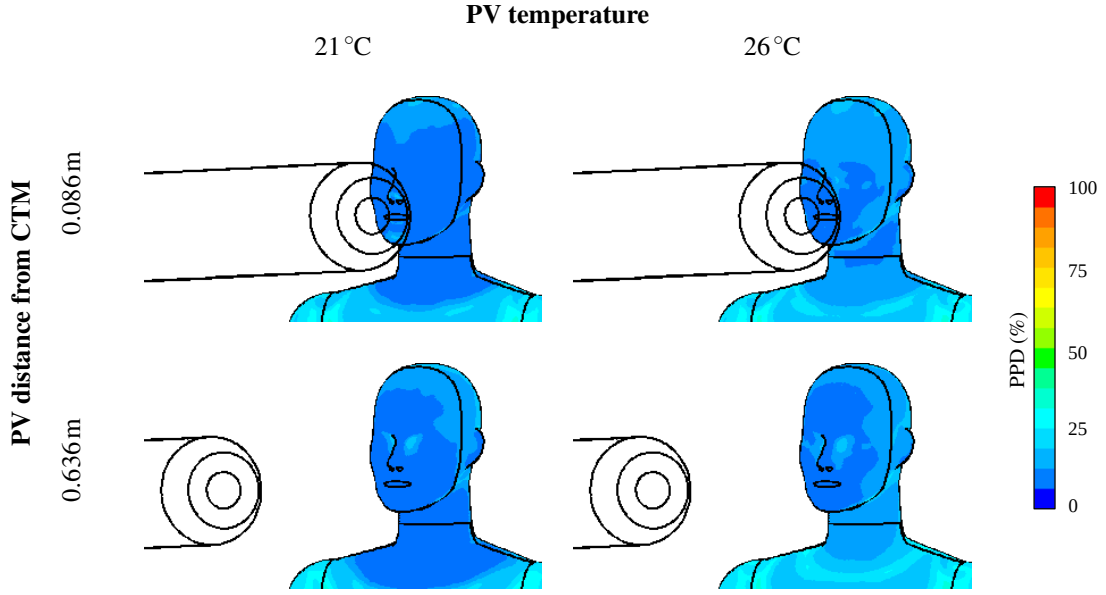

FIGURE 5.37: Contours of PPD (%) on the CTM face for the extreme PV distances and temperatures.

The distribution of PMV on the CTM face can be seen from the probability density function (Figure 5.38), weighted according to cell size as for the MAOA distribution (§5.2.2, Figure 5.19). Generally, the graphs show bimodal distributions, one mode corresponding to the areas influenced by the PV and the other mode in the unaffected region. The PMV probability distribution for PV = 26 °C was fairly consistent with 2 sharp modal peaks and a small range, which was independent of PV distance. For the PV nozzle closer to

the breathing zone, the distribution of PMV with PV = 21 °C had a larger range values, with corresponding lower probability modal values. The shape of the distribution tended towards that of PV = 26 °C as the PV distance increased.

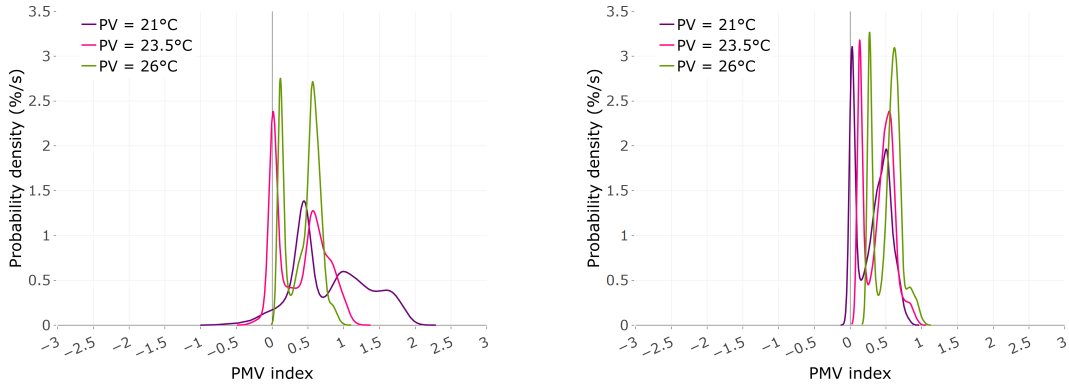

(a) PV at 0.086 m from face.

(b) PV at 0.636m from face.

FIGURE 5.38: Distributions of PMV index on the CTM face for the different PV distances and PV temperatures.

It was noted in §4.4.2 (Figure 4.26) that the profiles of PMV along the PV jet axis followed the no thermal mass case until the thermal boundary layer on the CTM face was encountered. This held true irrespective of PV temperature or distance from the breathing zone (Figure 5.39).

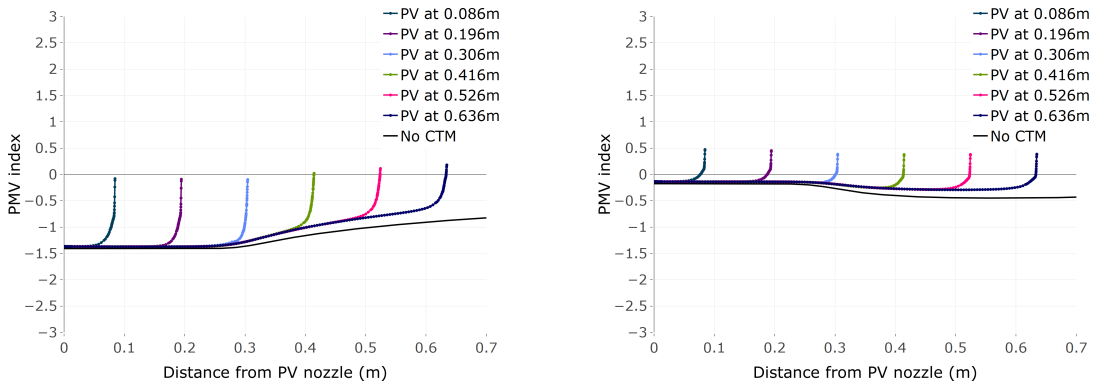

(a) PMV index with distance from PV nozzle, PV at 21 °C

(b) PMV index with distance from PV nozzle, PV at 26 °C

FIGURE 5.39: Graphs of PMV index and PPD along the centreline comparing the different PV locations and different PV temperatures.

5.3.3 Sensitivity to perturbations in domain thermal boundary conditions

Small perturbations (±0.5 °C) of the thermal boundary conditions on the computational domain affected the temperature within the domain (§5.1.4, Table 5.2), which consequently impacted the thermal comfort. Table 5.13 shows that the PMV index within the domain varied more with domain boundary perturbations than it did with larger variations in the PV flow temperature. For example, the values on the CTM surface

reduced by around 14 % for the baseline BCs $-0.5\,^{\circ}$C, with a corresponding increase of around 9 % for the baseline BCs $+0.5\,^{\circ}$C.

PV	**PMV index**					
Temperature	**Domain**	**CTM**	**Domain**	**CTM**	**Domain**	**CTM**
21 °C	-0.154	0.682	-0.028	0.797	0.054	0.872
26 °C	-0.142	0.697	-0.015	0.812	0.068	0.886
	(BCs - 0.5 °C)		(Baseline BCs)		(BCs + 0.5 °C)	

TABLE 5.13: Volume average PMV index in the domain and surface average PMV on the CTM for the perturbations in thermal boundary conditions, with the PV at 0.306 m from the CTM breathing zone.

Although the surface temperature of the CTM did not fluctuate much with the boundary perturbations (Figure 5.40), the PMV index did (Figure 5.41). As the domain became slightly cooler, the PV jet had a greater influence on the CTM face and neck, considerably more so for the cooler PV jet flow.

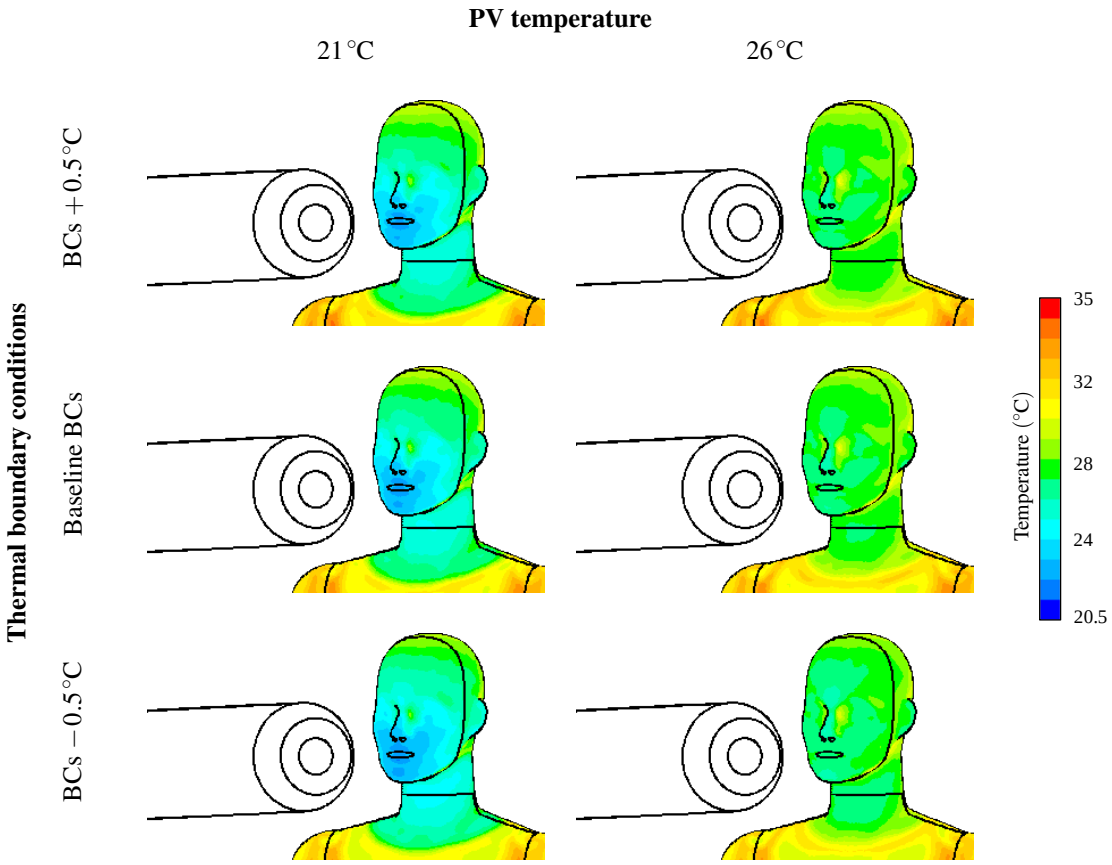

FIGURE 5.40: Contours of temperature (°C) on the CTM face to illustrate the effects of the perturbations to thermal boundary condition with the PV at 21 °C and 26 °C, 0.306 m from the breathing zone.

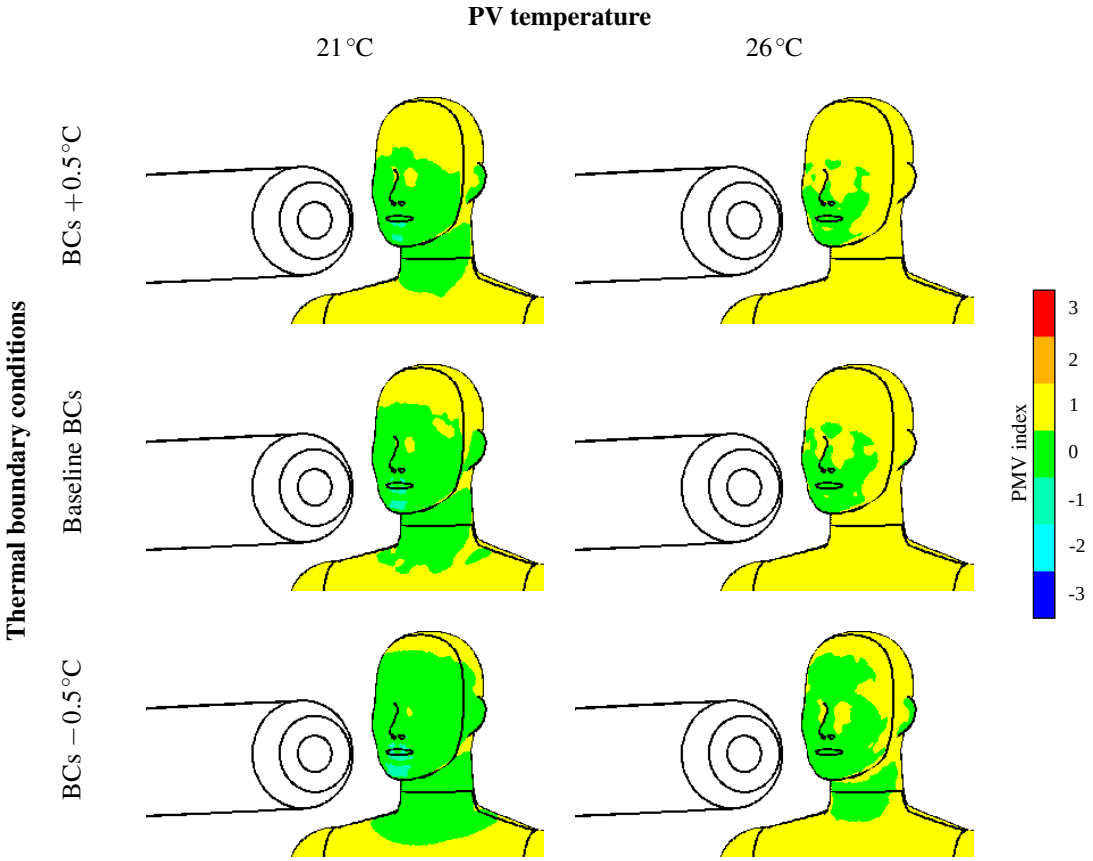

FIGURE 5.41: Contours of PMV index on the CTM face to illustrate the effects of the perturbations to thermal boundary condition with the PV at 21 °C and 26 °C, 0.306 m from the breathing zone.

5.3.4 Summary

This section discussed the thermal comfort prediction on the CTM, primarily using the PMV index. The following key observations were made:

1. Thermal comfort on the CTM only fluctuated in the regions affected by the PV flow.
2. The dominant factor in overall thermal comfort (in the domain and on the CTM surface) was the ambient conditions, prescribed by the thermal boundary conditions.
3. PMV on the CTM surface was less sensitive to PV distance than it was to PV temperature.

6. Impact of PV use in a multi-occupant environment

Contents

The work contained within this chapter explores the interactions that can occur with more than one occupant. To this end, the work considered addresses domains of different widths, with different separations between two CTM's to consider the effect this has on the airflow in the room (§6.2), the air quality in the breathing zones (§6.3) and relevant thermal comfort metrics (§6.4) for single and double PV usage.

6.1 Simulation descriptions

The baseline model with one CTM in the domain was extended widthways to cater for two CTM's and two PV systems. To keep the set-up as similar as possible between the cases, the inlet and outlet remained in the same position with respect to the first CTM and a further inlet and outlet were provided for the second CTM, accordingly. Furthermore, for all cases considered, each CTM had it's own PV nozzle, the axis of which remained aligned with the centreline of the CTM, as in the single CTM cases.

Multiple configurations were considered: two distances of PV nozzle from the breathing zone (0.306 m and 0.636 m) over five separation distances between the PV systems (0.75 m, 1.0 m, 1.25 m, 1.5 m and 1.75 m). These separation distances cover the typical range that would be encountered in shared office environments, for example. As described in earlier chapters, there are very few numerical studies that focus on multiple occupants in indoor environments. Figure 6.1 shows two of the computational domains, namely the PV nozzles at 0.636 m from their respective CTMs, spaced 0.75 m apart (Figure 6.1a) and

also for the PV nozzles at 0.306 m, spaced 1.75 m apart (Figure 6.1b). The domains ranged in width from 2.78 m to 3.78 m, keeping the CTM's the same distance from the side walls. The air change rate for each domain was kept constant at 5.13 ACH and was controlled by the rate of air through two wall inlets ($0.142\,\mathrm{m\,s^{-1}} - 0.199\,\mathrm{m\,s^{-1}}$), one immediately behind each occupant. Similarly, one outlet was positioned above each occupant, as seen in Figure 6.1. The same grid refinement zones were adhered to with respect to the CTM, PV nozzle, inlets and outlets (§3.4). This gave meshes ranging in size from 8.6 to 9.4 million cells. All other simulation parameters remained unchanged from those in Chapter 5.

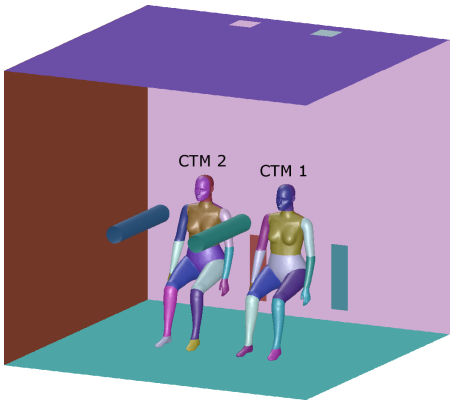

(a) PV at 0.636 m, 0.75 m apart.

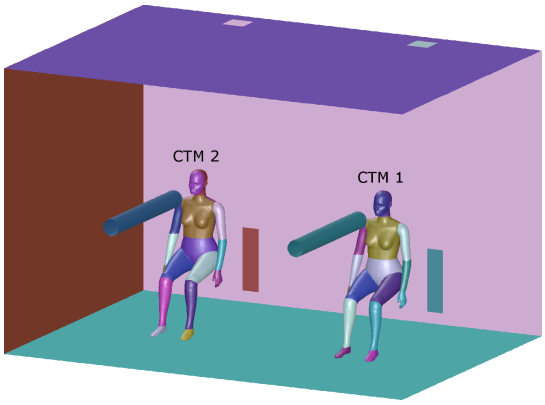

(b) PV at 0.306 m, 1.75 m apart.

FIGURE 6.1: Two computational domains for the two CTM PV simulations.

6.2 Room airflow

This section serves to illustrate the differences in flow within the computational domains described in §6.1 (Figure 6.1), comparing the two CTM cases with the equivalent single CTM cases described in previous chapters. In addition to the different computational domains, several configurations of PV flow are presented. These include no PV flow (§6.2.1), a single PV flow for single and double CTM occupancy (§6.2.2) and both PV flows at the same and differing PV temperatures (§6.2.3).

6.2.1 No PV flow

The flows from the wall inlet enter and sink as cooler denser air (Figure 6.2a). Unlike the single CTM case, despite still being located directly behind the CTM, the inlet flows are drawn to the centre of the domain and they do not remain symmetrical underneath the CTM (Figure 6.3). Instead, they merge and interact, move upwards and cause regions of constructive interference and recirculation around the lower limbs of the CTMs (Figures 6.2b and 6.4). In reality, leg movement of a person would mix this flow slightly, however it would still create a pool of cooler air close to the floor.

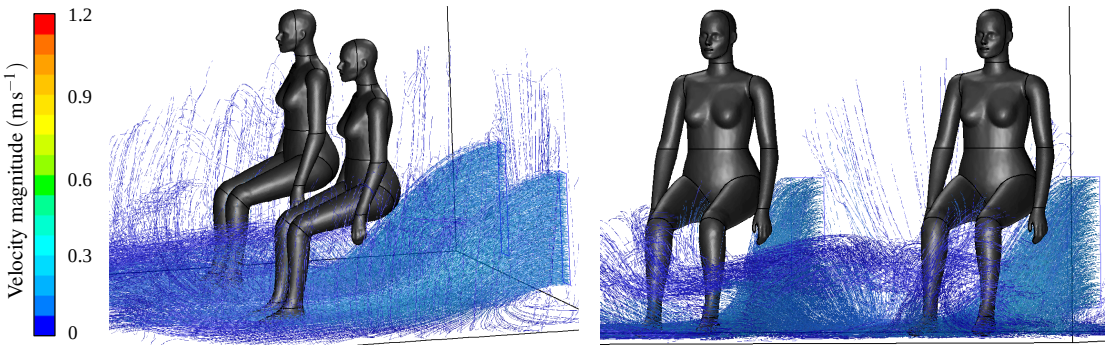

(a) Side view. (b) Front view.

FIGURE 6.2: Side and front views of pathlines coloured by velocity magnitude (m s^{-1}) released from the wall inlets with 2 CTM's, 1.25 m apart and no PV.

More disruption in the central region was found for the wall inlets closer to each other. The air from the wall inlet that did not tend towards the centre of the domain instead took a significant amount of the clean, fresh air up the side walls of the domain (Figure 6.4). As with the single CTM case, the behaviour of the air flow in the lower regions of the domain was insensitive to the presence of the PV flow higher in the domain.

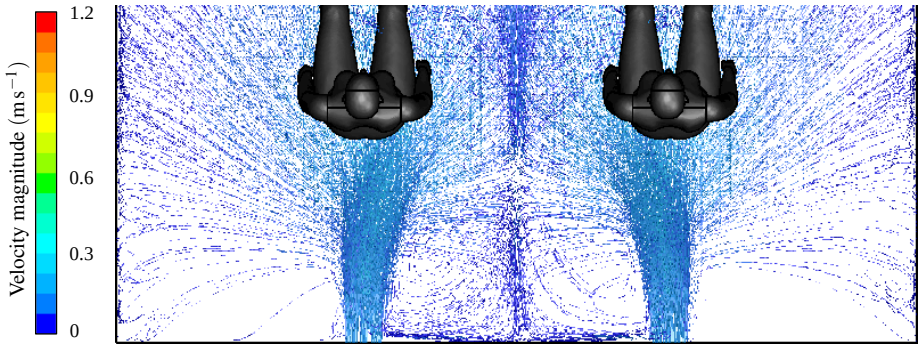

FIGURE 6.3: Top view of pathlines coloured by velocity magnitude (m s^{-1}) released from the wall inlets with 2 CTM's, 1.25 m apart and no PV.

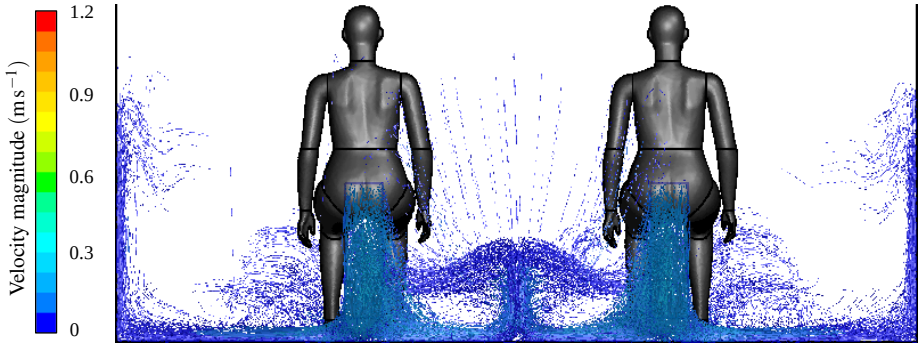

FIGURE 6.4: Rear view of pathlines coloured by velocity magnitude (m s^{-1}) released from the wall inlets with 2 CTM's, 1.25 m apart and no PV.

Without the influence of a PV system the thermal plume exhibited very nearly the same behaviour as the single CTM case (§3.4.4, Figures 3.28a and 3.30). The convective boundary layers and thermal plumes, seen in Figures 6.5 and 6.6, rose up the respective CTM's and left as thermal plumes. These plumes were not symmetric over each CTM, instead they were drawn towards each other, in the centre of the domain, as if to coalesce if given enough room height. This was exacerbated when the CTM's were closer and less pronounced when they were further apart. The air that travelled up with the plumes was then directed down towards the centre of the domain (Figure 6.6). Recirculation cells were formed, with air rising up the side walls and down in the centre of the domain.

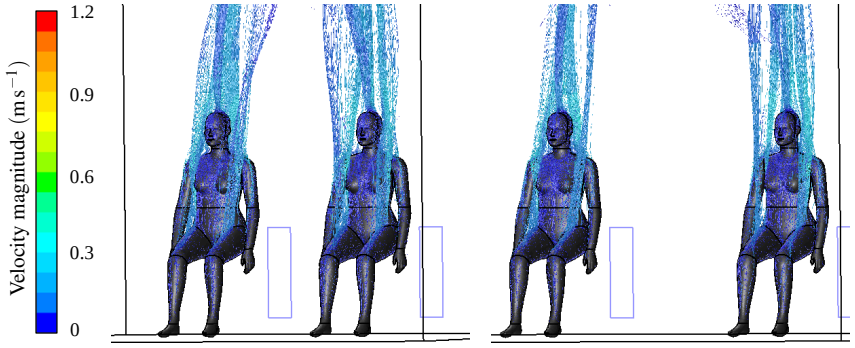

(a) 1 m apart. (b) 1.5 m apart.

FIGURE 6.5: Pathlines coloured by velocity magnitude (m s^{-1}) released from the CTM surface, with no PV.

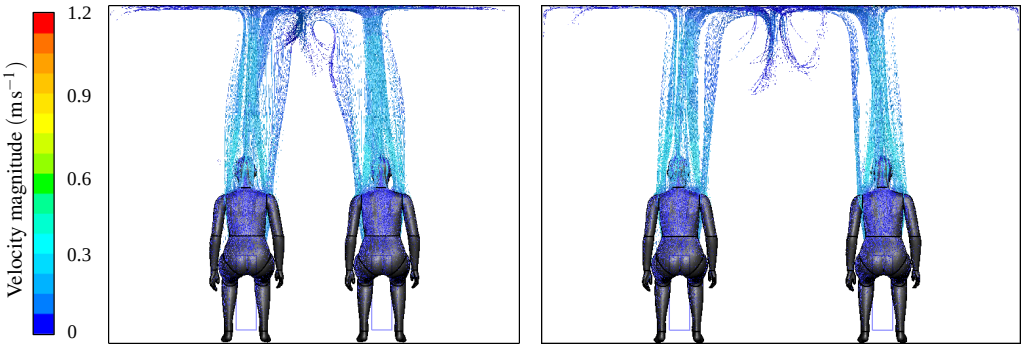

(a) 1 m apart. (b) 1.5 m apart.

FIGURE 6.6: Rear view of pathlines coloured by velocity magnitude (m s^{-1}) released from the CTM surface, with no PV.

Figure 6.7 shows contours of velocity magnitude in vertical planes in the domain for two representative cases without a PV tube, namely where the PV separations would be 1 m and 1.5 m apart. The CTMs are labelled on their torsos for identification. The features described in the pathlines above (Figures 6.2, 6.4, 6.5 and 6.6) are also evident in these contours, which show the behaviour of the wall inlet and thermal plumes.

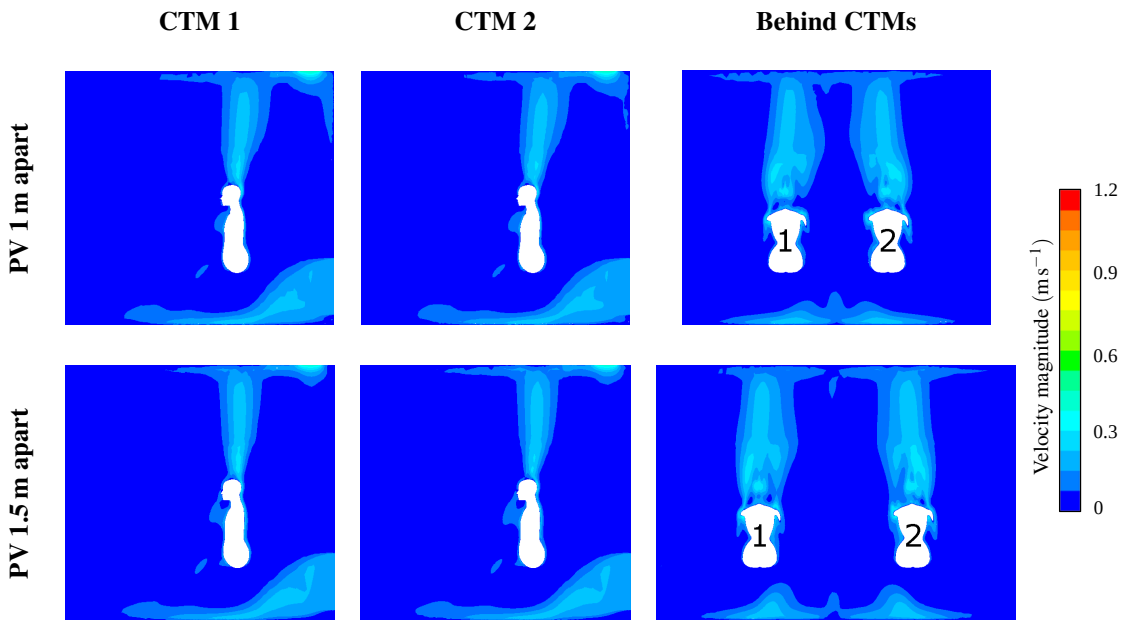

FIGURE 6.7: Contours of velocity magnitude $(\mathrm{m\,s^{-1}})$ on vertical planes in the domain for two CTM's, 1 m and 1.5 m apart with no PV flow.

The surface temperatures of the CTM were not symmetric either (Figures 6.8, 6.9 and 6.10), as they were cooler on the sides closer to the walls than they were on the surfaces nearest the other CTM (due to radiative heating). The mean surface temperature at 1 m apart (Figure 6.8b) was marginally larger all over the CTM than at 1.5 m apart (Figure 6.9b). The maximum values were more similar between the corresponding CTM body parts at 1.5 m (Figure 6.9c) than at 1 m (Figure 6.8c). However, the minimum temperature was slightly higher when the CTMs were closer together (Figures 6.8a and 6.9a). In general, the surface temperatures on the CTMs were very similar to the single case (§3.4.5, Figure 3.43), albeit without the reduction in temperatures predominantly around the face and head due to the PV flow.

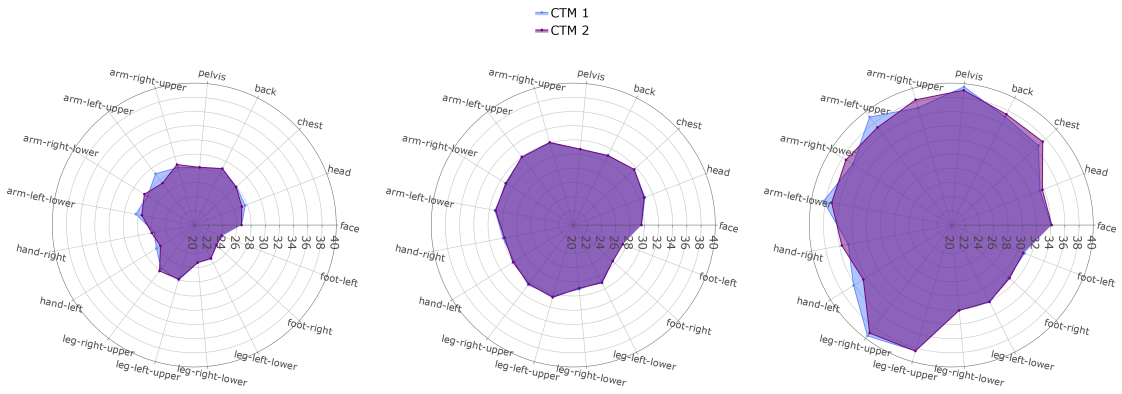

(a) Minimum value. (b) Mean value. (c) Maximum value.

FIGURE 6.8: Radar charts of the minimum, mean and maximum values of total temperature (°C) on the CTM surface for two CTM's, 1 m apart.

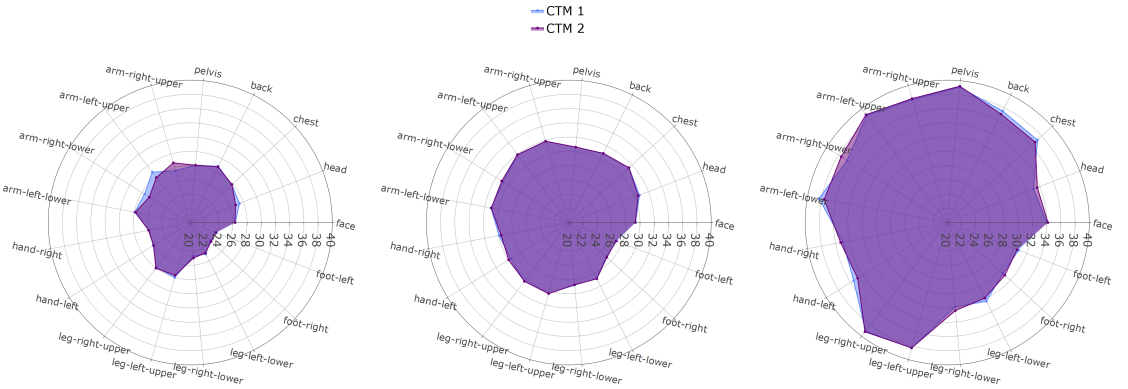

(a) Minimum value. (b) Mean value. (c) Maximum value.

FIGURE 6.9: Radar charts of the minimum, mean and maximum values of total temperature (°C) on the CTM surface for for two CTM's, 1.5 m apart.

Despite the thermal boundary layers being warmer on the CTMs facing the centre of the domain, this was the coolest region in the domain as it was furthest from the radiation emitted by the walls. It can be seen in Figure 6.10 that the wider domain was cooler with the higher stratification levels of the cooler air. The volume average temperature was marginally different in these two cases, 23.02 °C and 22.86 °C for the 1 m and 1.5 m separations respectively, either side of the 22.92 °C for the single CTM case with no PV flow.

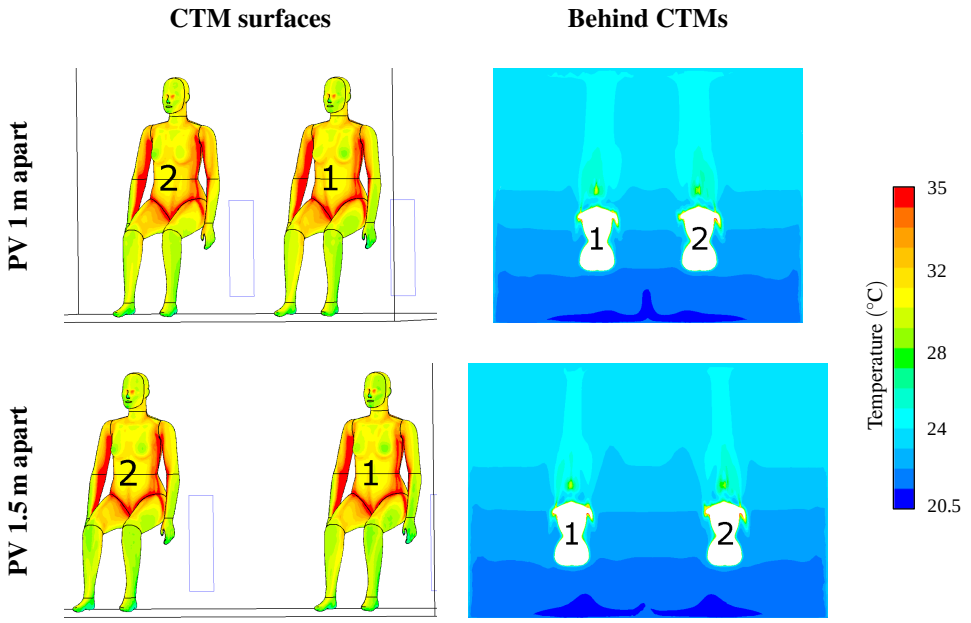

FIGURE 6.10: Contours of temperature (°C) on the CTM surfaces and on the vertical planes behind the CTMs, 1 m and 1.5 m apart with no PV flow.

6.2.2 Effect of only one PV flow

Under the influence of a single PV system at 23.5 °C, directed at CTM 1, the asymmetry in the thermal plumes was still apparent. Two distances of the PV nozzle from the breathing zone are shown in Figures 6.11 and 6.12. The first has the PV nozzle located at the end of the zone of jet flow establishment (at 0.306 m) and the second is outside this zone in the established flow (at 0.636 m). The thermal plumes under the influence of the PV jet broadly behave as expected from the single CTM case (§5.1.1, Figure 5.5), with the exception of asymmetry due to the phenomenon of the attraction between thermal plumes. Greater disruption to the plumes was found with the PV nozzle located further away from the breathing zone; this is particularly evident in Figure 6.12b.

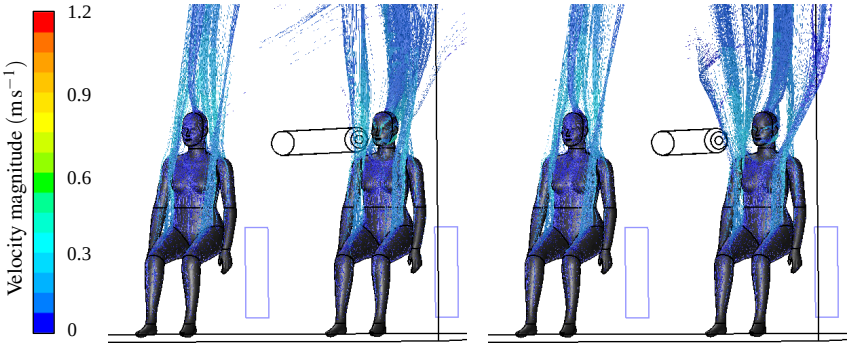

(a) PV at 0.306 m. (b) PV at 0.636 m.

FIGURE 6.11: Pathlines coloured by velocity magnitude (m s^{-1}) released from the CTM surface, with one PV flow at 23.5 °C, 1.25 m apart.

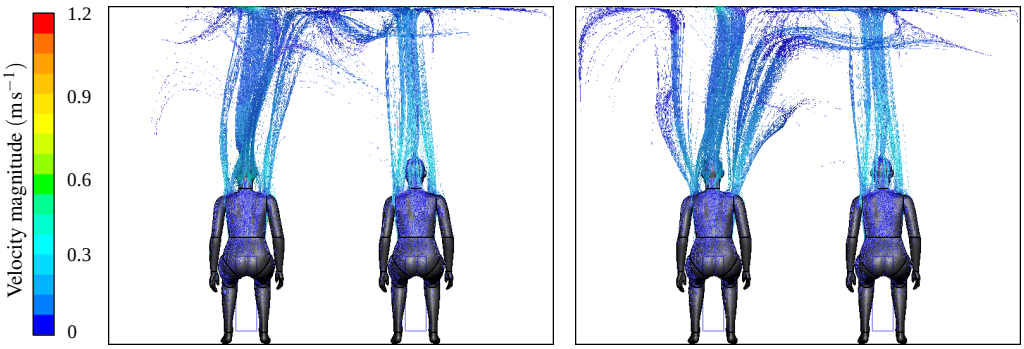

(a) PV at 0.306 m. (b) PV at 0.636 m.

FIGURE 6.12: Rear view of pathlines coloured by velocity magnitude (m s^{-1}) released from the CTM surface, with one PV flow at 23.5 °C, 1.25 m apart.

Figure 6.13 shows four representative cases, two for each of the separations shown in Figure 6.7 above (1 m and 1.5 m), which again highlight the similarities with the single CTM case (§5.1.2, Figure 5.8), albeit exhibiting asymmetry between CTM plumes. As with the no PV cases, increasing the separation distance between the CTMs reduced the impact that the thermal plume from CTM 1 had on the plume of CTM 2

(which had no PV jet). Again, the closer the proximity of the CTMs to each other, the warmer the domain was found to be (Table 6.1), albeit by only $\sim 0.25\,^{\circ}\mathrm{C}$.

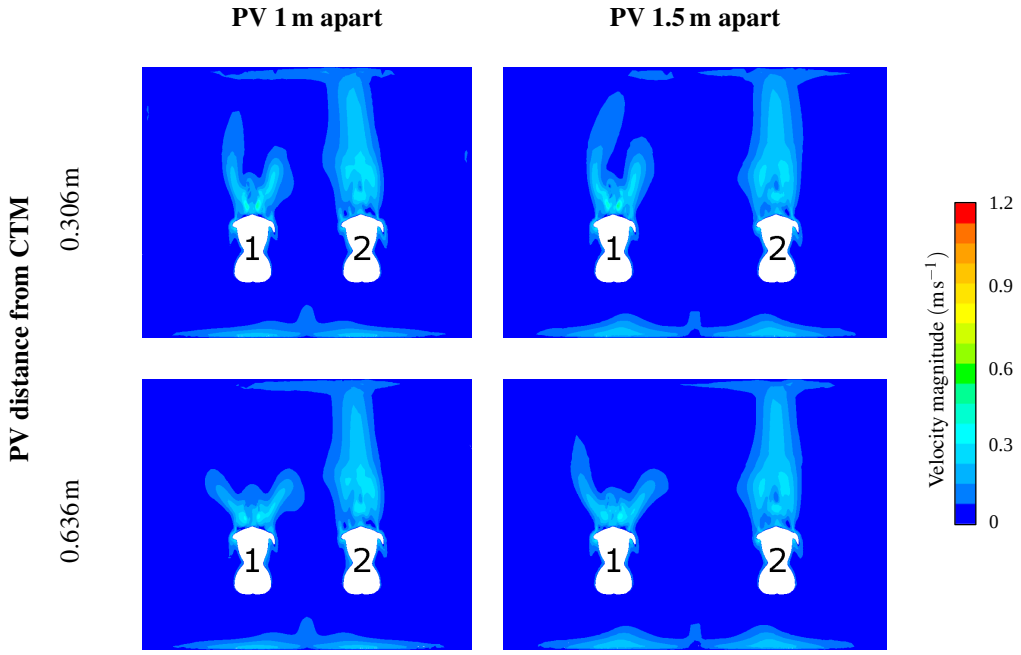

FIGURE 6.13: Contours of velocity magnitude $(\mathrm{m\,s^{-1}})$ on the vertical planes behind the CTM's head for different PV distances and separation distances, with no flow from PV 2 and PV 1 at 23.5 °C.

	Single CTM		Two CTM, PV separation	
PV distance from BZ	**No PV**	**PV 23.5 °C**	**1 m**	**1.5 m**
0.306 m	22.92 °C	23.11 °C	23.24 °C	22.98 °C
0.636 m	22.92 °C	23.12 °C	23.14 °C	22.98 °C

TABLE 6.1: Volume average room temperature (°C) for 2 CTMs, with no flow from PV 2 and PV 1 at 23.5 °C, for different PV/CTM separations.

6.2.3 Effect of both PV flows

The addition of a PV jet for CTM 2 (also at 23.5 °C as for CTM 1) led to thermal plumes (Figure 6.14) which behaved in a similar manner to the single PV case (Figure 6.13) in that they were attracted to each other. The general nature of the plumes was commensurate with that of the single CTM cases for the comparable PV distances from the breathing zone, as described earlier.

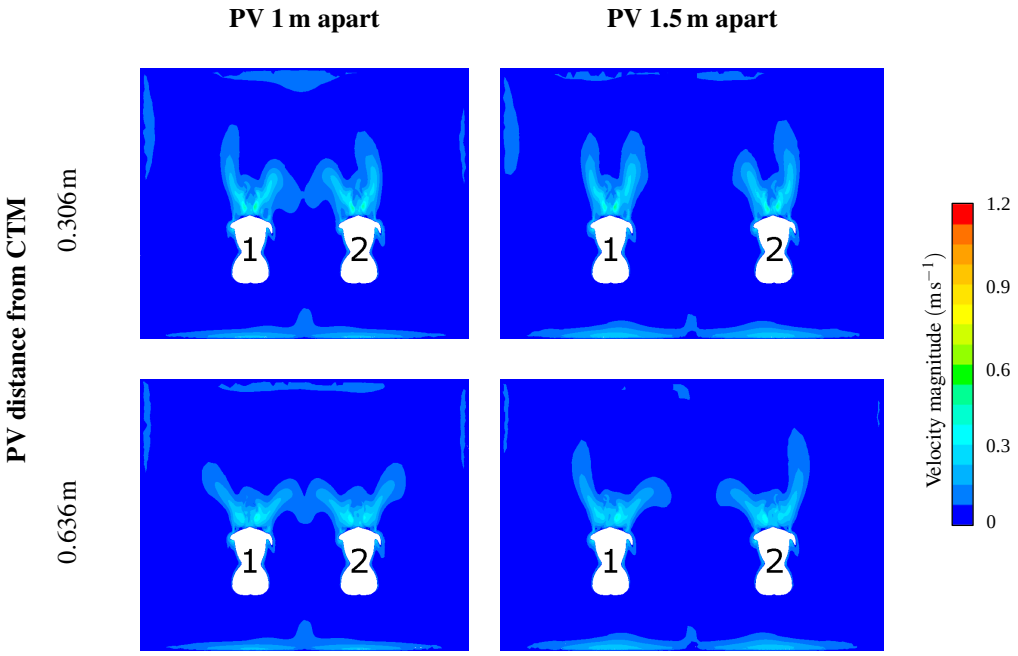

FIGURE 6.14: Contours of velocity magnitude ($m s^{-1}$) on the vertical planes behind the CTM's head for different PV distances and separation distances, with both PV flows at 23.5 °C.

As with the previous cases, the volume average room temperature decreased by between 0.2 °C and 0.3 °C with increasing distance between the CTMs and the corresponding width increase in the domain (Table 6.2). For the PV separation at 1 m apart, the domain was slightly warmer than the single CTM domain, and slightly cooler for the 1.5 m separation. These small differences have been shown to impact the trajectory of the PV jet (especially in the established flow region) and where it impinges on the CTM, in addition to the resultant thermal comfort in the domain.

		Two CTM, PV separation	
PV distance from BZ	**Single CTM**	**1 m**	**1.5 m**
0.306 m	23.11 °C	23.36 °C	23.08 °C
0.636 m	23.12 °C	23.27 °C	23.08 °C

TABLE 6.2: Volume average room temperature (°C) with 2 CTMs for different PV distances and separation distances, with both PV flows at 23.5 °C.

Another variation considered was a distinct variation in the PV air temperatures entering the domain. With the PV flow for CTM 1 set at a lower temperature (21 °C) than the PV flow for CTM 2 (26 °C), 21 °C and 26 °C respectively, the thermal plumes behaved as expected combining the knowledge from the single CTM cases and the attraction of multiple thermal plumes (Figure 6.15). Under these asymmetric conditions, the volume average temperature in the room was more uniform, irrespective of the PV separation (Table 6.3), warmer than the single CTM cases.

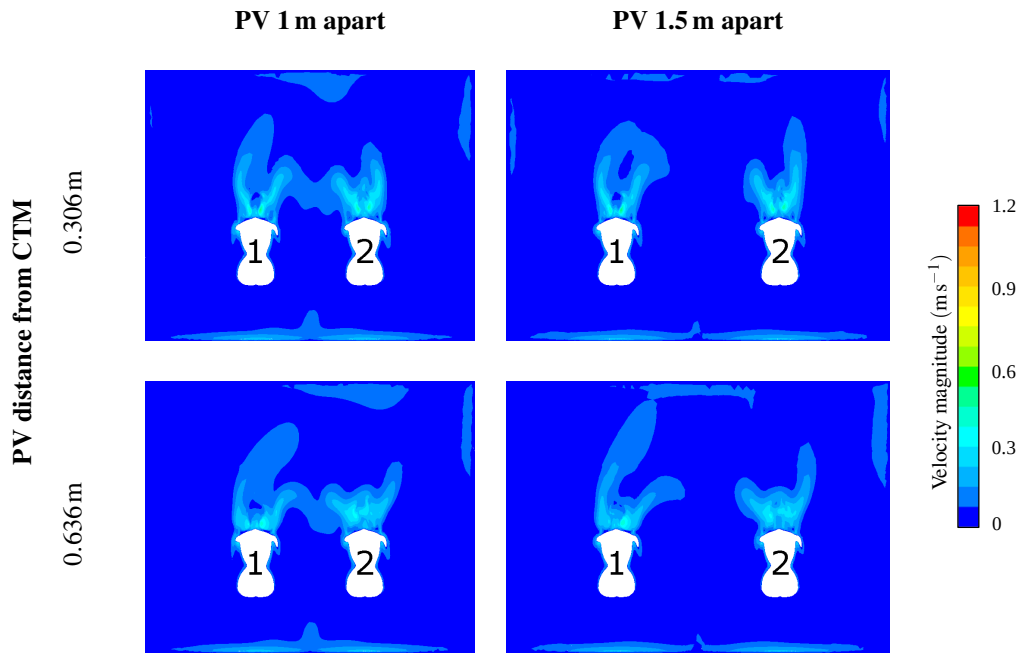

FIGURE 6.15: Contours of velocity magnitude ($m s^{-1}$) on the vertical planes behind the CTM's head for different PV distances and separation distances, with the PV 2 flow at 26 °C and PV 1 at 21 °C.

	Single CTM		Two CTM, PV separation	
PV distance from BZ	**PV 21 °C**	**PV 26 °C**	**1 m**	**1.5 m**
0.306 m	23.06 °C	23.15 °C	23.21 °C	23.25 °C
0.636 m	23.06 °C	23.16 °C	23.26 °C	23.27 °C

TABLE 6.3: Volume average room temperature (°C) with 2 CTMs for different PV distances and separation distances, with the PV 2 flow at 26 °C and PV 1 at 21 °C.

6.2.4 Summary

The main features raised in this section are highlighted below.

1. The primary source of ventilation from the wall inlets was attracted towards the centre of the domain. They interacted and caused recirculation regions around the lower limbs of the CTMs. This became less pronounced with increasing separation distance.

2. Once the air that rose with the thermal plume reached the ceiling, it was redirected down towards the centre of the domain and recirculation cells were formed, with air rising up the side walls and down in the centre of the domain.

3. Under symmetric conditions, the domains were warmer when the CTMs were closer together and cooler when they were spaced further apart. Despite only being small differences, they have been shown to impact the trajectory of the PV jet (especially in the established flow region) and where it impinges on the CTM, in addition to the resultant thermal comfort in the domain.

4. Thermal plumes were attracted to each other, which weakened with separation distance.

5. The thermal plumes behave as expected under the influence of PV and mutual attraction. This is consistent with other studies of coalescing thermal plumes.

6.3 Air quality in the breathing zones

The focus of this section is on the differences in the air quality in the breathing zone of the CTM's in the domain in the scenarios simulated in §6.2 above, comparing both CTM's in the domain with respect to the single CTM cases. As in previous chapters, the air quality is determined using the mean age of air (MAOA).

6.3.1 No PV flow

As covered in detail in the previous sections, the mean age of air is dependant on the air flow characteristic in the room, which are very different for these larger domains, and with more than one occupant. Figure 6.16 shows the contours of MAOA on the surfaces of the two CTM's with no PV flows. Generally, the distributions were comparable to the single CTM case (§4.3.1, Figure 4.12b), with fresher, younger air found near the floor of the domain and older air further up on the body. The main difference was that as the domain was widened and the separation between the CTM's (and their respective inlets and outlets) was increased, there was more younger air found around the side walls of the domain (rising from the inlet flows) and the older air was concentrated in the centre of the domain between the CTM's (after rising with the thermal plumes and redirected downwards upon reaching the ceiling), leading to an asymmetric distribution on each CTM.

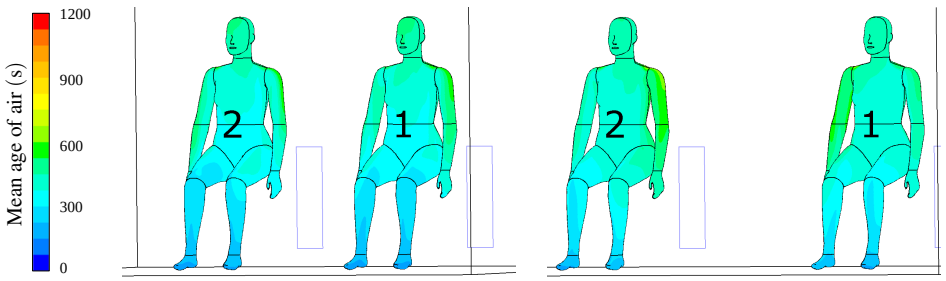

(a) PV 1 m apart. (b) PV 1.5 m apart.

FIGURE 6.16: Contours of MAOA (s) on the CTM surfaces for different PV distances, with no PV flow.

The values of MAOA found in the breathing zone (Table 6.4) were all within $\sim 10\,\%$ of the single CTM case, however they tended to be older for increased CTM separation and younger when closer together (in a correspondingly smaller domain). As previously noted, the domain was slightly warmer for closer CTM spacing and cooler when spaced further apart. Some differences were observed between the CTMs. However, for each individual CTM, similar values were found for their respective mouth, nostrils and both BZ samples.

	Mean MAOA (s)				
	Single CTM	**CTM 2**	**CTM 1**	**CTM 2**	**CTM 1**
Mouth	389	382	387	431	421
Nostrils	399	386	392	438	426
BZ2	397	385	390	435	425
BZ4	407	388	394	440	430
		(1 m apart)		(1.5 m apart)	

TABLE 6.4: Mean MAOA values at CTM mouth and nostrils for the single CTM and the two CTM cases with no PV flow.

6.3.2 Effect of only one PV flow

With one PV flow, at 23.5 °C, directed at CTM 1, the MAOA distribution on the surface of CTM 2, without PV flow, remained consistent with those found for no PV flows (Figure 6.17). CTM 1, however, had a greater variation of MAOA values around the CTM heads, irrespective of PV distance or CTM separation. Significantly older air was found near the top of the CTM 1 head, due to the disruption to the local air flows caused by the PV jet, as with the single CTM case presented previously (§4.3.1, Figure 4.14b). On the majority of the CTM bodies, the asymmetry in the MAOA distribution was still evident, where it was older in the centre and younger closer to the walls and floor. The youngest air on any CTM was found in the breathing zone with the PV nozzle closest to the CTM.

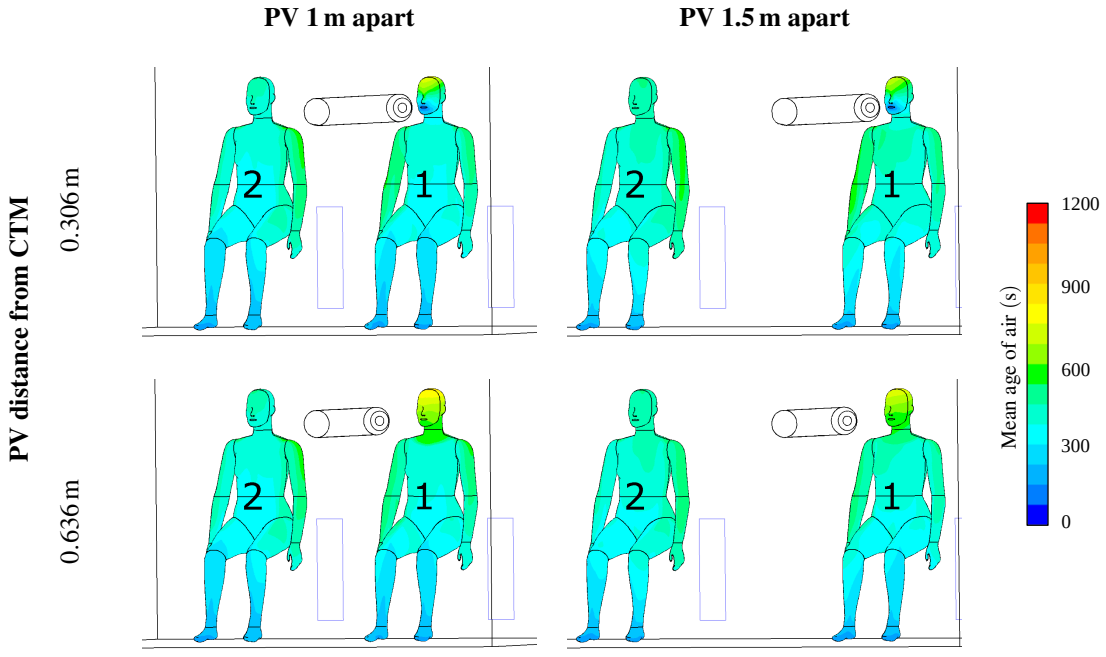

FIGURE 6.17: Contours of MAOA (s) on the CTM surfaces for different PV distances and separation distances, with no flow from PV 2 and PV 1 at 23.5 °C.

Irrespective of the PV proximity to the adjacent CTM, the MAOA in the breathing zone was broadly comparable for all CTM 2 cases and with the single CTM case with no PV flow (Tables 6.5 and 6.6). At

larger separation distances (1.5 m in the tables), the MAOA in the breathing zone for CTM 2 was actually smaller than the corresponding double no PV cases (Table 6.4), which could indicate greater mixing in the domain and therefore moving further from displacement ventilation. The values of MAOA in the breathing zone for CTM 1 are all smaller than the corresponding single case with a PV flow of 23.5 °C. The values decrease slightly with increased separation distance for the breathing zone at the end of the zone of flow establishment (Table 6.5) and are significantly less in the established flow region (Table 6.6). Given that it has already been shown that the further the PV nozzle is from the breathing zone, the greater it disrupts the flow, this supports the postulation above that the air is mixed more than pure displacement ventilation.

	Mean MAOA (s)					
	Single CTM		**CTM 2**	**CTM 1**	**CTM 2**	**CTM 1**
	no PV	PV 23.5 °C	no PV	PV 23.5 °C	no PV	PV 23.5 °C
Mouth	389	107	374	84	376	73
Nostrils	399	276	381	231	380	202
BZ2	397	170	378	136	378	124
BZ4	407	292	384	238	382	225
			(1 m apart)		(1.5 m apart)	

TABLE 6.5: Mean MAOA values at CTM mouth and nostrils for the single CTM and the two CTM cases for the PV 0.306 m from the breathing zone, with no flow from PV 2 and PV 1 at 23.5 °C.

	Mean MAOA (s)					
	Single CTM		**CTM 2**	**CTM 1**	**CTM 2**	**CTM 1**
	no PV	PV 23.5 °C	no PV	PV 23.5 °C	no PV	PV 23.5 °C
Mouth	389	572	371	538	388	487
Nostrils	399	593	378	558	392	502
BZ2	397	573	375	539	390	487
BZ4	407	577	381	529	394	490
			(1 m apart)		(1.5 m apart)	

TABLE 6.6: Mean MAOA values at CTM mouth and nostrils for the single CTM and the two CTM cases for the PV 0.636 m from the breathing zone, with no flow from PV 2 and PV 1 at 23.5 °C.

6.3.3 Effect of both PV flows

The differences of the MAOA distributions on the adjacent CTMs (and their respective breathing zones) observed in the no PV flow cases (Figure 6.16, Table 6.4) was also apparent when both PV flows were set to 23.5 °C, close to the ambient temperature in the rooms (Figure 6.18, Tables 6.7 and 6.8). In all cases, irrespective of PV proximity to the CTM, or the CTM separation, CTM 2 experienced older MAOA on the top of the head. This translated to older MAOA values in the breathing zone for CTM 2 than CTM 1. The youngest air was found with the largest separation distance between the CTMs, with the marginally cooler domain.

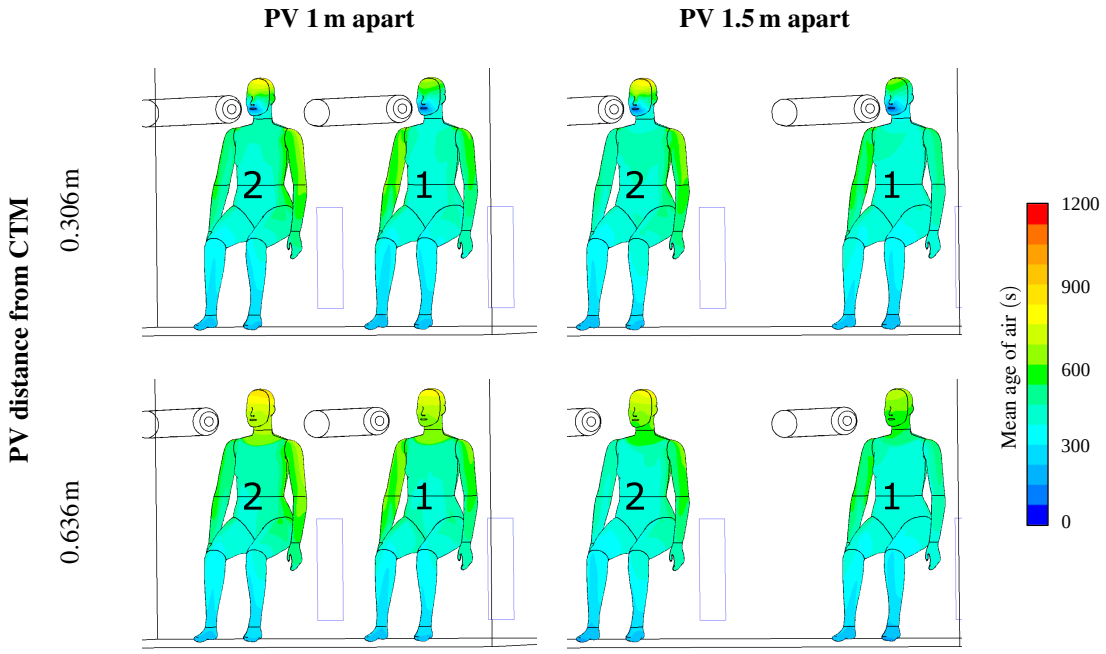

FIGURE 6.18: Contours of MAOA (s) on the CTM surfaces for different PV distances and separation distances, with both PV flows at 23.5 °C.

	Mean MAOA (s)				
	Single CTM	**CTM 2**	**CTM 1**	**CTM 2**	**CTM 1**
Mouth	107	92	77	77	66
Nostrils	276	236	202	229	185
BZ2	170	153	130	134	114
BZ4	292	269	235	243	207
		(1 m apart)		(1.5 m apart)	

TABLE 6.7: Mean MAOA values at CTM mouth and nostrils for the single CTM and the two CTM cases with the PV 0.306 m from the breathing zone, with PV at 23.5 °C.

	Mean MAOA (s)				
	Single CTM	**CTM 2**	**CTM 1**	**CTM 2**	**CTM 1**
Mouth	572	557	529	537	498
Nostrils	593	569	539	554	511
BZ2	573	558	530	538	499
BZ4	577	563	534	541	502
		(1 m apart)		(1.5 m apart)	

TABLE 6.8: Mean MAOA values at CTM mouth and nostrils for the single CTM and the two CTM cases with the PV 0.636 m from the breathing zone, both PV flows at 23.5 °C.

Introducing asymmetry to the domain in the form of PV flows at different temperatures (PV 2 flow at 26 °C and PV 1 at 21 °C) disrupted the flow patterns further. Near the ZFE, the contours of MAOA on the CTM

were not dissimilar to their single CTM counterparts (Figure 6.19). However, in the established flow (with the PV nozzle further from the CTM), differences emerged. In the single CTM cases (§5.2.2, Figure 5.18), the warmer PV flow (at 26 °C) generated the oldest MAOA on the CTM head with the PV 0.636 m from the breathing zone. In this asymmetric double CTM case it was the cooler PV flow (at 21 °C). Another contrasting feature from this example was the MAOA increasing in the breathing zone as the CTMs were spaced further apart (Tables 6.9 and 6.10), unlike the other cases considered in this chapter.

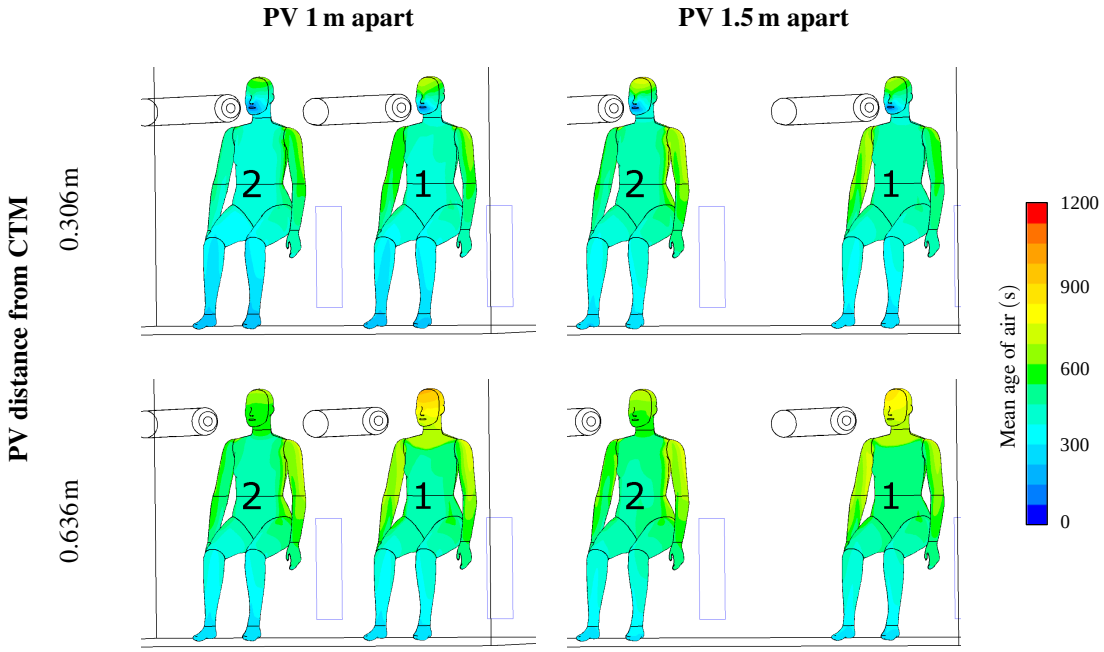

FIGURE 6.19: Contours of MAOA (s) on the CTM surfaces for different PV distances and separation distances, with PV 2 flow at 26 °C and PV 1 at 21 °C.

	Mean MAOA (s)					
	Single CTM		CTM 2	CTM 1	CTM 2	CTM 1
	PV 26 °C	PV 21 °C	PV 26 °C	PV 21 °C	PV 26 °C	PV 21 °C
Mouth	104	123	80	101	96	111
Nostrils	221	283	173	253	227	280
BZ2	157	175	128	156	158	171
BZ4	263	279	219	266	280	291
			(1 m apart)		(1.5 m apart)	

TABLE 6.9: Mean MAOA values at CTM mouth and nostrils for the single CTM and the two CTM cases for the PV 0.306 m from the breathing zone, with PV 2 flow at 26 °C and PV 1 at 21 °C.

	Mean MAOA (s)					
	Single CTM		CTM 2	CTM 1	CTM 2	CTM 1
	PV 26 °C	PV 21 °C	PV 26 °C	PV 21 °C	PV 26 °C	PV 21 °C
Mouth	565	501	422	559	508	626
Nostrils	572	521	420	584	507	648
BZ2	565	504	423	563	509	629
BZ4	567	508	425	567	512	632
			(1 m apart)		(1.5 m apart)	

TABLE 6.10: Mean MAOA values at CTM mouth and nostrils for the single CTM and the two CTM cases for the PV 0.636 m from the breathing zone, with PV 2 flow at 26 °C and PV 1 at 21 °C.

6.3.4 Summary

The following observations can be drawn from the results presented in this section:

1. The addition of a second CTM alters the flow regimes and air quality in a room.
2. Airflow, and hence air quality, in the domain was very dependant on the room geometry and inlet flows. The air quality changed not only with changes to the PV jet flow and thermal plumes, but also with separation distance between the CTMs and the room width.
3. The younger air found in comparable cases may be a result of greater mixing in the domain, moving further from displacement ventilation.
4. Increased mixing suggests that this may potentially increase contamination in the breathing zone due to mixing with the bulk flow, despite the air being younger.
5. Under identical PV conditions, consistently younger MAOA in the BZ for CTM 1 than CTM 2, which may be due to asymmetry in the laser scanned CTM used or a modelling choice, such as turbulence model used or steady state simulation. This too warrants further investigation.

6.4 Thermal comfort

As in previous chapters, the thermal comfort metric used to compare the impact of the PV flows on the surface of the CTMs was the PMV index. Previous results have shown that the wider domain PMV values changed very little with the variations in PV temperature as this metric is more dependant on the ambient temperature in the domain. The largest changes occurred on the surface of the CTM, with values shifting according to the heat loss due to the impinging PV jet flow. The results in this chapter highlight the differences between the single and the double CTM occupancy, hence only the surface PMV values are presented and discussed.

It was highlighted in §6.2 that, under symmetric conditions for each CTM, when the CTMs were close

(say 1 m separation between their centres) that the overall room temperature was warmer than the corresponding case with a single CTM. As the separation distance was increased, this temperature dropped. Furthermore, the effect of radiative heating between the CTMs was greater when in close proximity to each other (Figures 6.8 and 6.9), leading to asymmetric distribution of temperature across their surfaces. It was shown previously that both the air temperature surrounding the CTM (§5.3.3) and the surface temperature of the CTM (§4.4) are critical factors in determining thermal comfort (which would be true in what ever metric was used to predict it).

6.4.1 No PV flow

For practical purposes, the distributions of PMV index on the CTM surfaces (Figure 6.20) were very similar to the single CTM, higher where radiative heating had a greater influence (such as under the arms). Due to the large discretisation steps (integer values) between the indices, asymmetry was not readily apparent in the contours. Considering the numerical values, these again were very similar with the single CTM case, namely approaching a value of 1, meaning slightly warm (Table 6.11). There was an increase associated with the slight rise temperature in the domain with closer proximity of the CTMs.

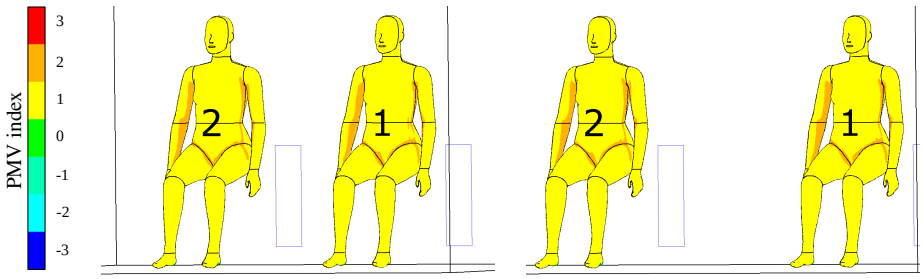

(a) PV 1 m apart. (b) PV 1.5 m apart.

FIGURE 6.20: Contours of PMV index on the CTM surfaces for different PV distances, with no PV flow.

	Mean PMV index				
	Single CTM	**CTM 2**	**CTM 1**	**CTM 2**	**CTM 1**
Face	0.757	0.809	0.807	0.783	0.783
Whole body	0.817	0.869	0.868	0.851	0.850
		(1 m apart)		(1.5 m apart)	

TABLE 6.11: Mean PMV index on CTM surfaces for the single CTM and the two CTM cases with no PV flow.

6.4.2 Effect of only one PV flow

Here, again, barely any differences were apparent from the contours of PMV index on the CTMs compared to their equivalent single cases (Figure 6.21). The distance of the PV nozzle from the CTM face made more

impact on the thermal comfort level than the separation of the CTMs. This is supported by the mean values on the CTM surfaces (Tables 6.12 and 6.13), with marginal increases due to increased room temperature when the CTMs were closer.

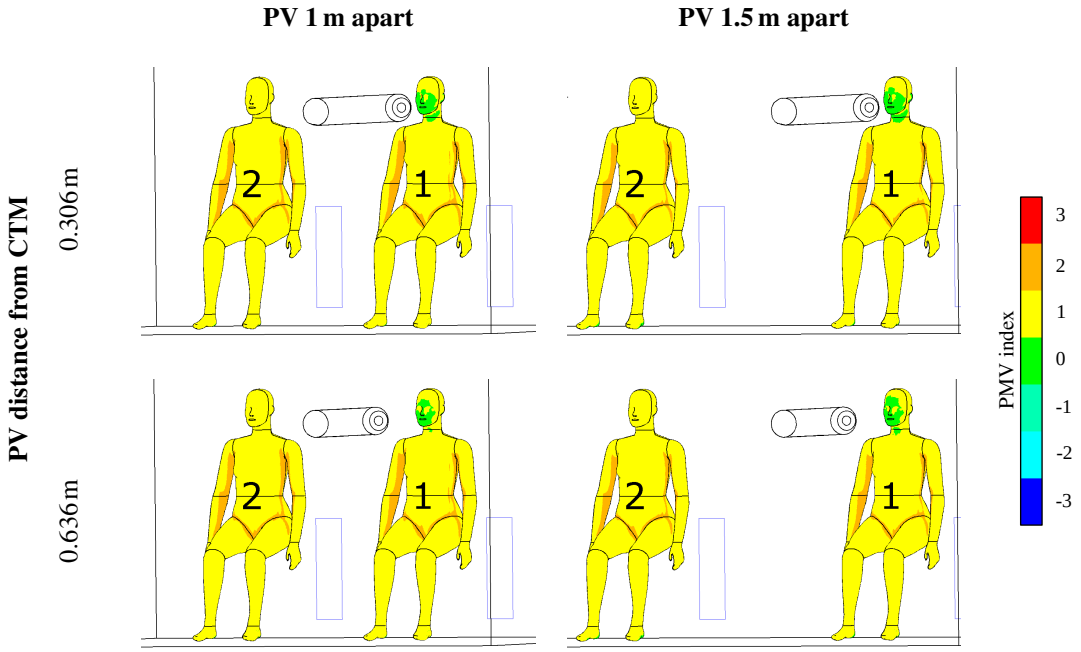

FIGURE 6.21: Contours of PMV index on the CTM surfaces for different PV distances and separation distances, with no flow from the left PV and the right at 23.5 °C.

	Surface average PMV index					
	Single CTM		CTM 2	CTM 1	CTM 2	CTM 1
	no PV	PV 23.5 °C	no PV	PV 23.5 °C	no PV	PV 23.5 °C
Face	0.757	0.405	0.815	0.448	0.767	0.411
Whole body	0.817	0.805	0.880	0.856	0.840	0.817
			(1 m apart)		(1.5 m apart)	

TABLE 6.12: Surface average PMV index on CTM surfaces for the single CTM and the two CTM cases for the PV 0.306 m from the breathing zone, no PV flow on the left and the right PV at 21 °C.

	Surface average PMV index					
	Single CTM		CTM 2	CTM 1	CTM 2	CTM 1
	no PV	PV 23.5 °C	no PV	PV 23.5 °C	no PV	PV 23.5 °C
Face	0.757	0.478	0.813	0.518	0.767	0.480
Whole body	0.817	0.810	0.876	0.857	0.839	0.822
			(1 m apart)		(1.5 m apart)	

TABLE 6.13: Surface average PMV index on CTM surfaces for the single CTM and the two CTM cases for the PV 0.636 m from the breathing zone, no PV flow on the left and the right PV at 21 °C.

6.4.3 Effect of both PV flows

Under symmetric conditions, the PMV values on both CTMs generated contours comparable to the single CTM case with the same PV flow conditions (Figure 6.22). The numerical values (Tables 6.14 and 6.15) indicate that these were slightly higher than the single CTM case and also the cases presented above where there was one PV flow with two CTMs present in the domain (§6.4.2). In all cases the higher PMV was found in the domain with a larger temperature.

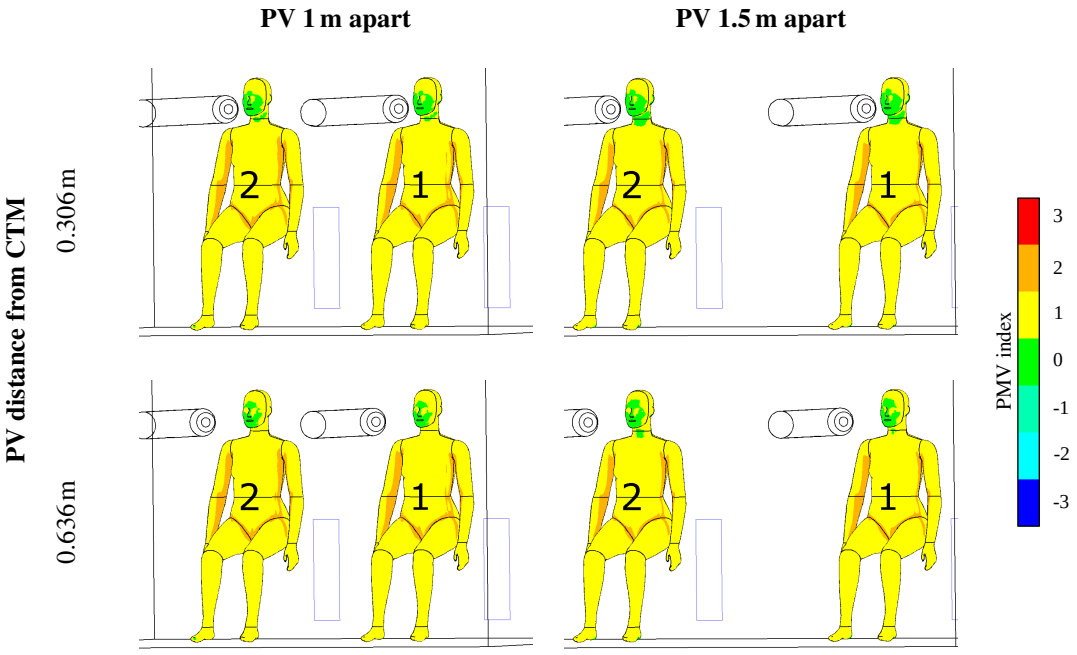

FIGURE 6.22: Contours of PMV index on the CTM surfaces for different PV distances and separation distances, with both PV flows at 23.5 °C.

	Mean PMV index				
	Single CTM	**CTM 2**	**CTM 1**	**CTM 2**	**CTM 1**
Face	0.405	0.454	0.453	0.420	0.418
Whole body	0.805	0.871	0.869	0.825	0.824
		(1 m apart)		(1.5 m apart)	

TABLE 6.14: Mean PMV index on CTM surfaces for the single CTM and the two CTM cases, with both PV flows at 23.5 °C.

	Surface average PMV index				
	Single CTM	**CTM 2**	**CTM 1**	**CTM 2**	**CTM 1**
Face	0.478	0.525	0.526	0.494	0.496
Whole body	0.810	0.868	0.867	0.830	0.831
		(1 m apart)		(1.5 m apart)	

TABLE 6.15: Mean PMV index on CTM surfaces for the single CTM and the two CTM cases with the PV 0.636 m from the breathing zone, with PV at 23.5 °C.

Under the asymmetric PV flow conditions (PV 2 flow at 26 °C and PV 1 at 21 °C), the contour plots of PMV index on the CTM surfaces again behaved as in the single CTM cases, commensurate with PV flow temperature and distance from the CTM Figure 6.23. All domains with two CTMs present were warmer than their single CTM counterparts, leading to slightly increased PMV index values on the CTM surfaces (Tables 6.16 and 6.17).

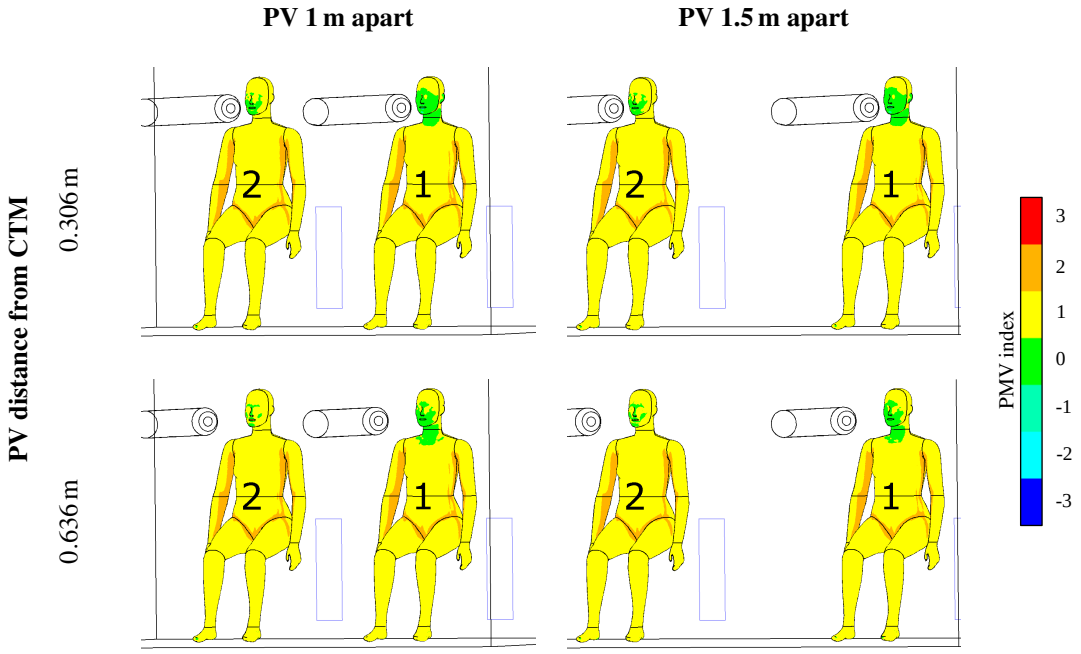

FIGURE 6.23: Contours of PMV index on the CTM surfaces for different PV distances and separation distances, with the left PV flow at 26 °C and the right at 21 °C.

	Surface average PMV index					
	Single CTM		CTM 2	CTM 1	CTM 2	CTM 1
	PV 26 °C	PV 21 °C	PV 26 °C	PV 21 °C	PV 26 °C	PV 21 °C
Face	0.521	0.295	0.570	0.341	0.548	0.315
Whole body	0.812	0.797	0.878	0.863	0.853	0.838
			(1 m apart)		(1.5 m apart)	

TABLE 6.16: Surface average PMV index on CTM surfaces for the single CTM and the two CTM cases for the PV 0.306 m from the breathing zone, with the left PV flow at 26 °C and the right at 21 °C.

	Surface average PMV index					
	Single CTM		CTM 2	CTM 1	CTM 2	CTM 1
	PV 26 °C	PV 21 °C	PV 26 °C	PV 21 °C	PV 26 °C	PV 21 °C
Face	0.533	0.442	0.580	0.508	0.559	0.484
Whole body	0.817	0.803	0.877	0.864	0.860	0.848
			(1 m apart)		(1.5 m apart)	

TABLE 6.17: Surface average PMV index on CTM surfaces for the single CTM and the two CTM cases for the PV 0.636 m from the breathing zone, with the left PV flow at 26 °C and the right at 21 °C.

6.4.4 Summary

1. PMV index was particularly sensitive to the room conditions, with an increase in domain temperature leading to an increase in PMV value.

2. The behaviour of the PMV distributions on the surface of the CTMs was consistent with the single CTM cases, allowing for variations in domain temperature and with marginal asymmetry do to radiative heating.

7. Discussion

Contents

The outcomes of the research presented in this thesis fall into two broad categories. The first is concerned with the simulation process, whilst the second are the results generated. This aim of this chapter is to relate the findings presented in Chapters 3, 4, 5 and 6 to the research aims and objectives listed in section 1.1.1, with an emphasis on filling the gaps in knowledge highlighted in the literature in Chapter 2.

The chapter begins with a brief recap of the background and the scope of the work (§7.1), addressing why the research was necessary and which aspects were focussed on. The methods used for the research are reviewed (§7.2), presenting the strategy, key themes and limitations of the simulation processes. Notable features of the general airflow in the domain is discussed (§7.3), along with the novel work pertaining to the interaction of the PV flow and the convective boundary layer. Some of the key findings concerning air quality (§7.4) and thermal comfort (§7.5) are also discussed and these were published in two conference papers [Gilkeson et al., 2018a,b]. Finally, a summary of the main research highlights are described (§7.6) before some useful modelling guidelines for indoor airflow modelling of PV systems is presented (§7.7).

7.1 Background and scope of research

As described in the background Chapter 2, personalised ventilation systems offer a means for improving indoor living by creating bespoke micro-environments [Melikov, 2004]. Achieving personalised ventilation control has the potential to improve thermal comfort, air quality and it also has the potential to minimise infection from airborne micro-organisms which can be present indoors.

It has also been shown that personal control can achieve greater comfort levels in transient conditions [Zhang et al., 2010b], however, to date there are no clear target areas or parameters guiding personalised environmental control [Parkinson and de Dear, 2017]. Furthermore, even though there are many studies

on various PV designs, to the authors knowledge, there are no clear guidelines for the design and deployment of PV systems, nor is there a widely accepted modelling process for characterising the interaction of PV flows with room air. The purpose of the work contained within this thesis was to address these gaps in knowledge by systematically investigating PV operation in small rooms through steady-state Computational Fluid Dynamics (CFD) simulations. Factors such as PV placement, PV jet temperature and the effect of room boundary conditions were all studied before considering the behaviour of PV systems for two occupants. The following subsections explore key aspects of these findings including an appraisal of the modelling approach chosen and recommendations for the simulation process itself.

7.2 Computational strategy for research

An objective of this research was to develop a suitable computational strategy for modelling personalised ventilation systems under steady state conditions, using the commercial CFD package ANSYS Fluent. Based on the findings from the literature review, it was clear from the outset that the computational approach had to cater for some challenging flow physics with the added complication of integrating radiation effects on the thermal environment.

7.2.1 Radiation

Deevy et al. [2008] and Sørensen and Voigt [2003] are amongst several authors to have observed a better correlation between room airflow CFD modelling and experimental data when radiation was accounted for, highlighting the importance of this modelling aspect, not only in thermal comfort calculations but also in the effect it has on convection and mixing of the flow. Prior to embarking on creating the computational domains to evaluate PV systems, the fundamental requirement for a representative radiation field had to be considered first. Accordingly, a benchmark validation case for radiation was considered (§3.1). The Discrete Ordinates (DO) radiation model was compared to an analytical solution of a radiation field produced within a cube, with one face heated more than the others and hence emitting more radiation. After a systematic study the DO model was found to perform well giving physical results using 5 control angles (for both polar and azimuth angles), 2 pixels per angle and 1st order upwind discretisation of the radiative transport equations.

The extra computational cost inured by increasing from 1^{st} to 2^{nd} order spatial discretisation for the radiative transport equations was not justified and all results indicated that the errors (with respect to the analytical solution) were significantly larger. As explained in section 2.4.6, the settings used with the DO model required 200 radiative transport equations to be solved per iteration. When this was implemented in the domain containing the computational thermal manikin (CTM), the effect was to increase the size of each simulation data file by an order of magnitude. A typical data file was more than 7 GB for the single CTM simulations and over 15 GB for the double CTM ones, placing large demands on the ability to post

process and analyse the results. Thus, the simulation results presented in this thesis contain radiation fields which are at the limit of what can be achieved with the meshes used and the resources available. Nevertheless, the resulting radiation fields were detailed and physical satisfying the requirement to include this important aspect of indoor airflow modelling [Sørensen and Voigt, 2003].

7.2.2 Model development

In terms of generating the flow field, the benchmark ventilation case set out by Khalifa et al. [2009] and Russo et al. [2009] was used as the basis for the model used in the results chapters. As outlined in section 3.4, the benchmark case had some complicated flow features such as swirl from a four-way floor diffuser. To isolate the PV flow (which was central to the work contained in this thesis), the floor diffuser was replaced with a low-level rectangular wall inlet and the complex outlet system was replaced with a simplified square pressure outlet on the ceiling. This produced a displacement ventilation regime which served as a background flow pattern, exploiting the effects of buoyancy where the cool inlet supply displaced the warm air above it [Chen et al., 2015], effectively separating the breathing zone from the pollutants [Liddament, 2000]. It should be noted that simplification of the benchmark domain did not affect the PV flow structure in the breathing zone. Also, the location of the outlet had little impact on flow within the domain and its influence was negligible in regions of interest in the breathing zone.

Inside the solution domain, two different manikin shapes were considered, namely an upright cylinder and a more realistic CTM based on STL data from a real scan of a thermal manikin [CFD Benchmarks, 2014]. The cylinder had an identical surface area and height as the seated CTM. This allowed for a comparison between these two manikin types in terms of their overall influence on the flow field, air quality and thermal comfort (these aspects will be discussed later). Another important element of the domain shape was the introduction of the PV nozzle. Following on from the benchmark case, the jet axis was positioned horizontally and in line with the midpoint between the nose and mouth (for cases with the CTM). To ensure a physically realistic velocity profile for the flow immediately leaving the PV tube, it was essential to significantly refine the surface mesh on the PV nozzle. Later simulations demonstrated that moving axially away from the nozzle, the velocity profiles show that the PV jet flow developed and decayed as expected, with the zone of flow establishment (ZFE) occurring within the empirically anticipated region [Albertson et al., 1950] .

7.2.3 Meshing strategy

The overall meshing strategy within the domain required high quality meshes of consistent quality and the flexibility to refine areas of interest. Therefore, a predominantly hexahedral mesh structure was used with numerous pre-defined refinement areas around walls, inlets, the outlet, the PV tube and the CTM/cylinder (§3.4.3). This mesh topology is known to exhibit less numerical diffusion than unstructured ones [Versteeg and Malalasekera, 2007] which is an undesirable and non-physical artefact, purely numerical in origin,

therefore it should be minimised as far as practicably possible. Fine mesh settings, including an inflation layer of 10 cells, were applied to the surfaces of the manikin which was essential for capturing details of the convective boundary layer (CBL) on either the CTM or cylinder surfaces (depending on the geometry studied).

The mesh settings which were taken forward throughout the results chapters were determined from a rigorous grid independence study outlined in section 3.4.8. For the single CTM cases, a fine mesh of 5.4 million cells was found to be grid independent. Results computed on the medium mesh (1.3 million cells) were qualitatively very similar to the fine mesh results, whereas the coarse mesh (382k cells) solution missed key features of the flow field such as details of the plume and particularly the PV jet. Quantitative analysis justified the decision to use the fine mesh as, this solution was the only one to capture the full length of the zone of flow establishment (ZFE) which is critical given the nature of this research. The Grid Convergence Index (GCI) [Roache, 1994, 1997, 1998a] was used to determine the discretisation error between the medium and fine grid solutions based on volume averaged total temperature within the domain. An error of 0.4% was determined which gave confidence in the mesh design.

7.2.4 Laminar-turbulence transition model

RANS simulations assume isotropic turbulence, which may not necessarily reflect reality. Pure laminar flows and established turbulent flows can be successfully modelled numerically, however regimes that exist between these extremes are more challenging to characterise and simulate. In the majority of the computational domain considered here, the air movement was very slow (mean values of $0.024\,\mathrm{m\,s^{-1}}$ and mode of $0.007\,\mathrm{m\,s^{-1}}$), with only a small region potentially experiencing fully developed turbulent flow, as defined by the Reynolds and Rayleigh numbers. To be applicable, traditional turbulence models require that turbulent flow be established, which was not the case here. Simulation software guidelines [ANSYS, Inc., 2013, 2014] advocate the use of newer models which have the ability to deal with regions transitioning from laminar to turbulent flow over low Reynolds number formulations of traditional models.

During the course of this research, the Transition SST $k-\omega$ turbulence model was found to be well-suited to capturing a range of Reynolds numbers from laminar, through the transitional range and to turbulent flow regions. This relatively new model [Langtry et al., 2006; Menter et al., 2006b] has been found to perform well in these conditions. It was successfully benchmarked against a range of experimental data for turbo-machinery and aerodynamic applications, for which the transition to turbulence is notoriously difficult to replicate [Menter et al., 2006b].

One of the test cases considered a wind turbine which operated in relatively slow wind conditions with a low free-stream turbulent intensity of 0.02%. The resulting flow field around each turbine blade was initially laminar around the leading edge before a natural transition process took place. The Transition SST $k-\omega$ turbulence model was able to replicate transition locations and overall drag with good

agreement to experimental data [Langtry et al., 2006]. More recently the same model has very closely matched the flow field from free jets impinging on a flat plate [Petera and Dostál, 2016] which is relevant to the PV jet simulated within this thesis, which impinged onto either a CTM or cylinder. One further illustration of the capabilities of this model comes from the study by Xu et al. [2017] who showed excellent agreement between numerical and experimental predictions of airflow, temperature distributions and particle deposition in the human airway.

Grafsrønningen and Jensen [2015] confirmed, using a simulated buoyant plume over a heated cylinder, that this turbulence model was not calibrated to deal with the onset of turbulence due to buoyancy, as stated in the solver guides [ANSYS, Inc., 2013, 2014]. This may have had an effect on the simulated air quality measurements in the cases without PV flow as Licina et al. [2014] found that the convective boundary layer from a seated thermal manikin transitioned from laminar to turbulent flow as it moved higher up body, entraining surrounding air into breathing zone. However, the primary purpose of the simulations in this thesis was to consider the PV flow which was the dominant flow feature in the breathing zone.

Balancing the evidence available in literature, the Transition SST $k-\omega$ turbulence model was chosen to simulate PV flows. It was found to perform reliably and consistently with good convergence characteristics.

7.2.5 Validation

As already discussed, the benchmark ventilation case [Khalifa et al., 2009; Russo et al., 2009] formed the basis of the model used in the results chapters of the thesis. One of the motivations for using this benchmark case was the availability of experimental data of the air quality index (AQI) in close proximity to a thermal manikin [CFD Benchmarks, 2014]. Results from the CFD validation (§3.2) showed that when a passive scalar was used to emulate SF_6, a good agreement of AQI was found in the breathing zone. The largest AQI value (cleanest air) in the breathing zone was replicated by CFD data and so were the AQI gradients within +/-3R from the centreline of the jet axis, where R is the PV nozzle diameter. This illustrated that the computational strategy employed in the present study was capable of modelling a PV system that potentially improved air quality within the breathing zone (which was the focus of this research). It is acknowledged that outside of the breathing zone the AQI match is poorer with an under-prediction of AQI in the CFD results, compared to experiments. However, this was mitigated by the fact that there were experimental uncertainties regarding where key SF_6 tracer measurements were taken, particularly the exhaust values which dictate the calculated AQI values [CFD Benchmarks, 2014].

In addition to air quality measurements, the velocity of the PV jet was also measured [Khalifa et al., 2009] and the CFD predictions were in very close agreement with the profile, including its decay moving further away from the nozzle. No other measurements were available to those described above but they were sufficient to give confidence that the computational approach employed throughout produces physically correct flow features.

7.2.6 Model accuracy

As described in section 2.4.1, a necessary pathway for producing credible CFD simulations is to apply the widely-accepted principles of verification and validation (V&V). Verification does not determine whether simulation outputs are correct, but it determines their accuracy and the appropriateness of the fidelity level used [AIAA, 1998]. In seeking high fidelity simulations which were accurate, firstly, the double precision version of the solver (ANSYS Fluent) was used throughout. This meant that all computations are carried out using 16 significant figures (compared to 8 s.f. for single precision) to minimise round-off errors to a negligible level. Secondly, all simulations were run for a significant number of iterations to eliminate convergence errors due to stopping simulations before they have properly converged. The third major source of numerical error in computations is discretisation error which occurs due to the finite size of the mesh used. As discussed in section 7.2.3 the discretisation error was determined to be 0.4% for volume averaged room temperature when comparing medium and fine meshes; the difference in the computed values was just 1/20th of a degree. Based on this, the fine mesh structure was deemed acceptable and used throughout this work.

Validation is the second element of V&V, where numerical model results are assessed in terms of whether the outputs are physical. As explained in section 7.2.5 above, the computational results were compared to experimental data [CFD Benchmarks, 2014; Khalifa et al., 2009; Russo et al., 2009] which was focused in the breathing zone and a good match was shown. The extent of the zone of flow establishment (ZFE) produced by the PV tube also matched known experimental data of the diffusion of submerged jets [Albertson et al., 1950]. Other physical features seen in the resulting flow fields were stratification in the domain due to the overall displacement flow, thermal plumes emanating from the CTM and the response of PV flow temperature was also physical; warmer air caused the jet to deflect upward whereas cooler air was less buoyant and so the jet deflected downwards. Overall, these flow features and the validation with experimental data gave confidence in the suitability of the modelling approach, particularly in the breathing zone.

7.3 Airflow patterns

The displacement ventilation regime dominated the airflow behaviour, especially for cases with no PV jet. In the centre of the room, the CTM interacted with the room airflow, acting as an obstacle to PV flows. In Chapters 3 and 4 two representations of a person in a small room were considered, namely an upright cylinder and a seated CTM with identical surface areas. The rationale behind using simplified models of people, such as a cylinder, cuboid or multi-block CTM, is often to reduce the computational burden, usually through less stringent mesh requirements. However, the main drawback found from using cylinders is the lack of important details in the CBL and around the body. The analysis showed that a realistically shaped thermal mass (i.e. the CTM) with natural thermal boundary conditions (i.e. heat flux) is essential

if the general flow regime in the domain is required. This is consistent with the experimental findings of Zukowska et al. [2007a] who found that detailed geometries produce thermal plumes which are distributed above the head and above the legs (in the seated position). Other authors have also highlighted accuracy problems when comparing flow fields between cylinders and CTMs, with significant differences in the flow structure and velocity distributions seen around these shapes [Nielsen, 2004] and in the breathing zone [Russo and Khalifa, 2010]. In contrast, the simplified shape of an upright cylinder leads to an unusually concentrated thermal plume which was also seen in the simulation results in this thesis. This underlines the need to use an accurate CTM shape, especially in the seated position. To the author's knowledge, no other study has used simulated PV flows with a cylinder, nor made comparisons with a more detailed geometric representation.

The convective boundary layer (CBL) is important due to the interaction with the fluid flow in the room, IAQ and thermal comfort [Licina et al., 2015c]. There are two driving forces behind the CBL and thermal plume: the velocity of the surrounding air is responsible for convective heat release and the magnitude of the temperature gradient between the body surface and the surrounding air drives the convection which is directly linked to the strength and speed of the plume generated [Voelker et al., 2014]. Although the CTM in the simulations did not specify clothing, the surface temperatures generated (with the heat flux boundary condition) were consistent with those found on the outer surface of a physical clothed manikin [Licina et al., 2014], so airflow characteristics would be closer to reality.

The airflow patterns observed in the computational domain containing the CTM were significantly altered by the introduction of the PV flows, compared to the no PV cases. In particular, the thermal plume generated by the CTM dramatically changed shape depending on the PV temperature and its proximity to the CTM face. As such, the fluid flow surrounding the heat source had a significant impact on the nature of the plume itself, which is highly sensitive to the airflow around it. This agrees with the experimental findings of Licina et al. [2015c]. In order to explore this sensitivity two parameters were varied, the PV temperature (21 °C, 23.5 °C and 26 °C), and the proximity of the PV jet in relation to the CTM (for six distances), along the jet axis. For simplicity, a constant PV jet velocity of $1.184\,\mathrm{m\,s^{-1}}$ was used based on the benchmark case [Khalifa et al., 2009; Russo et al., 2009].

In all cases, the PV jet pierced the CBL around the CTM face, redirecting and splitting the thermal plume behind it. For a given PV jet position, the PV flow temperature affected where the jet impinged on the CTM and this in turn characterised the shape of the plume. For example, a warm PV temperature of 26 °C caused the plume to impact the top of the bluff CTM face (typically the forehead) which acted as a barrier to the plume, allowing it to be more upright. In contrast, cooler jets at 21 °C descended, impacting the lower and more streamlined portion of the CTM face (such as the jaw and neck) which enabled the PV jet to push and incline the thermal plume away from the CTM. This effect was more pronounced for larger PV distances because the jet temperature has more space to take effect on its trajectory (as illustrated in

Figure 5.2). All air temperatures were cooler than the CBL and all PV flows were observed to descend immediately before impinging onto the CTM.

PV jets placed in close proximity to the front of the CTM led to enhanced recirculation where the jet interacted with the CBL. In general, warmer jets increased the energy in the plume and enhanced the resulting buoyancy forces, whereas cooler jets kept the jet lower in the room with correspondingly denser air. Overall, the temperature of the PV jet with respect to the ambient room temperature was the dominant thermal parameter concerning the PV jet trajectory. It should be noted that although the PV velocity was not varied, the range of PV jet distances studied indirectly changed the air velocity at the CTM face, depending on whether it was inside or outside the zone of flow establishment. To the author's knowledge, the sensitivity of the thermal plume shape and orientation to PV location and temperature have not been studied before and so they are new contributions to knowledge which warrant further investigation.

An interesting observation from the PV parametric study was that locating the PV system too far away from the breathing zone led to disruption to the displacement ventilation strategy. This caused a change towards mixed ventilation for the entire domain, leading to a poorer ventilation pattern overall. This is a key observation for PV system design, however, it also warrants further investigation to see if it is applicable in different settings.

The results in Chapter 6 describe the flow field when two CTMs are included in a room with the same background air change rate as for the single CTM cases and an individual PV jet, per CTM. The most interesting observation was that the two thermal plumes tended to move towards each other as they rose to the ceiling. This happened irrespective of the distance between the CTMs which was varied from 0.75 m to 1.75 m, however, the strength of this mutual attraction reduced with increasing CTM separation. These results agree with Kaye and Linden [2004] who investigated coalescing axisymmetric turbulent salt plumes in water. The effect was also investigated during World War II to see if parallel turbulent line plumes would be effective at removing fog from British airfields [Rouse et al., 1953]. Even at low heights above the ground the thermal plumes were observed to draw together ensuring that no ambient fluid remained between them. Indeed the coalescence of thermal plumes has been used to develop fog clearing systems [Kunkel, 1979] and although it is not directly relevant to this work, it illustrates a useful application of the very same effect.

The mutual attraction phenomena described above has an impact on other flow features in the room. In particular, it was found to set up a recirculation cell in the centre of the room. As the thermal plumes rose until they reached the ceiling, they were redirected downwards and mutual attraction drew them to the centre of the room. Rising air currents from the side walls contributed to this recirculation cell structure. The PV flows were largely unaffected by the mutual attraction and the resulting circulation cell.

7.4 Air quality

Computational simulations afford the luxury of being to directly measure variables of interest, something that can be limited in physical experiments. To directly ascertain any improvements made, or deteriorations caused, by the use of a PV system, the mean age of air can be simulated as a proxy for air quality. As stated in §2.2.4, local mean age of air (MAOA) is, statistically, the average time taken for fresh supply air to reach a spatial location [Chanteloup and Mirade, 2009; Meiss et al., 2013] and is effectively a direct measure of air quality [Simons et al., 1999]. MAOA was calculated as a post-process to the simulations, by solving a user defined scalar (UDS) transport equation in a user defined function (UDF). This is provided in Appendix A.1. Air was specified with a low diffusivity ($2.88 \times 10^{-5} \mathrm{m}^2\,\mathrm{s}^{-1}$), with a zero age at the inlets (representing fresh air). The MAOA predictions were directly compared across all cases and also used to determine AQI for direct comparison with the experimental data [CFD Benchmarks, 2014; Khalifa et al., 2009; Russo et al., 2009]. The MAOA distribution is highly dependent on the air velocity flow field, highlighting sensitive areas not necessarily apparent from just considering the air velocities alone. MAOA can accurately represent air quality in regions of interest, such as a PV jet and BZ. Using a simplified shape such as a cylinder can give an indication of the air quality in the BZ which is useful if details of the flow around realistic CTM's is not required. Calculating MAOA along a PV jet axis (in the absence of any thermal mass) can be used to determine the suitable placement of a PV system for improved air quality.

The MAOA was found to be more sensitive to the distance between the PV nozzle and breathing zone than small variations in temperature. As has already been alluded to, a poorly located PV jet can cause a significant deterioration in air quality compared with no PV, for the displacement ventilation regime considered. The local flow physics can have an impact on variations in sample volume and hence incomplete statistical analysis may be misleading. Small perturbations to the thermal boundary conditions in the room have a negligible effect in the areas dominated by the PV flow. A PV jet without a thermal mass can be used to give an indication of the air quality in the zone of flow establishment (ZFE) at a breathing zone using the mean values in sample volumes of 2 cm3 and 4 2 cm^3 and 4 $\mathrm{cm}^3$3 for the mouth and nostrils respectively.

The addition of a second CTM alters the flow regimes and air quality in a room. Airflow, and hence air quality, in the domain was highly sensitive to the room geometry and inlet flows. The air quality changed not only with changes to the PV jet flow and thermal plumes, but also with separation distance between the CTMs and the room width. The younger air found in comparable cases may be a result of greater mixing in the domain, moving further from displacement ventilation. Therefore, this warrants further investigation. Greater mixing may increase contamination in the breathing zone due to mixing with the bulk flow, despite the air being younger. Under identical PV conditions, consistently younger MAOA was found in the BZ one of the CTMs compared to the other. This may be due to asymmetry in the laser scanned CTM used or a modelling choice, such as the turbulence model used. This too warrants further investigation.

7.5 Thermal comfort

In Chapter 4, thermal comfort was determined as a post-process step with a UDF to determine the operative temperature, PMV and PPD values, shown in Appendices A.2 and A.1 respectively. The operative temperature metric combines the temperature and radiation fields, offering no further information pertaining to comfort levels.

Two different forms of PMV calculation were compared. The first form ("original") used the calculated radiation field at every location whilst the second form ("modified") replaced these values with the volume average radiation in the domain. The rationale behind the modification was that the Fanger's original thermal comfort equations (Equations 2.8 and 2.13) were based on single values of temperature and radiation in the room. CFD calculations, however, discretise the domain into (in these cases) millions of cells and determines the value for every cell. It has already been shown in Chapter 3 (§3.4.4) that the radiation field was a lot warmer near the CTM surface. Averaging the radiation throughout the room made the prediction more in-line with Fanger's original predictions [Fanger, 1972] rather than using a disproportionately high value near to a thermal mass.

Section 2.3 discussed at length different factors involved in thermal comfort, with sophisticated thermo-physiological models designed to be capable of dealing with localised variations in skin temperature (see §2.3.5 and §2.3.7). It is acknowledged that whilst PMV may not be considered as the best, or even perhaps the most appropriate metric to use on the CTM surface, it is one that reflects a number of relevant variables, such as a change in local air temperature and (by reduction in surface temperature using the heat flux BC) the effect of air velocity from the PV flow. Given that there are a wide range of different metrics, yielding such a wide range of predictions, and that in reality, thermal comfort a highly individual sensation (making predictions inherently difficult) [Lee et al., 2017; Schweiker et al., 2017a], a metric that reflects the important aspects was not deemed unreasonable. Furthermore, it is practical to design for an average occupant, especially given that PMV remains an international standard [d'Ambrosio Alfano et al., 2017] which is recognisable, extensively validated with known limitations, easily calculated and comparable.

There was little or no difference between the original and modified UDF's when there was no thermal mass present, or in the surrounding domain. The presence of a single thermal mass made a small difference to the overall predicted thermal comfort metrics. Irrespective of choice of thermal boundary condition or UDF, regions not dominated by the presence of thermal mass predicted same thermal comfort metric as those without a thermal mass. The original UDF over-predicted the thermal comfort metrics in the thermal boundary layer, which was exacerbated by the constant heat flux boundary condition, giving physically unrealistic predictions which propagated into the volume averaged values for the domain. This was consistent with [Farag and Khalil, 2015] who modelled thermal comfort on an aeroplane and presented data on planes in the domain showing that PMV was +3 near the surface of a CTM, giving PPD values of 100 %. Liu et al. [2013] also found elevated PPD values on the surface of

CTMs whilst investigating the thermal environment around passengers in an aircraft cabin.

The constant temperature boundary condition gave an indication of thermal comfort in ambient conditions, however it cannot be used to investigate the effects of air flow or draughts, unlike the constant heat flux boundary condition which was more physically realistic. The cylinder can give an indication of the thermal comfort at the surface of a CTM as the thermal comfort metrics are more sensitive to the thermal boundary conditions than either the shape of the thermal source or the choice of UDF. If thermal comfort is required, and local flows are involved, the heat flux boundary condition is the most suitable. A realistically shaped thermal source is required if local information is needed, for instance the values of thermal comfort metrics on a face. The modified UDF provided a compromise between the original PMV thermal comfort equation (with limited information) and the CFD calculations (with an abundance of information) and brought the PMV/PPD metrics into a more realistic range.

It was seen in Chapter 5 that the thermal comfort metrics on the CTM were fairly constant over the surface with the exception of the facial area influenced by the PV jet, were they were found to change more with PV temperature than with PV distance (and hence air velocity). This has been observed experimentally, for example by Alsaad and Voelker [2018]. The dominant factors in overall thermal comfort (in the domain and on the CTM surface) were the ambient conditions, prescribed by the thermal boundary conditions. Small perturbations to the thermal boundary conditions in the room had negligible effect in the areas dominated by the PV flow. Results from Chapter 6 strengthened the assertion that the PMV index was particularly sensitive to the room conditions, with an increase in domain temperature (from the second CTM) leading to an increase in PMV value. The behaviour of the PMV distributions on the surface of the CTMs were consistent with the single CTM cases, allowing for variations in domain temperature and with marginal asymmetry due to radiative heating. For the variations in ambient and PV air temperatures, the facial and whole body PMV values found (with the modified UDF) were consistent with those found experimentally by Yang et al. [2010] with 32 human test subjects in similar thermal scenarios (albeit with a ceiling mounted PV system). This reiterates the fact that the results obtained were physically representative.

7.6 Summary

The mean age of air was found to be more sensitive to the distance between the PV nozzle and breathing zone than small variations in temperature. A PV system located too far from the breathing zone can disrupt a displacement ventilation strategy, causing a change towards mixed ventilation for the entire domain. A poorly located PV jet can cause a significant deterioration in air quality compared to no PV, yet still improve the thermal comfort. PMV considers the thermal state for the whole body, other methods may be used to determine local thermal comfort which may important, depending on local sensitivities such as the face. Irrespective of this, achieving thermal comfort and improving perceived air quality (through greater air movement around the face and breathing zone due to the PV jet flow) does not guarantee actual

improvements in air quality where the fresh supply air reaches the breathing zone.

For the cases with two CTMs the flow field in the domain exhibited the additional feature of the thermal plumes being attracted to each other. In combination with the wall inlet and PV flows, this set up two large circulation cells which drew air from the sides of the room towards the centre. Fundamentally, there was little difference to thermal comfort when compared with the single CTM cases. However, higher temperatures were seen on the sides of each CTM which were facing each other which was due to radiative heating. It was found that personalised ventilation had much more of an impact on air quality than it did on thermal comfort. This is because air quality is largely dependent on the airflow structure, whereas thermal comfort is influenced substantially more by radiation, for the air speeds and temperatures considered in this study. It was observed that the PV flow for one occupant had more impact on the air quality for another occupant than it did on their thermal comfort.

7.7 Some guidelines for setting up CFD simulations with personalised ventilation

The discussion has so far largely focussed on the significant elements of results from the work contained in this thesis. Through the process of obtaining these results, many crucial aspects relating to the simulation process itself were also found. These are presented as a helpful framework depicted in the flow chart in Figure 7.1. The chart shows that if thermal comfort metrics are not required then a thermal mass is not necessary, as the presence of a thermal load increases the ambient temperature (and radiative temperature) in the domain which is the dominant factor in the PMV calculation. The original UDF to calculate PMV gave the same prediction as the modified one (which used the volume averaged radiative temperature) when there was no thermal mass present. The radiation field close to a heat source was found to artificially increase the PMV metrics, which was mitigated by using the modified UDF.

The remaining questions concern the geometric shape and boundary conditions of the thermal mass. If draughts, or localised airflows such as PV ventilation, are included in the simulation process then the heat flux boundary condition should be employed. If this is not the case then the less realistic constant temperature boundary condition is sufficient to give an indication of the thermal comfort metrics. The final question relates to the importance of room airflow. If details of the flow are unimportant then as simple shape, such as a cylinder, can be used which has the benefit of less computational cost with less complicated meshes, for example. If, however, the flow patterns in the domain are required, then a representative shape like a CTM must be employed to capture important flow features. A logical extension of this would be to include other important features such as furniture and other obstacles in the context of personalised ventilation airflow simulations.

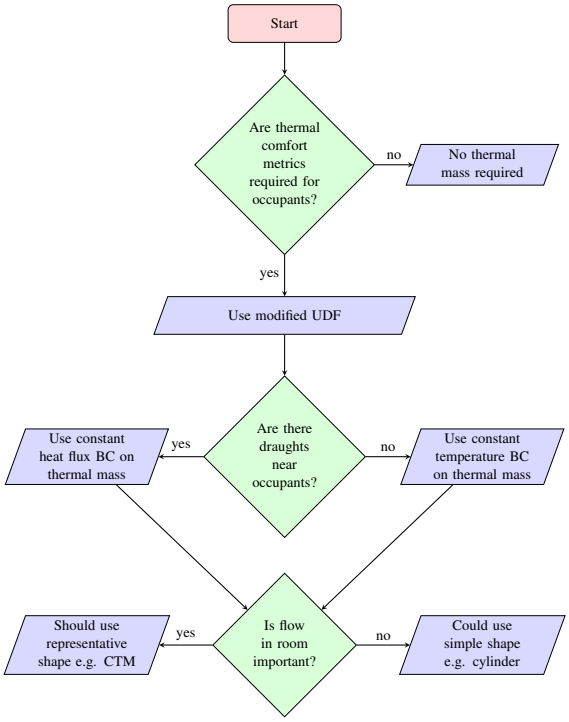

FIGURE 7.1: Flowchart with guidelines for setting up CFD simulations with personalised ventilation

8. Conclusions

Contents

8.1 Main findings

This investigation utilised Computational Fluid Dynamics (CFD) modelling to explore the impact of personalised ventilation (PV) on airflow patterns, thermal comfort and air quality in a small room. In developing the CFD methods, the findings extended the current knowledge of computational modelling of PV systems, resulting in guidelines for research and practice. Furthermore, insights were found regarding the complex flow field around a computational thermal mass (CTM), situated in a small room under the influence of a displacement ventilation regime.

If details of the flow field in small spaces are unimportant, a simplified CTM in the form of an upright cylinder is suitable, thereby simplifying the modelling process. A PV jet with no thermal mass in the domain can give an indication of where best to place the PV nozzle, for a given set of conditions. In situations where thermal comfort is important and better resolution of the flow field is required, the use of realistically shaped CTMs is crucial. The heat flux type boundary condition should also be employed if draughts are present near occupants (e.g. from PV flow).

The combination of a CTM in close proximity to a PV jet illustrated the complex nature of the flow field, particularly in the breathing zone and around the CTM. There exists a strong interaction between the PV jet, the convective boundary layer around the CTM and the thermal plume. If the PV jet is placed too far away from the CTM (outside of the zone of flow establishment), air quality can be impaired. However, PV jet temperature plays an important role as well, influencing where the jet impinges on the occupant. Extending the work to two CTMs in a room highlighted some subtle but important differences to the single CTM case. Both thermal plumes tended to move towards each other with the strength of attraction greater when the CTMs were in closer proximity. This mutual plume attraction phenomenon set up two large recirculation currents in the room which were somewhat different to the single CTM flow fields.

Overall, a significant conclusion from this research is that PV systems can be very effective for improving air quality and thermal comfort if used appropriately, however they can also prove to be detrimental to the overall indoor environment when poorly placed. Improvements to thermal comfort do not guarantee enhanced air quality. These observations underline the importance of intelligently designing PV systems which function across the widest possible range of operating conditions.

8.2 Future work

By the very nature of research, it is often necessary to implement modelling assumptions to simplify the problem under investigation. Sometimes it is necessary to limit the parameters of interest but this does not negate the validity of the findings. It may, however, place limitations on their scope and/or applicability in other scenarios. Several of the key assumptions and simplifications have already been discussed in context in Chapter 7, whereas others are acknowledged below. Many of these present suitable avenues for future investigations to extend the contributions to knowledge contained in this thesis.

Ultimately, the subject(s) in the context of personalised ventilation are the occupants in indoor environments. When simulating PV flows in physical experiments, thermal manikins are often used to represent people, which may be for ease of physically measuring parameters experimentally [Licina et al., 2014], to ensure repeatability or for ethical reasons, for example. One of the advantages of utilising numerical simulations is that the shape and form of occupants can be represented with high geometrical accuracy by a computational thermal manikin (CTM), as was used in this thesis. What was not accounted for in the models was clothing, whereas physical manikins can readily be clothed or unclothed (as in Licina et al. [2014], for example). It is acknowledged that numerically simulating the effects of clothing on thermal performance is an important consideration. Whether physical or computational thermal manikins are used, another key limitation is that they typically remain stationary. Manikins do not move whereas a human test subject would, be that through variations in the location and orientation of the body, the limbs and/or the head.

It is accepted that more experimental data for comparison would have been desirable. However, carrying out physical experiments was beyond the scope of this study and no other suitable test cases were found. Future work could address this, and incorporate the effect of additional thermal manikins.

Considering the displacement ventilation regime used in this thesis, it is reasonable to expect that, for example, simulated movement of the lower legs would disrupt the airflow from the wall inlet but this would not have any significant effect on the airflow in the breathing zone. In contrast, head movements would change the position of the mouth and the nostrils, moving them out of the targeted area of the PV jet to the detriment of the occupant. In reality, people change position several times every minute, moving an average 0.225m to either side and 0.27m axially [Melikov and Pokora, 2014]. This is an important consideration warranting future investigation although it is acknowledged that it would be extremely challenging to implement both experimentally and numerically.

For the simulations detailed in this thesis, the CTM was essentially floating to avoid the complication of including conduction in the calculations, but obviously this is unrealistic. Furthermore, no furniture was included such as desks and chairs. These have been shown to impact both the general airflow in rooms and the convective boundary layer around people [Melikov, 2015]. Tables can hinder and suppress the peak

velocities of the CBL, making PV more effective as penetration of the less-intense CBL is easier to achieve [Licina et al., 2014]. Future investigations could build on the parametric studies in this thesis concerning the PV air temperature and distance from the breathing zone, accounting for the effects of the reduced CBL, due to blockage from furniture.

Another important aspect of the simulation approach used here is that steady state simulations were used; these can give an indication of a snapshot in time where conditions are not changing. Such simulations can be relatively cheap in terms of computational cost (the time taken and the resources required), however they may not yield identical results to time averaged transient simulations which incur a far greater computational cost. Comparisons of time averaged transient simulations with the steady state ones presented here, using the Transition SST model, would indicate whether the reduced computational cost of the steady state simulations is a worthwhile trade-off for potential loss in accuracy. Full transient simulations could cater for the cyclic effects of a breathing CTM, transient fluctuations in the simulated temperatures and, with suitable dynamic/moving mesh regions, the impact of occupant movements.

Of all the findings reported in this thesis one of the most important was the discovery that a poorly located PV jet can cause a significant deterioration in air quality compared to no PV at all (thus defeating the object of having PV), yet still improve the thermal comfort. This counter-intuitive finding underlines the need to intelligently position PV systems in indoor environments. Ultimately, the goal is to improve both air quality and thermal comfort for the widest range of expected airflow and room conditions. Engineers try to achieve such goals with systematic parametric studies, however, the complex non-linear nature of this problem lends itself to the immense potential of numerical optimisation. For example, metamodelling has the potential to identify global optimum design solutions which satisfy the objective functions [Forrester et al., 2008; Jones, 2001; Keane and Nair, 2005] which in this case would be to improve air quality and thermal comfort. The added advantage of metamodels is that they typically sample the entire design space, allowing a range of operating conditions to be considered enabling good and bad operational areas to be found. Based on the work in this thesis, suitable design variables would be PV position, temperature and PV jet velocity. Incorporating these into a formal design optimisation problem would present a very interesting and worthwhile challenge.

Furthermore, to accurately and reliably predict the ventilation effectiveness of PV systems, it is essential to capture aspects of breathing, including the transient nature of inhaling and exhaling. There have been no studies exploring this whilst also accounting for thermal comfort and cross-contamination. This lends itself to a multi-objective design optimisation problem. Another issue is a lack of knowledge surrounding multiple occupants in such environments; most existing studies only consider single occupants. Therefore, it is crucial to address these clear gaps in knowledge to inform design guidance of PV systems at an early stage in their development and deployment.

Appendices

A ANYSYS Fluent UDFs (user defined functions)

A.1 Mean age of air, PMV and PPD

```
/*****************************************************/
/*  Fluent 6 user-defined functions for              */
/*  calculating the mean age of air and the          */
/*  PMV and PPD thermal comfort parameters           */
/*  according to ISO 7730                            */
/*****************************************************/

/*  Diffusivity for mean age of air
    is solved using a user-defined scalar (UDS).  This
    calculation can be performed after the normal
    problem has already been solved ... just turn off
    all of the previous equations being solved for
    and activate solution of the UDS-0
    equation.  Make sure to select

    - mean_age_diff as the uds diffusivity in the materials panel
    - mass flow rate as the uds flux function
    - mean_age_source as the uds volumetric source term in
      all fluid regions
    - set uds-0 = 0.0 at all inlets

    mean age of air calculations do not require
    any energy, radiation, or species transport
    calculations to have been performed.

    PMV and PPD are computed using user-defined memory udm-0 and udm-1.
    The values are computed on demand (pmv_fcn).
    The prerequisites for calculating PMV and PPD are that energy, radiation
    and species transport calculations for water vapor in air must
    have been performed.
    Radiation model must be either P1 or DO.
*/

/*****************************************************/

#include "udf.h"

DEFINE_DIFFUSIVITY(mean_age_diff, c, t, i)
{
  return C_R(c,t)*2.88e-05+C_MU_EFF(c,t)/0.7;
}

DEFINE_SOURCE(mean_age_source, c, t, dS, eqn)
{
```

```
45    dS[eqn]=0;
46    return C_R(c,t);
47  }
48
49  #define CLO 1.00  /* user input - clothing (clo) */
50
51  /*****************************************************/
52  /* CLO is the total thermal insulation for garments worn  */
53  /* the table below is from ISO 7730 table E.2      */
54  /* 1 clothing unit = 1 clo = 0.155 m^2 K / W              */
55  /*  Garment Description Thermal Insulation (clo)  */
56  /*                 */
57  /*  UNDERWEAR            */
58  /*  panties          0.03     */
59  /*  underpants with long legs   0.10     */
60  /*  singlet          0.04     */
61  /*  T-shirt          0.09     */
62  /*  shirt with long sleeves      0.12     */
63  /*  panties and bra        0.03     */
64  /*                 */
65  /*  SHIRTS - BLOUSES           */
66  /*  short sleeves        0.15     */
67  /*  light-weight, long sleeves     0.20     */
68  /*  normal, long sleeves       0.25     */
69  /*  flannel shirt, long sleeves   0.30     */
70  /*  light-weight blouse, long sleeves 0.15     */
71  /*                 */
72  /*  TROUSERS             */
73  /*  shorts           0.06     */
74  /*  light-weight         0.20     */
75  /*  normal           0.25     */
76  /*  flannel          0.28     */
77  /*                 */
78  /*  DRESSES - SKIRTS           */
79  /*  light skirts (summer)      0.15     */
80  /*  heavy skirt (winter)       0.25     */
81  /*  light dress, short sleeves     0.20     */
82  /*  winter dress, long sleeves     0.40     */
83  /*  boiler suit        0.55     */
84  /*                 */
85  /*  SWEATERS             */
86  /*  sleeveless vest        0.12     */
87  /*  thin sweater         0.20     */
88  /*  sweater          0.28     */
89  /*  thick sweater        0.35     */
90  /*                 */
91  /*  JACKETS              */
92  /*  light, summer jacket       0.25     */
93  /*  jacket           0.35     */
94  /*  smock          0.30     */
95  /*                 */
96  /*  HIGH-INSULATIVE, FIBRE-PELT        */
97  /*  boiler suit        0.90     */
98  /*  trousers         0.35     */
99  /*  jacket           0.40     */
100 /*  vest           0.20     */
101 /*                 */
102 /*  OUTDOOR CLOTHING           */
103 /*  coat           0.60     */
104 /*  down jacket        0.55     */
105 /*  parka          0.70     */
106 /*  fibre-pelt overalls      0.55     */
107 /*                 */
108 /*  SUNDRIES             */
109 /*  socks          0.02     */
110 /*  thick, ankle socks       0.05     */
111 /*  thick, long socks      0.10     */
112 /*  nylon stockings        0.03     */
```

```
113 /*  shoes (thin soled)      0.02    */
114 /*  shoes (thick soled)     0.04    */
115 /*  boots          0.10    */
116 /*  gloves           0.05    */
117 /*                */
118 /*********************************************************/
119
120 #define MET 1.0   /* user input - metabolic rate (met) */
121
122 /*********************************************************/
123 /* metabolic rate depends on activity level of occupants  */
124 /* the table below is from ISO 7730 table A.1      */
125 /*  Activity     Metabolic Rates (met)   */
126 /*                */
127 /*  reclining       0.8   */
128 /*                */
129 /*  seated, relaxed       1.0   */
130 /*                */
131 /*  sedentary activity          */
132 /*  (office, dwelling, school, laboratory)  1.2   */
133 /*                */
134 /*  standing, light activity        */
135 /*  (shopping, laboratory, light industry 1.6   */
136 /*                */
137 /*  standing, medium activity       */
138 /*  (shop assistant, domestic work,       */
139 /*    machine work)     2.0   */
140 /*                */
141 /*  Walking on the level:         */
142 /*    2 km/h        1.9   */
143 /*    3 km/h        2.4   */
144 /*    4 km/h        2.8   */
145 /*    5 km/h        3.4   */
146 /*                */
147 /*********************************************************/
148
149 #define WME 0.0 /* user input - external work (normally 0) */
150
151 real radiationTemperature(cell_t c, Thread *t)
152 {
153   real incidentRadiation;
154   if (sg_p1 && FLUID_THREAD_P(t))
155     incidentRadiation = C_P1(c,t);
156   else if (sg_disco)
157     {
158       int i;
159       real Ia=0;
160       int nb= MAX(1,sg_bee_gees);
161       for (i=0;i<nb;i++)
162         Ia += C_STORAGE_R_XV(c,t,SV_DO_IRRAD,i);
163       incidentRadiation = Ia;
164     }
165   else
166     incidentRadiation = 0.0;
167
168   return pow(incidentRadiation/4.0/5.67e-8,0.25);
169 }
170
171 DEFINE_ON_DEMAND(pmv_fcn)
172 {
173   Domain *domain;
174   Thread *t;
175   cell_t c;
176   int N;
177
178   real TAA;  /* air temperature (K) */
179   real TRA;  /* mean radiant temperature (K) */
180   real VEL;  /* relative air velocity (m/s) */
```

```
181   real PA;   /* water vapor pressure (Pa) */
182   real ICL, M, W, MW, FCL, HCF, TA, TR, TCLA;
183   real P1, P2, P3, P4, P5, XN, XF;
184   real EPS, ERROR, HCN, HC=0.0, TCL;
185   real HL1, HL2, HL3, HL4, HL5, HL6;
186   real TS, PMV, PPD;
187   real velv,velu,velw;
188
189   domain = Get_Domain(1);
190   thread_loop_c (t,domain)
191   {
192     if(FLUID_THREAD_P(t))
193     {
194       begin_c_loop_all (c,t)
195       {
196         TAA = C_T(c,t);
197         velu = C_U(c,t);
198         velv = C_V(c,t);
199         velw = C_W(c,t);
200         VEL = sqrt(velu*velu + velv*velv + velw*velw);
201         PA = C_YI(c,t,0)*(C_P(c,t)+101325.); /* PA is absolute */
202         /*************************************************************/
203         /********** modification here for volume average radiation ******/
204         /*************************************************************/
205         /*TRA = radiationTemperature(c,t);*/
206         TRA = 296.90564; /* example value */
207         /*************************************************************/
208         /*************************************************************/
209
210         /***************** begin generic coding of ISO 7730 ************/
211         /*                 */
212         /*  Moderate thermal environments --      */
213         /*  Determination of the PMV and PPD indices and    */
214         /*  specification of the conditions for thermal comfort */
215         /*                 */
216         /*  ISO 7730 Second Edition 1994-12-15      */
217         /*************************************************************/
218
219         ICL = 0.155 * CLO; /* thermal insulation of the clothing in m^2K/W */
220         M = MET * 58.15; /* metabolic rate in W/m^2 */
221         W = WME * 58.15; /* extrnal work in W/m^2 */
222         MW = M - W; /* internal heat production in the human body */
223
224         /* clothing area factor */
225
226         if(ICL<0.078)
227           FCL = 1 + 1.29 * ICL;
228         else
229           FCL = 1.05 + 0.645 * ICL;
230
231         HCF = 12.1 * sqrt(VEL); /* heat transfer coeff by forced convection */
232         TA = TAA - 273; /* air temperature in deg C */
233         TR = TRA - 273; /* mean radiant tempeature in deg C */
234
235         /* calculate surface temperature of clothing iteratively */
236
237         TCLA = TAA + (35.5-TA) / (3.5 * (6.45*ICL + 0.1)); /* first guess */
238         P1 = ICL * FCL;
239         P2 = P1 * 3.96;
240         P3 = P1 * 100;
241         P4 = P1 * TAA;
242         P5 = 308.7 - 0.028 * MW + P2 * pow((TRA/100.),4.);
243         XN = TCLA /100.;
244         XF = XN;
245         N = 0;     /* N: number of iterations */
246         EPS = 0.00015;  /* stop criteria in iteration */
247         ERROR = 100. * EPS;
248
```

```
249           while (fabs(ERROR)>EPS && N<150)
250           {
251             XF = (XF+XN)/2.;
252             /* heat transfer coefficient by natural convection */
253             HCN = 2.38 * pow(fabs(100.*XF-TAA), 0.25);
254             if (HCF > HCN)
255               HC = HCF;
256             else
257               HC = HCN;
258
259             XN = (P5 + P4 * HC - P2 * pow(XF,4.) ) / ( 100. + P3 * HC);
260             ERROR = XN - XF;
261             ++N;
262           }
263           if(N>=150) printf("iteration limit exceeded %d iterations \n", N);
264
265           TCL = 100. * XN - 273; /* surface temperature of the clothing */
266
267           /* heat loss components */
268
269           /* heat loss diffusion through skin */
270           HL1 = 3.05 * 0.001 * (5733 - 6.99*MW - PA);
271
272           /* heat loss by sweating (comfort) */
273           if (MW > 58.15 )
274         HL2 = 0.42 * (MW - 58.15);
275           else
276         HL2 = 0.0;
277
278           /* latent respiration heat loss */
279           HL3 = 1.7 * 0.00001 * M * (5867. - PA);
280
281           /* dry respiration heat loss */
282           HL4 = 0.0014 * M * (34.-TA);
283
284           /* heat loss by radiation */
285           HL5 = 3.96 * FCL * (pow(XN,4.) - pow((TRA/100.),4.));
286
287           /* heat loss by convection */
288           HL6 = FCL * HC * (TCL - TA);
289
290           /* calculate PMV and PPD */
291
292           /* thermal sensation transfer coefficient */
293           TS = 0.303 * exp(-0.036*M) + 0.028;
294
295           /* predicted mean vote (PMV) */
296           PMV = TS * (MW-HL1-HL2-HL3-HL4-HL5-HL6);
297
298           /* predicted percentage dissatisfied (PPD) */
299           PPD = 100. - 95.*exp(-0.03353*pow(PMV,4.) - 0.2179*pow(PMV,2.));
300
301           /****************** end generic coding of ISO 7730 **********/
302
303           C_UDMI(c,t,0) = PMV;
304           C_UDMI(c,t,1) = PPD;
305         }
306         end_c_loop_all (c,t)
307       }
308     }
309 }
```

A.2 Operative temperature

```
/*****************************************************/
/*  Fluent UDF for calculating          */
/*  operative temperature         */
/*  CIBSE Guide A equation (1.2)          */
/*****************************************************/

/* version 1 by Natalie Gilkeson 2018 */

/*****************************************************/

/*  The operative (resultant) temperature is computed
    using user-defined memory udm-0.
    The values are computed on demand (op_res_temp).
    The prerequisites for calculating PMV and PPD are
    that energy and radiation must have been performed.
    Radiation model must be either P1 or DO.
*/

/*****************************************************/

#include "udf.h"

real radiationTemperature(cell_t c, Thread *t)
{
  real incidentRadiation;
  if (sg_p1 && FLUID_THREAD_P(t))
    incidentRadiation = C_P1(c,t);
  else if (sg_disco)
    {
      int i;
      real Ia=0;
      int nb= MAX(1,sg_bee_gees);
      for (i=0;i<nb;i++)
        Ia += C_STORAGE_R_XV(c,t,SV_DO_IRRAD,i);
      incidentRadiation = Ia;
    }
  else
    incidentRadiation = 0.0;

  return pow(incidentRadiation/4.0/5.67e-8,0.25);
}

DEFINE_ON_DEMAND(op_res_temp)
{
  Domain *domain;
  Thread *t;
  cell_t c;

  real THETAC;    /* operative (resultant) temperature, Celsius */
  real THETAAI;   /* indoor air temperature, Celsius */
  real THETAR;    /* mean radiant temperature, Celsius */
  real H;   /* = h_c / (h_c + h_r) */

  real TAA;  /* air temperature (K) */
  real TRA;  /* mean radiant temperature (K) */
  real VEL;  /* relative air velocity (m/s) */

  real velv,velu,velw;

  domain = Get_Domain(1);
  thread_loop_c (t,domain)
  {
    if(FLUID_THREAD_P(t))
    {
      begin_c_loop_all (c,t)
      {
```

```
67          TAA = C_T(c,t);
68          velu = C_U(c,t);
69          velv = C_V(c,t);
70          velw = C_W(c,t);
71          VEL = sqrt(velu*velu + velv*velv + velw*velw);
72          TRA = radiationTemperature(c,t);
73
74          THETAAI = TAA - 273.15;
75          THETAR = TRA - 273.15;
76          H = sqrt(10*VEL);
77
78          THETAC = ((THETAAI * H) + THETAR) / (1 + H);
79
80          C_UDMI(c,t,0) = THETAC;
81        }
82        end_c_loop_all (c,t)
83      }
84    }
85  }
```

References

Acheson, D. J. (2001). *Elementary Fluid Dynamics*. Clarendon Press, Oxford. ISBN 0198596790.

Aftab, S., Rafie, A. M., Razak, N. and Ahmad, K. (2016). Turbulence model selection for low reynolds number flows. *PloS one* **11**, e0153755.

AIAA (1998). Guide for the Verification and Validation of Computational Fluid Dynamics Simulations. *AIAA G-077-1998* .

Albertson, M. L., Dai, Y. B., Jenson, R. A. and Rouse, H. (1950). Diffusion of submerged jets. *Transactions of the American Society of Civil Engineers* **115**, 639–664.

Alsaad, H. and Voelker, C. (2018). Evaluating the body cooling effect of personalised ventilation systems. In *Roomvent & Ventilation 2018 Proceedings*. Espoo, Finland, Scandinavian Federation of Heating, Ventilation and Sanitary Engineering. ISBN 978-952-5236-48-4.

Anderson, J. D. (1995). *Computational Fluid Dynamics. The Basics with Applications*. McGraw-Hill. ISBN 0071132104.

Andreasi, W. A. and Lamberts, R. (2006). Thermal comfort in buildings located in regions of hot and humid climate of brazil. *Proc Comfort and Energy Use in Buildings-Getting them Right. London: Network for Comfort and Energy Use in Buildings* .

ANSYS, Inc. (2013). ANSYS® Fluent, Release 15.0, Theory Guide.

ANSYS, Inc. (2014). ANSYS® Fluent, Release 15.0, User's Guide.

ANSYS, Inc. (2015). ANSYS Fluent webpage. [Online. Accessed 2015-04-25]. www.ansys.com/Products.

Apte, M. G., Fisk, W. J. and Daisey, J. M. (2000). Associations between indoor CO_2 concentrations and sick building syndrome symptoms in U.S. office buildings: an analysis of the 1994-1996 BASE study data. *Indoor Air* **10**, 246–257.

Araújo, V. M. D. and Araújo, E. H. S. (1999). The applicability of iso 7730 for the assessment of the thermal conditions of users of the buildings in natal-brazil. In *Proceedings of Indoor Air. Edinburgh*.

Arens, E., Humphreys, M. A., de Dear, R. and Zhang, H. (2010). Are 'class A' temperature requirements realistic or desirable? *Building and Environment* **45**, 4–10.

Arens, E., Zhang, H. and Huizenga, C. (2006a). Partial-and whole-body thermal sensation and comfort—part i: Uniform environmental conditions. *Journal of thermal Biology* **31**, 53–59.

Arens, E., Zhang, H. and Huizenga, C. (2006b). Partial-and whole-body thermal sensation and comfort—part ii: Non-uniform environmental conditions. *Journal of thermal Biology* **31**, 60–66.

ASHRAE (2004). *ANSI/ ASHRAE Standard 55-2004, Thermal Comfort Conditions for Human Occupancy*. American Society of Heating, Air-Conditioning, and Refrigeration Engineers, Inc.

Awbi, H. (1998). Energy efficient room air distribution. *Renewable Energy* **15**, 293–299.

Babich, F., Cook, M., Loveday, D. and Cropper, P. (2016). Numerical modelling of thermal comfort in non-uniform environments using real-time coupled simulation models. *Proceedings of Building Simulation and Optimisation 2016: 3rd IBPSA-England Conference* , 4–11.

Barlow, J. B., Rae, W. H. and Pope, A. (1999). *Low Speed Wind Tunnel Testing*. John Wiley & Sons, 3

edition. ISBN 0471557749.

Berselli, L. C., Iliescu, T. and Layton, W. J. (2006). *Mathematics of Large Eddy Simulation of Turbulent Flows*. Springer. ISBN 3540263160.

Bertin, J. J. and Smith, M. L. (1979). *Aerodynamics for Engineers*. Prentice-Hall. ISBN 0130182346.

Bivolarova, M., Kierat, W., Zavrl, E., Popiolek, Z. and Melikov, A. (2017). Effect of airflow interaction in the breathing zone on exposure to bio-effluents. *Building and Environment* **125**, 216–226.

Bjørn, E. and Nielsen, P. V. (2002). Dispersal of exhaled air and personal exposure in displacement ventilated rooms. *Indoor air* **12**, 147–164.

Boerstra, A. C., Kulve, M. T., Toftum, J. r., Loomans, M. G., Olesen, B. W. and Hensen, J. L. (2015). Comfort and performance impact of personal control over thermal environment in summer: results from a laboratory study. *Building and Environment* **87**, 315–326.

Bogdan, A. and Chludzinska, M. (2010). Assessment of Thermal Comfort Using Personalized Ventilation. *HVAC&R Research* **16**, 529–542.

Bogdan, A., Koelblen, B. and Chludzińska, M. (2016). Influence of a breathing process on the perception of the thermal environment using personalised ventilation. *Building and Environment* **96**, 80–90.

Bolashikov, Z., Melikov, A. and Spilak, M. (2013). Experimental investigation on reduced exposure to pollutants indoors by applying wearable personalized ventilation. *HVAC & R Research* **19**, 37–41.

Brager, G., Zhang, H. and Arens, E. (2015). Evolving opportunities for providing thermal comfort. *Building Research and Information* **43**, 274–287.

British Standards Institute (2002). BS EN ISO 10551:2001. Ergonomics of the thermal environment. Assessment of the influence of the thermal environment using subjective judgement scales.

British Standards Institute (2006). BS EN ISO 7730:2005. Ergonomics of the thermal environment. Analytical determination and interpretation of thermal comfort using calculation of the PMV and PPD indices and local thermal comfort criteria.

British Standards Institute (2008). BS EN ISO 15251:2007. Indoor environmental input parameters for design and assessment of energy performance of buildings addressing indoor air quality, thermal environment, lighting and acoustics.

British Standards Institute (2014). BS EN ISO 13379:2007. Ventilation for non-residential buildings — Performance requirements for ventilation and room-conditioning systems.

Cant, S. R. (2002). High-Performance Computing in Computational Fluid Dynamics: Progress and Challenges. *Philosophical Transactions of the Royal Society A* **360**, 1211–1225.

Cao, G., Awbi, H., Yao, R., Fan, Y., Sirén, K., Kosonen, R. and Zhang, J. J. (2014). A review of the performance of different ventilation and airflow distribution systems in buildings. *Building and Environment* **73**, 171–186.

Cermak, R., Melikov, A., Forejt, L. and Kovar, O. (2006). Performance of personalized ventilation in conjunction with mixing and displacement ventilation. *HVAC&R Research* **12**, 295–311.

CFD Benchmarks (2014). CFD benchmarks webpage resources. [Online]. [Accessed 2014-09-04]. Available from: www.cfd-benchmarks.com.

Chanteloup, V. and Mirade, P. S. (2009). Computational fluid dynamics (CFD) modelling of local mean age of air distribution in forced-ventilation food plants. *Journal of Food Engineering* **90**, 90–103.

Chao, H. J., Schwartz, J., Milton, D. K. and Burge, H. A. (2003). The Work Environment and Workers' Health in Four Large Office Buildings. *Environmental Health Perspectives* **111**, 1242–1248.

Chen, H., Janbakhsh, S., Larsson, U. and Moshfegh, B. (2015). Numerical investigation of ventilation performance of different air supply devices in an office environment. *Building and Environment* **90**, 37–50. ISSN 03601323.

Chludzińska, M. and Bogdan, A. (2015). The effect of temperature and direction of air flow from the personalised ventilation on occupants ' thermal sensations in office areas. *Building and Environment* **85**, 277–286.

Chung, T. J. (2002). *Computational Fluid Dynamics*. Cambridge University Press. ISBN 0521594162.

CIBSE, Guide A (2015). *CIBSE Guide A: Environmental Design*. 8 edition. ISBN 978-1-906846-55-8.

Clancy, E. (2011). *CIBSE Knowledge Series: Indoor Air Quality and Ventilation. KS17*. ISBN 978-1-906846-19-0.

Craven, B. a. and Settles, G. S. (2006). A Computational and Experimental Investigation of the Human Thermal Plume. *Journal of Fluids Engineering* **128**, 1251.

Cruceanu, I., Maalouf, C., Colda, I. and Lachi, M. (2013). Parametric study and energy analysis of a personalized ventilation system. *International Journal of Mathematical Models and Methods in Applied Sciences* **7**, 141–148.

Dalewski, M., Melikov, A. K. and Vesely, M. (2014). Performance of ductless personalized ventilation in conjunction with displacement ventilation: Physical environment and human response. *Building and Environment* **81**, 354–364.

d'Ambrosio Alfano, F. R., Olesen, B. W. and Palella, B. I. (2017). Povl Ole Fanger's impact ten years later. *Energy and Buildings* **152**, 243–249. ISSN 03787788.

Davidson, P. A. (2004). *Turbulence. An Introduction for Scientists and Engineers*. Oxford University Press. ISBN 0198529481.

Davoodi, F., Hasanzadeh, H., Alireza, S. and Maerefat, M. (2017). Developing a new individualized 3-node model for evaluating the e ff ects of personal factors on thermal sensation. *Journal of Thermal Biology* **69**, 1–12.

de Dear, R. and Brager, G. (1998). Developing an adaptive model of thermal comfort and preference. *ASHRAE Transactions* **104**, 1–18.

De Dear, R. J., Akimoto, T., Arens, E. A., Brager, G., Candido, C., Cheong, K. W. D., Li, B., Nishihara, N., Sekhar, S. C., Tanabe, S., Toftum, J., Zhang, H. and Zhu, Y. (2013). Progress in thermal comfort research over the last twenty years. *Indoor Air* **23**, 442–461.

de Dear, R. J. and Brager, G. S. (2002). Thermal comfort in naturally ventilated buildings: revisions to ASHRAE Standard 55. *Energy and Buildings* **34**, 549–561.

de Paula Xavier, A. A. and Lamberts, R. (2000). Indices of thermal comfort developed from field survey in brazil. *TRANSACTIONS-AMERICAN SOCIETY OF HEATING REFRIGERATING AND AIR CONDITIONING ENGINEERS* **106**, 45–58.

Deevy, M., Sinai, Y., Everitt, P., Voigt, L. and Gobeau, N. (2008). Modelling the effect of an occupant on displacement ventilation with computational fluid dynamics. *Energy and Buildings* **40**, 255–264.

Demuren, A. and Grotjans, H. (2009). Buoyancy-Driven Flows—Beyond the Boussinesq Approximation. *Numerical Heat Transfer, Part B: Fundamentals* **56**, 1–22. ISSN 1040-7790.

Djamila, H. (2017). Indoor thermal comfort predictions: Selected issues and trends. *Renewable and Sustainable Energy Reviews* **74**, 569–580. ISSN 18790690.

Durbin, P. A. and Medic, G. (2007). *Fluid Dynamics with a Computational Perspective*. Cambridge University Press. ISBN 9780521850179.

Eastop, T. D. and Watson, W. E. (1992). *Mechanical services for buildings*. Harlow: Longman Scientific & Technical. ISBN 9780470217900.

ed. J. F. Thompson, Soni, B. K. and Weatherill, N. P. (1999). *Handbook of Grid Generation*. CRC Press. ISBN 0849326877.

ed. Thomas B. Gatski and Hussaini, M. Y. (1996). *Simulation and Modeling of Turbulent Flows*. Oxford University Press. ISBN 0195106431.

Enescu, D. (2017). A review of thermal comfort models and indicators for indoor environments. *Renewable and Sustainable Energy Reviews* **79**, 1353–1379. ISSN 18790690.

Engvall, K., Wickman, P. and Norbäck, D. (2005). Sick building syndrome and perceived indoor environment in relation to energy saving by reduced ventilation flow during heating season: a 1 year intervention study in dwellings. *Indoor Air* **15**, 120–126.

Etheridge, D. (2015). A perspective on fifty years of natural ventilation research. *Building and Environment* **In Press**, 1–10. ISSN 03601323.

Euler, L. (2008). General Principles of the Motion of Fluids. *Physica D* **237**, 1825–1839.

Fang, L., Clausen, G. and Fanger, P. O. (1998a). Impact of Temperature and Humidity on Perception of Indoor Air Quality During Immediate and Longer Whole-Body Exposures. *Indoor Air* **8**, 276–284.

Fang, L., Clausen, G. and Fanger, P. O. (1998b). Impact of Temperature and Humidity on the Perception of Indoor Air Quality. *Indoor Air* **8**, 80–90.

Fang, Z., Liu, H., Li, B., Baldwin, A., Wang, J. and Xia, K. (2015). Experimental investigation of personal air supply nozzle use in aircraft cabins. *Applied Ergonomics* **47**, 193–202.

Fanger, P. O. (1972). *Thermal comfort: analysis and applications in enivironmental engineering*. New York; London: McGraw-Hill Book Company. ISBN 0070199159; 9780070199156.

Fanger, P. O., Ipsen, B. M., Langkilde, G., Olesen, B. W., Christensen, N. K. and Tanabe, S. (1985). Comfort Limits for Asymmetric Thermal Radiation. *Energy and Buildings* **8**, 225–236.

Fanger, P. O. and Toftum, J. (2002). Extension of the PMV model to non-air-conditioned buildings in warm climates. *Energy & Buildings* **34**, 533–536.

Fanger, P. O. et al. (1970). Thermal comfort. analysis and applications in environmental engineering. *Thermal comfort. Analysis and applications in environmental engineering.* .

Farag, A. M. and Khalil, E. E. (2015). Numerical analysis and optimization of different ventilation systems for commercial aircraft cabins. In *Aerospace Conference, 2015 IEEE*. IEEE.

Faulkner, D., Fisk, W. J., Sullivan, D. P. and Wyon, D. P. (1999). Ventilation Efficiencies of Desk-Mounted Task / Ambient Conditioning Systems. *Indoor Air* **9**, 273–281.

Federspiel, C. C. (1999). Air-Change Effectiveness: Theory and Calculation. *Indoor Air* **9**, 47–56.

Fisk, W. J., Faulkner, D., Palonen, J. and Seppänen, O. (2002). Performance and costs of particle air filtration technologies. *Indoor Air* **12**, 223–234.

Fisk, W. J., Faulkner, D., Sullivan, D. and Baljman, F. (1997). Air Change Effectiveness and Pollutant Removal Efficiency during Adverse Mixing Conditions. *Indoor Air* **7**, 55–63.

Fisk, W. J., Mirer, A. G. and Mendell, M. J. (2009). Quantitative relationship of sick building syndrome symptoms with ventilation rates. *Indoor Air* **19**, 159–165.

Fisk, W. J., Seppanen, O., Faulkner, D. and Huang, J. (2005). Economic Benefits of an Economizer System: Energy Savings and Reduced Sick Leave. *ASHRAE Transactions* **111**, 673–679.

Forrester, A., Sobester, A. and Keane, A. (2008). *Engineering Design Via Surrogate Modelling: A Practical Guide*. WileyBlackwell. ISBN 0470060689.

Fountain, M., Brager, G. and de Dear, R. (1996). Expectations of indoor climate control. *Energy and Buildings* **24**, 179–182.

Fu, M., Weng, W. G., Chen, W. W. and Luo, N. (2016). Review on modeling heat transfer and thermoregulatory responses in human body. *Journal of Thermal Biology* **62**, 189–200.

Gao, N. and Niu, J. (2004). CFD study on micro-environment around human body and personalized ventilation. *Building and Environment* **39**, 795–805.

Gao, N. and Niu, J. (2006). Transient CFD simulation of the respiration process and inter-person exposure assessment. *Building and Environment* **41**, 1214–1222.

Gao, N., Niu, J. and Zhang, H. (2006). Coupling CFD and Human Body Thermoregulation Model for the Assessment of Personalized Ventilation. *HVAC&R Research* **12**, 497–518.

Geomagic Studio (2014). Webpage for Geomagic Studio. [Online]. [Accessed 2014-12-11]. Available from: `www.geomagic.com/`.

Gilkeson, N., Khan, M. and Noakes, C. (2018a). Computational fluid dynamics simulations of personalised ventilation: Sampling air quality in the breathing zone. In *Indoor Air 2018 Proceedings*. Philadelphia, PA, USA. (**Accepted**).

Gilkeson, N., Khan, M. and Noakes, C. (2018b). Computational fluid dynamics simulations of personalised ventilation: The effect of distance and temperature on thermal comfort and air quality. In *Roomvent & Ventilation 2018 Proceedings*. Espoo, Finland, Scandinavian Federation of Heating, Ventilation and Sanitary Engineering. ISBN 978-952-5236-48-4.

GOV.UK (2014). Webpage on the Health and Safety Executive. [Online]. [Accessed 2014-10-01]. Available from: www.gov.uk/government/organisations/health-and-safety-executive.

Grafsrønningen, S. and Jensen, A. (2015). Unsteady reynolds averaged navier–stokes simulations of a buoyant plume above a cylinder. *Proceedings of the Institution of Civil Engineers-Engineering and Computational Mechanics* **168**, 35–42.

Habchi, C., Chakroun, W., Alotaibi, S., Ghali, K. and Ghaddar, N. (2016a). Effect of shifts from occupant design position on performance of ceiling personalized ventilation assisted with desk fan or chair fans. *Energy and Buildings* **117**, 20–32.

Habchi, C., Ghali, K., Ghaddar, N., Chakroun, W. and Alotaibi, S. (2016b). Ceiling personalized ventilation combined with desk fans for reduced direct and indirect cross-contamination and efficient use of office space. *Energy Conversion and Management* **111**, 158–173.

Habchi, C., Ghali, K., Ghaddar, N. and Shihadeh, A. (2015). Chair fan-enhanced displacement ventilation for high IAQ : Effects on particle inhalation and strati fi cation height. *Building and Environment* **84**, 68–79.

Halvoňová, B. and Melikov, A. K. (2010). Performance of "ductless" personalized ventilation in conjunction with displacement ventilation: Impact of disturbances due to walking person(s). *Building and Environment* **45**, 427–436.

Havenith, G., Holme, I. and Parsons, K. (2002). Personal factors in thermal comfort assessment : clothing properties and metabolic heat production. *Energy and Buildings* **34**, 581–591.

Health and Safety Executive (2014). HSE Guidance webpages on thermal comfort. [Online]. [Accessed 2014-10-01]. Available from: `www.hse.gov.uk/temperature/thermal/index.htm`.

Hirsch, C. (2007). *Numerical Computation of Internal and External Flows. The Fundamentals of Computational Fluid Dynamics*. Elsevier. ISBN 9780750665940.

Hirst, E. (1971). Buoyant jets discharged to quiescent stratified ambients. *Journal of Geophysical Research* **76**, 7375–7384. ISSN 2156-2202.

Höppe, P. (2002). Different aspects of assessing indoor and outdoor thermal comfort. *Energy and buildings* **34**, 661–665.

Horikiri, K., Yao, Y. and Yao, J. (2015). Numerical optimisation of thermal comfort improvement for indoor environment with occupants and furniture. *Energy and Buildings* **88**, 303–315.

HSE (2013). Workplace (Health, Safety and Welfare) Regulations 1992, Approved Code of Practice and Guidance. ISBN 978 0 7176 6583 9.

Huizenga, C., Zhang, H., Arens, E. and Wang, D. (2004). Skin and core temperature response to partial- and whole-body heating and cooling. *Journal of Thermal Biology* **29**, 549–558.

Humphreys, M. A. and Nicol, J. F. (1998). Understanding the adaptive approach to thermal comfort. *ASHRAE transactions* **104**, 991.

Huser, A. and Biringen, S. (1993). Direct Numerical Simulation of Turbulent Flow in a Square Duct. *Journal of Fluid Mechanics* **257**, 65–95.

Hwang, R.-L., Cheng, M.-J., Lin, T.-P. and Ho, M.-C. (2009a). Thermal perceptions, general adaptation methods and occupant's idea about the trade-off between thermal comfort and energy saving in hot–humid regions. *Building and Environment* **44**, 1128–1134.

Hwang, R.-L., Lin, T.-P., Liang, H.-H., Yang, K.-H. and Yeh, T.-C. (2009b). Additive model for thermal comfort generated by matrix experiment using orthogonal array. *Building and Environment* **44**, 1730–1739.

Ishihara, T., Gotoh, T. and Kaneda, Y. (2009). Study of High–Reynolds Number Isotropic Turbulence by Direct Numerical Simulation. *Annual Review of Fluid Mechanics* **41**, 165–180.

Ishii, A., Sakakibara, N., Katayama, T., Tsutsumi, J. and Nishida, M. (1990). An experimental study on human sensation to airflow in naturally ventilated rooms. *Environment International* **16**, 61–70.

Jaakkola, J. J. and Miettinen, P. (1995). Ventilation rate in office buildings and sick building syndrome. *Occupational and Environmental Medicine* **52**, 709–714.

Jaakkola, J. J. K., Tuomaala, P. and Seppänen, O. (1994). Air Recirculation and Sick Building Syndrome: A Blinded Crossover Trial. *American Journal of Public Health* **84**, 422–428.

Jin, Q., Li, X., Duanmu, L., Shu, H., Sun, Y. and Ding, Q. (2012). Predictive model of local and overall thermal sensations for non-uniform environments. *Building and Environment* **51**.

Jones, D. R. (2001). A Taxonomy of Global Optimization Methods Based on Response Surfaces. *Journal of Global Optimization* **21**, 345–383.

Junjing, Y., Sekhar, C., Cheong, D. and Raphael, B. (2014). Performance evaluation of an integrated Personalized Ventilation – Personalized Exhaust system in conjunction with two background ventilation systems. *Building and Environment* **78**, 103–110.

Kaczmarczyk, J., Melikov, A., Bolashikov, Z., Nikolaev, L. and Fanger, P. O. (2006). Human Response to Five Designs of Personalized Ventilation. *HVAC&R Research* **12**, 367–384.

Kaczmarczyk, J., Melikov, A. and Fanger, P. O. (2004). Human response to personalized ventilation and mixing ventilation. *Indoor Air* **14**, 17–29.

Kaczmarczyk, J., Melikov, a. and Sliva, D. (2010). Effect of warm air supplied facially on occupants' comfort. *Building and Environment* **45**, 848–855.

Kalmár, F. (2015). Innovative method and equipment for personalized ventilation. *Indoor Air* , 297–306.

Kalmár, F. and Kalmár, T. (2013). Alternative personalized ventilation. *Energy and Buildings* **65**, 37–44.

Karjalainen, S. (2012). Thermal comfort and gender: a literature review. *Indoor Air* **22**, 96–109.

Katić, K., Li, R. and Zeiler, W. (2016). Thermophysiological models and their applications: A review. *Building and Environment* **106**, 286–300.

Kaye, N. and Linden, P. (2004). Coalescing axisymmetric turbulent plumes. *Journal of Fluid Mechanics* **502**, 41–63.

Keane, A. J. and Nair, P. B. (2005). *Computational Approaches for Aerospace Design: The Pursuit of Excellence*. J. Wiley. ISBN 0470855401.

Khalifa, H. E., Janos, M. I. and Dannenhoffer, J. F. (2009). Experimental investigation of reduced-mixing personal ventilation jets. *Building and Environment* **44**, 1551–1558.

Khattree, R. and Rao, C. R. (2003). *Statistics in Industry. Handbook of Statistics*, volume 22. Elsevier. ISBN 0444506144.

King, M.-F., Noakes, C., Sleigh, P. and Camargo-Valero, M. (2013). Bioaerosol deposition in single and two-bed hospital rooms: A numerical and experimental study. *Building and Environment* **59**, 436–447.

Kingma, B. R., Schweiker, M., Wagner, A. and van Marken Lichtenbelt, W. D. (2017). Exploring internal body heat balance to understand thermal sensation. *Building Research and Information* **45**, 808–818.

Koelblen, B., Psikuta, A., Bogdan, A., Annaheim, S. and Rossi, R. M. (2017). Thermal sensation models: a systematic comparison. *Indoor Air* **27**, 680–689. ISSN 16000668.

Koelblen, B., Psikuta, A., Bogdan, A., Annaheim, S. and Rossi, R. M. (2018). Thermal sensation models: Validation and sensitivity towards thermo-physiological parameters. *Building and Environment* **130**, 200–211. ISSN 03601323.

Kunkel, B. A. (1979). A modern thermo-kinetic warm fog dispersal system for commercial airports. *Journal of Applied Meteorology* **18**, 794–803.

Langtry, R. B., Menter, F., Likki, S., Suzen, Y., Huang, P. and Völker, S. (2006). A correlation-based transition model using local variables—part ii: test cases and industrial applications. *Journal of Turbomachinery* **128**, 423–434.

Launder, B. and Sandham, N. (2002). *Closure Strategies for Turbulent and Transitional Flows*. Cambridge University Press. ISBN 0521792088.

Lee, S., Bilionis, I., Karava, P. and Tzempelikos, A. (2017). A Bayesian approach for probabilistic classification and inference of occupant thermal preferences in office buildings. *Building and Environment* **118**, 323–343.

Li, X., Niu, J. and Gao, N. (2013). Co-occupant's exposure to exhaled pollutants with two types of

personalized ventilation strategies under mixing and displacement ventilation systems. *Indoor air* **23**, 162–171.

Li, Y., Leung, G. M., Tang, J. W., Yang, X., Chao, C. Y., Lin, J. Z., Lu, J. W., Nielsen, P. V., Niu, J., Qian, H., Sleigh, A. C., Su, H. J., Sundell, J., Wong, T. W. and Yuen, P. L. (2007). Role of ventilation in airborne transmission of infectious agents in the built environment – a multidisciplinary systematic review. *Indoor Air* , 2–18.

Li, Y. and Nielsen, P. V. (2011). CFD and ventilation research. *Indoor Air* **21**, 442–453.

Licina, D., Melikov, A., Pantelic, J., Sekhar, C. and Tham, K. W. (2015a). Human convection flow in spaces with and without ventilation: Personal exposure to floor-released particles and cough-released droplets. *Indoor Air* **25**, 672–682.

Licina, D., Melikov, A., Sekhar, C. and Tham, K. W. (2015b). Air temperature investigation in microenvironment around a human body. *Building and Environment* **92**, 39–47.

Licina, D., Melikov, A., Sekhar, C. and Tham, K. W. (2015c). Human convective boundary layer and its interaction with room ventilation flow. *Indoor air* **25**, 21–35.

Licina, D., Melikov, A., Sekhar, C. and Tham, K. W. (2015d). Transport of Gaseous Pollutants by Convective Boundary Layer around a Human Body. *Science and Technology for the Built Environment* **4731**, 00–00. ISSN 2374-4731.

Licina, D., Pantelic, J., Melikov, A., Sekhar, C. and Tham, K. W. (2014). Experimental investigation of the human convective boundary layer in a quiescent indoor environment. *Building and Environment* **75**, 79–91.

Liddament, M. and Orme, M. (1998). Energy and ventilation. *Applied Thermal Engineering* **18**, 1101–1109.

Liddament, M. W. (2000). A review of ventilation and the quality of ventilation air. *Indoor Air* **10**, 193–199.

Linden, P. F. (1999). The fluid mechanics of natural ventilation. *Annual review of fluid mechanics* **31**, 201–238.

Liu, L. and Li, Y. (2012). Simulation of interpersonal transport of expiratory droplets and droplet nuclei between two standing manikins. In *Proceedings of the 10th International conference, Healthy Buildings*, volume 3.

Liu, S., Schiavon, S., Kabanshi, A. and Nazaroff, W. W. (2017). Predicted percentage dissatisfied with ankle draft. *Indoor Air* **27**, 852–862. ISSN 16000668.

Liu, S., Xu, L., Chao, J., Shen, C., Liu, J., Sun, H., Xiao, X. and Nan, G. (2013). Thermal environment around passengers in an aircraft cabin. *HVAC&R Research* **19**, 627–634.

Liua, L., Nielsen, P. V., Lia, Y., Jensen, R. L., Litewnicki, M. and Zajasb, J. (2009). The thermal plume above a human body exposed to different air distribution strategies. In *The International Conference & Exhibition Healthy Buildings [HB2009]*.

Macpherson, R. K. (1962). The assessment of the thermal environment. A review. *British journal of industrial medicine* **19**, 151–64.

Maier, J. and Marggraf-Micheel, C. (2015). Weighting of climate parameters for the prediction of thermal comfort in an aircraft passenger cabin. *Building and Environment* **84**, 214–220.

Makhoul, A., Ghali, K. and Ghaddar, N. (2013). Desk fans for the control of the convection flow around occupants using ceiling mounted personalized ventilation. *Building and Environment* **59**, 336–348.

Mayer, E. (1997). A new correlation between predicted mean votes (pmv) and predicted percentages of dissatisfied (ppd). In *roceedings of Healthy Buildings/IAQ '97, Bethesda*.

Mazej, M. and Butala, V. (2012). Investigation in the Characteristics of the Personal Ventilation Using Computational Fluid Dynamics. *Indoor and Built Environment* **21**, 749–771.

McMullan, R. (2012). *Environmental Science in Building*. Building and Surveying Series. Palgrave Macmillan. ISBN 9780230290808.

Meiss, A., Feijó-Muñoz, J. and García-Fuentes, M. A. (2013). Age-of-the-air in rooms according to the

environmental condition of temperature: A case study. *Energy and Buildings* **67**, 88–96.

Melikov, A., Ivanova, T. and Stefanova, G. (2012). Seat headrest-incorporated personalized ventilation: Thermal comfort and inhaled air quality. *Building and Environment* **47**, 100–108.

Melikov, A. and Pokora, P. (2014). Occupant body movement and seat occupancy rate for design of desk micro-environment. *Proceedings of ROOMVENT 2014, 13th SCANVAC International Conference on Air Distribution in Rooms* .

Melikov, A. K. (2004). Personalized ventilation. *Indoor Air* **14**, 157–167.

Melikov, A. K. (2015). Human body micro-environment: The benefits of controlling airflow interaction. *Building and Environment* **91**, 70–77.

Melikov, A. K. and Knudsen, G. L. (2007). Human response to an individually controlled microenvironment. *HVAC&R Research* **13**, 645–660.

Melikov, A. K., Skwarczynski, M. A., Kaczmarczyk, J. and Zabecky, J. (2013). Use of personalized ventilation for improving health , comfort , and performance at high room temperature and humidity. *Indoor Air* , 250–263.

Mendell, M. J. and Smith, A. H. (1990). Consistent pattern of elevated symptoms in air-conditioned office buildings: a reanalysis of epidemiologic studies. *American Journal of Public Health* **80**, 1193–1199.

Menter, F., Langtry, R. and Völker, S. (2006a). Transition modelling for general purpose cfd codes. *Flow, turbulence and combustion* **77**, 277–303.

Menter, F. R., Langtry, R. B., Likki, S., Suzen, Y., Huang, P. and Völker, S. (2006b). A correlation-based transition model using local variables—part i: model formulation. *Journal of Turbomachinery* **128**, 413–422.

MeshLab (2014). Webpage for MeshLab. [Online]. [Accessed 2014-12-11]. Available from: `www.meshlab.net/`.

Modest, M. F. (2013). *Radiative Heat Transfer (3rd Edition)*. Elsevier. ISBN 978-0-12-386944-9.

Moin, P. and Mahesh, K. (1988). Direct Numerical Simulation: A Tool in Turbulence Research. *Annual Review of Fluid Mechanics* **30**, 539–578.

Moran, J. (1984). *An Introduction to Theoretical and Computational Aerodynamics*. Wiley. ISBN 0471874914.

Murakami, S., Kato, S. and Zeng, J. (2000). Combined simulation of airflow, radiation and moisture transport for heat release from a human body. *Building and environment* **35**, 489–500.

Naumov, A. L., Tabunshchikov, I. A., Kapko, D. V. and Brodach, M. M. (2015). Research of the microclimate formed by the local DCV. *Energy & Buildings* **90**, 1–5.

Nicol, J. F. and Roaf, S. (2017). Rethinking thermal comfort. *Building Research and Information* **45**, 711–716.

Nielsen, P., Hyldgaard, C. E., Melikov, A., Andersen, H. and Soennichsen, M. (2007a). Personal Exposure Between People in a Room Ventilated by Textile Terminals—with and without Personalized Ventilation. *HVAC&R Research* **13**, 635–643.

Nielsen, P., Jiang, H. and Polak, M. (2007b). Bed with integrated personalized ventilation for minimizing cross infection. Roomvent 2007. In *10th International Conference on Air Distribution in Rooms, Helsinki*.

Nielsen, P. V. (2004). Computational fluid dynamics and room air movement. *Indoor Air* **14**, 134–143.

Nielsen, P. V. (2009). Control of airborne infectious diseases in ventilated spaces. *Journal of the Royal Society Interface* **6**, S747–S755.

Nielsen, P. V. (2015). Fifty years of CFD for room air distribution. *Building and Environment* **91**, 78–90.

Nielsen, P. V., Allard, F., Awbi, H. B., Davidson, L. and Schälin, A. (2007c). *Computational Fluid Dynamics in Ventilation Design REHVA Guidebook No 10*. Rehva. ISBN 9782960046892.

Parkinson, T. and De Dear, R. (2015). Thermal pleasure in built environments: Physiology of alliesthesia. *Building Research and Information* **43**, 288–301.

Parkinson, T. and de Dear, R. (2017). Thermal pleasure in built environments: spatial alliesthesia from air movement. *Building Research and Information* **45**, 320–335.

Parkinson, T., De Dear, R. and Candido, C. (2016). Thermal pleasure in built environments: Alliesthesia in different thermoregulatory zones. *Building Research and Information* **44**, 20–33.

Pasut, W., Arens, E., Zhang, H. and Zhai, Y. (2014). Enabling energy-efficient approaches to thermal comfort using room air motion. *Building and Environment* **79**, 13–19.

Patankar, S. V. (1980). *Numerical Heat Transfer and Fluid Flow*. Hemisphere. ISBN 0070487405.

Pejtersen, J., Allermann, L., Kristensen, T. S. and Poulsen, O. M. (2006). Indoor climate, psychosocial work environment and symptoms in open-plan offices. *Indoor Air* **16**, 392–401.

Petera, K. and Dostál, M. (2016). Heat transfer measurements and cfd simulations of an impinging jet. In *EPJ Web of Conferences*, volume 114. EDP Sciences.

Pope, S. (2000). *Turbulent Flows*. Cambridge University Press. ISBN 9781139643351.

Prasad, P. and Ravindran, R. (1985). *Partial Differential Equations*. New Delhi : Wiley Eastern. ISBN 0852267223.

Psikuta, A., Allegrini, J., Koelblen, B., Bogdan, A., Annaheim, S., Martínez, N., Derome, D., Carmeliet, J. and Rossi, R. M. (2017). Thermal manikins controlled by human thermoregulation models for energy efficiency and thermal comfort research – A review. *Renewable and Sustainable Energy Reviews* **78**, 1315–1330.

Ramalho, O., Wyart, G., Mandin, C., Blondeau, P., Cabanes, P.-A., Leclerc, N., Mullot, J.-U., Boulanger, G. and Redaelli, M. (2015). Association of carbon dioxide with indoor air pollutants and exceedance of health guideline values. *Building and Environment* , 1–10ISSN 03601323.

Rasche, S. B., Ullinger, M. B., Orfeld, M. M., Ebhardt, H. J. G. and Ischof, W. B. (2001). Why do Women Suffer from Sick Building Syndrome more often than Men? – Subjective Higher Sensitivity. *Indoor Air* **11**, 217–222.

Rathakrishnan, E. (2012). *Elements of Heat Transfer*. CRC Press. ISBN 9781439878910.

Refresh (2015). Webpage for Refresh: Remodelling building design sustainability from a human-centred approach - EPSRC Challenging Engineering award 2012. [Online]. [Accessed 2015-01-16]. Available from: `www.refresh-project.org.uk/`.

Richardson, L. F. (1911). The approximate arithmetical solution by finite differences of physical problems involving differential equations, with an application to the stresses in a masonry dam. *Philosophical Transactions of the Royal Society of London. Series A, Containing Papers of a Mathematical or Physical Character,* **210**, 307–357.

Roache, P. J. (1994). Perspective: A method for uniform reporting of grid refinement studies. *Journal of Fluids Engineering* **116**, 405–413.

Roache, P. J. (1997). Quantification of uncertainty in computational fluid dynamics. *Annual Review of Fluid Mechanics* **29**, 123–160.

Roache, P. J. (1998a). *Verification and Validation in Computational Science and Engineering*. Hermosa Publishers. ISBN 0913478083.

Roache, P. J. (1998b). Verification of Codes and Calculations. *AIAA Journal* **36**, 696–702. AIAA 0001-1452.

Roetzel, A., Tsangrassoulis, A., Dietrich, U. and Busching, S. (2010). A review of occupant control on natural ventilation. *Renewable and Sustainable Energy Reviews* **14**, 1001–1013.

Rostron, J. (1997). *Sick building syndrome: concepts, issues, and practice*. London: E & FN Spon. ISBN 9780419215301.

Rouse, H., Baines, W. and Humphreys, H. (1953). Free convection over parallel sources of heat. *Proceedings of the Physical Society. Section B* **66**, 393.

Runeson, R., Wahlstedt, K., Wieslander, G. and Norbäck, D. (2006). Personal and psychosocial factors and symptoms compatible with sick building syndrome in the Swedish workforce. *Indoor Air* **16**, 445–453.

Rupp, R. F., Vásquez, N. G. and Lamberts, R. (2015). A review of human thermal comfort in the built environment. *Energy and Buildings* **105**, 178–205. ISSN 03787788.

Russo, J. S., Dang, T. Q. and Khalifa, H. E. (2009). Computational analysis of reduced-mixing personal ventilation jets. *Building and Environment* **44**, 1559–1567.

Russo, J. S. and Khalifa, H. E. (2010). Cfd assessment of intake fraction in the indoor environment. *Building and Environment* **45**, 1968–1975.

Salmanzadeh, M., Zahedi, G., Ahmadi, G., Marr, D. R. and Glauser, M. (2012). Computational modeling of effects of thermal plume adjacent to the body on the indoor airflow and particle transport. *Journal of Aerosol Science* **53**, 29–39.

Santner, T. J., Williams, B. J. and Notz, W. I. (2003). *The Design and Analysis of Computer Experiments*. Springer. ISBN 0387954201.

Schellen, L., Loomans, M. G., Kingma, B. R., de Wit, M. H., Frijns, A. J. and van Marken Lichtenbelt, W. D. (2013). The use of a thermophysiological model in the built environment to predict thermal sensation: Coupling with the indoor environment and thermal sensation. *Building and Environment* **59**, 10–22.

Schweiker, M., Fuchs, X., Becker, S., Shukuya, M., Dovjak, M., Hawighorst, M. and Kolarik, J. (2017a). Challenging the assumptions for thermal sensation scales. *Building Research and Information* **45**, 572–589.

Schweiker, M., Kingma, B. R. M. and Wagner, A. (2017b). Evaluating the performance of thermal sensation prediction with a biophysical model. *Indoor Air* **27**, 1012–1021. ISSN 09056947.

Seppänen, O. and Fisk, W. J. (2002). Association of ventilation system type with SBS symptoms in office workers. *Indoor Air* **12**, 98–112.

Seppänen, O. and Fisk, W. J. (2003). A Conceptual Model to Estimate Cost Effectiveness of the Indoor Environment Improvements. In *Proceedings of the Healthy Buildings 2003 Conference, Singapore*.

Seppanen, O. and Fisk, W. J. (2005). A Model to Estimate the Cost Effectiveness of the Indoor Environment Improvements in Office Work. *ASHRAE Transactions* **111**, 663–679.

Seppänen, O., Fisk, W. J. and Faulkner, D. (2005). Control of Temperature for Health and Productivity in Offices Control of Temperature for Health and Productivity in Offices. *ASHRAE Transactions* **111**, 680–686.

Seppänen, O., Fisk, W. J. and Lei, Q. H. (2006a). Effect of Temperature on Task Performance in Office Environment. Technical report, Lawrence Berkeley National Laboratory.

Seppänen, O., Fisk, W. J. and Lei, Q. H. (2006b). Ventilation and performance in office work. *Indoor Air* **16**, 28–36.

Seppänen, O., Fisk, W. J. and Mendell, M. J. (2002). Ventilation Rates and Health. *ASHRAE Journal* **44**, 56–58.

Seppänen, O. A., Fisk, W. J. and Mendell, M. J. (1999). Association of Ventilation Rates and CO 2 -Concentrations with Health and other Responses in Commercial and Institutional Buildings. *Indoor Air* **9**, 226–252.

Serth, R. W. (2007). *Process Heat Transfer*. Academic Press.

Shan, X., Yang, E. H., Zhou, J. and Chang, V. W. (2018). Human-building interaction under various indoor temperatures through neural-signal electroencephalogram (EEG) methods. *Building and Environment* **129**, 46–53.

SI 1992/3004 (1992). Workplace (Health, Safety and Welfare) Regulations, Order 1992.

Simons, M., Waters, J. and White, P. (1999). Local mean age of air: Predictive techniques compared. *Building Services Engineering Research and Technology* **20**, 211–218.

Simonson, C. J., Salonvaara, M. and Ojanen, T. (2002). The effect of structures on indoor humidity – possibility to improve comfort and perceived air quality. *Indoor Air* **12**, 243–251.

Skyberg, K., Skulberg, K. R., Eduard, W., Skå ret, E., Levy, F. and Kjuus, H. (2003). Symptoms prevalence among office employees and associations to building characteristics. *Indoor Air* **13**, 246–252.

Sørensen, D. N. and Nielsen, P. V. (2003). Quality control of computational fluid dynamics in indoor environments. *Indoor Air* **13**, 2–17.

Sørensen, D. N. and Voigt, L. K. (2003). Modelling flow and heat transfer around a seated human body by computational fluid dynamics. *Building and Environment* **38**, 753–762.

Spalart, P. R. (1988). Direct Simulation of a Turbulent Boundary Layer up to Re_θ = 1410. *Journal of Fluid Mechanics* **187**, 61–98.

Spalart, P. R. and Allmaras, S. R. (1992). A one-equation turbulence model for aerodynamic flows. *AIAA-92-0439* .

Sun, W., Tham, K. W., Zhou, W. and Gong, N. (2007). Thermal performance of a personalized ventilation air terminal device at two different turbulence intensities. *Building and Environment* **42**, 3974–3983.

Sundell, J. (2004). On the history of indoor air quality and health. *Indoor Air* **14**, 51–58.

Sundell, J., Levin, H., Nazaroff, W. W., Cain, W. S., Fisk, W. J., Grimsrud, D. T., Gyntelberg, F., Li, Y., Persily, A. K., Pickering, A. C., Samet, J. M., Spengler, J. D., Taylor, S. T. and Weschler, C. J. (2011). Ventilation Rates and Health: Multidisciplinary Review of the Scientific Literature. *Indoor Air* **21**, 191–204.

Tanabe, S.-i., Haneda, M. and Nishihara, N. (2015). Workplace productivity and individual thermal satisfaction. *Building and Environment* **91**, 42–50.

Teodosiu, C., Ilie, V. and Teodosiu, R. (2014). Appropriate CFD Turbulence Model for Improving Indoor Air Quality of Ventilated Spaces. *Mathematical Modelling in Civil Engineering* **10**, 28–42.

Tham, K. W. (1993). Conserving Energy Without Sacrificing Thermal Comfort. *Building and Environment* **28**, 287–299.

Thynell, S. T. (1998). Discrete-ordinates method in radiative heat transfer. *International Journal of Engineering Science* **36**, 1651–1675.

Toftum, J. (2004). Air movement – good or bad? *Indoor Air* **14**, 40–45.

Tu, J., Yeoh, G. H. and Liu, C. (2008). *Computational FLuid Dynamics: A Practical Approach*. Butterworth-Heinemann. ISBN 9780750685634.

van Hoof, J. (2008). Forty years of Fanger's model of thermal comfort : comfort for all? *Indoor Air* **18**, 182–201.

van Hoof, J., Mazej, M. and Hensen, J. L. (2010). Thermal comfort: research and practice. *Frontiers in Bioscience* **15**, 765–788.

van Marken Lichtenbelt, W., Hanssen, M., Pallubinsky, H., Kingma, B. and Schellen, L. (2017). Healthy excursions outside the thermal comfort zone. *Building Research and Information* **45**, 819–827.

Versteeg, H. and Malalasekera, W. (2007). *An Introduction to Computational Fluid Dynamics : The Finite Volume Method*. Longman Scientific and Technical, 2 edition. ISBN 9789131274983.

Veselá, S., Kingma, B. R. and Frijns, A. J. (2017). Local thermal sensation modeling—a review on the necessity and availability of local clothing properties and local metabolic heat production. *Indoor Air* **27**, 261–272. ISSN 16000668.

Veselý, M. and Zeiler, W. (2014). Personalized conditioning and its impact on thermal comfort and energy performance – A review. *Renewable and Sustainable Energy Reviews* **34**, 401–408.

Voelker, C. and Alsaad, H. (2018). Simulating the human body's microclimate using automatic coupling of CFD and an advanced thermoregulation model. *Indoor Air* , 1–11ISSN 09056947.

Voelker, C., Maempel, S. and Kornadt, O. (2014). Measuring the human body's microclimate using a thermal manikin. *Indoor air* , 567–579.

Walters, D. K. and Cokljat, D. (2008). A three-equation eddy-viscosity model for reynolds-averaged navier–stokes simulations of transitional flow. *Journal of fluids engineering* **130**, 121401.

Wang, M., Lin, C. H. and Chen, Q. (2012). Advanced turbulence models for predicting particle transport in enclosed environments. *Building and Environment* **47**, 40–49.

Ward, I. C. (2004). *Energy and environmental issues for the practising architect: a guide to help at the*

initial design stage. London: Thomas Telford. ISBN 9780727732163.

Wargocki, P., Sundell, J., Bischof, W., Brundrett, G., Fanger, P. O., Gyntelberg, F., Hanssen, S. O., Harrison, P., Pickering, A., Seppänen, O. and Wouters, P. (2002). Ventilation and health in non-industrial indoor environments: report from a European Multidisciplinary Scientific Consensus Meeting (EUROVEN). *Indoor Air* **12**, 113–128.

Wargocki, P., Wyon, D. P., Baik, Y. K., Clausen, G. and Fanger, P. O. (1999). Perceived Air Quality, Sick Building Syndrome (SBS) Symptoms and Productivity in an Office with Two Different Pollution Loads. *Indoor Air* **9**, 165–179.

Wargocki, P., Wyon, D. P. and Fanger, P. O. (2000a). Productivity is affected by the air quality in offices. *Proceedings of Healthy Buildings* **1**, 635–640.

Wargocki, P., Wyon, D. P., Sundell, J., Clausen, G. and Fanger, P. O. (2000b). The Effects of Outdoor Air Supply Rate in an Office on Perceived Air Quality, Sick Building Syndrome (SBS) Symptoms and Productivity. *Indoor Air* **10**, 222–236.

Wilcox, D. C. (1994). *Turbulence Modeling for CFD*. DCW Industries, Inc. ISBN 0963605100.

Wolfshtein, M. (2009). Some comments on turbulence modelling. *International Journal of Heat and Mass Transfer* **52**, 4103–4107.

Wolkoff, P., Clausen, P. a., Jensen, B., Nielsen, G. D. and Wilkins, C. K. (1997). Are We Measuring the Relevant Indoor Pollutants? *Indoor Air* **7**, 92–106.

Wood, R. (2015). *Experimental and Theoretical Studies of Contaminant Transport Due to Human Movement in a Hospital Corridor*. Ph.D. thesis, University of Leeds.

Wu, W. and Lin, Z. (2015). An experimental study of the influence of a walking occupant on three air distribution methods. *Building and Environment* **85**, 237.e1–237.e8.

Wyon, D. P. (2004). The effects of Indoor Air Quality on Performance and Productivity. *Indoor Air* **14**, 92–101.

Xu, C., Nielsen, P. V., Liu, L., Jensen, R. L. and Gong, G. (2018). Impacts of airflow interactions with thermal boundary layer on performance of personalized ventilation. *Building and Environment* **135**, 31–41. ISSN 03601323.

Xu, J., Kim, J.-H., Hong, H. and Koo, J. (2015). A systematic approach for energy efficient building design factors optimization. *Energy and Buildings* **89**, 87–96.

Xu, X., Ni, S., Fu, M., Zheng, X., Luo, N. and Weng, W. (2017). Numerical investigation of airflow, heat transfer and particle deposition for oral breathing in a realistic human upper airway model. *Journal of thermal biology* **70**, 53–63.

Yang, B., Sekhar, S. C. and Melikov, A. K. (2010). Ceiling-mounted personalized ventilation system integrated with a secondary air distribution system–a human response study in hot and humid climate. *Indoor Air* **20**, 309–19.

Yang, J., Ni, S. and Weng, W. (2017). Modelling heat transfer and physiological responses of unclothed human body in hot environment by coupling CFD simulation with thermal model. *International Journal of Thermal Sciences* **120**, 437–445. ISSN 12900729.

Yoon, D. W., Sohn, J. Y. and Cho, K. H. (1999). The comparison on the thermal comfort sensation between the results of questionnaire survey and the calculation of the pmv values. In *Proceedings of Indoor Air 1999. Edinburgh*.

Zelensky, P., Barták, M., Hensen, J. and Vavricka, R. (2013). Influence of turbulence model on thermal plume in indoor air flow simulation. In *Proceedings of the 11th REHVA World Congress & 8th international Conference on IAQVEC (CLIMA 2013)," Energy efficient, smart and healthy buildings", June 16-19, 2013, Prague*.

Zhai, Y., Zhang, Y., Zhang, H., Pasut, W., Arens, E. and Meng, Q. (2015). Human comfort and perceived air quality in warm and humid environments with ceiling fans. *Building and Environment* **90**, 178–185.

Zhang, H., Arens, E., Huizenga, C. and Han, T. (2010a). Thermal sensation and comfort models for non-uniform and transient environments, part II: Local comfort of individual body parts. *Building and*

Environment **45**, 389–398.

Zhang, H., Arens, E., Huizenga, C. and Han, T. (2010b). Thermal sensation and comfort models for non-uniform and transient environments, part III: Whole-body sensation and comfort. *Building and Environment* **45**, 399–410.

Zhang, H., Arens, E. and Pasut, W. (2011). Air temperature thresholds for indoor comfort and perceived air quality. *Building Research & Information* **39**, 134–144.

Zhang, H., Huizenga, C., Arens, E. and Yu, T. (2005). Modeling Thermal Comfort in Stratified Environments. In *Proceedings of Indoor Air*.

Zhang, X., Su, G., Yu, J., Yao, Z. and He, F. (2015). PIV measurement and simulation of turbulent thermal free convection over a small heat source in a large enclosed cavity. *Building and Environment* **90**, 105–113.

Zhang, X., Wargocki, P., Lian, Z. and Thyregod, C. (2017). Effects of exposure to carbon dioxide and bioeffluents on perceived air quality, self-assessed acute health symptoms, and cognitive performance. *Indoor Air* **27**, 47–64.

Zhang, Z., Zhang, W., Zhai, Z. J. and Chen, Q. Y. (2007). Evaluation of Various Turbulence Models in Predicting Airflow and Turbulence in Enclosed Environments by CFD: Part 2—Comparison with Experimental Data from Literature. *HVAC&R Research* **13**, 871–886.

Zhao, Q., Zhao, Y., Wang, F., Wang, J., Jiang, Y. and Zhang, F. (2014). A data-driven method to describe the personalized dynamic thermal comfort in ordinary office environment: From model to application. *Building and Environment* **72**, 309–318.

Zukowska, D., Melikov, A. and Popiolek, Z. (2007a). Thermal plume above a simulated sitting person with different complexity of body geometry. In *Proc Roomvent*, volume 7.

Zukowska, D., Popiolek, Z. and Melikov, A. (2007b). Impact of personal factors and furniture arrangement on the thermal plume above a human body. *Roomvent 2007 : Proceedings of the 10th International Conference on Air Distribution in Rooms* **3**, 137–144.